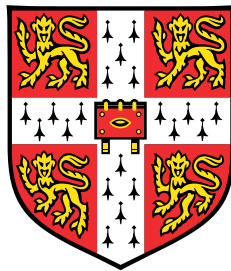


# First-principles structure prediction of extreme nanowires



**Jamie Michael Wynn**

Cavendish Laboratory  
University of Cambridge

This dissertation is submitted for the degree of  
*Doctor of Philosophy*

Christ's College

August 2018

Supervisor: Dr Andrew Morris



## Declaration

This thesis is the result of my own work and includes nothing which is the outcome of work done in collaboration except as when stated otherwise in the text. It is not substantially the same as any that I have submitted, or, is being concurrently submitted for a degree or diploma or other qualification at the University of Cambridge or any other University or similar institution except where specified in the text. It contains fewer than 60,000 words.

Parts of Chapter 3 have been published in the article:

J Wynn, PVC Medeiros, A Vasylenko, J Sloan, D Quigley, AJ Morris: “*Phase diagram of germanium telluride encapsulated in carbon nanotubes from first-principles searches*”, Physical Review Materials 1 (7), 073001, 2017.

Parts of Chapter 4 are included in an article under preparation:

J Wynn, PVC Medeiros, A Vasylenko, J Sloan, D Quigley, AJ Morris: “*First-principles predictions of the structure and Raman spectra of encapsulated AgCl nanowires*”.

The AIRSS code for low-dimensional systems described in Chapter 2 was also used in the following publications:

A Vasylenko, J Wynn, PVC Medeiros, AJ Morris, J Sloan, D Quigley: “*Boosting electronic transport in carbon nanotubes*”, Physical Review B 95 (12), 121408, 2017.

PVC Medeiros, S Marks, J Wynn, A Vasylenko, QM Ramasse, D Quigley, J Sloan, AJ Morris: “*Single-Atom Scale Structural Selectivity in Te Nanowires Encapsulated Inside Ultranarrow, Single-Walled Carbon Nanotubes*”, ACS Nano 11 (6), 6178, 2017

A Vasylenko, S Marks, J Wynn, PVC Medeiros, QM Ramasse, AJ Morris, J Sloan, D Quigley: *“Electronic Structure Control of Sub-nanometer 1D SnTe via Nanostructuring within Single-Walled Carbon Nanotubes“*, ACS Nano 12 (6), 6023, 2018

Jamie Michael Wynn

August 2018

## **Acknowledgements**

I am grateful to my supervisor, Andrew Morris, for his valuable advice and guidance throughout the project, and also to my collaborators, particularly Paulo Medeiros, Andrij Vasylenko and David Quigley. I would also like to thank the members of my research group and my CDT cohort for useful discussions. I am grateful to Matthew Evans, Angela Harper, James Darby, Can Kocer, Joseph Nelson, and Ben Irwin for proof-reading parts of the thesis, and also to Michael Rutter for technical support.



# Abstract

Low-dimensional systems are an important and intensely studied area of condensed matter physics. When a material is forced to adopt a low-dimensional structure, its behaviour is often dramatically different to that of the bulk phase. It is vital to predict the structures of low-dimensional systems in order to reliably predict their properties. To this end, the *ab initio* random structure searching (AIRSS) method, which has previously been used to identify the structures of bulk materials, has been extended to deal with the case of nanowires encapsulated inside carbon nanotubes. Such systems are a rapidly developing area of research with important nanotechnological applications, including information storage, energy storage and chemical sensing.

The extended AIRSS method for encapsulated nanowires (ENWs) was implemented and used to identify the structures formed by germanium telluride, silver chloride, and molybdenum diselenide ENWs. In each of these cases, a number of novel nanowire structures were identified, and a phase diagram predicting the ground state nanowire structure as a function of the radius of the encapsulating nanotube was calculated. In the case of germanium telluride, which is a technologically important phase-change material, the potential use of GeTe ENWs as switchable nanoscale memory devices was investigated.

The vibrational properties of silver chloride ENWs were also considered, and a novel scheme was developed to predict the Raman spectra of systems which can be decomposed into multiple weakly interacting subsystems. This scheme was used to obtain a close approximation to the Raman spectra of AgCl ENWs at a fraction of the computational cost that would otherwise be necessary. The encapsulation of AgCl was shown to produce substantial shifts in the Raman spectra of nanotubes, providing an important link with experiment.

A method was developed to predict the stress-strain response of an ENW based on a polygonal representation of its surface, and was used to investigate the elastic response of molybdenum diselenide ENWs. This was used to predict stress-radius phase diagrams for MoSe<sub>2</sub> ENWs, and hence to investigate stress-induced phase change within such systems.

The X-ray diffraction of ENWs was also considered. A program was written to simulate X-ray diffraction in low-dimensional systems, and was used to predict the diffraction patterns of some of the encapsulated GeTe nanowire structures predicted by AIRSS. By modelling the interactions within a bundle of nanotubes, diffraction patterns for bundles of ENWs were obtained.

# Contents

<b>Abbreviations</b>	<b>xi</b>
<b>1 Introduction</b>	<b>1</b>
1.1 Overview . . . . .	1
1.2 Encapsulated nanowires . . . . .	4
1.3 Carbon nanotubes and their properties . . . . .	7
<b>2 Methods</b>	<b>13</b>
2.1 Density functional theory . . . . .	13
2.1.1 Mean-field theories for the many-body problem . . . . .	13
2.1.2 The Hohenberg-Kohn theorems . . . . .	15
2.1.3 The Kohn-Sham equations and DFT . . . . .	15
2.2 DFT in practice . . . . .	17
2.3 Geometry optimisations . . . . .	22
2.4 Lattice vibrations . . . . .	23
2.5 Raman spectroscopy . . . . .	26
2.6 Molecular dynamics . . . . .	28
2.7 Crystal structure prediction . . . . .	29
2.8 Automated quasi-1D symmetry analysis . . . . .	34
2.9 AIRSS for encapsulated nanowires . . . . .	39
<b>3 Encapsulated GeTe nanowires and phase change</b>	<b>45</b>
3.1 Structure search . . . . .	46
3.2 Crystalline phases at finite temperatures . . . . .	55
3.3 Crystalline-amorphous phase change . . . . .	60
3.3.1 Molecular dynamics force field for GeTe . . . . .	61

---

3.3.2	Crystallisation from supercooled liquid . . . . .	64
3.3.3	Glass transition . . . . .	74
3.4	Ferroelectricity . . . . .	80
3.4.1	The Modern Theory of Polarisation . . . . .	81
3.4.2	Ising-like model . . . . .	86
3.5	Conclusion . . . . .	105
<b>4</b>	<b>Encapsulated AgCl nanowires and Raman spectroscopy</b>	<b>109</b>
4.1	Structure search . . . . .	109
4.2	Raman spectroscopy . . . . .	116
4.2.1	Linear chains . . . . .	117
4.2.2	Larger systems . . . . .	123
4.2.3	Double-walled nanotubes . . . . .	129
4.3	Conclusion . . . . .	132
<b>5</b>	<b>Encapsulated MoSe<sub>2</sub> nanowires and elasticity</b>	<b>135</b>
5.1	Structure search . . . . .	136
5.2	Elastic response . . . . .	146
5.2.1	Method . . . . .	146
5.2.2	Application to MoSe <sub>2</sub> nanowires . . . . .	152
5.3	Conclusion . . . . .	158
<b>6</b>	<b>Diffraction in ENWs</b>	<b>161</b>
6.1	Bundles of ENWs . . . . .	167
6.2	Conclusion . . . . .	173
<b>7</b>	<b>Conclusion</b>	<b>175</b>
	<b>Bibliography</b>	<b>179</b>

# Abbreviations

AIMD	Ab-initio molecular dynamics
AIRSS	Ab-initio random structure searching
BZ	Brillouin zone
CNT	Carbon nanotube
DFPT	Density functional perturbation theory
DFT	Density functional theory
DOS	Density of states
DRAM	Dynamical random access memory
DWNT	Double-walled nanotube
ENW	Encapsulated nanowire
FFT	Fast Fourier transform
FRAM	Ferroelectric random access memory
GGA	Generalised gradient approximation
GST	Germanium antimony telluride
LDA	Local density approximation

LHS	Left-hand side
LOWESS	Locally weighted scatterplot smoothing
MD	Molecular dynamics
MWNT	Multi-walled nanotubes
PES	Potential energy surface
PSO	Particle swarm optimisation
RBM	Radial breathing mode
RHS	Right-hand side
RMSE	Root-mean-squared error
SWNT	Single-walled nanotube
TEM	Transmission electron microscopy
TMDC	Transition metal dichalcogenides

# Chapter 1

## Introduction

### 1.1 Overview

A low-dimensional system is one whose size in one or more dimensions is restricted enough to alter its behaviour relative to the bulk phase. This change in behaviour has made low-dimensional materials the subject of significant interest in recent years [1–8], both because of their nanotechnological applications and because their exotic behaviour makes them physically interesting in their own right.

This thesis focuses on the first-principles prediction and analysis of quasi-1D materials – also known as nanowires – encapsulated inside carbon nanotubes. Originally discovered by Radushkevich and Lukyanovich in 1952 [9], and rediscovered by Iijima in 1991 [10], carbon nanotubes have drawn enormous research attention because of their unusual structure and remarkable properties. Their exceptional physical strength and chemical inertness means that they can both act as templates for the formation of nanowires inside their central cavity, and also protect those nanowires from external perturbations.

Because knowledge of the crystal structure of a material’s bulk phase is not sufficient to deduce the structures of its lower-dimensional allotropes, low-dimensional materials present a significant structure-prediction challenge even in systems which are well-characterised in the bulk. To this end, for this project the AIRSS (*Ab initio* random structure searching) method [11] has been adapted for the prediction of the structures of encapsulated nanowires.

Throughout this thesis, there is a particular focus on the thinnest possible nanowires, with radii of at most around 1 nm, and potentially as narrow as a single atom in diameter. This represents the very lowest possible length scale of a quasi-1D atomic system, so we will use the term ‘extreme nanowires’ to refer to them. While much research has focused on wider radii than these, it is at the small-radius limit considered in this thesis that the finite-size effects that differentiate the behaviour of 1D systems from 3D systems are at their most dramatic, which makes it a particularly interesting case to consider.

In this first chapter, the general background of this thesis is introduced, followed by a review of the theory, properties and prior research on carbon nanotubes and encapsulated nanowires (ENWs). Where a method is applied only in one particular section of the thesis, it is introduced in the relevant chapter in which it is applied, rather than in the first chapter.

In chapter 2, the computational methods used in this thesis for the prediction of encapsulated nanowires’ structures are described, with a particular focus on the adaptation of AIRSS for the prediction of quasi-1D materials.

In chapter 3, the AIRSS method is applied to the case of germanium telluride ENWs, and a number of novel structures are predicted. These predictions are shown to be in good agreement with published experimental imagery of GeTe ENWs. The properties of such ENWs are then studied from first principles. Finite temperature effects are introduced via phonon calculations within the harmonic approximation, and the presence of metastable structures is predicted at larger nanotube radii.

GeTe is an important phase-change material [12, 13], and in so far as those phase-change properties are preserved when encapsulated inside narrow carbon nanotubes, GeTe ENWs could form extremely compact and well-isolated memory elements in electronic devices. The phase-change properties of encapsulated GeTe nanowires were therefore studied, with a classical potential used to make the calculations tractable. The results suggest that phase-change properties persist even down to very narrow radii, and that the melting point is reduced, with the potential consequence that less energy could be required for switching. GeTe is also noted for its ferroelectric properties [14]. By performing first-principles calculations within the modern theory of polarisation [15], a ferroelectric distortion is predicted within a GeTe nanowire. By parameterising an Ising-like model using DFT calculations on GeTe nanowires,

the nature of ferroelectricity in GeTe nanowires, and its variation with respect to temperature and nanowire length, is studied.

Chapter 4 focuses particularly on the Raman spectroscopy of ENWs. First, the case of AgCl ENWs is studied via the AIRSS method, with a number of new structures identified once again. The Raman spectra of such nanowires are then considered. A novel method is introduced to obtain a good approximation to the Raman spectra of ENWs at a small fraction of the computational cost. This method is used to calculate the Raman spectra of AgCl nanowires encapsulated within both a single-walled and double-walled carbon nanotube.

In chapter 5, the structures of molybdenum diselenide ENWs are predicted. Transition metal dichalcogenides have drawn considerable research interest due to their layered structures. By applying the AIRSS method to MoSe<sub>2</sub> ENWs, predictions as to the ground-state structure as a function of the radius of the encapsulating nanotube are once again obtained. Because of the 2:1 stoichiometry of MoSe<sub>2</sub>, these structures are quite unusual in the low-radius limit, and a particularly notable case of an exceptionally strong bond between the nanowire and the nanotube occurs as a result of this. At larger radii, a number of phases derived from the layered bulk structure are identified, including two structures which constitute unusual instances of double-layered nanowires.

A formalism is then described for calculating the response of an ENW to applied stress, and applied to some MoSe<sub>2</sub> ENW structures predicted by the AIRSS search to be the ground state for certain nanotube radii. This involves converting the atomic structure of the nanowire into a polygonal representation of its surface, from which forces resulting from an applied stress may then be derived. One may then calculate the first-order response of the system to stress from a second-order representation of its Born-Oppenheimer surface. In this case, this representation of the Born-Oppenheimer surface is extracted from a density functional theory (DFT) harmonic phonon calculation, and the resulting stress response is analysed in terms of the system's normal modes.

In chapter 6, the theory of diffraction is applied to the case of ENWs. As part of this a code implementing said formalism was written, and is applied to some of the previously identified GeTe ENW structures. In addition, the case of a bundle of ENWs, which is often encountered experimentally [16–19], is considered within the context of diffraction. By parameterising an effective inter-nanotube interaction from DFT

calculations, the resulting effect on the diffraction pattern of a bundle of nanotubes is predicted.

Finally, Chapter 7 gives a summary of the thesis, and describes potential avenues for future work.

## 1.2 Encapsulated nanowires

After Iijima's 1991 rediscovery of carbon nanotubes (CNTs), interest soon followed in the possibility of filling nanotubes with another substance. In 1992, first-principles calculations predicted that CNTs exhibit a capillary effect capable of drawing molecules inside them [20], and in 1993, this effect was used experimentally to fill nanotubes with molten lead [21]. More recent studies have often used a vapour-phase method in which the substance of interest is placed in contact with the sample of CNTs to be filled and then sublimated at high temperature in a vacuum, so that the gas vapour then fills the nanotubes. The system is then cooled so that the substance solidifies, forming nanowires inside the nanotubes [22]. A steam-treating procedure is commonly used to open the ends of the nanotubes prior to filling [23, 24]. Usually the cooling process during which the filling material solidifies into a nanowire is performed slowly, which facilitates the formation of an ordered, crystalline phase [19, 16]; for example, ref. 24 reports the cooling of encapsulated metal halides down to below their melting point at a rate of  $0.42 \text{ K min}^{-1}$ .

As previously discussed, the confinement of a material to a single dimension may dramatically alter its behaviour. Perhaps the best example of this are carbon nanotubes themselves, which – despite an almost-unaltered local bonding structure – transform from semimetals, in the 2D case of a graphene sheet, into either metals or semiconductors in the case of a nanotube. This being the case, the confinement of materials to one dimension by encapsulating them inside carbon nanotubes offers the possibility of creating allotropes which differ hugely, both in terms of their structures and their functional properties, from the bulk. In many cases, such 1D substances may not even be mechanically stable as free-standing structures, and therefore may be impossible to create without the use of the nanotube as a confining mechanism, as has been shown to be the case for some nanowire structures made of tellurium [25]. In this case, ENWs

offer the possibility of forming and technologically utilising structures that otherwise could not even exist.

The study of encapsulated nanowires (ENWs) inside carbon nanotubes is a rapidly growing field of research, with numerous potential applications, of which an overview will now be given.

Carbon nanotubes have been used as chemical sensors, in which molecules adsorbed onto the surface are detected via the resulting modulation of the nanotube's electrical properties. The 1D geometry of the nanotubes is ideal because of its high surface area-to-volume ratio [26–28], which maximises the per-volume capacity for the adsorption of molecules. These devices work using the fact that when a molecule is adsorbed onto the surface, it functions as a dopant, and thereby affects the resistivity of the nanotube. These changes in resistivity are measured by passing a current through the nanotube. The nanotube thus functions as a so-called chemiresistor. It has been shown that in some cases, filling the nanotube can enhance this effect, increasing the performance of the gas sensor. For example, ref. 29 reports a threefold increase in the sensitivity of multi-walled carbon nanotube-based methane gas sensors upon filling the nanotube with vanadium oxide.

ENWs are also promising candidates in information storage. In contrast to the above example of chemical sensors, in which the nanowire is there to modulate the behaviour of the nanotube, in this case the nanotube functions simply to confine the nanowire and protect it from any external perturbations. The relative chemical inertness of carbon nanotubes makes them ideal for this application, and the compactness of the system means that ENW-based memory could have an extremely high information density. Ferromagnetic iron-cobalt ENWs, for example, have been proposed as high-density magnetic storage devices [30]. ENWs of germanium telluride, a well-known and heavily researched phase change material, have also been suggested as nanoscale phase-change memory devices [19], and a large part of Chapter 3 is devoted to investigating their potential as such.

An important potential application of nanowires is as building blocks in nanoscale electronic devices. As the demand for ever more compact transistors for semiconductor devices begins to near its physical limits, nanowire-based transistors have been identified as one possible way to extend the lifetime of Moore's law [31], and as a result there has been much interest in using semiconducting nanowires as components in transistors [32,

6, 33]. Metallic nanowires have also been studied for their potential applications as interconnects [34, 35]. Many nanowires are narrow enough that the phenomenon of conductance quantisation – which arises from the effects of the finite width of the nanowire on the electronic energy levels – becomes important. Encapsulating such nanowires inside carbon nanotubes has the additional advantage of protecting them from oxidation, which would otherwise affect the nanowire’s electronic properties [36]. Superconductivity has also been demonstrated in tin encapsulated nanowires [37].

Experiments show that metallic CNTs can be significantly better conductors than copper [38, 39], and nanotube-based transistors have been realised [40]. The insertion of a nanowire into a CNT can potentially affect the CNT’s electronic properties: encapsulating beryllium inside metallic carbon nanotubes has been predicted to decrease their resistivity by as much as a factor of a half by enhancing the decay of phonon modes that would otherwise contribute strongly to the resistivity by scattering with current-carrying electrons [41], thereby enhancing carbon nanotubes’ already-exceptional [42] conductivity.

ENWs have found a number of more novel applications. Nanothermometers consisting of CNTs filled with gallium have been created, in which the position of the meniscus level of gallium within the nanotube varies linearly with temperature due to thermal expansion. The thermometer is read by using a TEM microscope to identify the position of the meniscus and thus the temperature [43]. In this application the unusually small thermal expansion coefficient of carbon nanotubes [44] becomes useful, since one would otherwise have to account for the variation in the shape of the nanotube itself.

Nanotubes filled with copper iodide have been shown to function as nanoscale pipettes, with the application of a bias voltage allowing precise control of the amount of CuI released due to the resulting electromigration forces [45]. By choosing the sign of the applied field, material can be either deposited from the nanotube or drawn inside it. The fine manipulation of material on an atomic scale provided by such devices has potential uses in the fabrication of other nanoscale devices.

Carbon nanotubes have been employed as field-emission devices [46, 47], with electron emission induced by the application of an electric field. This phenomenon has potential applications in display technology and electron-beam devices, and there is evidence that these field-emission properties may be enhanced via the encapsulation of ferromagnetic nanowires inside the nanotube [48].

In addition to the applications of encapsulated nanowires, carbon nanotubes can act as templates for the synthesis of nanowires [49–52]. The nanotubes’ chemical inertness and the possibility of controlling the radius of the central cavity via the selection of an appropriate chiral vector makes them highly useful for such a role. Having synthesised the nanowires using carbon nanotubes as templates, they can then be used for any of the broad range of technological purposes for which free-standing nanowires have been applied. These include chemical sensing [53–56], in which, just as in the case of nanotube chemical sensors, the 1D geometry of the system maximises the capacity for adsorbed molecules. Additionally, so-called ‘forests’ of aligned nanowires are an intensively studied option for next-generation solar photovoltaics (PV) [57–59]. Nanowire-based solar cells have been shown to provide exceptional power output [5], but are somewhat limited by their high production cost compared to traditional solar PV materials such as crystalline silicon, and significant research efforts have been directed at finding manufacturing processes to create such materials cheaply [60]. Nanowires have also been investigated for use as optical fibres [61].

In summary, encapsulated nanowires represent a large and relatively unexplored class of materials whose properties can differ significantly relative to the bulk, often with important nanotechnological applications. Because their structures can bear little resemblance to the bulk, predicting their structures is essential in order to understand their behaviour. This thesis presents a fully general methodology for predicting the structures of ENWs from first principles, describes some applications of this methodology from which novel nanowire structures have been identified, and presents prediction and analysis of the properties of these structures.

## 1.3 Carbon nanotubes and their properties

In terms of the allotropes it can form, carbon is an exceptionally versatile element. In the bulk the most well-known polymorphs are diamond and graphite, but there is also Lonsdaleite, which is formed under high pressure and was discovered in 1967 in the traces of a meteor impact [62]. Under certain conditions, it has also been shown to amorphise [63]. In addition to these, carbon also possesses lower-dimensional allotropes with a number of remarkable properties. In 2D it forms graphene, which is equivalent to a single layer of graphite [64].

The electronic configuration of the carbon atom is  $1s^2 2s^2 2p^2$ . In graphene (and graphite), the valence  $2s$  and  $2p$  orbitals hybridise to form three in-plane orbitals pointing towards the three neighbouring carbon atoms, and a single unhybridised  $p$  orbital whose lobes are oriented out of the plane [65]. This process is known as  $sp^2$  hybridisation. Each  $sp^2$  orbital then bonds covalently with the corresponding  $sp^2$  orbital from a neighbouring C atom, forming a  $\sigma$  bond. The remaining  $p$  orbitals also bond with the corresponding  $p$  orbitals of the neighbouring C atoms, forming  $\pi$  bonds. The  $\pi$  bonds in graphene are particularly crucial, because they are weaker than the  $\sigma$  bonds and as a result form the states around the Fermi level, with bonding states just below it and antibonding states just above it.

The structure of graphene, along with its basis vectors, is shown on fig. 1.1. The electronic structure of graphene near the Fermi level can be described quite accurately via a tight-binding approach in which only the  $\pi$  orbitals are considered. The tight-binding derivation is given in full in ref. 66, and shows that that the band structure resulting from this method is given approximately by

$$E(\mathbf{k}) - \mu = \pm \gamma_0 \sqrt{3 + 2 \cos(\mathbf{k} \cdot \mathbf{a}_1) + 2 \cos(\mathbf{k} \cdot \mathbf{a}_2) + 2 \cos(\mathbf{k} \cdot (\mathbf{a}_1 - \mathbf{a}_2))} \quad (1.1)$$

where  $\mu$  is the Fermi level,  $\mathbf{a}_1$  and  $\mathbf{a}_2$  are the lattice vectors as shown on fig. 1.2, and the  $\pm$  sign indicates either the conduction or the valence band.  $\gamma_0$  is a hopping matrix element between nearest-neighbour  $p$  orbitals which is usually treated in practice as a fitting parameter. This band structure is plotted on fig. 1.2.

A particularly notable property of graphene's band structure is that, near the Fermi level, the dispersion is linear. The points in  $k$ -space at which this occurs – which are clearly visible on fig. 1.2 – are known as Dirac cones. This has important consequences for transport properties, since the effective electron mass – which plays an important role in the electronic transport resulting from an applied electric field – is determined by the second derivative of the energy with respect to  $\mathbf{k}$ . As a result, the effective electron mass near the Fermi level in graphene is zero. The name 'Dirac cone' derives from the fact that such a system of massless fermions may be described by the Dirac equation [67].

A carbon nanotube is a quasi-1D material which may be regarded as a graphene sheet which has been rolled up to form a tube. With the lattice vectors shown on fig. 1.1, the first step to transforming from the geometry of graphene to that of a carbon nanotube

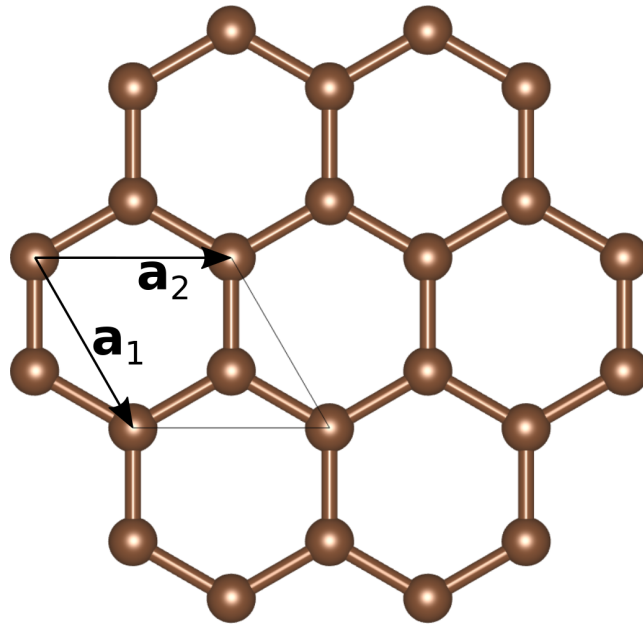


Figure 1.1 The hexagonal structure of graphene, with the primitive unit cell and the associated lattice vectors  $\mathbf{a}_1$  and  $\mathbf{a}_2$  indicated.

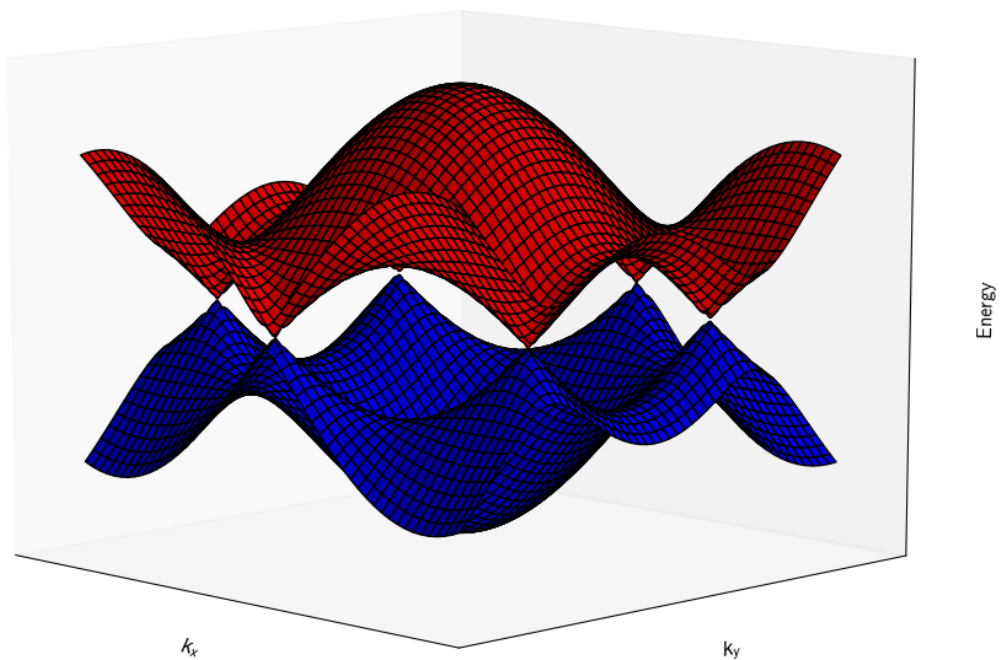


Figure 1.2 The tight-binding band structure of graphene, showing the valence band in blue and the conduction band in red.

is to define the chiral vector,

$$\mathbf{C} = n\mathbf{a}_1 + m\mathbf{a}_2. \quad (1.2)$$

This vector is defined as the vector along which the graphene sheet is ‘rolled up’ to form the tube, i.e. travelling parallel to  $\mathbf{C}$  corresponds to traveling around the diameter of the tube. Because of this, it is necessary that the graphene structure is periodic with respect to translations by  $\mathbf{C}$ . This means that  $\mathbf{C}$  must be a lattice vector, and so  $n$  and  $m$  must be integers. This discretisation has a number of important consequences for the structures and properties of nanotubes, as will be shown later.

One can also obtain from eq. 1.2 the radius of the nanotube in terms of  $n$  and  $m$ :

$$R = \frac{|\mathbf{C}|}{2\pi} = \frac{\sqrt{3}a_0}{2\pi} \sqrt{n^2 + m^2 + nm}, \quad (1.3)$$

where  $a_0$  is the bond length between adjacent carbon atoms.

Having defined the chiral vector, the lattice vector of the nanotube,  $\mathbf{T}$ , (nanotubes have only one lattice vector because they are periodic only in one direction) is then fixed by the requirement that it must point perpendicularly to  $\mathbf{C}$ . As with the chiral vector, the structure must be periodic with respect to translations through  $\mathbf{T}$ , and therefore it must be a lattice vector:

$$\mathbf{T} = p\mathbf{a}_1 + q\mathbf{a}_2, \quad (1.4)$$

with integer  $p$  and  $q$ . By imposing orthogonality between  $\mathbf{T}$  and  $\mathbf{C}$ , one can obtain [68]

$$\mathbf{T} = \frac{2m+n}{d_R}\mathbf{a}_1 - \frac{2n+m}{d_R}\mathbf{a}_2, \quad (1.5)$$

where  $d_R = d$  if  $n - m$  is a multiple of  $3d$ , and  $d_R = 3d$  otherwise. Here  $d$  is the highest common divisor of  $n$  and  $m$ .

From eq. 1.5, one can also derive the periodic length of the nanotube:

$$L = |\mathbf{T}| = \frac{\sqrt{3}}{d_R}R, \quad (1.6)$$

where  $R$  is the nanotube’s radius as given by eq. 1.3.

The radius and periodicity of a carbon nanotube are therefore uniquely determined by the chiral vector  $(n, m)$ , and can only adopt discrete set of values. Nanotubes

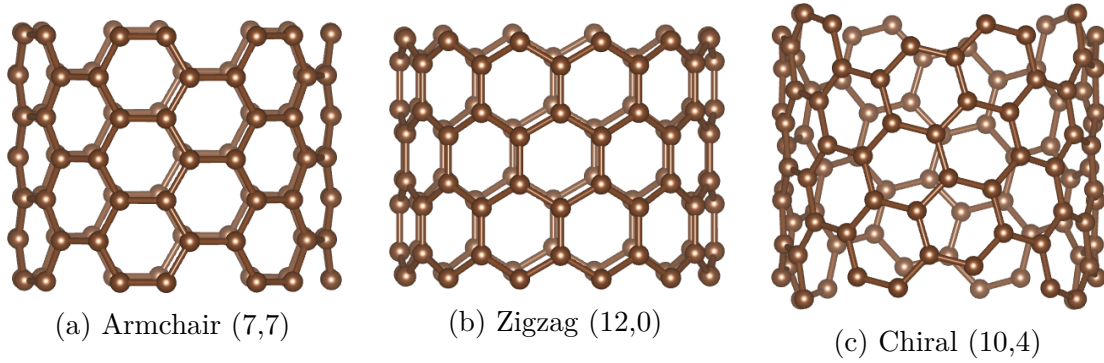


Figure 1.3 Examples of the three classes of carbon nanotubes.

are conventionally grouped based on their chiral vectors into three main categories: armchair nanotubes, for which  $n = m$ ; zigzag nanotubes, for which  $n > 0$  and  $m = 0$ ; and chiral nanotubes, for which  $n$  and  $m$  are nonzero but not equal [69]. An example of each of these categories is shown on fig. 1.3.

Because of the analogy between the physical structure of a nanotube and a graphene sheet, their electronic structures are also deeply linked. In fact, to a good approximation, one may obtain the band structure of a carbon nanotube from that of graphene by simply identifying the set of graphene  $\mathbf{k}$ -points which are commensurate with the periodicity of the nanotube (i.e. which satisfy  $\mathbf{k} \cdot \mathbf{C} = 2\pi s$  for some integer  $s$ ). This is known as the zone-folding approximation [66], and its validity is generally stronger in wider nanotubes whose curvature is less extreme, and in which the local bonding environments of the carbon atoms are therefore more similar to those found in graphene.

The zone-folding approximation implies that the most important factor in determining a nanotube's electronic structure is whether any of the Dirac points are commensurate with the periodicity of the nanotube. If they are, then it follows that the nanotube is a metal. One can show [69] that the condition for this to occur is

$$2n + m = 3s, \quad (1.7)$$

with  $s$  an integer. It follows immediately that all armchair nanotubes are conducting (since  $n = m$ ), and that, of the zigzag and chiral nanotubes, some are conductors and others are not (depending on the particular values of  $n$  and  $m$ ).

Due to the 1D nature of CNTs, their densities of states exhibit a number of van Hove singularities, an example of which is shown on fig. 5.3. These occur whenever one of the bands exhibits a stationary point, since each band's contribution to the density of states at a particular energy is inversely proportional to the band gradient at that energy [70]. These singularities have important consequences for the optical properties of nanotubes, with unusually sharp features in the absorption spectrum corresponding to transitions between the van Hove singularities [71].

Thanks to their unusual properties, a huge number of applications for carbon nanotubes have been identified, some hypothetical and some already realised. The strength of the covalent carbon bonds in CNTs gives them exceptional tensile strength of the order of tens of GPa, placing them amongst the strongest materials ever discovered [72, 73]. CNTs can also be woven into flexible yet exceptionally strong 2D sheets [74], whose strength has led to their identification as a potential material to form the tether of a space elevator [75].

In medicine, they have been proposed as vehicles for drug delivery, via the functionalisation of active molecules on their surfaces [76], and as probes for biological imaging [77] (although there are also long-standing questions over their biological toxicity [78]).

The focus of this section, and (for the most part) of this thesis as a whole, has been on so-called single-walled nanotubes (SWNTs). However, there also exist multi-walled nanotubes (MWNTs) which consist of multiple concentrically nested SWNTs. These systems have their own distinct properties with their own distinct applications. For example, double-walled nanotubes (DWNTs) have been used in the experimental implementation of nanoscale linear bearings [79].

# Chapter 2

## Methods

### 2.1 Density functional theory

#### 2.1.1 Mean-field theories for the many-body problem

To describe the behaviour of solid-state materials quantum-mechanically, one must in principle solve the Schrödinger equation for the many-body wavefunction of the electrons and nuclei. However, the large difference in mass between the electrons and the nuclei leads to a separation of timescales such that the nuclei move much more slowly than the electrons, and as a result one can (to a good approximation) solve for the behaviour of the electrons by treating them as moving in the purely classical Coulomb potential of nuclei fixed in space; this approach is known as the Born-Oppenheimer approximation [80]. The time-independent Schrödinger equation for the many-body electron wavefunction,  $\psi$ , then becomes (in atomic units) [81]

$$E\psi = \left[ -\frac{\hbar^2}{2m_e} \sum_i \nabla_i^2 + \sum_{i,j>i} \frac{e^2}{|\mathbf{r}_i - \mathbf{r}_j|} + \sum_{i,\alpha} \frac{-Z_\alpha e^2}{|\mathbf{r}_i - \mathbf{R}_\alpha|} + \sum_{\alpha,\beta>\alpha} \frac{Z_\alpha Z_\beta e^2}{|\mathbf{R}_\alpha - \mathbf{R}_\beta|} \right] \psi, \quad (2.1)$$

where sums over Latin indices are over electrons, and sums over Greek indices are over nuclei. The  $\mathbf{r}_i$  and  $\mathbf{R}_\alpha$  are the electronic position operators and nuclear positions, respectively, and  $Z_\alpha$  is the proton number of nucleus  $\alpha$ , and  $\nabla_i^2$  is the Laplacian with respect to the position of the  $i$ -th electron.  $E$  is the total energy,  $e$  is the elementary charge,  $m_e$  is the electron mass, and  $\hbar$  is the reduced Planck constant.

Even with the Born-Oppenheimer approximation, this equation rapidly becomes unsolvable in practice, because the cost to do so scales exponentially with the number of electrons ( $\psi$  is a function of  $3N$  variables, where  $N$  is the number of electrons). This problem may be tackled within the Hartree approximation by treating each electron as moving in the averaged Coulomb potential of all of the others. As a result, the  $i$ -th electron is subject to a potential [81]

$$V_H^i(\mathbf{r}) = \sum_{j \neq i} \int d^3\mathbf{r}_j \frac{|\phi_j(\mathbf{r}_j)|^2}{|\mathbf{r}_i - \mathbf{r}_j|}, \quad (2.2)$$

where the sum is over all electrons other than the  $i$ -th electron, and  $\phi_i$  is the orbital occupied by the  $i$ -th electron. Each electron's behaviour is now described by a one-electron Schrödinger equation in which it is coupled to all of the other electrons indirectly via its interaction with the Hartree potential, eq. 2.2. The many-body problem is thereby replaced with a single-particle picture in which each particle experiences an effective potential  $V_H^i$ . This makes calculations on many-electron systems tractable, but at the cost of a decrease in accuracy because the effects of exchange and correlation are neglected. The former is an interaction arising from the antisymmetry of many-body fermion wavefunctions [82]; the latter refers to the error arising from the fact that within the true many-body wavefunction, the electrons become correlated, whereas the Hartree approach describes them as though they were independent (by assigning each electron to a different single-particle state, and allowing them to interact only indirectly via the Hartree potential) [83].

The Hartree-Fock equations are a more sophisticated development of this concept in which electrons interact indirectly with each other not only via the Hartree potential, eq. 2.2, but also via a term describing the exchange interaction resulting from the antisymmetry of the many-fermion wavefunction. This method corresponds to a many-body electron wavefunction derived from a single Slater determinant [84], which correctly behaves antisymmetrically under permutation of electron indices, but neglects the full effects of electron correlation.

Taking these ideas to their conclusion, one might wonder whether a mean-field theory could be constructed along the same lines of the Hartree or Hartree-Fock theory but which can give exactly correct answers – in other words, can the effective potential within a single-particle picture be chosen to give answers which match precisely with

the exact many-body results? The answer is, in principle, yes, as the following section will explain.

### 2.1.2 The Hohenberg-Kohn theorems

The Hohenberg-Kohn theorems [85] are general results for quantum-mechanical systems interacting with external potentials, so they apply to all condensed-matter systems of many electrons interacting with nuclei via the Coulomb potential. These theorems form the theoretical foundation of density-functional theory. The first theorem states that there exists a one-to-one mapping between the external potential  $V_{\text{ext}}(\mathbf{r})$  and the electron number density  $n(\mathbf{r})$ . This implies that the electron density contains, in principle, sufficient information to infer  $V_{\text{ext}}$  and hence construct the many-body Schrödinger equation and solve it. Since this would give the ground-state energy of the system, it therefore follows that the ground state energy must be some functional of the number density. Having established this, the second Hohenberg-Kohn theorem proves that there exists a variational principle associated with this functional; in other words, the ground state electron density  $\rho_{\text{gs}}$  is that which minimises the total energy  $E$ :

$$\rho_{\text{gs}} = \arg \min_{\rho} E[\rho], \quad (2.3)$$

where the square brackets indicate that  $E$  is a functional on  $\rho$ .

### 2.1.3 The Kohn-Sham equations and DFT

The Kohn-Sham equations [86] build on the Hohenberg-Kohn theorems to convert the variational principle for the number density into a practically solvable problem. The first step in deriving the equations is to write the total energy of the system as

$$E_{\text{tot}} = T_0[n] + \int V_{\text{ext}}(\mathbf{r})n(\mathbf{r})d^3\mathbf{r} + \int V_H(\mathbf{r})n(\mathbf{r})d^3\mathbf{r} + E_{\text{xc}}[n]. \quad (2.4)$$

In order, the terms in the right-hand side of the above are the kinetic energy, the interaction between the electrons and the external potential, the interaction between the electrons and the Hartree potential, and finally the so-called exchange-correlation functional, which is an error term defined to contain all contributions to the energy not captured by the preceding three terms. The existence of this functional follows from

the Hohenberg-Kohn theorems. Note that the kinetic energy term,  $T_0[n]$ , is defined not as the true kinetic energy of the system, but as that of a non-interacting system with the same number density. Any difference between this and the true kinetic energy is (by definition) included in the exchange-correlation functional.

Having written the energy in this way, one can impose a Lagrange multiplier,  $\mu$ , to fix the total number of electrons and then find the Euler-Lagrange equations corresponding to the minimisation of the energy functional eq. 2.4, which are (where  $\delta$  denotes a functional derivative)

$$\frac{\delta T_0}{\delta n(\mathbf{r})} + V_{\text{ext}}(\mathbf{r}) + \int \frac{n(\mathbf{r}')}{|\mathbf{r} - \mathbf{r}'|} d^3\mathbf{r}' + \frac{\delta E_{\text{xc}}}{\delta n(\mathbf{r})} = \mu. \quad (2.5)$$

However, exactly the same Euler-Lagrange equations would be obtained if one were to minimise the total energy of a system of non-interacting fermions moving in an effective potential, with the single-particle states being solutions to a Schrödinger equation,

$$-\frac{\hbar^2}{2m} \nabla^2 \phi + V_{\text{eff}}(\mathbf{r})\phi = \epsilon\phi, \quad (2.6)$$

with the effective potential,  $V_{\text{eff}}$ , chosen as

$$V_{\text{eff}}(\mathbf{r}) = V_{\text{ext}}(\mathbf{r}) + V_H(\mathbf{r}) + \frac{\delta E_{\text{xc}}}{\delta n(\mathbf{r})}, \quad (2.7)$$

in order to match eq. 2.5. This shows that, for a system of interacting electrons, the ground state number density can be calculated by solving a fictitious system of noninteracting fermions coupled to the number density via a suitably chosen effective potential. This represents the logical endpoint of the Hartree and Hartree-Fock approaches, since the result is a mean-field theory whose accuracy is in principle perfect. However, the exchange-correlation functional cannot be determined precisely, and must therefore be approximated. As a result, while DFT is in principle exact, in practice its accuracy is limited by that of the approximation used for the exchange-correlation functional (in addition to considerations of numerical accuracy).

A vast array of schemes to approximate the exchange-correlation functional have been proposed over the years. The simplest is the surprisingly accurate local density approximation (LDA), in which the exchange-correlation energy density at a point in space is approximated using the corresponding exchange-correlation energy density of a free electron gas  $\epsilon^{\text{FEG}}$  at that same number density [87], which is then integrated

over all space to give an expression for the total exchange-correlation energy:

$$E_{xc}^{\text{LDA}}[n] = \int \epsilon^{\text{FEG}}(n(\mathbf{r})) d^3\mathbf{r} \quad (2.8)$$

More complex approximations for  $E_{xc}$  include terms in the exchange-correlation energy density which depend on the gradient of the exchange-correlation functional rather than its value alone, as in the commonly used PBE (Perdew, Burke and Ernzerhof) functional [88].

The solution of equation 2.6 is the central objective in density-functional theory. Since the orbitals depend on the number density but the number density depends on the orbitals, the equation must be solved self-consistently for  $n(\mathbf{r})$ ; in other words, a set of Kohn-Sham orbitals must be identified such that the number density resulting from the orbitals leads to a Kohn-Sham equation whose solutions are that same set of orbitals. In practical DFT calculations this results in a loop in which  $n(\mathbf{r})$  is iterated to self-consistency, which is shown in fig 2.1.

## 2.2 DFT in practice

So far, density-functional theory has been described in a purely mathematical way. What follows is a brief overview of the methods used to apply the theory practically to real systems.

One of the most fundamental choices that must be made in implementing density-functional theory is the choice of basis set. A given Kohn-Sham orbital,  $|\phi\rangle$ , is in practice represented with respect to some basis:

$$|\phi\rangle = \sum_{\alpha} c_{\alpha} |\chi_{\alpha}\rangle \quad (2.9)$$

Throughout this work, the DFT code CASTEP [89] is used for all electronic structure calculations (except when stated otherwise). CASTEP represents the orbitals using a plane wave basis set. This choice has several advantages: periodic boundary conditions are built in naturally, making it well-suited for calculations on crystals, and the simplicity and universality of the basis makes it applicable to a wide range of systems. Because there are an infinite number of plane waves commensurate with the periodicity of a given unit cell, the plane-wave basis is therefore in principle infinite as well. To

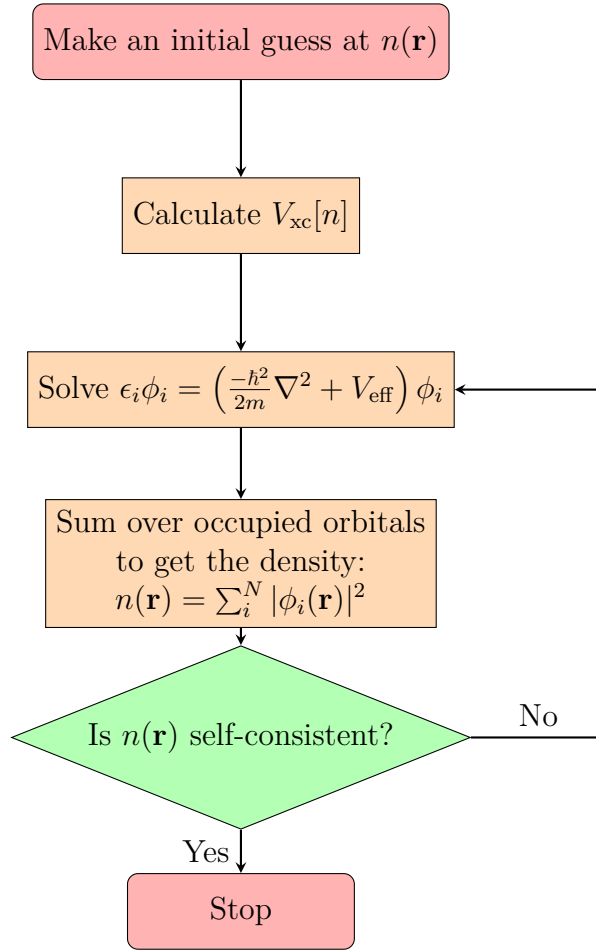


Figure 2.1 Flowchart showing the general process by which the Kohn-Sham equations are solved self-consistently in DFT.

deal with this, the basis is truncated so that it only contains plane waves below a certain energy. This causes an error in the calculation, and the result must therefore be converged with respect to the chosen basis set cut-off to ensure that this error is not unacceptably large.

Another approach taken by some DFT codes is to use a basis of orbitals that are similar to atomic orbitals. This means that relatively few basis functions are required, but convergence with respect to the basis set is more complex because atomic orbitals are characterised by multiple quantum numbers whereas plane waves are determined purely by their wavevector. Additionally, spurious forces can arise due to the fact that the basis orbitals move with the nuclear positions. However, one important benefit of using such localised basis sets is that linear scaling may become possible. In principle, the computational cost of DFT scales as  $O(N^3)$  where  $N$  is the number of atoms.

With a localised basis set, however, matrices such as overlap matrices between basis functions become ‘nearsighted’, with matrix elements only becoming large for basis functions that are in close proximity to each other. By exploiting this property, one can solve the Kohn-Sham equations in  $O(N)$  computational time, as implemented in e.g. the Siesta code [90]. A similar approach is taken by the ONETEP code, which achieves linear scaling using the nearsightedness of the single-particle density matrix for a dynamically optimised basis of local orbitals known as nonorthogonal generalised Wannier functions (NGWFs) [91].

In the case of systems whose Hamiltonians are periodic in space, such as crystals, the form of the solutions is given by

$$\phi_{\mathbf{k}}(\mathbf{r}) = e^{i\mathbf{k}\cdot\mathbf{r}}u_{\mathbf{k}}(\mathbf{r}), \quad (2.10)$$

where  $u_{\mathbf{k}}(\mathbf{r})$  has the periodicity of the unit cell. This result is known as Bloch’s theorem [92]. As a consequence of this theorem, the set of Kohn-Sham orbitals and energies varies continuously with the crystal momentum,  $\mathbf{k}$ . An important aspect of Bloch’s theorem is that  $k$ -space is *periodic*. That is, the Bloch function in eq. 2.10 could also be rewritten as

$$\phi_{\mathbf{k}}(\mathbf{r}) = e^{i(\mathbf{k}-\mathbf{q})\cdot\mathbf{r}}(e^{i\mathbf{q}\cdot\mathbf{r}}u_{\mathbf{k}}(\mathbf{r})), \quad (2.11)$$

and if  $e^{i\mathbf{q}\cdot\mathbf{r}}$  has the periodicity of the unit cell, then so will the function  $e^{i\mathbf{q}\cdot\mathbf{r}}u_{\mathbf{k}}(\mathbf{r})$ . In this case the original Bloch function of crystal momentum  $\mathbf{k}$  has been rewritten as a Bloch function of crystal momentum  $\mathbf{k} - \mathbf{q}$  with a different cell-periodic part. The set of vectors  $\mathbf{q}$  satisfying the condition that  $e^{i\mathbf{q}\cdot\mathbf{r}}$  has the periodicity of the cell define a lattice known as the *reciprocal lattice*. As a result, all physically possible orbitals can be expressed using a crystal momentum that lies inside the unit cell of the reciprocal lattice; any orbital whose crystal momentum lies outside this unit cell may be translated inside it via the above argument. This reciprocal lattice unit cell is known as the Brillouin zone (BZ).

Any quantity which is a sum over all occupied orbitals then becomes an integral over the BZ; the band energy, for example, is

$$E = \int_{BZ} \sum_{n,\text{occ}} \epsilon_n(\mathbf{k})d^3\mathbf{k}, \quad (2.12)$$

where the sum is over all occupied Kohn-Sham eigenstates, and  $\epsilon_n(\mathbf{k})$  is the energy of the  $n$ -th occupied eigenstate with crystal momentum  $\mathbf{k}$ . In practice it is of course impossible to numerically integrate over all crystal momenta  $\mathbf{k}$  within the BZ. The integral is therefore approximated by a sum over a discrete set of  $\mathbf{k}$ -values throughout the BZ, with the Kohn-Sham orbitals computed at each  $\mathbf{k}$ . Similarly to the finite basis set cutoff, the calculation must be converged with respect to the accuracy with which the BZ is sampled. The most common scheme chosen for this sampling is the Monkhorst-Pack scheme, consisting of a grid of points uniformly spaced in the BZ [93]. As this Monkhorst-Pack grid becomes finer and finer, the accuracy of the total energy and other derived quantities asymptotically approaches the true value of the integral over the BZ.

In general, core electrons will remain tightly bound to the nucleus and largely impervious to other factors such as interactions with other nuclei. As a result, time spent solving the Kohn-Sham equations for core states is largely time wasted. To ‘freeze’ the core electrons in place and thereby save that time would therefore be very beneficial. This leads to the idea of a pseudopotential, an effective potential describing the potential experienced by the valence electrons due to both the nucleus and the core electrons.

Pseudopotentials are generally constructed by first performing a DFT calculation on an isolated atom of the element in question that includes every electron, including the core electrons. This so-called ‘all-electron’ calculation generates the orbitals of both the core and valence electrons. Then, the core electrons are removed, and a potential is constructed which, when applied to the valence electrons, gives valence orbitals which – beyond a chosen distance from the nucleus – give the same orbitals as in the all-electron case. Fig. 2.2 shows an example of this: the pseudo-wavefunction and the all-electron wavefunction agree outside of the chosen core radius. One can also see that the pseudopotential has been chosen so that the pseudo-wavefunction oscillates more slowly in the vicinity of the nucleus than in the all-electron case. This is another advantage of pseudopotentials, since it enables a lower basis set cut-off to be used.

The actual procedure of constructing an appropriate pseudopotential is not uniquely defined, and a number of schemes exist [94–96]. Commonly the task is treated as an optimisation problem in which one wants to simultaneously maximise the agreement between the pseudo-wavefunction and all-electron wavefunction outside the chosen

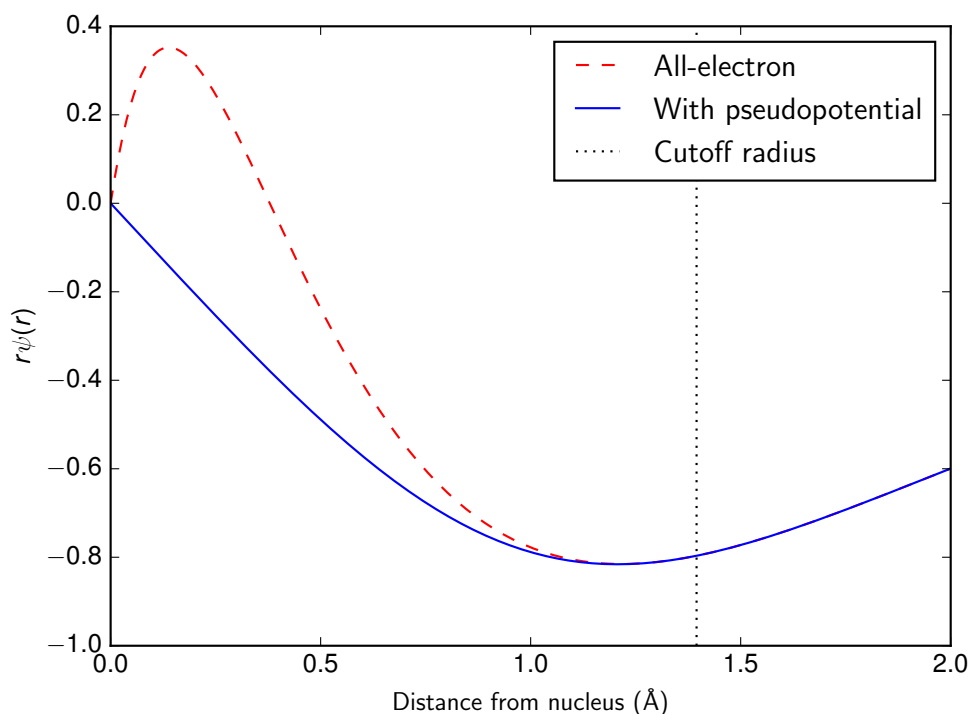


Figure 2.2 A  $2s$  state of an isolated carbon atom shown both as calculated from an all-electron calculation, and with a pseudopotential generated by CASTEP.

cutoff radius, whilst minimising the extent to which high-frequency components are present in the plane-wave expansion of the pseudo-wavefunction.

Because pseudopotentials are constructed with a particular system as a reference, this only guarantees that the pseudopotential gives the same answers for that particular reference system. When pseudopotentials are used with systems other than that used to perform the all-electron calculation, there is inevitably some level of error. The extent to which a pseudopotential can give accurate results for a range of different systems is known as its transferability. Pseudopotentials which have larger radii and which treat more electrons as core are computationally cheaper, but also less transferable.

The two most commonly used varieties of pseudopotential are norm-conserving [97] and ultrasoft [98] pseudopotentials. One of the conditions imposed on norm-conserving pseudopotentials is that, for each valence orbital, the total charge contained within the cutoff radius of each atom must be the same for both the all-electron wavefunction and the pseudo-wavefunction. Ultrasoft pseudopotentials relax this condition, which allows the pseudopotential to be more effectively chosen to minimise any high-frequency components in the pseudo-wavefunction. However, the cost is that this missing charge

– known as the *augmentation charge* – must be put back in to construct the total charge density, and this adds an extra layer of complexity since terms involving the augmentation charge then appear in the equations. This problem is especially acute where derivatives with respect to the density are required, as in the case of density functional perturbation theory (DFPT) [99].

## 2.3 Geometry optimisations

One of the most common calculations performed within DFT is that of geometry optimisation. This refers to the relaxation of a structure into a local minimum of the energy landscape. After this relaxation the forces will all be zero (to within some tolerance). This involves repeatedly solving the Kohn-Sham equations, calculating the forces, and then applying an optimisation algorithm to minimise the energy based on those calculated forces. The simplest approach would be to perform the calculation via a method in which an atomic position is slightly perturbed and the derivative of the energy with respect to it is calculated via a finite difference method by solving the Kohn-Sham equations repeatedly. However, this would be very expensive, especially with increasing system size. Fortunately, the forces can be obtained much more quickly using the Hellman-Feynman theorem [100], which states that

$$\frac{dE}{d\lambda} = \left\langle \psi \left| \frac{dH}{d\lambda} \right| \psi \right\rangle, \quad (2.13)$$

where  $E$  is the total energy,  $|\psi\rangle$  is the system's ground state,  $H$  is the Hamiltonian and  $\lambda$  is some arbitrary parameter on which  $H$  depends. Thus, one need only solve the Kohn-Sham equations for  $|\psi\rangle$ , and then repeatedly recalculate eq. 2.13 with  $\lambda$  corresponding to the variation of an atom's coordinates to obtain all of the forces. In practice one often wishes to allow the lattice to vary as well to minimise the energy, in which case the Hellman-Feynman theorem is also used to obtain energy derivatives with respect to the lattice parameters.

Though the Hellman-Feynman theorem allows efficient evaluation of energy derivatives, it is still important to relax the system to a local minimum of the energy landscape in as few steps as possible. A commonly used algorithm for these purposes is the Broyden-Fletcher-Goldfarb-Shanno (BFGS) [101] algorithm. This algorithm is based on the Hessian matrix, which is the matrix of second derivatives of the energy  $E$  with

respect to the parameters  $\mathbf{x}$  being optimised:

$$H_{\alpha\beta} = \frac{\partial^2 E}{\partial x_\alpha \partial x_\beta}. \quad (2.14)$$

The BFGS algorithm builds up an approximation to the inverse of the Hessian over the course of the geometry optimisation, and at each step performs an update of the position by approximating the energy landscape about the current position as quadratic.

Geometry optimisations are a key component of the AIRSS structure searching method, as described later in section 2.7.

## 2.4 Lattice vibrations

In real systems, both thermal effects and external perturbations cause the atoms to vibrate. These dynamical effects can generally be described to a good approximation within the DFT energy landscape. Under the assumption that the vibrations are small in amplitude (an assumption known as the harmonic approximation), the potential energy landscape can be expanded quadratically about equilibrium:

$$E(\{\mathbf{u}_i\}) = E_0 + \underbrace{\sum_{i\alpha} \frac{\partial E}{\partial u_{i\alpha}} \Big|_{\mathbf{u}=0}}_{=0 \text{ at equilibrium}} u_{i\alpha} + \frac{1}{2} \sum_{i\alpha j\beta} \frac{\partial^2 E}{\partial u_{i\alpha} \partial u_{j\beta}} \Big|_{\mathbf{u}=0} u_{i\alpha} u_{j\beta} \quad (2.15)$$

where  $u_{i\alpha}$  is the displacement of the  $i$ -th atom in the  $\alpha$ -th Cartesian direction relative to the stable structure, and the subscript  $\mathbf{u} = 0$  indicates that the derivatives are to be evaluated at equilibrium.

Dropping the  $E_0$  for convenience since global shifts in the energy landscape have no effect on the system's dynamics, one can then write down the Lagrangian:

$$\mathcal{L} = \sum_{i\alpha} \frac{1}{2} m_i \dot{u}_{i\alpha}^2 - \frac{1}{2} \sum_{i\alpha j\beta} \frac{\partial^2 E}{\partial u_{i\alpha} \partial u_{j\beta}} \Big|_{\mathbf{u}=0} u_{i\alpha} u_{j\beta} \quad (2.16)$$

where  $m_i$  is the mass of the  $i$ -th atom and  $\dot{u}_{i\alpha} = \partial u_{i\alpha} / \partial t$ .

The matrix of second derivatives appearing on the RHS is known as the force constant matrix,  $\Phi$ :

$$\Phi_{i\alpha j\beta} = \left. \frac{\partial^2 E}{\partial u_{i\alpha} \partial u_{j\beta}} \right|_{\mathbf{u}=0}. \quad (2.17)$$

The Euler-Lagrange equations of motion following from eq. 2.16 are then

$$m_i \ddot{u}_{i\alpha} = - \sum_{j\beta} \Phi_{i\alpha j\beta} u_{j\beta}. \quad (2.18)$$

We now redefine the notation slightly so that  $u_{i\alpha}$  becomes  $u_{i\alpha}^c$ , with  $i$  referring to the  $i$ -th atom in the unit cell and  $c$  ‘indexing’ different unit cells in the lattice. (Clearly in a 3D crystal we technically require three indices, but we ignore this detail for notational convenience.) Then in eq. 2.18 the sum on the RHS can be written as a double sum, over unit cells  $c'$  and over atoms within the  $c'$ -th unit cell:

$$m_i \ddot{u}_{i\alpha}^c = - \sum_{j\beta} \sum_{c'} \Phi_{i\alpha j\beta}^{cc'} u_{j\beta}^{c'}, \quad (2.19)$$

We now assume for the atomic displacements a travelling wave solution of wavevector  $\mathbf{k}$  and frequency  $\omega$ :

$$u_{i\alpha}^c = \epsilon_{i\alpha} e^{i(\mathbf{k} \cdot \mathbf{R}_c - \omega t)}, \quad (2.20)$$

where  $\mathbf{R}_c$  is the position of the origin of the  $c$ -th unit cell, and the *polarisation vector*,  $\epsilon$ , describes the direction and magnitude of each atom’s displacement. (Here  $\epsilon$  is not written in bold to distinguish it from three-component vectors such as  $\mathbf{R}$  and  $\mathbf{k}$ .) Substituting eq. 2.20 into eq. 2.19 gives, after a little algebra,

$$\sum_{j\beta} \left[ \sum_{c'} \Phi_{i\alpha j\beta}^{cc'} e^{i\mathbf{k} \cdot (\mathbf{R}_{c'} - \mathbf{R}_c)} \right] \epsilon_{j\beta} = \omega^2 m_i \epsilon_{i\alpha}. \quad (2.21)$$

This very nearly has the form of an eigenvalue equation in  $\epsilon$ , except for the  $m_i$  on the RHS. To symmetrise the equation into an eigenvalue problem, we define

$$D_{i\alpha j\beta} = \sum_{c'} \frac{1}{\sqrt{m_i m_j}} \Phi_{i\alpha j\beta}^{cc'} e^{i\mathbf{k} \cdot (\mathbf{R}_{c'} - \mathbf{R}_c)}, \quad (2.22)$$

where the lack of dependence on  $c$  follows because the translational invariance of the crystal implies that  $\Phi_{i\alpha j\beta}^{cc'}$  must depend only on the position of  $c'$  relative to  $c$ , and not

on their absolute positions. In order to complete the transformation of eq. 2.21 into an eigenvalue problem, we also redefine the polarisation vector elements as  $\epsilon_{i\alpha} \rightarrow \epsilon_{i\alpha}\sqrt{m_i}$ , so that eq. 2.21 now becomes

$$\sum_{j\beta} D_{i\alpha j\beta} \epsilon_{j\beta} = \omega^2 \epsilon_{i\alpha}, \quad (2.23)$$

which is an eigenvalue problem for the eigenvectors  $\epsilon$  and eigenvalues  $\omega^2$  of  $D$ . The matrix  $D$ , defined in eq. 2.22, is known as the dynamical matrix [81]. It can be identified from this definition as the Fourier transform of the force constant matrix,  $\Phi$ .

The main computational cost in DFT phonon calculations is the calculation of the elements of the force constant matrix. The simplest method to do this is the finite displacement method in which each atom in turn is perturbed slightly in each of the Cartesian directions, and the forces on all of the other atoms are evaluated, giving one ‘row’ of the force constant matrix [99]. However, this method can prove very expensive because all phonon  $\mathbf{q}$ -vectors other than  $\mathbf{q} = 0$  break the translational periodicity of the cell, necessitating a supercell of periodicity commensurate with that of the phonon mode. Density-functional perturbation theory (DFPT) avoids this issue by calculating the force constant matrix perturbatively [102], which does not require a supercell.

In the harmonic approximation, the phonons act as independent bosonic quasiparticles [103], with the result that each phonon mode is occupied according to the Bose-Einstein distribution (beyond the harmonic approximation, phonon-phonon interactions begin to occur [104]). Using this, and given that the energy levels of a harmonic oscillator are given by  $(n + 1/2)\hbar\omega$  with  $\omega$  the frequency of the oscillator and  $n \in \mathbb{Z}$ , one can express the vibrational free energy of the system as an integral over its vibrational density of states [105]:

$$F_{\text{vib}}(T) = k_B T \int_0^\infty \ln \left( 2 \sinh \left( \frac{\hbar\omega}{k_B T} \right) \right) g(\omega) d\omega, \quad (2.24)$$

Using this expression, one can obtain more accurate energetics at finite temperatures (and even at  $T = 0$  since the equation includes a zero-point energy contribution). In addition to this, phonon analysis has other applications: it can be used to identify mechanical instabilities, which manifest in the form of imaginary phonon mode frequencies, indicating the presence of a solution to the equations of motion whose amplitude

grows over time. It also provides an important link with experiment in the form of Raman spectroscopy, which is discussed in the next section.

## 2.5 Raman spectroscopy

Raman spectroscopy is a method in which a system's vibrational properties are probed by irradiating it with a laser in order to drive the system into a different vibrational state, from which its de-excitation is measured [106]. An incoming photon – which is coupled to the electron density via the polarisation – is absorbed by the system, which enters an unstable, excited state before dropping into either the initial vibrational state (known as Rayleigh scattering), a higher-energy vibrational state (Stokes-Raman scattering) or a lower-energy vibrational state (Anti-Stokes-Raman scattering). As the system decays into its final state, it emits a photon in the process. Where the energy of the final vibrational state is higher than that of the initial state, the energy gained by the system results in a decrease in energy – and thus of wavenumber – of the emitted photon (and vice versa for the anti-Stokes-Raman case). This shift is known as the *Raman shift*. In Raman spectroscopy one usually adopts units in which the factor of  $2\pi$  is not included in the wavenumber [107], so that the Raman shift is (from energy conservation)

$$\Delta w = \frac{1}{\lambda'} - \frac{1}{\lambda}, \quad (2.25)$$

where  $\lambda'$  and  $\lambda$  are the wavelengths of the emitted and absorbed photon, respectively. The energy of the emitted photon is measured with a detector, giving  $\lambda'$ , and  $\lambda$  is just the laser wavelength, so  $\Delta w$  can then be calculated. This wavelength must correspond to a difference in energy between two of the system's vibrational states, and so Raman scattering provides information about the system's phonon spectrum.

Since a sample will have many possible vibrational states, there are many possible Raman shifts depending on which are the initial and final vibrational states of the system. The result is therefore a spectrum of Raman shifts, with each peak corresponding to a transition between two vibrational modes.

One can understand the physical origin of Raman scattering from a semiclassical treatment of the problem (here we follow that given in ref. 107). When a sample interacts with an electric field  $\mathbf{E}$ , a dipole  $\boldsymbol{\mu}$  is induced which is related to  $\mathbf{E}$  via the polarisability,  $\alpha$ :

$$\boldsymbol{\mu} = \alpha \mathbf{E}. \quad (2.26)$$

In general, lattice vibrations will induce changes in the polarisability,  $\alpha$ ; the first-order response of  $\alpha$  with respect to the displacement of the system along a normal mode vector is

$$\alpha(Q) = \alpha(0) + \left. \frac{\partial \alpha}{\partial Q} \right|_{Q=0} Q, \quad (2.27)$$

where  $Q$  parameterises the normal mode so that  $Q = 0$  corresponds to mechanical equilibrium. Note that  $\alpha$  will in general be tensor-valued.  $Q$  will oscillate with time at the frequency of the normal mode,  $\omega_m$ , so that one can write  $Q = Q_0 \cos(\omega_m t)$ . Similarly, since in the Raman scattering case the electric field of interest is due to a photon incident on the system, the electric field takes the form  $\mathbf{E} = \mathbf{E}_0 \cos(\omega t)$ . Substitution of the above into eq. 2.26 then gives

$$\boldsymbol{\mu}(t) = \alpha(0) \mathbf{E}_0 \cos(\omega t) + \left. \frac{\partial \alpha}{\partial Q} \right|_{Q=0} \mathbf{E}_0 (\cos((\omega - \omega_m)t) + \cos((\omega + \omega_m)t)). \quad (2.28)$$

The induced dipole therefore oscillates with three different frequency components, and consequently will emit radiation at each of those frequencies. The first term on the RHS corresponds to re-emission at the same frequency, which is Rayleigh scattering; the second corresponds to the excitation of the system into a higher-energy vibrational state and the emission of a photon whose energy is lower than that of the incident photon, i.e. Stokes-Raman scattering; and the third corresponds to a transition into a lower vibrational state and the emission of a higher-energy photon, which is anti-Stokes-Raman scattering.

In the general case  $\partial \alpha / \partial Q$  will be an anisotropic tensor, which will impact the Raman-scattered photons' polarisation and the intensity of scattering [106]. Measurements of the polarisation of Raman-scattered photons therefore provide information about the symmetry of  $\partial \alpha / \partial Q$ , and by extension of the phonon modes themselves. In many cases, a phonon mode's Raman intensity will be zero by symmetry; this occurs when the polarisability is to first order unchanged by the phonon mode, rendering all but the Rayleigh scattering term of eq. 2.28 equal to zero.

The Rayleigh scattering contribution is not of interest in Raman spectroscopy, since it does not provide information about the vibrational energy levels of the system. It is

the photons emitted due to Stokes-Raman and anti-Stokes-Raman scattering which are of interest, since their frequency shift relative to the (known) frequency of the incoming photon corresponds to an energy difference between two vibrational modes.

Additionally, Stokes-Raman scattering is more likely than anti-Stokes-Raman scattering because the latter case requires the system to start in a higher-energy state, which will be less well-occupied with phonons as per Bose-Einstein statistics, so although the distribution of peaks in the Raman spectrum is symmetrical, their intensities are not [108].

## 2.6 Molecular dynamics

Molecular dynamics (MD) is the simulation of the finite-temperature time-evolution of a many-atom system, usually within the Born-Oppenheimer approximation. This is done via numerical integration: a finite timestep is selected (chosen to be much less than any of the characteristic timescales of the system's dynamics) and the positions and momenta of every atom are integrated forward using the forces on each atom. The result of such a simulation is a trajectory through the configuration space of a system [109].

The crucial ingredient in the MD formalism is the choice of Hamiltonian, from which the forces are derived. One can use the DFT Hamiltonian, solving the Kohn-Sham equations at every timestep. This is known as *ab-initio* molecular dynamics (AIMD), and wavefunction extrapolation methods in which the atomic displacements are used to generate a highly accurate initial guess at the Kohn-Sham orbitals using the previous timestep's orbitals as a starting point render this surprisingly affordable computationally. However, it is often still too expensive, and often must use a cheaper, more approximate choice of Hamiltonian in which the electronic degrees of freedom are not treated explicitly. This is known as a force field. Generally, force fields are generated by selecting a physically plausible form for the total energy and parameterising it using either *ab initio* or empirical data.

More recent developments in force field generation include machine learning-based approaches such as neural network potentials [110, 111] and Gaussian Approximation Potentials (GAP) [112, 113]. These are highly general schemes that avoid the need to impose a particular analytic form for the total energy, enabling them to reach

impressive levels of accuracy, although at the cost that more data are required to fit the potential, and evaluating it tends to be more expensive relative to the more traditional variety of force field in which an explicit functional form is imposed.

## 2.7 Crystal structure prediction

Structure prediction represents a particular case of a very general problem: that of searching for a global minimum in a high-dimensional space. Many algorithms have been proposed for tackling such problems without being too susceptible to getting stuck in local minima, and a fairly large subset of these have been applied to the specific problem of structure prediction.

*Ab initio* random structure searching (AIRSS) [11] is a method for the computational prediction of crystal structures from first principles. The underlying idea is simple: crystal structures are generated at random, and then relaxed using forces calculated using DFT into a local minimum of the Born-Oppenheimer potential energy surface (PES). As long as this process has been repeated enough times to sample the space of possible structures well, the lowest-energy structure found should be the most thermodynamically stable structure. The method is therefore essentially a brute-force random sampling of structure space. The result is a set of structures in which each basin of attraction in the PES is sampled on average in proportion to its size.

Genetic algorithms use an evolutionary scheme in which the most-promising (i.e. lowest-energy) of each ‘generation’ of crystal structures are used to begin the next generation, via some crossover method in which two structures are combined. Ref. 114 used such a scheme, together with a crossover method in which a periodic cut is taken through each of the two parent cells and combined to produce the child cell, to predict the stable structures of carbon. Another approach is particle swarm optimisation (PSO) as implemented by e.g. the CALYPSO code [115]. PSO is a global optimisation method in which a number of particles – in this case each of them corresponding to a single point in structure space – are optimised simultaneously, but are coupled to each other such that if one of them finds a low-energy minimum, the others will be attracted to it. Other methods that have been used for structure prediction include basin hopping [116–118] and minima hopping [119–121]. Both of these methods involve jumping between the basins of attraction of the potential energy landscape. The former

does so via a Monte Carlo method, and the latter via a biased molecular dynamics simulation.

Because these other techniques are generally more complex than AIRSS, they bring with them additional difficulties: principally, a number of hyperparameters and methodological details arise which must be chosen appropriately for the algorithm to perform well. In a genetic algorithm, for example, one must choose the mutation rate, the population size, the genetic representation and crossover scheme, and so on. By contrast, AIRSS is relatively parameter-free, and those parameters which do enter the method usually have intuitive physical meanings, e.g. one generally chooses to reject (prior to geometry optimisation) structures in which atoms are too close, where the value of ‘too close’ can be chosen with reference to the atoms’ Van der Waals radius.

AIRSS is agnostic to the question of how the energy landscape is calculated. One could therefore apply the same algorithm using other methods such as a classical potential or a Gaussian approximation potential, which would run much more quickly than DFT. However, all such methods are limited by the fact that they are essentially interpolative: the potential is fitted to some training set of structures whose energies are known (usually by calculating them within DFT). Because of this, only with a first-principles method such as DFT can one reliably use AIRSS to find structures which were not already known to begin with.

Perhaps because of its simplicity, AIRSS has proven highly successful in a wide range of contexts. It has revealed exotic high-pressure phases in hydrogen [122], aluminium [123], ammonia [124], and silane [125]. It has also been used to map out the succession of phase transitions through which battery materials pass as the battery charges and discharges [126–129].

In addition to studies of bulk structure, AIRSS has also been used to predict the structures of point defects in materials. In this case, the cell is initialised to a supercell of the known bulk structure, and then a defect is created by randomising (inserting, removing, and repositioning atoms) a small region within that supercell. The result is then geometry optimised. Defect AIRSS has led to greater understanding of the behaviour of hydrogen, nitrogen, oxygen and lithium impurities within silicon [130, 131], as well as of the use of zirconolite for nuclear waste encapsulation [132].

The PyAIRSS code, which was previously written as part of my MPhil project, was extended with new functionality for the structure prediction calculations in this thesis.

The code is written in Python and interfaces with CASTEP for all electronic structure calculations. PyAIRSS takes as input an initial unit cell and a series of commands, which are then executed sequentially. Each command performs an action (such as adding an atom, randomising the position of atoms, and geometry optimising the cell) and the commands can appear in any order, so the result is a flexible system where the procedure by which the structure is generated can be customised extensively by the user, even without any programming knowledge. The code is fully parallel, which facilitates structure searching calculations on large computing clusters thanks to the embarrassingly parallel scaling of AIRSS.

The simplest practical implementation of AIRSS is to generate initial structures simply by putting atoms at random locations in a unit cell with randomly chosen lattice parameters. However, the large majority of crystal structures in nature possess a number of symmetry operators (other than simple translation through the lattice vectors) under which the structure is invariant. As a result, AIRSS searches generally find the global minimum structure much more rapidly if the structure is created subject to the constraints of a randomly chosen space group.

The imposition of symmetry constraints is a significant complication in constructing initial structures in AIRSS searches. When a symmetry group is imposed on a structure, the atomic positions are no longer independent of one another: if any atom is mapped onto another atom by the application of one of the symmetry group's operators, then those atoms' positions can no longer be varied independently without breaking the symmetry. In the same vein, atoms can no longer be inserted at arbitrary locations, because doing so may also break the chosen symmetry group.

These symmetry considerations are described by so-called Wyckoff positions [133]. Each symmetry group has a corresponding set of Wyckoff positions which give all possible sets of symmetrically equivalent locations in the cell. For example, the point group  $m$  consists of a single mirror plane and the identity operator. As a result, it has two Wyckoff positions (which are shown on fig. 2.3): choosing the mirror plane to be along the line  $x = 0$ , the *general position* is  $(x, y), (-x, y)$ , and there is a *special position* at  $(0, y)$ . One consequence of this is that the question of where to insert atoms becomes coupled to the question of how many atoms to insert: in the example of point group  $m$ , atoms must in general be inserted into the unit cell two at a time in order not to break the mirror symmetry. On the other hand, because the  $y$ -axis is a fixed point of the mirror operation, atoms can be inserted one at a time into the special position  $(0, y)$ .

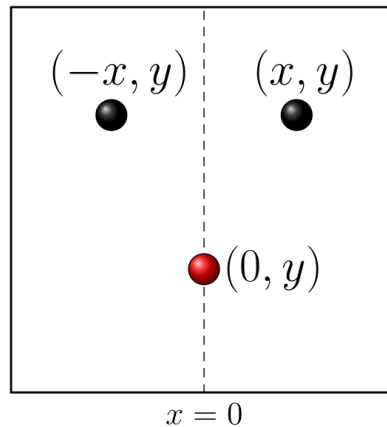


Figure 2.3 Schematic diagram of the Wyckoff positions of a simple 2D cell whose only symmetry element is a mirror plane collinear with the  $y$ -axis.

The problem of how to insert a given number of atoms into the cell by allocating them to a given set of Wyckoff points is equivalent to a problem known as the change-making problem [134], and is solved by PyAIRSS code using a recursive method. (Note that here the point group  $m$  has been chosen as an example for simplicity; in practice space groups are imposed, which describe translationally periodic structures, rather than point groups, which do not.)

PyAIRSS creates initial structures subject to the constraints of a particular symmetry group by randomly inserting atoms onto Wyckoff sites. The advantage of this over simpler methods, such as inserting atoms into the asymmetric unit of a structure and applying all of the operators in the chosen symmetry group to generate the entire unit cell, is that it leads to the occupation of special positions whose occupation would otherwise be vanishingly improbable (a randomly chosen point in 3D space is – ignoring floating-point arithmetic considerations – infinitely more likely to lie away from the  $xy$  plane than directly on it, for example.)

Another important consideration in AIRSS is that atoms in generated cells should never be unphysically close to each other, firstly because one can know a priori that no such structure will ever be energetically competitive and therefore searching that region of structure space is unnecessary, and secondly because excessive overlap between core regions can cause pathological behaviour in pseudopotential density functional theory (such that simply running the optimisation anyway and hoping that the atoms will move away from each other is not a reliable solution). Having generated a cell, PyAIRSS therefore attempts to push excessively close atoms apart before optimising

the cell with CASTEP. This must be done without violating the symmetry of the cell. To ensure this, for each group of symmetrically equivalent atoms, a set of operators are constructed which map a position  $\mathbf{h} = (x, y, z)$  to the set of locations  $\mathbf{r}_1 \dots \mathbf{r}_n$  at which each of the atoms sit. For example, for the above case with the space group  $m$ , the operators are chosen as

$$M_1 = \begin{pmatrix} 1 & 0 \\ 0 & 1 \end{pmatrix} \quad (2.29)$$

and

$$M_2 = \begin{pmatrix} -1 & 0 \\ 0 & 1 \end{pmatrix}. \quad (2.30)$$

The positions  $\mathbf{r}_1$  and  $\mathbf{r}_2$  of the two symmetrically equivalent atoms are then generated from  $\mathbf{h}$  via  $\mathbf{r}_i = M_i \mathbf{h}$ . The vector  $\mathbf{h}$  thus serves to parameterise all possible configurations of atoms occupying a given Wyckoff position such that the atoms can no longer move independently of one another, with the result that symmetry is guaranteed to be respected no matter what value  $\mathbf{h}$  takes. This approach also has the advantage that the cell is then described not with  $3N$  degrees of freedom (three per each atom), but with a reduced set of degrees of freedom that allow the cell only to vary within the constraints of the chosen symmetry group. This approach extends simply to cases where the dimensionality of the space corresponding to a Wyckoff position is lower than that of the whole cell: in the special position  $(0, y)$  on fig. 2.3, for example, the corresponding operator is

$$M = \begin{pmatrix} 0 & 0 \\ 0 & 1 \end{pmatrix}, \quad (2.31)$$

which is just a projection operator onto the  $y$ -axis. Thus  $\mathbf{h}$  can be any point in the cell, but the resulting atomic position  $\mathbf{r} = M\mathbf{h}$  will always sit on the  $y$ -axis. It should also be noted that in general the operators  $M_i$  which map  $\mathbf{h}$ -vectors to actual atomic positions also contain a translational component; that is,  $\mathbf{r}_i = M_i \mathbf{h} + \mathbf{t}_i$ .

The task of pushing apart atoms subject to symmetry is then performed by applying a simple repulsive hard-sphere potential to the cell and minimising the resulting energy with respect not to the atomic positions directly, but to the vector  $\mathbf{h}$  from which the atomic positions are calculated via the operators  $M_i$ . There will be one vector  $\mathbf{h}$  for each set of symmetrically equivalent atoms, and all of them are optimised simultaneously. This approach generalises naturally to cases with more constraints: for example, in constructing a cell of atoms inside a nanotube, an additional constraint keeping atoms

inside a cylindrical region collinear with the nanotube is required. An additional term is therefore added to the potential which acts to drive atoms back inside the cylinder. If after optimisation (which is done via applying the BFGS algorithm to the sum of all the potential terms) the total potential is zero, then all constraints have been satisfied and the cell is then optimised within DFT using CASTEP; otherwise, the whole process begins again, until a cell that satisfies all imposed constraints has been successfully generated.

The code estimates the total number of atoms a given Wyckoff point can hold via a Monte Carlo method in which the point is occupied at random and the fraction of times that this leads to overlap is calculated; the lower this fraction, the higher the effective capacity of the Wyckoff point. For example, in the case of Wyckoff positions corresponding to a single point in space, there will be overlap 100% of the time if two atoms are placed on this point, and therefore the effective capacity of the site is only one atom. These capacities are used to limit how many times each Wyckoff point is occupied, and thereby minimise the frequency of cases where the code is unable to push apart atoms without breaking symmetry.

## 2.8 Automated quasi-1D symmetry analysis

Because AIRSS searches result in datasets of thousands of structures, it is important to be able to efficiently comb through the results and identify the most promising candidate structures for further study. Many structures will appear multiple times in the results, so the efficient elimination of duplicates after the search is important – otherwise, computational time would be wasted performing calculations on the same structure multiple times (or at the very least, human labour would be wasted inspecting the predicted structures by eye to identify duplicates). The symmetry properties of a structure are a highly useful guide in this context: the symmetry group of a crystal provides at-a-glance information about its structure, and sharing the same space group is a necessary (but not sufficient) condition for two structures to be duplicates of each other. A symmetry-finding program for quasi-1D materials, ‘Symm1D’, was therefore written. Symmetry-finding in the 3D case is well-studied and there are multiple programs able to identify the space group of a 3D structure [135, 136], but to my knowledge, this is the first program to have been written to solve the quasi-1D case (despite the fact that it is simpler than the 3D case).

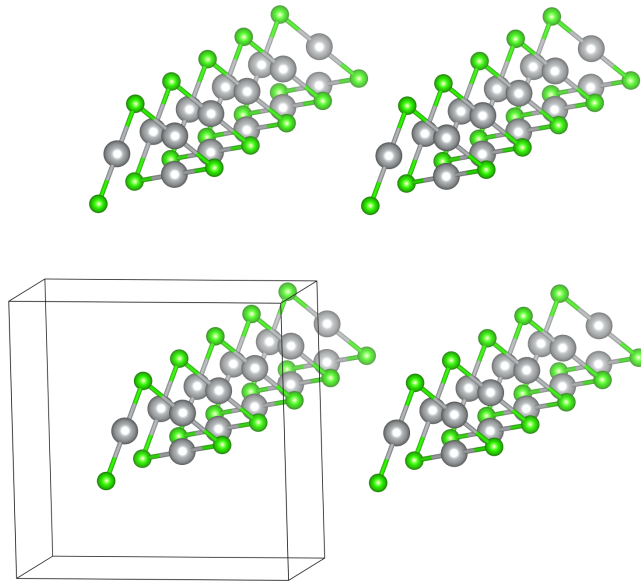


Figure 2.4 A helical AgCl nanowire, tiled as if it had 3D rather than 1D periodicity, as per the unit cell shown on the figure. The wire has a threefold screw axis, giving it  $P3_1$  rod group symmetry. However, when 3D periodicity is assumed, the threefold nature of the screw axis is incommensurate with the tetragonal lattice, resulting in an assigned space group of  $P1$ . This shows how the introduction of additional symmetries (in this case translational invariance in the  $x$  and  $y$  directions) can destroy symmetries as well as adding them.

The symmetry groups describing the symmetries of crystals with periodicity only in one direction are known as rod groups. In the following (and throughout this thesis) the  $z$ -direction is chosen to be the direction in which a given quasi-1D structure is periodic. Because there is no periodicity in the  $xy$  plane, the crystallographic restriction theorem – which states that only rotations of order 2, 3, 4 and 6 are possible in a crystal – does not apply to rotation axes parallel to the  $z$ -axis, and therefore rod groups may contain rotational (or rotoinversional) symmetries of arbitrary order. If the cell does indeed contain rotation axes whose order is not 2, 3, 4 or 6, then the rod group is referred to as non-crystallographic; otherwise, it is referred to as crystallographic. There are 75 crystallographic rod groups, which are standardised in Volume E of the International Tables for Crystallography, which classifies the subperiodic groups [137]. There are infinitely many non-crystallographic rod groups (as can be seen clearly from the fact that one can have rotation axes of arbitrary order). Symm1D is able to handle both of these cases, and in the crystallographic case it will return the Hermann-Mauguin space group symbol as standardised by the International Tables for Crystallography.

It should be noted that tiling a quasi-1D crystal in the  $xy$  directions can both add and remove symmetries. That the tiling can add symmetries is obvious – at the very least, it adds translational symmetry along the  $xy$  directions. An example showing that it can also remove symmetry is given by fig. 2.4. It follows from this that quasi-1D symmetry finding is not simply a ‘special case’ of 3D symmetry finding: the task of identifying the symmetries of a quasi-1D crystal cannot be solved simply by passing its unit cell into a 3D symmetry-finding algorithm and then discarding symmetries which do not apply to the true, quasi-1D structure.

What follows is a description of the algorithm that Symm1D uses to identify the rod group of a structure. The first step is to identify the structure’s periodicity. The primitive translation vector of the structure is the shortest vector which, when the structure is translated by that vector, maps each atom onto a different atom of the same element; in other words, the translation vector is the shortest vector  $\mathbf{c}$  such that, for all atomic positions  $\mathbf{r}_i$ ,  $\mathbf{r}_i + \mathbf{c}$  coincides with the position of another atom of the same element. The vector  $\mathbf{c}$  is identified by constructing, for each atom  $i$ , the set of vectors  $\mathbf{r}_j - \mathbf{r}_i$  connecting atom  $i$  to each atom  $j$  of the same element; the shortest vector common to each atom’s list (modulo the periodicity of the given cell) is identified, and this gives the primitive cell length. The primitive cell is then constructed using this information. Note that there is only one lattice type for structures with 1D periodicity, so that in contrast to the 3D case there are no choices to be made as regards the choice of setting – there is (up to a uniform translation) always a unique primitive cell.

Next, the principal rotational axis of the structure is identified – that is to say, the rotational axis which passes through the middle of the structure and which points in the periodic direction. This is done by exploiting the fact that because the structure is not periodic in the  $x$  and  $y$  directions, the  $x$  and  $y$  components of the structure’s centroid are well-defined, as simple averages over the  $x$  and  $y$  coordinates of every atom in the unit cell. Moreover, since the structure is by definition invariant under all of its symmetry operations, so must be its centroid. Therefore, the projection of the centroid in the  $xy$  plane must lie on the principal axis of the structure. Together with the fact that the principal axis is parallel to the  $z$ -direction, this means that the location of the centroid is sufficient to determine the principal axis. (In some low-symmetry cells, there will be no rotational symmetry about the principal axis, but the axis can still be uniquely defined in terms of the centroid.)

Having identified the location of the principal axis, the order of the rotational symmetry about that axis is then identified by trying all possible rotational operators up to the maximum possible order of rotation, which is equal to the lowest number of atoms of any single element in the cell. This upper bound on the order of rotation follows from the fact that repeatedly applying a rotation about the  $z$ -axis through an angle  $2\pi/n$  maps an atom whose angular coordinate (in a cylindrical coordinate system) is initially at  $\phi = \phi_0$  to a ring of  $n$  positions at  $\phi_0, \phi_0 + 2\pi/n, \dots, \phi_0 + (n-1)2\pi/n$ . For the cell to be invariant under the operator, there must be atoms of the same element at each of these  $n$  positions; this requirement applies to every element separately. Since an  $n$ -fold rotational invariance means invariance under a rotation through any multiple of  $2\pi/n$ , the stated upper bound follows.

Rotoinversions about the principal axis are somewhat more difficult to identify, since they are the combination of a rotation and an inversion through a point lying on the rotation axis, and the location of the inversion centre is not known *a priori*. While the fact that the inversion centre must lie on the rotation axis is sufficient to determine the  $x$  and  $y$  coordinates of the inversion centre, its  $z$  coordinate must still be found. The  $z$ -position is identified by using the fact that inversion of an atom at  $z$ -coordinate  $z_a$  through an inversion centre whose  $z$ -coordinate is  $z_0$  maps the atom to a new  $z$ -coordinate at  $z'_a = z_0 - (z_a - z_0)$ . This is unaffected by the rotational part  $R$ , since  $R$  only rotates about the  $z$ -axis and therefore does not affect the atoms'  $z$ -coordinates. The centroid of the coordinates  $z_a$  and  $z'_a$  is simply

$$\frac{z_a + z'_a}{2} = \frac{z_a + (z_0 - (z_a - z_0))}{2} = z_0. \quad (2.32)$$

i.e., the average of an atom's  $z$ -positions before and after applying the rotoinversion operator is the  $z$ -position of the inversion centre itself,  $z_0$ . If the structure is invariant under the operator, then this means that for every atom in the cell there is another atom in the cell such that the centroid of the two atoms'  $z$ -component is equal to  $z_0$ . This reduces the problem of identifying the centre of inversion to a loop over all possible pairs of atoms in the cell, each time computing their centroid and checking whether the structure is invariant under a rotoinversion operator whose centre of inversion lies at that centroid.

The previous argument regarding the invariance of the centroid implies that the set of fixed points of every symmetry operation of the structure must contain the  $xy$

component of the centroid. This is used throughout the code to significantly reduce the set of potential symmetry operations that must be tested for.

Another fact that can be used to reduce the set of possible symmetry operations is that the only possible mirror planes of the structure are those that are either normal to the principal axis or those that are parallel to it; any other mirror plane would leave the crystal pointing in a different direction. Similarly, the only possible rotations other than those about the principal axis are two-fold rotations whose axes are orthogonal to the principal axis and pass through it.

Screw axes are the combination of a rotation with a translation along the axis of rotation. They describe helical symmetries, which are particularly important in the case of quasi-1D structures. Since screw symmetries contain a translational part, that translational part must be in the  $z$ -direction. In a screw operator the axis of the rotational part is the same as that of the translational part, which means that the axis of the rotational part must also be along the  $z$ -direction. Symm1D identifies these symmetries by exploiting the fact that the projection operator onto the  $xy$  plane commutes with all rotation operators whose axes are along  $z$ , as can be seen by noting that the projection operator acts only on the  $z$ -position of the atom, whereas the rotation operator acts only on its polar angle,  $\phi$ . Therefore if the structure is invariant under a screw transformation

$$\mathbf{r}' = R\mathbf{r} + \mathbf{t}, \quad (2.33)$$

then applying the projection operator onto the  $xy$  plane,  $P_{xy}$ , and exploiting the fact that the commutator  $[P_{xy}, R]=0$ , it is also invariant under

$$P_{xy}\mathbf{r}' = RP_{xy}\mathbf{r}, \quad (2.34)$$

(since  $P_{xy}\mathbf{t} = 0$  because the translational part must be parallel to  $z$ ). But this describes a rotational symmetry of the vector  $P_{xy}\mathbf{r}$ . This means that every screw symmetry of a 1D crystal implies a rotational symmetry of the same order of the projection of that crystal onto the  $xy$  plane. The algorithm exploits this by computing that projection and identifying its rotational and rotoinversional symmetries. This is sufficient to determine the rotational part,  $R$ , of the screw operator. The translational part can then be computed by first noting that, upon applying an  $n$ -fold screw operation  $n$  times, the rotational part is  $R^n = I$  and so the result is simply a translation through  $n\mathbf{t}$ , where  $\mathbf{t}$  is the translational part of the screw operator. Therefore, the translational part

of any order- $n$  screw operator under which the structure is invariant must satisfy

$$n\mathbf{t} = m\mathbf{c}, \quad (2.35)$$

where  $\mathbf{c}$  is the primitive lattice vector and  $m \in \mathbb{Z}$ , so that  $m\mathbf{c}$  is also a lattice vector. (Otherwise the operator would not be commensurate with the periodicity of the lattice.) Substituting eq. 2.35 into eq. 2.33, the translational part of an order- $n$  screw symmetry may therefore be identified by testing for invariance under

$$\mathbf{r}' = R\mathbf{r} + \frac{m}{n}\mathbf{c}, \quad (2.36)$$

for increasing values of  $m$  until an  $m$  is found such that the structure is found to be invariant, at which point the translational part has been identified and is equal to  $m\mathbf{c}/n$ .  $m$  can always be chosen to be less than  $n$  in magnitude, since a translation through  $m\mathbf{c}/n$  is translationally equivalent to one through  $(m - n)\mathbf{c}/n$ .

An exactly analogous argument can be used to identify the glide planes: again, the translational part must be parallel to  $z$ , and the argument goes through as before except with  $R$  now being a mirror plane passing through the principal axis rather than a rotation matrix.

Having identified all possible symmetry elements of the crystal as described above, the Hermann-Mauguin symbol is then identified and – if the symmetry is crystallographic – formatted to match the International Tables.

While Symm1D is written in Python, it is nevertheless fast enough to identify the symmetry groups of thousands of structures in a few minutes, which is good enough for the purposes of postprocessing AIRSS calculations.

## 2.9 AIRSS for encapsulated nanowires

In this section a description is given of the adaptation of the AIRSS method for the prediction of ENWs' structures. All of the following method has been implemented in the PyAIRSS code in the form of new pragmas accessible to the user.

As described in section 2.7, the basic philosophy of AIRSS is to repeatedly generate physically reasonable initial structures and then relax them (via a DFT geometry

optimisation) into a local minimum of the potential energy surface. The lowest energy structures generated by the AIRSS search are then re-optimised in more accurate calculations, whereas initial searches are performed with coarser settings in order to maximise throughput. Whilst this general scheme is retained in adapting the AIRSS method for encapsulated nanowires, some unique challenges arise that are not present in the case of 3D bulk structures. Firstly, even with cells of fairly short periodicity, a large number of carbon atoms must be included: for example, a 7.21 Å-long cell of the armchair (6,6) SWNT includes 72 C atoms. To simulate this many atoms explicitly makes it difficult to attain the high throughput required to thoroughly sample the structure space. Moreover, at the start of an AIRSS calculation one does not know *a priori* the energetically optimal periodicity of the relaxed nanowire, which makes strain a significant problem as well.

Both of these problems are dealt with by appealing to the chemical inertness of the SWNT itself to justify replacing all of the carbon atoms with a purely classical external potential acting on the filling material. The potential is chosen to take the form of a repulsive Gaussian dependent only on distance from the central axis of the nanotube, peaking where that distance equals the radius of the nanotube. The potential was implemented in the CASTEP code, and its functional form chosen, by Paulo Medeiros, a collaborator. This approximation will be referred to as the *implicit nanotube* approximation, as opposed to the *explicit* treatment of the nanotube by fully simulating it atomistically within DFT. The functional form of the confining potential is

$$V(r) = V_0(e^{-\alpha(r-r_0)^2} + e^{-\alpha(r+r_0)^2}), \quad (2.37)$$

where  $r_0$ ,  $\alpha$  and  $V_0$  are parameters of the potential, and  $r$  is the radius as defined within cylindrical polar coordinates. It should be noted that the radius referred to this section is the distance between the axis of the nanotube and the ionic cores of the carbon atoms in the nanotube wall. In practice, the radius of the central cavity that is practically accessible to the filling material is somewhat smaller, by an amount of the order of the van der Waals radius of the carbon atoms in the nanotube wall.

While the implicit nanotube approximation may seem crude, note that in order for it to be justified we do not need it to leave formation energies unchanged; only the *relative ordering* (by energy) of the structures at each nanotube radius must be preserved. This is because, after an AIRSS search, the lowest-energy structures for each nanotube radius are identified and re-optimised with carbon atoms treated quantum-mechanically rather

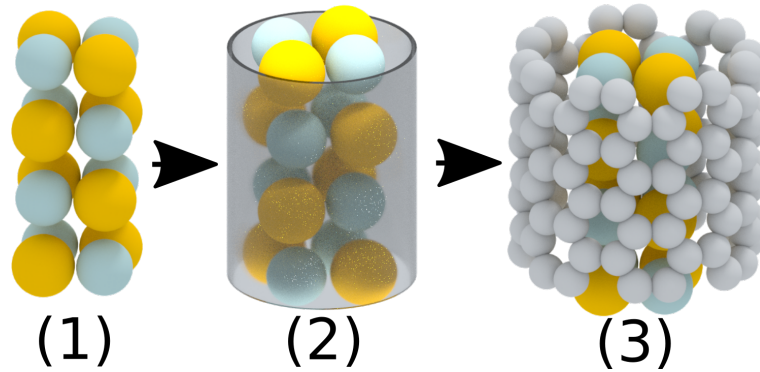


Figure 2.5 Flow diagram showing the structure searching methodology employed to predict encapsulated nanowire phases. An initial nanowire structure is randomly generated subject to the constraints of a randomly chosen rod group (1) and then relaxed inside the confining potential using DFT (2). Then the lowest-energy structures are re-relaxed with the carbon atoms treated quantum-mechanically (3).

than replaced by a confining potential. This strategy of an initial, cruder calculation (with a purely classical representation of the nanotube) followed by higher quality calculations on the most promising structures (with full DFT treatment of the nanotube) speeds up the initial structure searching calculations dramatically without undermining the accuracy of the final result. The approach is shown schematically in fig. 2.5.

Structure searching calculations were performed on germanium telluride nanowires to verify that the confining potential does indeed have little effect on which structures are the most energetically favourable at each nanotube radius. These searches generated around 1100 structures, with explicit treatment of the SWNT throughout. The set of structures predicted using the explicit nanotube was compared to the results of a structure search that used the implicit nanotube (details of which are given in chapter 3), and it was found that all energetically favourable structures located with full treatment of the SWNT were also found using the confining potential, and that some energetically favourable structures were *only* found using the confining potential, likely as a result of the effects of strain combined with the fact that only a discrete set of unit cell lengths is accessible as specified by eq. 1.6. These searches were performed using exactly the same scheme as the searches which used the confining potential; the only difference is that the SWNT was treated explicitly throughout rather than replacing it with a confining potential of equivalent radius (one consequence of which is that the nanowire and nanotube cannot independently optimise their periodic lengths).

A further test of the confining potential comparing the formation energies of nanowires in implicit and explicit nanotubes is described in section 4.1. Again, the results indicate that the confining potential provides a good approximation of the energetics of nanowire encapsulation, so that its use during the structure search is justified.

Physically, one can anticipate (and results in the following chapters confirm) that for small tube radii, the structure will primarily be determined by atomic close-packing considerations due to the effects of the confining potential on the wire; and that for large radii, the structure will become more ‘bulk-like’ (and in the limit of infinite radii, the optimal structure for the encapsulated nanowire will simply be a large cylindrical crystal of the bulk form of the filling material). To capture both of these extremes, a dual approach was used in which some initial structures were generated subject to the symmetry of a rod group, and some subject to the symmetry of a space group.

In the approach based on rod group symmetry, a random nanotube radius is selected along with a random cell length and some atoms of the filling material are inserted into the cylindrical confining potential, subject to the constraints of a randomly selected rod group. The structure is then relaxed to a minimum of the PES using CASTEP.

To select a rod group, the code first chooses at random whether the group should be crystallographic or non-crystallographic. In the former case, one of the 75 crystallographic groups is then chosen from a precomputed database. The database was built using the program WYCKPOS [138] which is hosted on the Bilbao crystallographic server [139, 140]. In the latter case, in the absence of an exhaustive database (there are infinitely many non-crystallographic rod groups), an integer  $n$  is chosen corresponding to a non-crystallographic order of symmetry (i.e. not 1, 2, 3, 4, or 6), and the rod group is chosen to be  $Pn$ . The corresponding Wyckoff positions for the chosen rod group are constructed (whereas they would otherwise be read from the precomputed database if the rod group had been crystallographic) and imposed on the cell as usual, as described in section 2.7.

In the case where a ‘bulk-like’ nanowire structure is desired, a random space group is selected and a bulk-like structure (i.e. one with 3D periodicity) is generated subject to the constraints of that space group, as in a normal AIRSS search. However, rather than geometry optimising it, a cylindrical cut-through of the cell is created, with the radius of the cylinder matching that of the chosen nanotube. At this point, the cut-through is tested to see if its stoichiometry is acceptable; if the stoichiometry of the atoms

contained in the cylindrical cut-through does not match the desired stoichiometry, then it is rejected and the whole process begins again from the start. If the stoichiometry is correct, the cylindrical cut-through is stretched or squashed to match with the periodic length of the unit cell containing the confining potential, and is then inserted into that cell inside the confining potential. The bulk structure from which the cut-through was taken is then discarded. At this stage the unit cell contains a cylinder-shaped cutout of a bulk-like structure, and is then geometry optimised using CASTEP with a confining potential included at the chosen nanotube radius.

These two approaches – rod group- and space group-based structure generation – each have their own merits: the former scheme helps to predict structures such as the narrow structures towards the top of table 3.1; and the latter scheme is more suited to predicting structures such as those at the bottom of the table that have a kind of translational order in the  $xy$  plane, even if that order is not truly periodic in the technical sense of the word.

In the structure searches, the lattice parameter  $c$  (the length of the unit cell in the  $z$ -direction) is permitted to vary, but  $a$ ,  $b$ ,  $\alpha$ ,  $\beta$  and  $\gamma$  are fixed during geometry optimisation. This eliminates problems with strain, since the cell can then expand and contract freely in the  $z$ -direction until the stress in that direction is zero; this is not an option when the nanotube is included explicitly.

For each optimised structure found, the formation energy of the encapsulated nanowire is calculated:

$$E_F = E_{\text{ENW}} - N_{\text{Fill}}\mu_{\text{Fill}}, \quad (2.38)$$

where  $E_{\text{ENW}}$  is the energy of the encapsulated nanowire,  $N_{\text{Fill}}$  is the number of formula units of the filling material, and  $\mu_{\text{Fill}}$  is the chemical potential for a single formula unit of filling material. Note that since the nanotube is not included explicitly in the structure search, no corresponding chemical potential term is required in eq. 2.38 for the carbon atoms in the above expression for the formation energy, even though the formation energy is that of an encapsulated nanowire, rather than of the nanowire on its own.

The energetic favourability of a structure is determined by its formation energy per atom; since the term  $N_{\text{Fill}}\mu_{\text{Fill}}$  shifts all of the per-atom formation energies by the same amount, the question of which structures have the lowest formation energy is unchanged by the choice of  $\mu_{\text{Fill}}$ . Although the true chemical potential should correspond to the

vapour phase of the filling material (assuming the nanowire is formed by the sublimation method), we are therefore free to choose to use the bulk form of the filling material as a reference from which to calculate  $\mu_{\text{Fill}}$ , safe in the knowledge that this cannot affect the structures' relative energetic favourability. As a result, formation energies in this thesis give the energy for the encapsulated nanowire to form relative to the bulk filling material outside of a pristine SWNT. While a more physical choice of  $\mu_{\text{Fill}}$  would be that of vapour-phase filling rather than bulk, choosing the bulk as the source was found to be more informative because one can then infer how close the filling structure is to the bulk (infinite radius) limit, since in this limit  $E_F$  must tend to zero as the structure becomes more bulk-like with larger nanotube radius.

The result of the structure search is a range of structures with different formation energies and in SWNTs of different radii. Since one would ideally like to predict the ground-state structure as a function of nanotube radius, the structures were grouped by nanotube radius, and the lowest-energy structures at each radius were singled out. Each of these structures was re-relaxed in multiple nanotubes of varying radii, with carbon atoms included explicitly within the DFT calculation rather than being approximated by a classical potential. For each nanowire structure, these calculations give the formation energy as a function of the radius of the encapsulating nanotube. From this, one can predict the ground state as a function of radius.

Whilst there are various ways this scheme could be extended, the basic method remains the same throughout. The following chapters describe the results of applying this scheme to multiple different systems.

# Chapter 3

## Encapsulated GeTe nanowires and phase change

Germanium telluride is a chalcogenide whose phase-change properties make it the subject of considerable interest due to its non-volatile memory applications [141–145]. In particular, it undergoes a reversible, temperature-induced crystalline-amorphous transition in which the resistance of the amorphous phase is multiple orders of magnitude lower than that of the crystalline phase [146, 147]. These phase-change properties make GeTe a prime candidate for information storage technology [148] and have led to much research activity, both on GeTe itself and on related phase-change materials such as the ternary alloy  $\text{Ge}_2\text{Sb}_2\text{Te}_5$  (also known as GST) [149–155].

Low-dimensional forms of GeTe have also drawn significant attention, with thin films having been used in the recent past as rewritable optical disk memory [156], and GeTe nanoparticles also having been investigated for their phase-change properties [157]. There has also been emerging interest in the technological potential of GeTe nanowires [158–162]. Experiments have found that, at least at larger radii, GeTe nanowires retain the bulk phase’s technologically useful phase-switching properties [163, 160], and that their melting temperature is lower than that of the bulk [164], hence they may be useful as phase-change components in low-power electronic devices. Lee *et al.* confirmed that with decreasing nanowire diameter comes a decrease in the current required to reset the material from the amorphous to the crystalline phase [165]. However, they studied only nanowires broader than 28 nm – much larger than the ‘extreme nanowire’ limit considered in this thesis. Recently, some experimental work

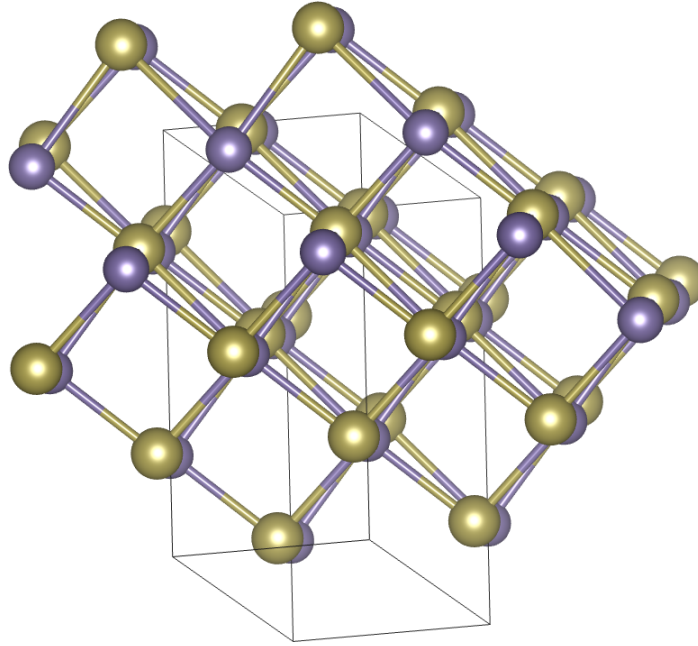


Figure 3.1 The  $\alpha$  phase formed by GeTe in ambient conditions; Ge atoms are blue, tellurium atoms are gold, and the unit cell is shown in wireframe.

has been performed on encapsulated GeTe extreme nanowires, with TEM imaging appearing to indicate the existence of a crystalline rocksalt-like phase [19].

Above 670 K, bulk GeTe adopts the rocksalt structure [166], with space group  $Fm\bar{3}m$ , as seen in many binary compounds. Below that temperature, however, it undergoes a ferroelectric distortion which slightly displaces the atoms from their position in the rocksalt structure, reducing its symmetry to  $R\bar{3}m$ . These two phases are referred to as  $\beta$  and  $\alpha$  GeTe, respectively. The latter phase is shown in fig. 3.1.

### 3.1 Structure search

The objective of the work described in this section is to predict the crystalline phases of GeTe nanowires encapsulated within single-walled carbon nanotubes (SWNTs), and to analyse their properties. Structure searches were performed using the scheme outlined in section 2.9. For the initial searches, ultrasoft pseudopotentials were used which treat as valence only the  $4s$  and  $4p$  orbitals of Ge and the  $5s$  and  $5p$  orbitals of Te. To ensure the convergence of these calculations, some test calculations were performed on a GeTe nanowire system at varying plane wave cut-off energy and Brillouin zone

$k$ -point sampling density. The plane wave basis set was truncated beyond energies of 300 eV, which was found to induce an error in the calculated formation energies of less than 15 meV per filling atom. The Brillouin zone (BZ) was sampled using a set of  $n$  points equally spaced along the  $\mathbf{c}^*$  axis. This is equivalent to a  $1 \times 1 \times n$  Monkhorst-Pack scheme.  $n$  was chosen to give a spacing between  $k$ -points along the periodic direction of  $0.05 \times 2\pi \text{ \AA}^{-1}$ , which was found to cause an error of under 10 meV per filling atom. The PBE exchange-correlation functional was used for the search, and for all other calculations in this thesis except where stated otherwise.

As described previously, after the initial search the most energetically favourable structures were selected, and higher-precision calculations were performed with the carbon atoms treated explicitly. For these calculations, CASTEP's on-the-fly pseudopotentials were used. These are harder and more accurate than those used for the initial search. The on-the-fly germanium pseudopotential also treated the  $3d$  electrons as valence, unlike the softer pseudopotential which was used for the initial searches, and a carbon pseudopotential was used which treated the  $2s$  and  $2p$  electrons as valence and the  $1s$  as core. The Te pseudopotential, while also harder than that used for structure searching, treated only the  $5s$  and  $5p$  electrons as valence, as before. A higher basis set cutoff of 500 eV was used, along with an improved  $k$ -point sampling of  $0.032 \times 2\pi \text{ \AA}^{-1}$ . The resulting formation energy errors associated with the convergence of these two parameters were found to be under 3 meV and 10 meV per filling atom, respectively. In the encapsulated nanowire supercells, mismatch between the nanowire and the tube was allowed to reach at most 4%; any proposed supercells with greater mismatch were rejected. Where mismatch occurred between the nanowire and the nanotube containing it, the wire was always stretched to match the DFT equilibrium length of the nanotube, rather than the other way around (since the wire is much less resistant to strain than the nanotube).

The geometry optimisations were performed at fixed lattice parameters, so that the periodicity of the encapsulated nanowire (i.e., the length of the unit cell) was constrained to be the same as that of the nanotube on its own. This is to avoid a spurious strain on the nanotube due to its incommensurability with the nanowire. To correct for the effects of strain on the nanowire, the strain energy was computed for each nanowire structure as a function of its strain,  $s$ . In keeping with usual definition of strain,  $s$  was defined as the fractional difference in length relative to the equilibrium length in the absence of a confining nanotube. This was done for a range of lengths in the vicinity

of that equilibrium length. For each calculation, the total strain energy was calculated as

$$E_{\text{str}} = E(s) - E(0), \quad (3.1)$$

where  $E(s)$  is the total energy at strain  $s$ , so that  $E(0)$  is the energy at the equilibrium length.

To interpolate these data points, a third-order polynomial fit was performed, generating an approximation to the strain energy function  $E_{\text{str}}(s)$ . Then, when computing the formation energies of filled nanotubes, the strain energy  $E_{\text{str}}$  was evaluated at the strain associated with the mismatch between the nanowire's optimised length and the length of the nanotube into which it is inserted. This strain energy was then subtracted off. The formation energy for the encapsulated nanowire is then

$$E_F = E_{\text{ENW}} - N_{\text{GeTe}}\mu_{\text{GeTe}} - N_C\mu_C - E_{\text{str}}(s), \quad (3.2)$$

where  $E_{\text{ENW}}$  is the DFT energy of the encapsulated nanowire system (with the tube included explicitly),  $N_C$  is the number of carbon atoms in the tube,  $\mu_C$  is the chemical potential of carbon derived from a DFT calculation of the tube on its own,  $N_{\text{GeTe}}$  is the number of GeTe formula units in the encapsulated nanowire, and  $\mu_{\text{GeTe}}$  is the chemical potential of one formula unit of GeTe which was taken from a DFT calculation on its bulk unit cell. (Note that because  $E_F$  depends only on  $\mu_{\text{GeTe}} = \mu_{\text{Ge}} + \mu_{\text{Te}}$ , we do not need to determine separately the values of  $\mu_{\text{Ge}}$  and  $\mu_{\text{Te}}$ .) For efficiency, lookup tables are maintained for  $\mu_C$  as a function of chiral vector and repeat length, so that if a particular nanotube appears in multiple different supercell calculations,  $\mu_C$  is not unnecessarily recalculated.

The choice of which nanotubes (i.e. which chiral vector and repeat length) to insert the nanowires into is based firstly on the number of atoms in the supercell (the fewer the better, to minimise computational cost); secondly, on the strain on the nanowire that would result from choosing the nanotube in question (with an upper limit of 4% imposed as discussed previously); and thirdly, on the thickness of the nanowire relative to that of the tube. This last condition is because the size of the gap between the nanowire and the nanotube walls will have a large effect on the energy cost of encapsulating the nanowire inside the nanotube: if the tube is too small so that there is extensive repulsion between wire and tube, the formation energy will be much too high for the structure to be physically relevant (and the nanowire is likely to be crushed by

the nanotube and therefore will probably be mechanically unstable anyway). On the other hand, if the nanotube is much wider than the nanowire, the formation energy of the encapsulated nanowire will essentially totally converged to its value at infinite tube radius, since the atoms of the wire and tube will be too far away to interact significantly. This also means that we are able to compute the limit of the formation energy at infinite tube radius very cheaply by simply simulating the nanowire on its own, with no carbon atoms and no confining potential.

As described in the previous section, the lowest-energy structures from the initial searches were re-relaxed in multiple nanotubes of different radii, with carbon atoms treated fully quantum-mechanically. For each nanowire structure, these calculations give the formation energy as a function of the radius of the encapsulating tube. These results are shown together on figs 3.2 and 3.3, on which each data point corresponds to a single supercell optimisation of a filled nanotube. Table 3.1 summarises the structure and symmetry of each structure appearing on these figures.

One can identify on fig. 3.2 a series of zero-temperature phase transitions as the radius grows and new structures become energetically favourable due to the greater size of the central cavity available to the nanowire. At very small radii, a series of Ge-Te dimers is formed, which the phase diagram shows is energetically preferable to the formation of a linear chain at all nanotube radii. At 3.7 Å the tube is wide enough that it becomes energetically favourable for a 1D chain of Ge and Te atoms to buckle into a zig-zag. At 4.8 Å, it becomes optimal to fit two of these zig-zags next to each other, increasing the coordination. Then, at 5.4 Å, a  $2 \times 2 \times \infty$  cut-through of the rocksalt-like GeTe bulk forms. Beyond 8 Å a larger number of phases become energetically competitive, with the ground state passing through a series of increasingly wide rocksalt-like cut-throughs (after  $P\bar{4}m2$ ,  $Pcc2$  then  $P\bar{4}mm$ ). The trend towards more bulk-like structures that is visually apparent is also confirmed by inspection of the bond length and angle distributions (not shown), with both distributions converging rapidly to the bulk as the system passes through the succession of ground state phases. The almost 90-degree bond angles seen in the bulk are apparent even in the  $Pm2m$  and  $P\bar{1}$  zigzag phases. The bonds are generally slightly shorter in the narrower phases than in the larger, more bulk-like phases, presumably due to the undercoordinated nature of the bonding. In summary, the observed sequence of phases shown in fig. 3.2 is  $P\infty \rightarrow Pm2m \rightarrow P\bar{1} \rightarrow P\bar{4}m2 \rightarrow Pcc2 \rightarrow P\bar{4}mm$ . A clear pattern is also evident in which phases that become energetically stable at larger radii are also more stable in

Structure	End-on view	Side-on view	3D view
$P_{\infty}$ (1D dimers)			
$P_{\infty}/m$ (1D chain)			
$Pm2m$ (Zig-zag)			
$P\bar{1}$ (Parallel zig-zag)			
$P\bar{4}m2$ (2x2 rocksalt)			
$P3mm$ (Diatomic rings)			
$P\bar{4}$ (Zincblende-like)			
$Pmm2$ -I (2x3 rocksalt)			
$P4/mmm$ -I (Monatomic rings)			
$Pmm2$ -II (Truncated 3x3 rock-salt)			
$P4/mmm$ -II (3x3 rocksalt)			
$P6/mmm$ (Monatomic rings)			
$P\bar{4}mm$ (Plus-shaped rocksalt)			
$Pcc2$ (2x4 rocksalt)			

Table 3.1 All GeTe filling structures shown on fig. 3.2, ordered by their width. Where two structures have the same symmetry, we distinguish them by appending a number in Roman numerals (e.g.  $P4/mmm$ -I).

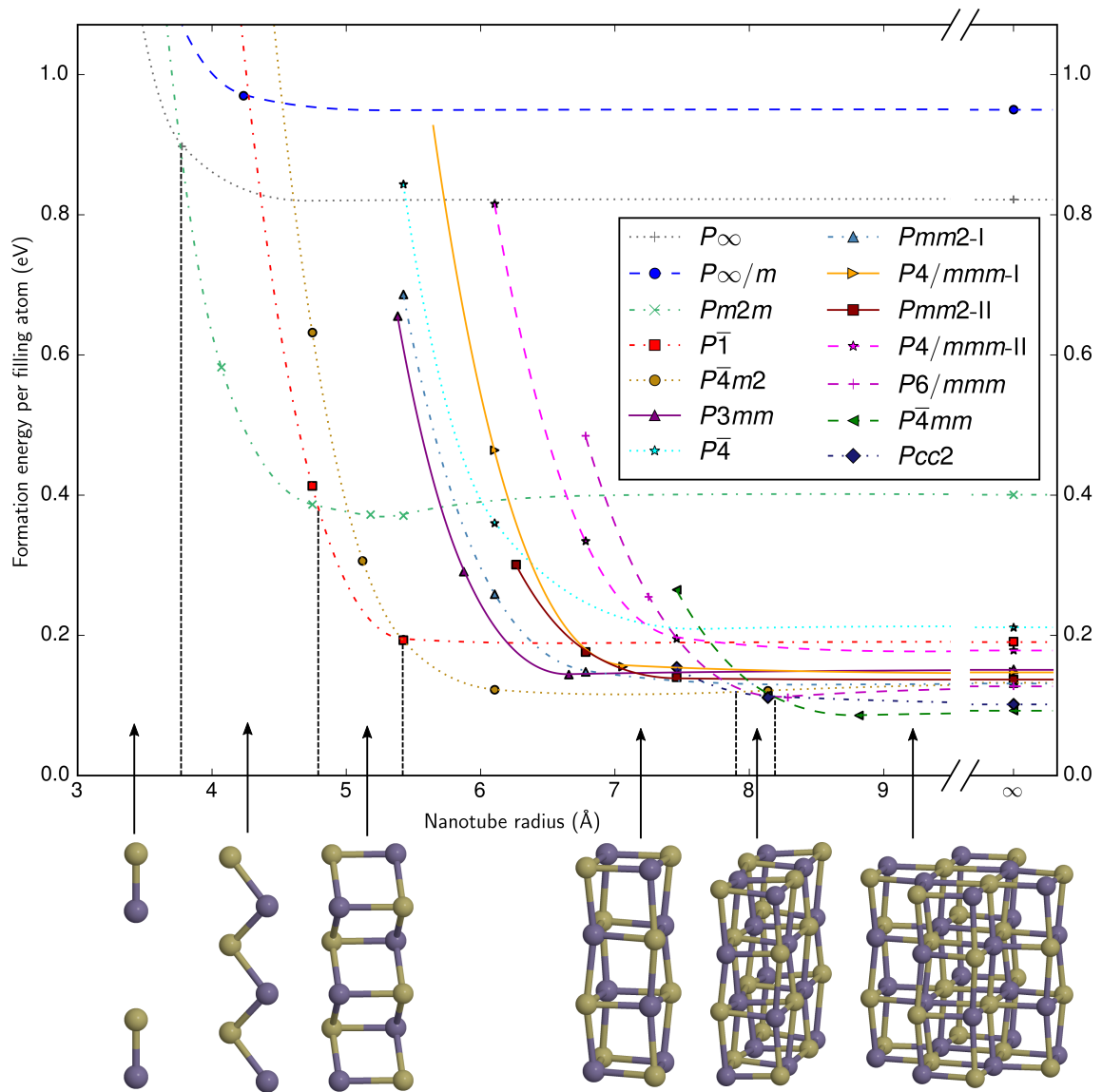


Figure 3.2 Phase diagram for encapsulated GeTe nanowires, annotated with the succession of ground-state structures as the chosen radius varies. Critical radii beyond which one structure overtakes another as the ground state are shown via vertical dotted lines.

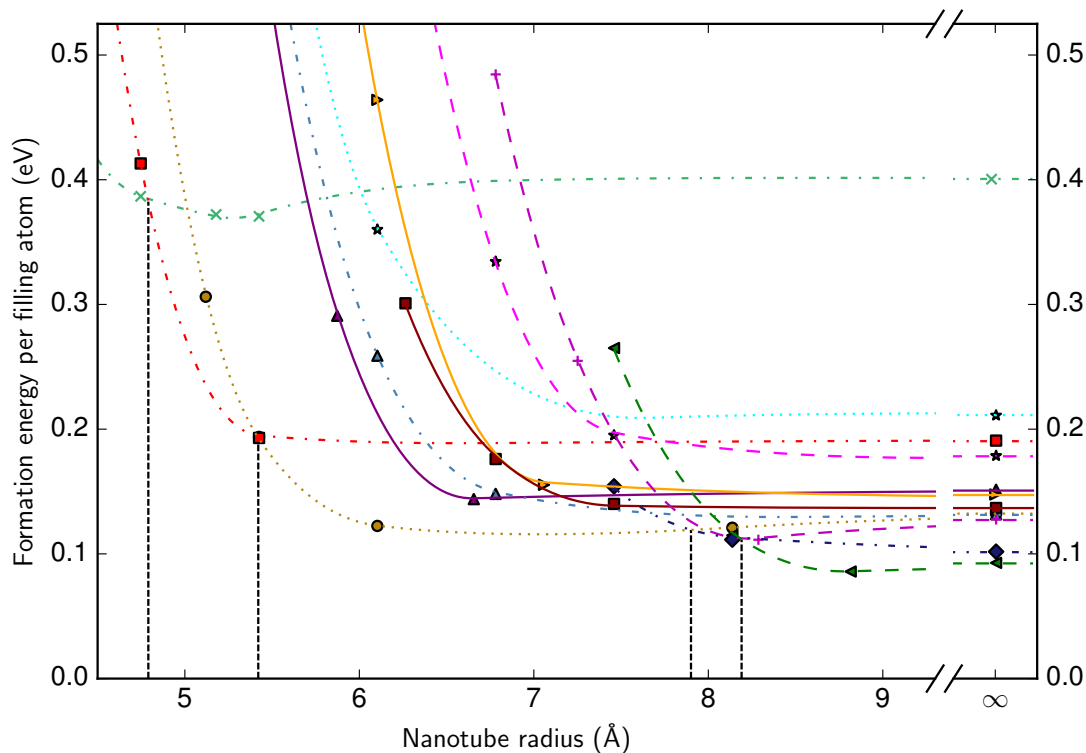


Figure 3.3 Close-up of the GeTe encapsulated nanowire phase diagram at larger values of the nanotube radius; the legend is the same as on fig. 3.2.

the large-radius limit. This pattern, which is also apparent in phase diagrams shown elsewhere in this work, is a consequence of the fact that the constraints of narrower nanotubes prevent structures from bonding in an energetically optimal manner.

The fact that the  $P\bar{4}mm$ , is followed by  $Pcc2$ , rather than something more square in cross-section, appears to be because the nanotube is able to distort slightly to accommodate the shape of the  $Pcc2$  structure.

It should be noted that carbon nanotubes of radii as small as 2.2 Å have been experimentally produced [167], so in principle all (finite) radii shown on the phase diagram are experimentally accessible. This is also true of the phase diagrams shown in chapters 4 and 5.

The electronic structure of the phases on the phase diagram was also investigated. These calculations were performed at the same convergence parameters as the polishing searches, but with the phases in their geometry-optimised structures in the absence of a confining nanotube. The band structures were obtained by first self-consistently

Structure	Band gap
$P_\infty$ (1D dimers)	2.58 eV, direct: $k = Z$
$P_\infty/m$ (1D chain)	None (conductor)
$Pm2m$ (Zig-zag)	1.49 eV, direct: $k = Z$
$P\bar{1}$ (Parallel zig-zag)	1.13 eV, indirect: $k = 0.14 \rightarrow \Gamma$
$P\bar{4}m2$ (2x2 rocksalt)	1.01 eV, direct: $k = Z$
$P3mm$ (Diatomic rings)	1.55 eV, direct: $k = \Gamma$
$P\bar{4}$ (Zincblende-like)	1.2 eV, indirect: $k = \Gamma \rightarrow 0.33$
$Pmm2$ -I (2x3 rocksalt)	0.92 eV, indirect: $k = 0.42 \rightarrow 0.49$
$P4/mmm$ -I (Monatomic rings)	None (conductor)
$Pmm2$ -II (Truncated 3x3 rocksalt)	1.19 eV, direct: $k = Z$
$P4/mmm$ -II (3x3 rocksalt)	0.6 eV, indirect: $k = Z \rightarrow 0.41$
$P6/mmm$ (Monatomic rings)	None (conductor)
$P\bar{4}mm$ (Plus-shaped rocksalt)	0.88 eV, direct: $k = 0.48$
$Pcc2$ (2x4 rocksalt)	1.11 eV, direct: $k = 0.48$

Table 3.2 The existence and nature of band gaps for the GeTe structures found in the search. Where a band gap is present, its position in the 1D Brillouin zone is indicated. Points in  $k$ -space are given in units of  $2\pi/c$ , so that the high-symmetry points  $\Gamma$  and  $Z$  correspond to  $k = 0$  and  $k = 1/2$  respectively. For example, the  $P\bar{1}$  structure has an indirect gap with the valence band maximum at  $k = 0.14$  and the conduction band minimum at  $\Gamma$ .

solving the Kohn-Sham equations, and then solving them non-self-consistently using the resulting Kohn-Sham potential. In the non-self-consistent calculations, 101  $k$ -points along the periodic direction were used. Rather than plotting every phase's band structure, which would take up a considerable amount of space, the most important features are summarised instead in table 3.2. The table shows that there is a considerable amount of variance in electronic properties between the different phases, with large variations in band gaps and their positions in the Brillouin zone. The ability to tune which phase forms by selecting a nanotube radius therefore also implies to an extent the ability to tune the electronic properties of GeTe ENWs.

In fig. 2a of ref. 19, a TEM image is shown of a  $2 \times 2$  rocksalt-like GeTe nanowire encapsulated within a nanotube about 6 Å in radius. This is a good match to the phase diagram on fig. 3.2, which predicts that at this radius, the  $2 \times 2$  rocksalt structure is the ground state. An image of a nanotube of radius around 5.5 Å also appears (fig. 2d in the paper), containing a phase which the authors attribute to a rhombohedral structure, but which appears to be a good match to the  $P\bar{1}$  double zig-zag structure (see

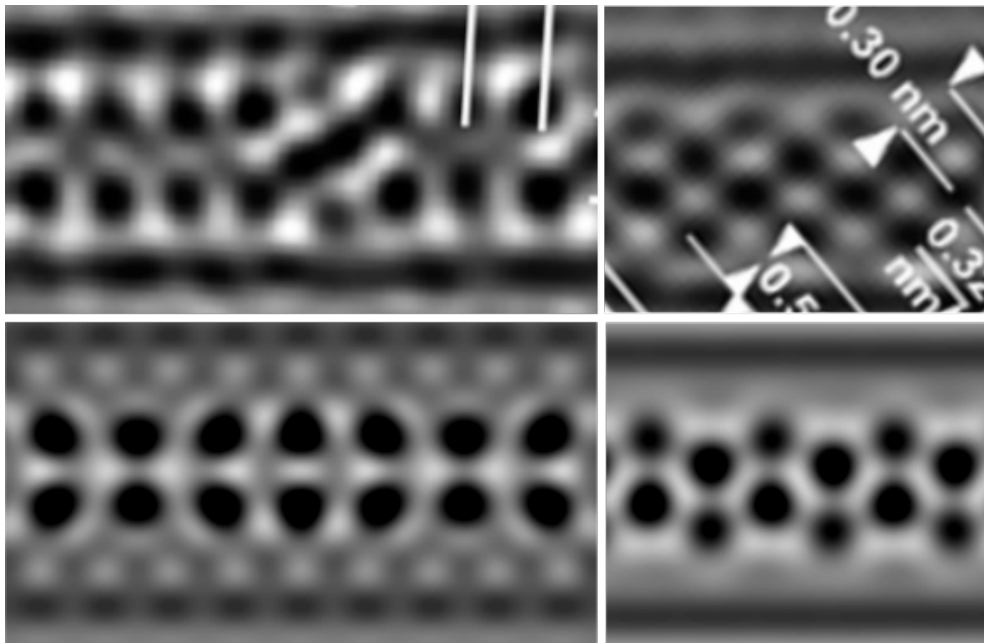


Figure 3.4 A comparison between experimental TEM imagery from ref. 19 (top) and simulated TEM imagery (bottom) generated from the polished GeTe structures predicted in this work using SimulaTEM’s ‘multislic’ package [168]. The structures shown are the  $P\bar{4}m2$  (left) and  $P\bar{1}$  (right) phases.

table 3.1), which at that radius is predicted to be energetically competitive with  $2 \times 2$  rocksalt (though not quite the ground state). A comparison between this experimental imagery and some simulated TEM imagery based on the predicted structures is shown on fig. 3.4.

Finally, to estimate the significance of dispersion effects, some calculations were performed in which the energy difference between the  $P\bar{1}$  and  $P\bar{4}m2$  phases in the (8,8) nanotube of radius  $5.42 \text{ \AA}$ . This point was chosen because it is extremely close to a phase transition on fig. 1, and so is of particular interest. In this recalculation, dispersion forces were calculated within the Tkatchenko-Scheffler scheme [169].  $5 \text{ \AA}$  of additional padding was added to the unit cells in the directions parallel to the axis of the nanotube, to deal with the increased range of the unwanted interaction with periodic neighbours. The energy difference between the two phases was found to shift by  $0.03 \text{ eV}$  per filling atom. Since this effect is small, the decision not to include dispersion forces was concluded to be justified; this is especially true given that one would ideally want to use a more advanced dispersion scheme such as MBD\*, for which the computational cost involved in computing the forces is very high for the

large cells under consideration. Note also that many dispersion-correction schemes are unlikely to be accurate for the unusual coaxial geometry considered here, having been parameterised semi-empirically to describe essentially pairwise interactions.

## 3.2 Crystalline phases at finite temperatures

The near-degeneracy of many of the phases, especially in wider nanotubes, suggests that at finite temperatures some of the metastable structures may become energetically competitive or even overtake the zero-temperature ground states in energetic favourability. To test this hypothesis, harmonic phonon calculations were performed to obtain the vibrational free energy of each phase as a function of temperature as described in section 2.4. These phonon calculations were performed within an implicit nanotube, and in each case the radius of the implicit nanotube was chosen to match that of the actual nanotube in which each structure was found to be most stable (relative to the other phases) on fig. 3.2.

The phonon calculations were performed at finer parameters than both the AIRSS search and the post-search polishing. The same pseudopotentials were used as for the phase diagram calculations, but each phase was now relaxed until the forces were less than  $1 \text{ meV } \text{\AA}^{-1}$ . The BZ was now sampled along the periodic direction with a spacing better than  $0.02 \times 2\pi \text{\AA}^{-1}$  in each case, and the plane-wave cut-off energy was increased to 600 eV. The dynamical matrix was computed using the supercell method, with each supercell's length along the periodic direction chosen to be at least  $30 \text{\AA}$ . The convergence of these settings was tested by performing some calculations at different cell lengths,  $k$ -point samplings and basis set cutoff energies. It was found that a  $30 \text{\AA}$ -long cell is converged enough to give most frequencies to within  $1 \text{ cm}^{-1}$  (with occasional exceptions), and to give vibrational free energies to within 1 meV per atom at 300 K. The errors in vibrational frequencies arising from the choice of plane-wave cutoff and the Brillouin zone sampling were also found to be usually less than  $1 \text{ cm}^{-1}$ .

Because the imposition of the confining potential on the structure breaks the translational invariance in the non-periodic directions, CASTEP's code was edited to change the implementation of the acoustic sum rule to only identify as acoustic the two modes corresponding to translation along, and rotation about, the periodic axis.

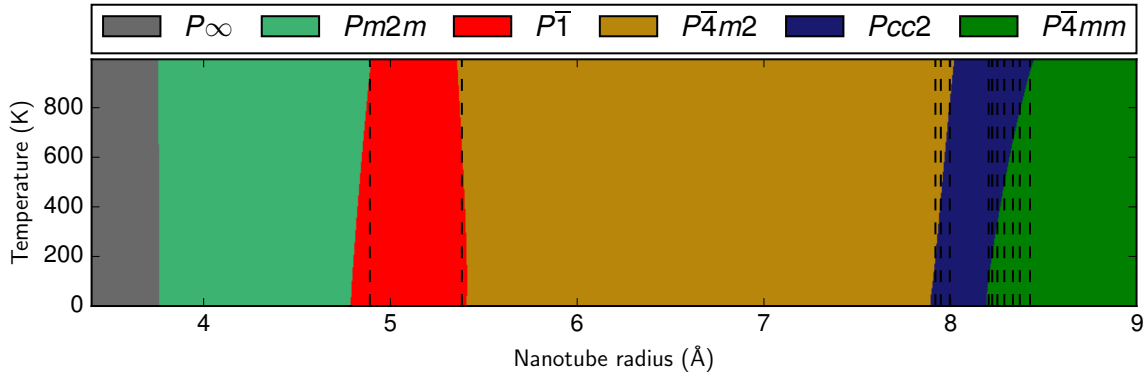


Figure 3.5 The variation of the ground-state nanowire structure with nanotube radius and temperature. Variations in vibrational contributions to the structures' free energies are seen to induce changes in the nanotube radii at which two ground state phases are in equilibrium as the temperature varies, with the result that for certain nanotube radii, a temperature-induced phase transition is expected; these radii are marked with vertical dotted lines, and their corresponding chiral vectors are indicated in table 3.3.

Using the vibrational free energies along with the DFT formation energies, the temperature- and radius-dependent free energy of formation was calculated:

$$F(R, T) = E_F(R) + F_{\text{vib}}(T). \quad (3.3)$$

This free energy is plotted on fig. 3.5. The figure indicates that finite temperature effects do not cause any phases which never form at zero temperature to become energetically favourable; however, the critical nanotube radii at which there are two degenerate ground state structures (shown as dashed vertical lines on fig. 3.2) do shift noticeably as temperature varies. An important consequence of this is that, for certain nanotube radii, heating up the ENW will induce a crystalline-crystalline phase transition. All sets of chiral vectors in which such a transition will occur were identified and are shown in table 3.3. These crystalline-crystalline transitions have no analogue in the bulk phase, and therefore suggest that GeTe behaves in a qualitatively different manner when strongly confined to one dimension.

Of course, the fact that one phase replaces another as the thermodynamic ground state does not necessarily mean that there will be an immediate phase transition in a real system. For example, diamond is slightly metastable [170], but does not immediately become graphite because two phases are separated by a large energy barrier. One could investigate the timescales over which the thermodynamic phase transitions identified in

Chiral vector	Radius (Å)	Structures	Temp. (K)
(9,5)	4.81	$P\bar{1} \rightarrow Pm2m$	310
(10,4)	4.89	$P\bar{1} \rightarrow Pm2m$	980
(12,3)	5.38	$P\bar{1} \rightarrow P\bar{4}m2$	630
(15,8)	7.92	$Pcc2 \rightarrow P\bar{4}m2$	220
(18,4)	7.95	$Pcc2 \rightarrow P\bar{4}m2$	460
(16,7)	8.00	$Pcc2 \rightarrow P\bar{4}m2$	860
(18,5)	8.20	$P\bar{4}mm \rightarrow Pcc2$	130
(15,9)	8.22	$P\bar{4}mm \rightarrow Pcc2$	230
(21,0)	8.22	$P\bar{4}mm \rightarrow Pcc2$	230
(20,2)	8.25	$P\bar{4}mm \rightarrow Pcc2$	340
(16,8)	8.29	$P\bar{4}mm \rightarrow Pcc2$	510
(19,4)	8.33	$P\bar{4}mm \rightarrow Pcc2$	680
(17,7)	8.37	$P\bar{4}mm \rightarrow Pcc2$	790
(21,1)	8.42	$P\bar{4}mm \rightarrow Pcc2$	950

Table 3.3 Nanotubes at which the finite-temperature calculations indicate the presence of a phase transition between 0 and 1000 K. In the ‘structures’ column, the lower-temperature phase is indicated on the left and the higher-temperature phase on the right.

this section will occur in practice by using techniques such as e.g. the kinetic activation relaxation technique (k-ART), which identifies barriers in the energy landscape between two phases of a system [171].

While table 3.3 gives the temperatures at which one phase’s free energy becomes lower than another, a further possibility is that of phases existing metastably even where they are not the lowest in free energy. To test this possibility, each structure’s Boltzmann abundance,  $\exp(-\beta F)/\mathcal{Z}$ , was computed (where  $F$  is the free energy per formula unit of the structure in question,  $\mathcal{Z}$  is the canonical partition function, and  $\beta = 1/k_B T$  is the inverse temperature). This calculation was performed – as before – for a range of values of the temperature and nanotube radius, and incorporated both the ground-state energetics as well as the vibrational free energy derived from the phonon calculation.

The resulting finite-temperature phase diagram is shown on figure 3.6. The diagram confirms that, at larger radius, multiple phases become energetically competitive, even at temperatures as low as a few hundred K.

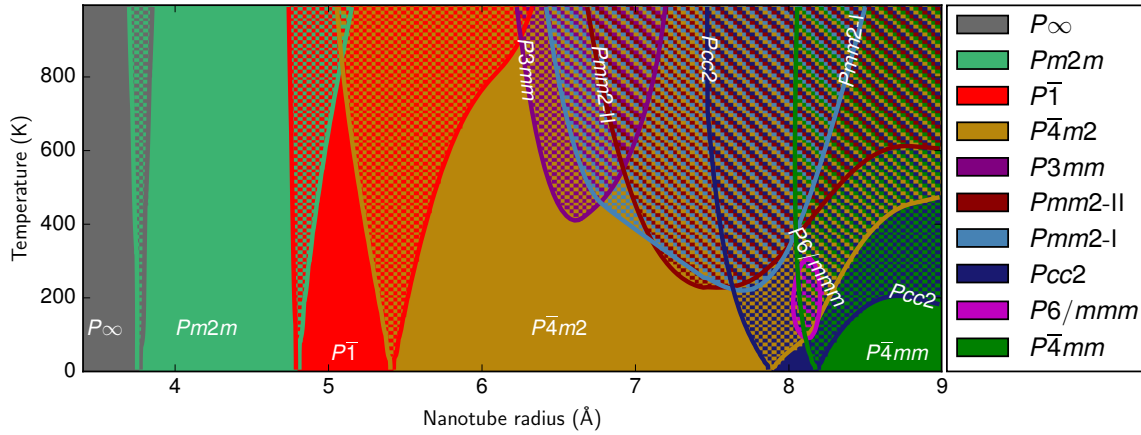


Figure 3.6 The abundance of the predicted nanowire phases as a function of nanotube radius and temperature. At each point of the diagram the Boltzmann probability,  $\exp(-\beta F)/\mathcal{Z}$ , is computed for each of the predicted nanowire phases within a canonical ensemble of encapsulated nanowires. Here  $F$  is the free energy per formula unit. For each phase, regions where the phase's Boltzmann probability is greater than 10% are bounded by a solid contour. Where this is true of multiple phases a checkerboard pattern is used to indicate the set of structures with probabilities greater than 10%.

So far the system under consideration has been an effectively infinitely long nanowire under periodic boundary conditions. Here we examine how the statistical mechanics are affected by the fact that in reality the nanowire will be of finite length – an important consideration for nanotechnological applications, for which the nanowire could potentially be quite short.

For nanotechnological applications, it is entirely possible that the nanotube could be short enough that the ENW inside may be a single crystal (rather than regions of different phases separated by phase boundaries). In that case, one can reasonably use  $\exp(-\beta E_F N)$  as the Boltzmann factor for a phase whose formation energy per formula unit is  $E_F$ , with  $N$  the total number of formula units in the crystal. Thus the statistical-mechanical abundance of each structure is a function not only of nanotube radius  $R$  and of temperature  $T$  but also of  $N$ . For given values of  $T$ ,  $R$  and  $N$ , one can calculate each structure's abundance and therefore the statistical probability that the nanowire is not in its ground state phase. By varying  $N$ , the point at which this probability falls below 10% was computed, which was defined as the point beyond which metastability is no longer likely. This process was repeated to obtain the variation of the value of  $N$  beyond which metastability is unlikely as a function of both  $T$  and  $R$ .

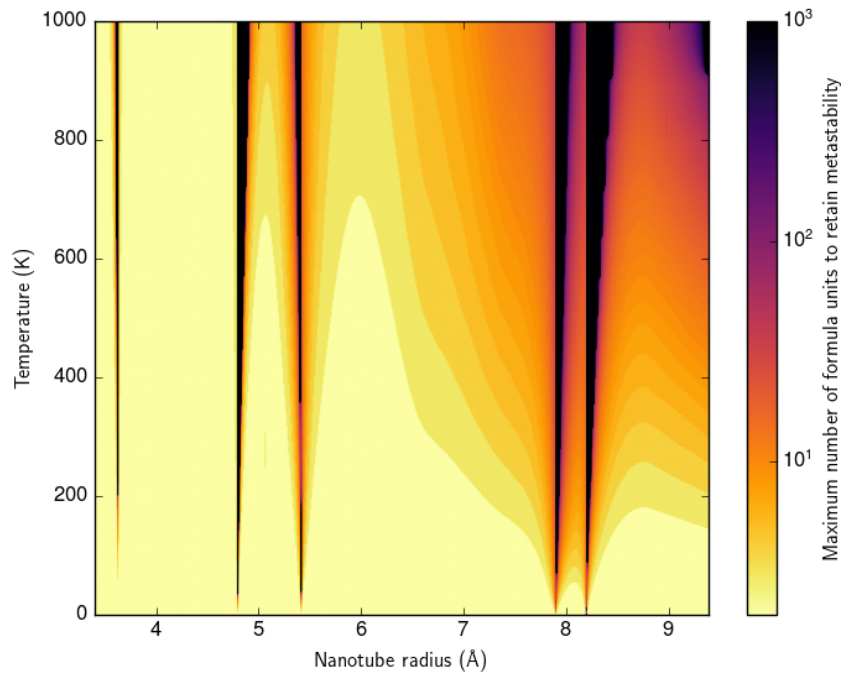


Figure 3.7 The length of a GeTe nanowire below which metastability is a significant possibility, plotted as a function of the radius of the encapsulated nanotube and the temperature. (The function is clipped to a maximum of  $N = 1000$  formula units.)

The results are shown on fig. 3.7. The most prominent features of these results are the divergences occurring in the vicinity of phase boundaries, at which the near-degeneracy of the ground state with one or more metastable phases leads to likely metastability even in very long nanowires. There is also – consistently with fig. 3.6 – a clear trend towards metastability in longer nanowires as the nanotube radius increases, due to the presence of many phases within a relatively narrow energy range at large nanotube radius (as can be seen from fig. 3.2).

A full study on the abundance of metastable regions within GeTe nanowires would need to include the energetic costs of grain boundaries between phases, which would require further AIRSS searches due to the possibility of interface reconstructions. As such, the results shown here merely represent a first approximation to the full physics of metastability in GeTe ENWs. Nevertheless, there are strong indications in these results that encapsulating GeTe inside carbon nanotubes results in rich and complex behaviour that is not seen in bulk GeTe.

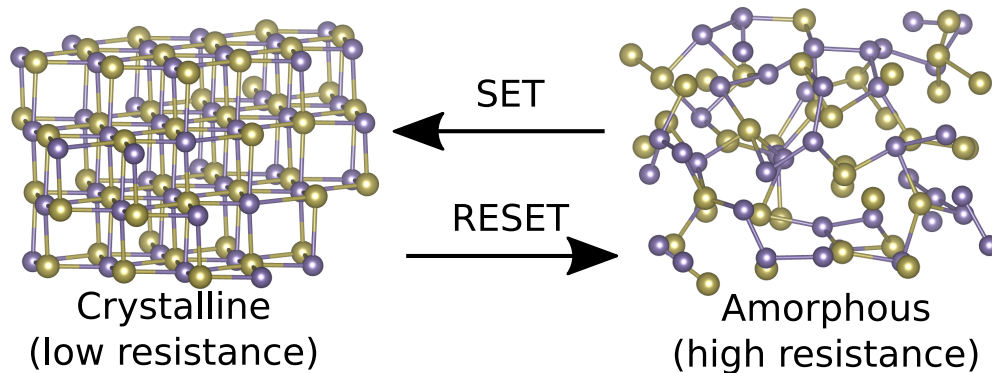


Figure 3.8 The two main solid states of germanium telluride, and the SET and RESET pulses used to induce phase change between them.

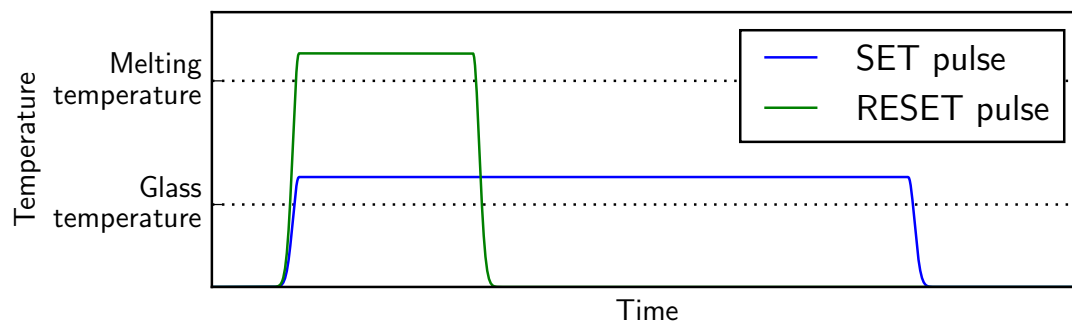


Figure 3.9 Schematic diagram showing the two kinds of temperature pulse by which phase change is induced in GeTe.

### 3.3 Crystalline-amorphous phase change

While the phase-change properties of bulk GeTe and of wide (tens of nanometres in diameter or larger) GeTe nanowires are relatively well-characterised [141, 172–174, 165, 175, 176, 149], those of atomically thin GeTe nanowires are not. The basic scheme by which phase switching is realised in GeTe is shown on figs. 3.8 and 3.9. In a RESET pulse, the phase change material is heated above its melting point  $T_m$ , and then rapidly quenched to below its glass transition temperature  $T_g$  [177].  $T_g$  is the point below which supercooled liquid undergoes a transition into an amorphous state. The cooling must be performed rapidly because the crystalline phase is the thermodynamic ground state below the melting point  $T_m$ . As a result, the material will crystallise if  $T_g < T < T_m$  for a sufficient amount of time. In a SET pulse, phase change material in the amorphous phase is heated to above  $T_g$  – causing it to transition into a supercooled liquid – but kept below  $T_m$ , above which the liquid would be the ground state and the

material would never crystallise. Crystalline nuclei then form within the supercooled liquid and grow until the whole substance is in the crystalline phase. Because of the time taken for this process to occur, the SET pulse takes longer than the RESET pulse. These processes form the basis of phase-change memory, with SET and RESET pulses corresponding to bit flips. The bit can then be read by measuring its electrical resistivity, which differs by multiple orders of magnitude between the crystalline and amorphous states [178]. In practice the SET and RESET pulses are generally applied using Ohmic heating, i.e. by passing a current through the material to generate heat. However, for our purposes it is simply the temperature that matters and we are essentially agnostic about how the temperature is manipulated. The objective of this section is to characterise the nature of these phase-change phenomena in GeTe ENWs via molecular dynamics simulations, with a particular focus on the technological implications.

### 3.3.1 Molecular dynamics force field for GeTe

To investigate phase change in GeTe ENWs, the force field introduced by Zipoli *et al.* in ref. 179 and applied in ref. 180 was used. This potential is based on the commonly used Tersoff potential [181], in which the potential energy is expressed as a sum over two-body terms  $V_{ij}$ :

$$E = \frac{1}{2} \sum_{i \neq j} V_{ij}, \quad (3.4)$$

where  $V_{ij}$  is defined as

$$V_{ij} = f_c(r_{ij})(A_{IJ}e^{-\lambda_{IJ}r_{ij}} - b_{ij}^{IJ}e^{-\mu_{IJ}r_{ij}}). \quad (3.5)$$

Note that uppercase indices  $I$  and  $J$  indicate dependence on the elements (Ge or Te) of atoms  $i$  and  $j$ .  $f_c$  is a smoothly varying cutoff function that keeps the interaction short-ranged:

$$f_c(r_{ij}) = \begin{cases} 1 & r_{ij} \leq R_{IJ} \\ 0 & r_{ij} \geq S_{IJ} \\ \frac{1}{2} \left( 1 + \cos \left( \pi \frac{r_{ij} - R_{IJ}}{S_{IJ} - R_{IJ}} \right) \right) & \text{otherwise} \end{cases} \quad (3.6)$$

The first and second terms in eq. 3.5 are the repulsive and attractive two-body terms, respectively. What distinguishes the Tersoff potential from simpler potentials is that  $b_{ij}^{IJ}$  is not a constant, but instead a function of the local coordinations of the  $i$ -th and

$j$ -th atoms. This allows the potential to reflect the fact that undercoordinated atoms will experience stronger attraction to other atoms due to their unsaturated bonding. In particular,  $b_{ij}^{IJ}$  is defined as

$$b_{ij}^{IJ} = \chi_{IJ}(1 + (\beta_I \xi_{ij}^{IJ})^{n_I})^{\frac{1}{2n_I}}. \quad (3.7)$$

The dependence on the atoms' local environments enters via

$$\xi_{ij}^{IJ} = \sum_{\substack{k \\ k \neq i \\ k \neq j}} f_c(r_{ij}) e^{\mu_{IJ} r_{ij} - \mu_{IK} r_{ik}} t_{ijk}^{IJK}, \quad (3.8)$$

with  $t_{ijk}^{IJK}$  being a three-body angle-dependent term, defined as:

$$t_{ijk}^{IJK} = 1 + \frac{c_I^2}{d_{IJK}^2} - \frac{c_I^2}{d_{IJK}^2 + \left( h_{IJK} - \cos \left( \pi \frac{\theta_{ijk} - \theta_0^I}{\pi - \theta_0^I} \right) \right)^2}, \quad (3.9)$$

where  $\theta_{ijk}$  is the three-body angle between atoms  $i$ ,  $j$  and  $k$ , with atom  $i$  being the central atom. Note that this  $t_{ijk}^{IJK}$  is a nonstandard modification of the usual Tersoff form.

Zipoli *et al.* follow the approach of Billeter *et al.* [182] of introducing an additional contribution to the energy which penalises non-ideal atomic coordinations:

$$E_{\text{coord}} = \sum_i E_i^c, \quad (3.10)$$

where  $E_i^c$  is defined for each atom as

$$E_i^c = c_2^I (\Delta z_i)^2 + \begin{cases} c_1^I \Delta z_i & z_i \geq z_0 \\ -c_1^I \Delta z_i & z_i < z_0 \end{cases} \quad (3.11)$$

The function  $\Delta z_i$  is defined as

$$\Delta z_i = \left[ |z_i - z_0^I| \right] + \begin{cases} 0 & z_i \leq z_T - z_B, \\ 1 & z_i \geq z_T + z_B, \\ \frac{1}{2} \left( 1 + \sin \left( \frac{\pi(z_i - z_T)}{2z_B} \right) \right) & \text{otherwise} \end{cases} \quad (3.12)$$

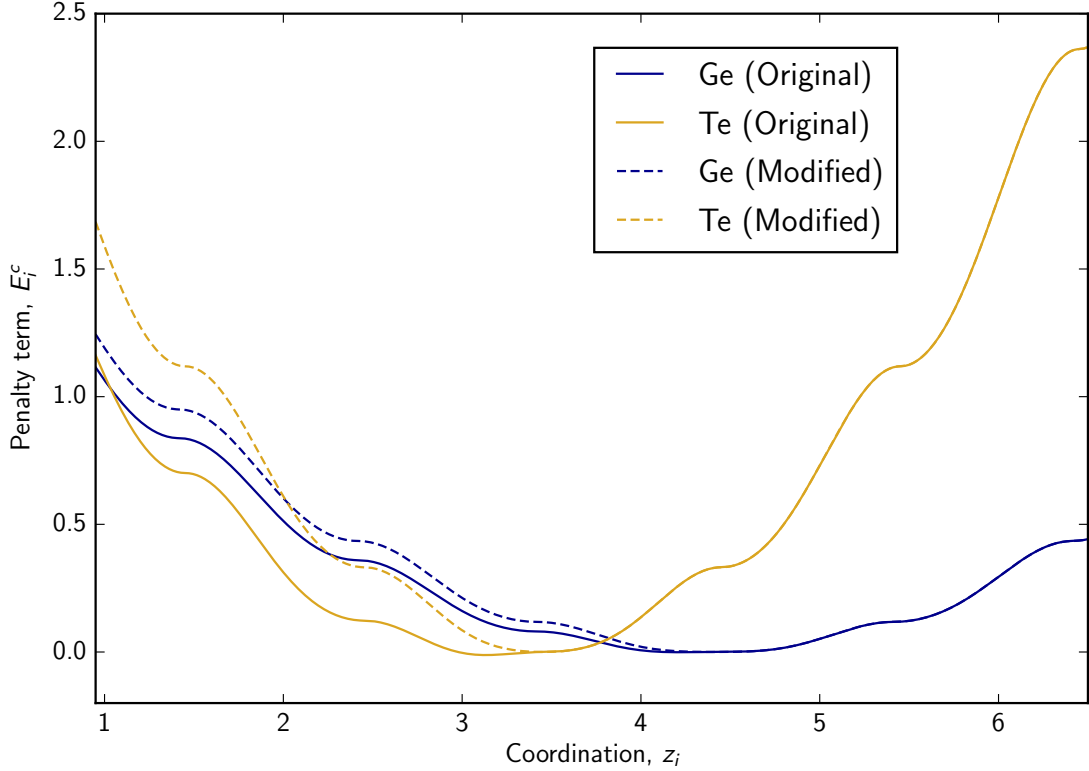


Figure 3.10 Coordination energy penalty terms as used in the GeTe potential of Zipoli *et al.*. Both the original form and the modified version used in this work are shown.

with  $z_T$ ,  $z_B$  and  $z_0^I$  being model parameters. The local coordination  $z_i$  is defined for each atom using the previously introduced functions  $f_c$  and  $b_{ij}^{I,J}$  as

$$z_i = \sum_{j \neq i} f_c(r_{ij}) b_{ij}^{I,J} \quad (3.13)$$

The full list of parameters for this potential, as well as information on its fitting and validation, are given by Zipoli *et al.* in ref. 179.

In this work, a slightly modified version of the potential described in Zipoli *et al.* was used. In particular, the coordination penalty was chosen to be

$$E_i^c = c_2^I (\Delta z_i)^2 + c_1^I \Delta z_i, \quad (3.14)$$

which is equivalent to always choosing the  $z_i \geq z_0$  case of eq. 3.11. The difference between the coordination terms is shown on fig. 3.10. The modified version here has a higher energetic penalty for undercoordinated atoms. The original potential was found

to be unstable to the formation of surfaces, with the consequence that in simulations of the crystallisation of bulk GeTe using said potential, a large number of voids were found to appear. By increasing the penalty for undercoordinated atoms, the modified potential used here stabilises the system against the formation of surfaces, which is particularly important for the simulation of low-dimensional systems.

Comparisons of some relevant properties between the two versions are shown in table 3.4. In general, the modified version more accurately describes measurable parameters – in particular the melting point and lattice parameters – at the cost of a slight increase in the RMSE in predicted energies. Since the melting properties of the material are particularly important for phase change, this small increase in RMSE was judged to be a justifiable price to pay for these benefits. Note that the modified version of the potential was not re-fitted; all the parameters are left unchanged. Such a re-fitting would require a prohibitively large computational cost (since a large training set of *ab initio* snapshots and energies would have to be generated) for a change in parameters that would likely be small (since the change in functional form is itself relatively minor). The RMSE is still quite low for a classical potential, even without re-fitting.

The potential was implemented in C++ within the LAMMPS molecular dynamics code [186] by extending and modifying LAMMPS' existing Tersoff potential class. Analytic derivatives were used in order to minimise numerical noise. The implementation was compared to an independent implementation of the potential written in Fortran by a collaborator<sup>1</sup>, and the two implementations were found to agree to machine precision on energies, forces, and stresses.

### 3.3.2 Crystallisation from supercooled liquid

Because the SET pulse (i.e. crystallisation) is slower than the RESET pulse (amorphisation), it is the crystallisation rate which is the limiting factor on the speed at which phase-change memory based on these principles can operate. The great interest in GeTe and its derivatives as phase-change memory results in large part from its unusually fast crystallisation, with crystallisation within 10 ns having been achieved for GeTe [187]. This rapid crystallisation has been attributed to the fragility of supercooled liquid GeTe [188]. A fragile liquid is a system in which there is a breakdown of the usual Stokes-Einstein relation,  $D \propto T/\eta$ , between the diffusivity  $D$  and the viscosity  $\eta$ . For

---

<sup>1</sup>David Quigley, Department of Physics, University of Warwick.

	Original	Modified	Target value
Bulk melting point (K)	$710 \pm 10$	$830 \pm 10$	998 [183]
$\alpha$ -GeTe volume ( $\text{\AA}^3/\text{atom}$ )	29.12	27.37	28.13 [184]
$\beta$ -GeTe volume ( $\text{\AA}^3/\text{atom}$ )	28.74	27.51	27.12 [185]
RMSE (solid nanowire) (meV/atom)	2.3	3.2	–
RMSE (liquid nanowire) (meV/atom)	9.0	9.6	–

Table 3.4 Differences between parameters derived from the original and modified versions of the GeTe potential. Melting points were obtained by simulating a crystalline-liquid interface and observing whether the crystalline phase grew or shrank for different temperatures. Volumes were calculated by performing a geometry optimisation on the structures, using the two versions of the potential and with DFT. Root-mean-squared errors (RMSE) were calculated relative to snapshots taken from CASTEP ab-initio molecular dynamics simulations of a 72-atom nanowire inside a confining potential, both in the liquid phase at 1000 K and in the crystalline phase at 200 K. Around 600 snapshots were used in total, and the energy of each was recalculated (within DFT again) without the confining potential to make the energies from DFT and from the force field comparable.

these liquids,  $D$  is higher at temperatures near  $T_g$  than the Stokes-Einstein relation would predict. As a result, crystallisation in a fragile liquid occurs more rapidly than one would expect given its viscosity at temperatures near  $T_g$  [189].

To characterise the phase-change behaviour of GeTe one can use the velocity,  $u$ , at which crystalline nuclei grow within the amorphous liquid.  $u$  is zero above  $T_m$  because any crystalline regions will melt, and is also zero below  $T_g$  because crystalline growth is then frozen out, since the amorphous phase is solid. Note that in 3D bulk simulations  $u$  corresponds to the growth rate of an approximately spherical nucleus whereas in this case it corresponds to that of an interface along a single periodic dimension.

To calculate the crystallisation speed  $u$ , molecular dynamics simulations were performed on an interface in a GeTe encapsulated nanowire between a crystalline region and a supercooled liquid region. For the crystalline region a cylindrical cut-through of GeTe's rocksalt-like phase was used, because the AIRSS results indicate that such structures are the ground state of GeTe nanowires above  $5.4 \text{\AA}$ . The liquid was generated via a simulation in which a rocksalt phase was melted with a linear temperature ramp

from 500 K to 1000 K over 10 ns. The interface cell was then constructed by joining the melted cell with the original rocksalt cell along the periodic direction. (Due to periodic boundary conditions, this cell in fact contains two interfaces.) To ensure that the simulation did not begin with extremely large forces in the vicinity of the interface, a geometry optimisation was then performed (at 0 K but using the force field, not DFT).

A timestep of 10 fs was used in the simulations, which was found to be about a tenth of the characteristic timescale of the atomic vibrations at the highest temperatures simulated. The simulations were run within the NPT ensemble, with both pressure and temperature regulated via the Nose-Hoover method [190, 191]. An implicit representation of the nanotube was used in the form of a simple quadratic confining potential,

$$E(r) = \begin{cases} k(r - R)^2 & r > R \\ 0 & \text{otherwise} \end{cases} \quad (3.15)$$

with  $k = 5 \text{ eV}/\text{\AA}^2$  and  $R$  the chosen nanotube radius. This represents a somewhat shallower confining potential than was used in the structure searches, to avoid numerical integration issues that can arise when exploring steep potential gradients with finite timesteps.

To characterise the level of crystallinity in the unit cell, the  $Q_6$  Steinhardt order parameter was used. This parameter is defined on an atom-by-atom basis as [192]

$$q_{6m}^i = \frac{\sum_j \sigma(r_{ij}) Y_{6m}(\mathbf{r}_{ij})}{\sum_j \sigma(r_{ij})}, \quad (3.16)$$

where  $\mathbf{r}_{ij}$  is the displacement vector between atoms  $i$  and  $j$ ,  $Y_{lm}$  are the spherical harmonics, and  $\sigma(r_{ij})$  is a switching function which picks out a particular distance so that only if atoms  $i$  and  $j$  are in each other's first coordination shell is there a large contribution to the sum. There are a number of reasonable choices for the form of  $\sigma$ ; here, the form used was

$$\sigma(r) = \frac{1 - \left(10 \cdot \frac{r-d_0}{d_0}\right)^n}{1 - \left(10 \cdot \frac{r-d_0}{d_0}\right)^m}, \quad (3.17)$$

with  $n = 6$ ,  $m = 12$ , and  $d_0$  equal to the nearest-neighbour Ge-Te distance in the crystalline phase (around  $2.9 \text{ \AA}$ ). These calculations of  $Q_6$  were performed using PLUMED [193].

Because  $m$  can run from  $-l$  to  $l$  for the spherical harmonic  $Y_{6m}$ , eq. 3.16 constitutes a  $(2l + 1)$ -component vector, and the local order parameter for the  $i$ -th atom can then be defined simply by the norm of this vector:

$$Q_6^i = \sqrt{\sum_{m=-6}^6 |q_{6m}^i|^2}. \quad (3.18)$$

This local order parameter was calculated every 50 timesteps (every 0.5 ps) for each atom in the nanowire. The average level of crystallinity was then obtained as a function of position along the periodic axis  $z$  by applying a LOWESS smoothing [194] to each atom's  $Q_6$  as a function of  $z$ . This is visualised on fig. 3.11, on which a timestep from a molecular dynamics trajectory is shown along with a plot of its local order. One can see that the spatial variation of the calculated local order parameter corresponds very well with the actual level of crystallinity that is visible in the cell. By manually checking a few test cases such as these, the condition to consider the unit cell crystalline at  $z$  was chosen to be  $Q(z) > Q_{\text{thresh}}$ , with  $Q_{\text{thresh}} = 0.45$ . With the condition for crystallinity defined, the interfaces are then simply given by the points where  $Q(z) = Q_{\text{thresh}}$ . By repeating this procedure at many timesteps across the course of the simulation, one can track the motion of the interfaces and thus the time-variation of the size of the crystalline region. The time-averaged growth rate,  $u$ , of the crystalline region is then simply the total growth of the crystalline region over the course of the simulation divided by the total length of time that was simulated.

After calculating the local order, each atom's  $Q_6$  was passed through a tanh function before then being averaged over as on fig. 3.11. This has the effect of pushing atoms' order parameters to more extreme values (either towards unity if  $Q_6 > Q_{\text{thresh}}$  or towards zero otherwise), which was found by examining a number of test cases by eye to produce more accurate assignments of ordered and disordered regions for a given snapshot.

A simpler approach would be to calculate the fraction of atoms whose local order parameters indicate crystallinity, and then inferring the size of the crystalline region from this fraction based on the assumption that the fraction of atoms that are crystalline should equal the fraction (by length) of the cell that is crystalline. There are a few problems with this approach: firstly, the densities of the crystalline and supercooled liquid phases are different (and in a temperature-dependent way, ruling out a solution

via calculating the densities of the amorphous and crystalline phases and weighting the calculation accordingly). As a result the fraction of atoms whose local environments are crystalline does not correspond to the fraction (by length or volume) of the cell which is crystalline. Secondly, at any given time some atoms'  $Q_6$  will be high by chance, even in the liquid phase, as can be seen on fig. 3.11 in which a few atoms within the liquid region are marked incorrectly as crystalline. In the naive approach, this would have the effect of inflating the calculated size of the crystalline region.

A confounding factor in the use of these simulations to determine the growth velocity,  $u$ , is the occurrence of secondary nucleation. In some cases it was found that, while the cell was crystallising, another crystalline nucleus formed spontaneously within the supercooled liquid phase. Because  $u$  is defined as the growth velocity of a crystalline interface with a supercooled liquid, any interactions with other crystalline regions will cause inaccuracies. To deal with this problem, the  $Q_6$ -based scheme just described was used to identify all crystalline-amorphous interfaces in the cell and, if either of the interfaces of the initial crystalline region are ever less than  $7.5 \text{ \AA}$  away from any other interface, the data beyond that timestep are ignored in the calculation of  $u$ . This also covers the case in which, near complete crystallisation, the crystalline region's two interfaces become very close and begin to interact with each other.

The output of a single one of these interface simulations is shown on fig. 3.12. The figure shows how a fit is made to the frame-by-frame calculations of the level of crystallinity to calculate the growth speed of the crystalline region.

To investigate the variation of the crystallisation with respect to both the temperature  $T$  and the nanotube radius  $R$ , simulations were performed at different values of each of these parameters. Three different nanotube radii were considered: 11, 14, and  $17 \text{ \AA}$ . These cells were around  $60 \text{ \AA}$  in length (though the length varies over the simulations depending on the temperature and level of crystallinity), and contained 384, 624, and 960 filling atoms, respectively.

There is a fairly large amount of random variation in the crystallisation dynamics in the cell sizes used here. To deal with this, the simulations were repeated 6 times for each radius and temperature, and the average growth speed  $u$  was taken. This also provides an error bar on calculated values of  $u$  in the form of the standard error of the mean.

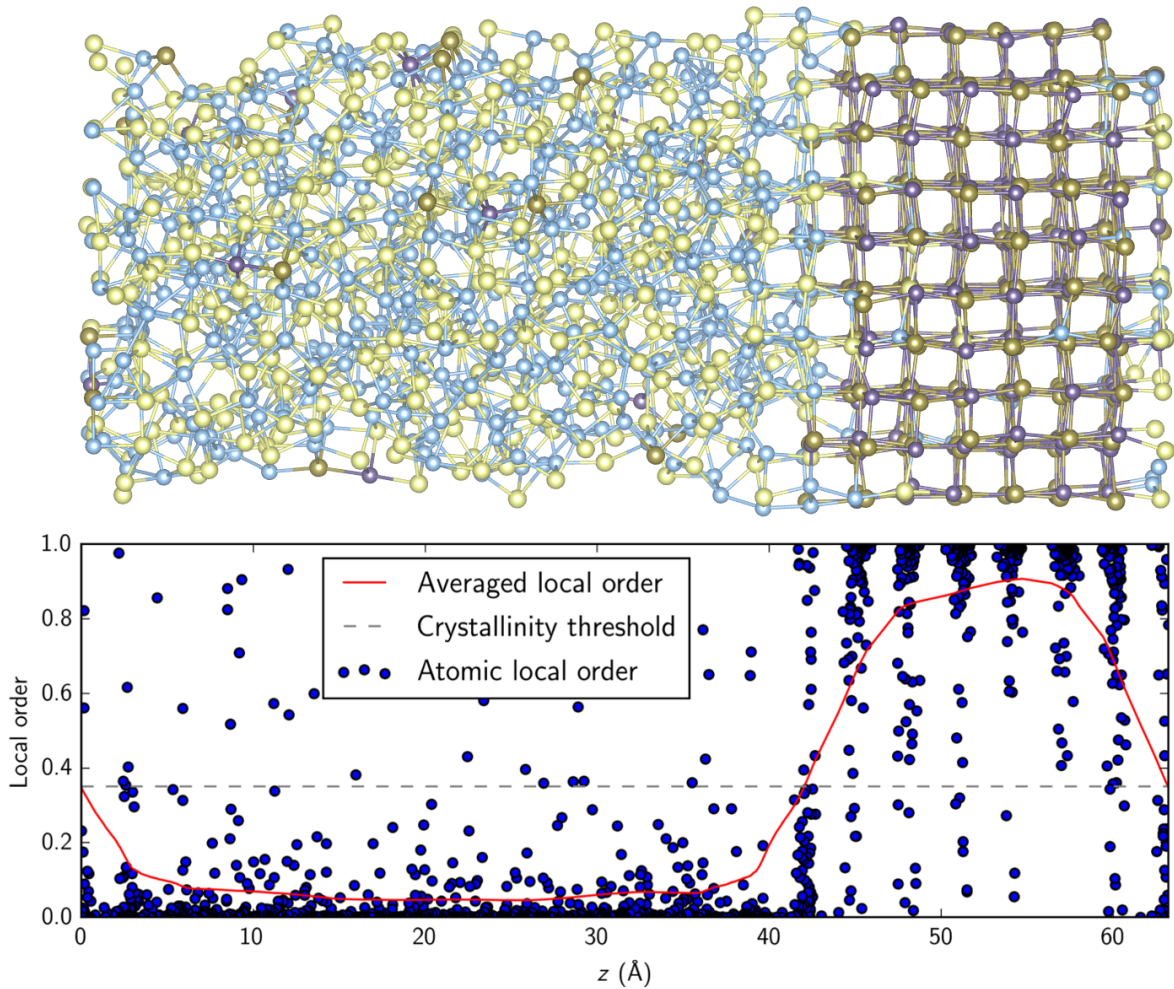


Figure 3.11 An MD snapshot of a GeTe nanowire in a 17 Å-radius nanotube, with atoms identified as crystalline based on their  $Q_6$  parameter assigned darker colours. In the lower graph, each atom's local  $Q_6$  is plotted (as a scatter diagram). The averaged local order calculated via LOWESS smoothing of the atoms' local  $Q_6$  is shown in red. The threshold for considering a region crystalline is also shown, and from this it can be seen that the amorphous and crystalline regions of the cell are correctly classified as below and above that threshold, respectively.

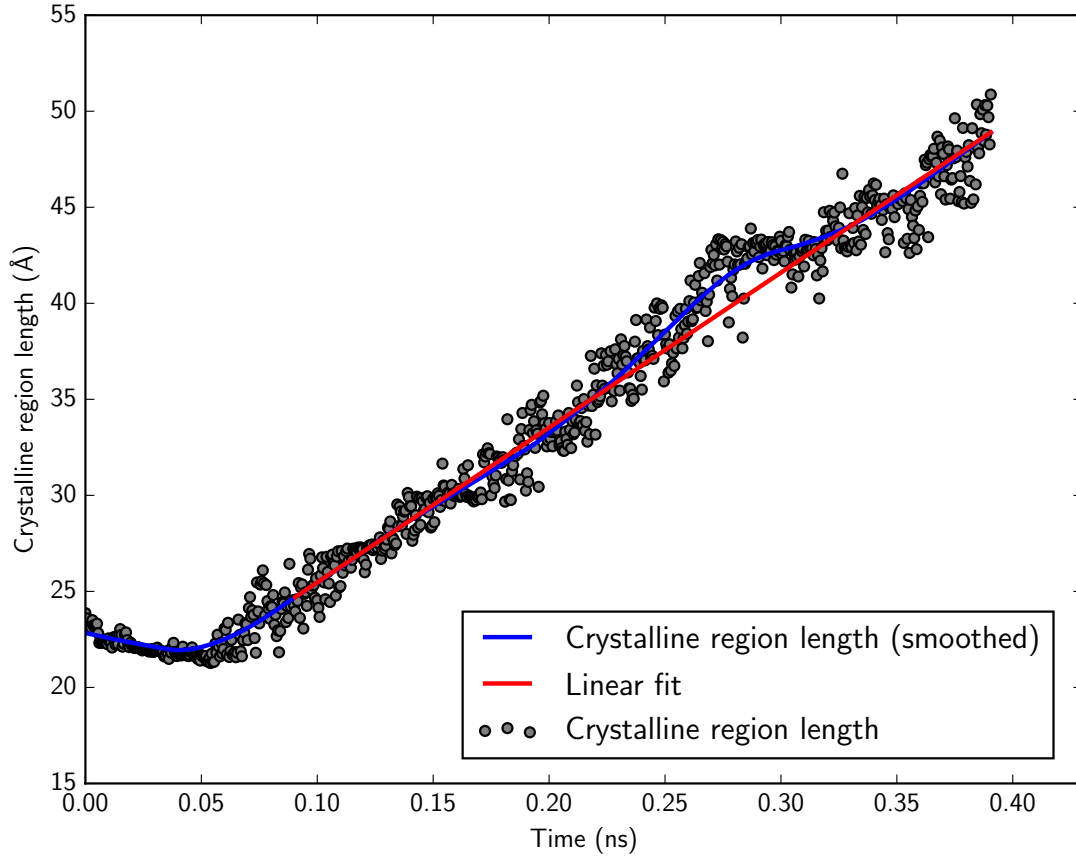


Figure 3.12 The length of the crystalline region as a function of time in a single simulation at 450 K in a nanotube of radius 17 Å. Also shown are a rolling average of the crystalline length, and the linear fit from which the growth speed is derived. The linear fit excludes the initial equilibration period which was not used in the fit.

Classical nucleation theory was used as a fitting function for  $u(T)$ . The theory is based on the principle that there are a number of sites on the interface between a crystalline region and a supercooled liquid region, and that the crystalline phase grows by atoms from the liquid phase adsorbing onto those sites. If the free energy difference between the crystal and the supercooled liquid is  $\Delta F = F_{\text{crystal}} - F_{\text{liquid}}$ , then the rate at which atoms from the liquid join onto the crystalline nucleus goes as  $\exp(-\beta\Delta F)$ , whereas the reverse process goes as  $\exp(\beta\Delta F)$ , as per Arrhenius' law.  $\Delta F$  will be a function of temperature which will (by definition) pass through zero at the melting point  $T_m$ , and will become more and more negative as temperature decreases below the melting point.

The functional form for the rate of growth of a crystalline nucleus predicted by classical nucleation theory is given by

$$u \propto D(e^{\Delta F/(2k_B T)} - e^{-\Delta F/(2k_B T)}), \quad (3.19)$$

where  $\Delta F$  is the free energy difference between the crystalline and liquid phases and  $D$  is the diffusion coefficient. Sosso *et al.* [195] found using molecular dynamics simulations of a neural network potential fitted to *ab initio* data that in bulk GeTe, the diffusion coefficient obeys to a good approximation an Arrhenius-like form

$$D = D_0 e^{-E_a/k_B T}, \quad (3.20)$$

and used this for the diffusion rate in eq. 3.19, along with Thompson and Spaepen's approximation for  $\Delta F$  [196],

$$\Delta F = \frac{\Delta H(T_m - T)}{T_m} \frac{2T}{T_m + T}. \quad (3.21)$$

The same approach is used here; however, where Sosso *et al.* used in eq. 3.20 a value of  $E_a$  derived from simulations of the bulk, here  $E_a$  (along with the other parameters in eq. 3.19) is treated as a fitting parameter. This is because the nanowire radii considered here are small enough that the parameters may differ significantly from the bulk. It should be noted that Sosso *et al.* only considered temperatures down to 500 K, which means that  $D$  may diverge from Arrhenius-like behaviour at lower temperatures. However, classical nucleation theory is unlikely to provide a good model at low temperatures anyway, especially once the process of crystallisation becomes strongly diffusion-limited and (ultimately) the liquid-glass transition occurs.

The equations above describe a tradeoff in which, at high (but below the melting point) temperatures, nucleation is slow because  $\Delta F$  is small in magnitude, and so the forward process of crystallisation is favoured only slightly over the reverse process. On the other hand, nucleation is also slow at low  $T$ , because then the diffusion coefficient becomes small, which hinders the rate at which atoms can find their way onto the sites on the surface of the growing crystalline nucleus. As a result, there is a temperature at which this tradeoff is optimised so as to maximise the rate of crystallisation. Since faster crystallisation rates imply faster switching times for phase-change memory, this

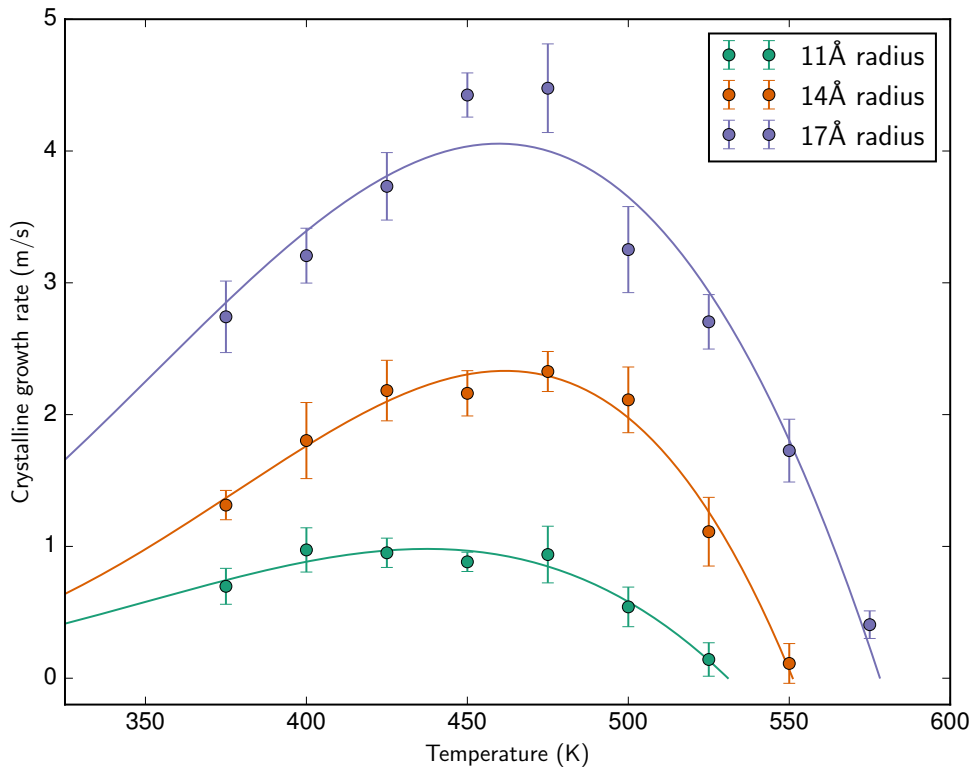


Figure 3.13 Crystalline growth velocities for three different radii of nanotube.

maximum growth velocity – and the temperature at which it occurs – are important quantities.

The calculated crystallisation speeds for varying nanotube radius and temperature are shown together on fig. 3.13, and some parameters derived from the fit are shown on table 3.5. From the figure, one can see that the melting point decreases as the nanotube radius decreases. This is a technologically promising finding: since a RESET pulse entails melting the material, a lower melting point implies lower energy usage in the context of phase-change memory. Phase-change nanowires may therefore not only be more efficient because they contain less material in total, but also because the energy cost is smaller *per atom*. In ref. 165, Lee *et al.* study GeTe nanowires of diameters between 28 and 200 nm and find a systematic decrease in the required current for a RESET pulse with respect to nanowire thickness, such that the required RESET current appears to scale approximately quadratically in the nanowire diameter. This is as one would expect: it is easy to show that to deliver a specific amount of

Nanotube radius (Å)	$T_m$ (K)	$u_{\max}$ (m/s)	$\arg \max u(T)$ (K)
11 Å	$531 \pm 6$	$0.98 \pm 0.07$	$437 \pm 12$
14 Å	$551 \pm 3$	$2.33 \pm 0.10$	$462 \pm 5$
17 Å	$578 \pm 2$	$4.06 \pm 0.12$	$460 \pm 5$

Table 3.5 Derived fitting parameters from fig. 3.13 and their errors: the melting point  $T_m$ , the maximum crystallisation speed  $u_{\max}$ , and the temperature at which that maximum speed occurs,  $\arg \max u(T)$ .

power per atom  $P_{\text{pa}}$  via Ohmic heating, one must apply a current

$$I = \sqrt{\frac{nP_{\text{pa}}}{\rho}} \pi R^2 \quad (3.22)$$

to the nanowire, where  $n$  is the atomic number density,  $\rho$  is the resistivity, and  $R$  is the radius of the nanowire. The significance of the results in this section is the implication that the required power  $P_{\text{pa}}$  may also be radius-dependent and therefore the scaling is, for sufficiently small nanowires, faster than quadratic, making narrow GeTe nanowires even more power-efficient than expected.

In ref. 175, Sun *et al.* found GeTe nanowires of 40 nm to 80 nm to melt at 663 K, i.e. lower than the bulk. This result is consistent with the trend found in this work for larger nanowires to melt at higher temperatures.

Another trend is that the crystalline growth velocity is lower for narrower nanotubes. This trend works against GeTe nanowires as phase-change memory: a lower  $u$  necessitates a longer SET pulse. By selecting the nanotube radius, one may therefore tune the phase-change properties of the nanowire so as to choose the desired tradeoff between the trends in switching speeds and energy costs.

Though there is significant variation apparent in the maximum crystallisation rate, the temperature at which that maximum rate occurs does not vary significantly. The energy cost of a SET pulse is therefore largely unchanged (and in practice is likely to be somewhat higher for narrower nanotubes, since they must be maintained at the required temperature for longer while the nanowire crystallises).

### 3.3.3 Glass transition

The glass transition temperature  $T_g$  is vital for characterising the phase-change properties of GeTe nanowires.  $T_g$  is the temperature at which a transition occurs between the supercooled liquid and the amorphous phase, and as a result it plays a role in both SET and RESET pulses: in the former, the temperature must be held above  $T_g$  in order for the system to crystallise. In the latter, the system must be quenched below  $T_g$  rapidly enough that it does not have enough time to crystallise whilst it is below  $T_m$  but above  $T_g$ .

Calculating  $T_g$  from molecular dynamics is problematic due to the fact that the true thermodynamic ground state for all  $T < T_m$  is the crystalline phase. As a result, it is imperative the system must not be allowed to crystallise. This issue is especially pronounced in GeTe, due to its fast crystallisation properties. In this work, crystallisation was avoided simply by quenching the system much more quickly than the timescale over which it crystallises – just as in an actual RESET pulse.

Although the amorphous state is solid, the fact that its structure is disordered like that of the supercooled liquid phase rules out an order parameter-based approach such as that used in the previous section. A different approach must therefore be used to identify the transition. A generic feature of liquid-glass transitions is an increase in the heat capacity above the transition temperature [197, 198]. Additionally, the behaviour is similar to a second-order transition in that there is no latent heat, so the heat capacity does not diverge (though characterising the order of the glass transition – and indeed characterising it as a phase transition at all – are somewhat problematic due to the fact that neither the amorphous phase nor the supercooled liquid phase are ever the thermodynamic ground state [199]). This change in heat capacity has been used, both experimentally [200, 201] and computationally [202], to identify  $T_g$ . (The change in the thermal expansion coefficient [203, 204] and viscosity [205, 206] have also been used similarly to identify  $T_g$ .)

The simulations used to find  $T_g$  via the change in specific heat used the same force field, timestep, and implicit representation of the nanotube as in the previous calculations used to identify the crystallisation rate. They were performed in three stages. In the first stage, the initially crystalline nanowire is heated well above its melting temperature to around 2000 K for 50 ps. This ensures that the system is fully melted, with no remnants of the initial crystalline phase. In the second stage, the system is held

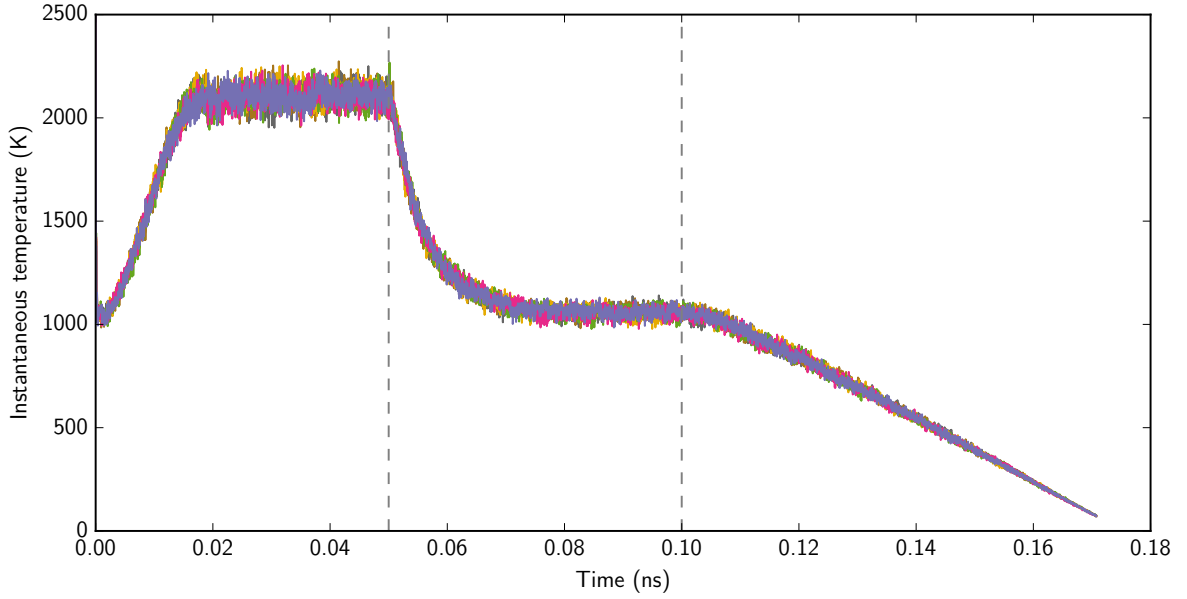


Figure 3.14 The instantaneous temperature as a function of time for 5 different simulations with a 17 Å-radius nanotube. The three different stages of the simulations described in the text are separated by vertical dashed lines.

at 1000 K for another 50 ps, creating a well-equilibrated liquid in preparation for the quench. In the final stage, the system is quenched to under 200 K via a smooth temperature ramp of  $14 \text{ K ps}^{-1}$  (corresponding to a duration of 70.7 ps for the final stage). This was found, by testing a number of different temperature ramps, to be roughly the slowest cooling rate at which crystallisation did not occur.

The instantaneous temperature as a function of time resulting from this scheme is shown on fig. 3.14. Here the instantaneous temperature is defined at each frame of the simulation via the usual result from the equipartition theorem,

$$T = \sum_{i=1}^N \frac{p_i^2}{3m_i k_B N}, \quad (3.23)$$

with  $N$  the number of particles, and with the  $i$ -th particle's momentum and mass defined as  $p_i$  and  $m_i$ .

To measure the change in heat capacity,

$$C_P = \left( \frac{\partial U}{\partial T} \right)_P, \quad (3.24)$$

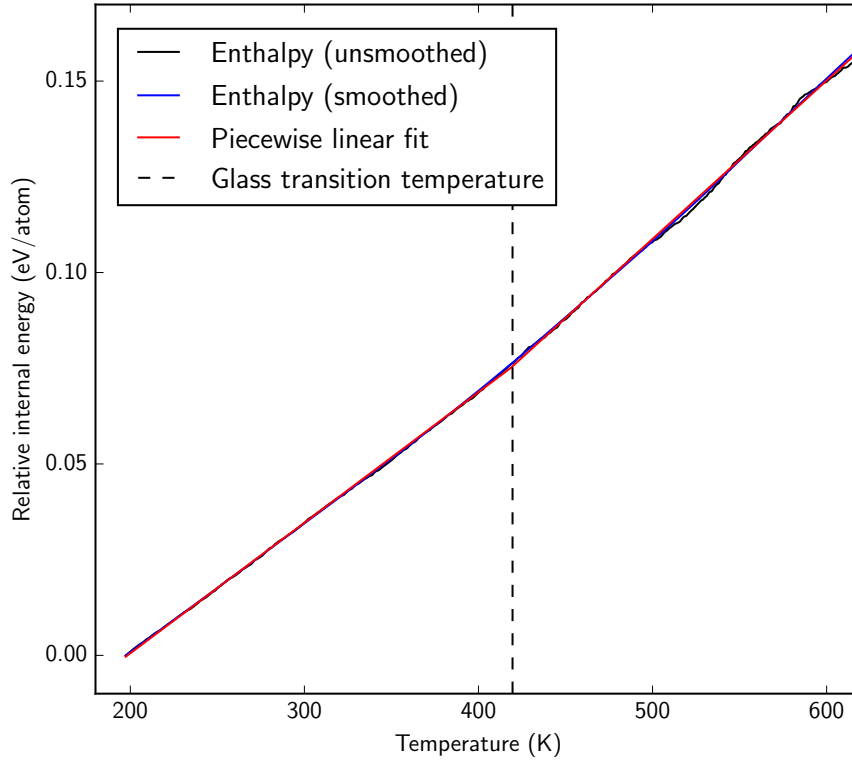


Figure 3.15 The internal energy of a nanowire of radius  $18.5 \text{ \AA}$  a function of temperature, during a quench to  $200 \text{ K}$ . The gradients of the piecewise linear fit – i.e. the fitted liquid and amorphous heat capacities – are  $0.41 \text{ meV K}^{-1}$  per atom and  $0.34 \text{ meV K}^{-1}$  per atom above and below the transition temperature, respectively.

the internal energy  $U$  and temperature  $T$  were recorded as a function of time, and then plotted against each other, giving  $U(T)$ . Then, a fit was performed to  $U(T)$  of the form

$$U(T) = U_0 + \begin{cases} (T - T_g)C_P^{\text{above}} & T > T_g \\ (T - T_g)C_P^{\text{below}} & T < T_g \end{cases} \quad (3.25)$$

This is a piecewise linear fit, with the fitting parameters being  $U_0$  (the internal energy at  $T_g$ ),  $C_P^{\text{above}}$  and  $C_P^{\text{below}}$  (the heat capacities either side of the transition), and  $T_g$ , the transition temperature itself. This is plotted for a single trajectory on fig. 3.15. As is clear from the figure, the change in heat capacity is not very large, but it is enough to be detectable.

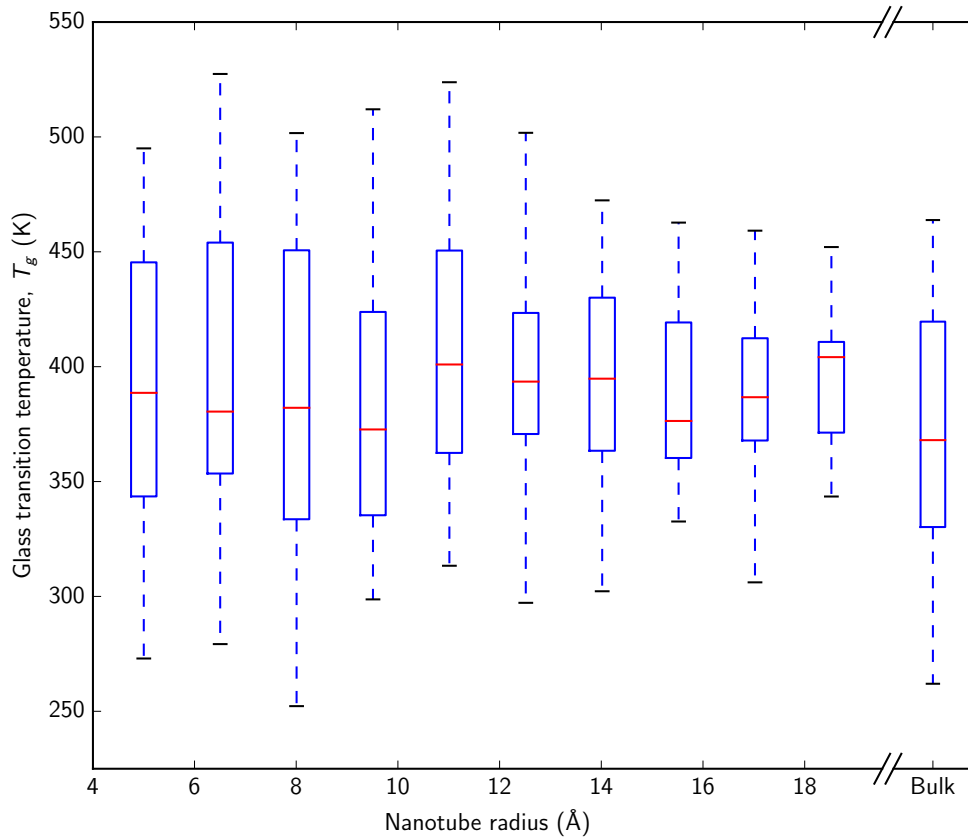


Figure 3.16 Box-and-whisker diagram of the glass transition temperature as a function of the radius of the encapsulating nanotube, together with that of the bulk. The red lines give the median, the boxes give the first and third quartiles, and the whiskers give the highest and lowest values.

These calculations were repeated for a number of different nanowire radii, and for a 1000-atom bulk cell. The procedure in the bulk was exactly the same as for the nanowire, except of course without the confining potential and with a barostat applied to all the cell degrees of freedom rather than just its length along  $z$ . These simulations occur over much shorter timescales than those used to identify the crystallisation rate, so it is affordable to perform more of them. The procedure just described was therefore repeated 20 times for each of the nanowire lengths considered and for the bulk, producing 220 simulations in total.

The results of this are shown on fig. 3.16. From the figure, there is no obvious trend in  $T_g$  with respect to nanotube radius. To check this more rigorously, a test was performed on the hypothesis that  $T_g$  is the same for all nanotube radii and for the bulk. Under

this hypothesis, the quantity

$$\epsilon = \sum_i \frac{T_g^i - \bar{T}_g}{\alpha_i^2} \quad (3.26)$$

should obey a chi-square distribution [207]. In the above,  $T_g^i$  is the melting temperature of the  $i$ -th nanotube (or of the bulk) averaged over its 20 simulations, i.e. there is one  $T_g^i$  for each of the boxes on fig. 3.16.  $\alpha_i$  is the standard error of the mean for  $T_g^i$ . The number of degrees of freedom in the chi-square distribution is then  $N - 1$ , since one degree of freedom is taken up by the use of the average  $\bar{T}_g$  in eq. 3.26. The result of this test is a p-value of 0.90. This means that there is no indication that any of the systems considered have different  $T_g$ , and in fact the p-value may even be considered anomalously high – often a p-value close to unity is indicative of overestimated error bars, although it may also just be a coincidence in this case.

One trend that is apparent on fig. 3.16 is that the spread in the calculated values of  $T_g$  is lower for larger nanotubes. However, this is not physically very important since it likely results from the fact that smaller system sizes experience larger fluctuations (relative to their system size), and such fluctuations can alter the fitted value of  $T_g$  away from its value in the thermodynamic limit. As a result, it is to be expected that larger nanowires have lower spread in  $T_g$ .

The results presented here are around 50 K lower than the experimental crystallisation temperature of 458 K reported in ref. 208. However, it should be noted that the crystallisation temperature is defined not as the glass transition temperature but as the temperature at which crystallisation is observed to begin in an experiment in which the sample is steadily heated. As one might imagine, this quantity is strongly dependent on the rate of heating: for sufficiently rapid heating rates, one can bypass crystallisation completely by exceeding the melting temperature before observable levels of crystallisation can occur. For slow heating rates, the crystallisation and glass temperatures are seen to converge together [209], since the supercooled liquid will always crystallise given sufficient time. This means that the fact that the results found here for  $T_g$  are lower than the experimentally reported crystallisation temperature is not necessarily a problem; one would expect them to be lower to some extent.

The fact that  $T_g$  seems to be no different for narrower nanotubes compared to bulk implies that the minimum energy cost per atom to induce a transition from amorphous to supercooled liquid is unchanged. It is a promising result that it is not significantly lower than in bulk, since at that point ambient temperatures could be enough to

melt the amorphous GeTe, thereby losing information. Indeed, GeTe's higher  $T_g$  relative to GST has been cited as an advantage of GeTe for exactly this reason, with a crystallisation temperature of 458 K for GeTe compared to 418 K for GST [208]. Even if this temperature is not reached, a higher  $T_g$  implies greater stability of the amorphous phase and therefore superior data retention characteristics [210].

It is known that  $T_g$  depends in practice on the cooling rate, with slower cooling producing a lower transition temperature [211]. This dependence is generally weak: typically an order of magnitude change in the cooling rate causes a change in  $T_g$  of around 3 to 5 K [199]. Nevertheless, one route for further investigation would be to examine the nature of this dependence in GeTe ENWs.

The reason that a comparison to bulk is given here but not in the previous section is that, in measuring the crystallisation rate, the geometries under consideration are fundamentally disanalogous: the crystallisation of bulk would be measured via consideration an interface between a spherical, crystalline nucleus and a surrounding supercooled liquid, whereas the crystallisation of nanowires is measured via consideration of a planar interface along  $z$ . These different geometries mean that the results are not directly comparable, since – as is well-known – the expected growth rate of a spherical, crystalline nucleus within a supercooled liquid is a function of its size. On the other hand, measuring  $T_g$  in the way performed here introduces no such problems.

A more precise study could also involve training a force field explicitly on *ab initio* data of encapsulated GeTe nanowires, but this would entail either (in the most expensive case) fitting a carbon-germanium-tellurium ternary potential, or alternatively fitting a germanium-tellurium potential if an implicit nanotube were used in the *ab initio* simulations to which the potential was fit. The former solution would likely require a shorter timestep due to the much lower mass of carbon relative to germanium and tellurium.

An important practical consideration in realising an actual phase-change memory device based on GeTe ENWs is that of how to pass a current through the wire. One option would be to use a conducting nanotube and apply a voltage difference between the caps at the ends of the nanotube. This option has the disadvantage that the nanotube would then conduct in parallel with the nanowire, which could make it harder to determine the conductivity of the nanowire (and therefore its state), and would also increase power usage. Another option which avoids these problems would be to use an

insulating nanotube and to modify the caps so as to form a direct connection with the rest of the circuit.

### 3.4 Ferroelectricity

The existence of a ferroelectric transition in a material implies that it has two different states of opposite polarisation and equal energy, separated by an energetic barrier. The polarisation can be set by the application of a sufficiently strong electric field, which leaves behind a remanent polarisation after it is removed. Because of this, ferroelectric materials can be used to store information, and the persistent nature of the remanent polarisation means that, in contrast to the DRAM (dynamic random access memory) which is used in most computers, FRAM (ferroelectric random access memory) does not require continual refreshing to retain the information stored within it. Modern DRAM refreshes around every 64 ms [212], leading to power consumption even when not reading or writing. FRAM may be considered intermediate between DRAM and typical solid-state non-volatile memory (i.e. flash memory), with some of the advantages of both. It is non-volatile, like flash memory, but its typical write cycle times of order 100 ns are orders of magnitude faster than those of flash memory [213] (though not as fast as those of DRAM). Because of these benefits, FRAM has been successfully commercialised in various electronic devices [214].

A key disadvantage of FRAM is that its read process is destructive: to identify which of the two polarisation states a memory cell is in, the ferroelectric is coerced into a particular polarisation state and if it was not already in that polarisation state then a current is created as the atoms switch the direction of their ferroelectric displacement. This means that after reading from FRAM, one must immediately write back the value that was just read, resetting it to its polarisation state prior to reading [215]. Otherwise, information will be lost upon reading.

As previously discussed, the  $\alpha$  phase of GeTe is ferroelectrically distorted relative to the  $\beta$  phase. This distortion is shown on fig. 3.17 for a GeTe nanowire. In this section, the ferroelectric properties of encapsulated GeTe nanowires will be considered in the context of their potential applications in FRAM devices.

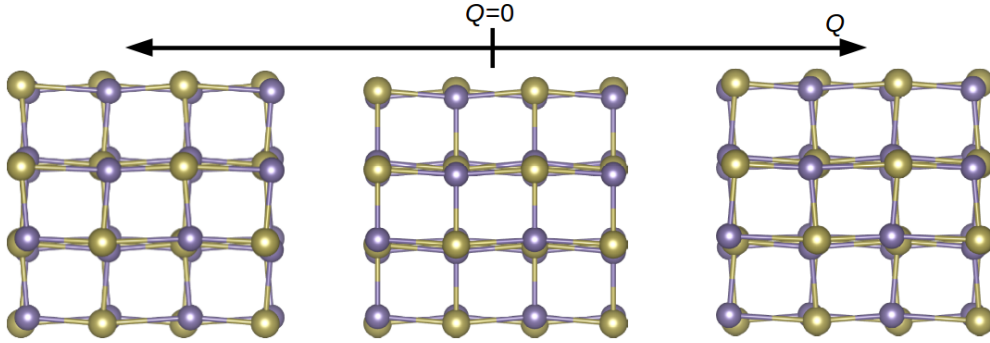


Figure 3.17 The ferroelectric distortion observed in GeTe, parameterised by the normal mode coordinate  $Q$ , as calculated for the  $P\bar{4}mm$  nanowire structure. The periodic axis runs left-to-right. One can see a displacement along the periodic axis of the positions of the Ge atoms, and a displacement of the position of the Te atoms in the opposite direction.

### 3.4.1 The Modern Theory of Polarisation

The electric polarisation of a system of particles is conventionally defined as

$$P = \sum_i q_i \mathbf{r}_i, \quad (3.27)$$

where the sum is over all of the particles in the system, with  $q_i$  and  $\mathbf{r}_i$  the charge and location of the  $i$ -th particle. (in the case of continuous charge distributions, this sum becomes an integral.) In practice, this apparently simple concept becomes problematic in the context of bulk materials with periodic boundary conditions. The value of  $P$  as calculated via equation 3.28 is in fact dependent on the choice of unit cell: if an atom of charge  $q$  were at fractional coordinates of  $(0, 0, 0)$ , then one could describe the same structure by placing it at  $(0, 0, 1)$  instead, but the polarisation as calculated using eq. 3.28 would differ between the two equivalent choices of setting by  $\Delta P = qc$ , where  $c$  is the third lattice vector.

The ferroelectric polarisation of a material can be more rigorously defined in terms of a flow of charge, within the formalism of the modern theory of polarisation [15]. As the system polarises, there is a shift in the positions both of the atomic nuclei and of the electrons. The induced polarisation can therefore be defined relative to the unpolarised state by

$$P_{\text{ferro}} = \sum_i q_i \mathbf{r}'_i - \sum_i q_i \mathbf{r}_i, \quad (3.28)$$

where the primed positions correspond to the polarised state and the unprimed positions to the centrosymmetric (unpolarised) state, and the sum runs over both the ionic cores and the electrons. The principal difficulty in calculating this quantity is in rigorously assigning a position to the electrons. (Clearly there are no such difficulties for the ions within the Born-Oppenheimer approximation.) This is done by introducing Wannier functions,

$$w_n(\mathbf{r} - \mathbf{R}) = \frac{\Omega}{(2\pi)^3} \int_{\text{BZ}} e^{-i\mathbf{k}\cdot\mathbf{R}} \psi_{n\mathbf{k}}(\mathbf{r}) d^3\mathbf{k}. \quad (3.29)$$

Unlike the Kohn-Sham orbitals (which are generally delocalised over the whole unit cell), Wannier functions provide a spatially localised description of the system's electronic eigenstates. We can then associate a location with each Wannier function as the expectation value of the position operator:

$$\mathbf{r}_n = \langle w_n | \hat{\mathbf{r}} | w_n \rangle \quad (3.30)$$

Using equation 3.29, one can show [216] that the resulting expression for the total electronic contribution to the polarisation is equivalent to

$$\mathbf{P}_{\text{elec}} = -\frac{2ie}{(2\pi)^3} \sum_n \left[ \int_{\text{BZ}} e^{-i\mathbf{k}\cdot\mathbf{R}} \left\langle u_{n\mathbf{k}} \left| \frac{\partial u_{n\mathbf{k}}}{\partial \mathbf{k}} \right. \right\rangle d^3\mathbf{k} \right] \quad (3.31)$$

with the sum running over occupied bands, and where  $e$  is the elementary charge. The result of this is that one can then compute the polarisation induced in a ferroelectric phase transition as the difference between the values of  $P$  given by equation 3.28 for the centrosymmetric and polarised states, with each electron contributing a term proportional to the shift in its Wannier centre. This formalism is implemented in the electronic structure code Quantum Espresso [217, 218] which was used to calculate polarisations in this section.

To take into account the impact of the applied electric field on the system, one cannot simply apply the electric field directly within a DFT calculation, because doing so leads to an electric potential which varies across different unit cells and therefore breaks translational symmetry. Instead, we first write the total energy density as

$$U_{\text{tot}} = U_{\text{DFT}} + \frac{1}{2} \mathbf{E} \cdot \mathbf{D}, \quad (3.32)$$

where the first term on the RHS is just the DFT total energy and the second term on the RHS gives the electrostatic energy associated with the charge distribution in the

system. (For clarity, we use  $U$  rather than  $E$  to refer to energies in this section.) Given that  $\mathbf{D} = \epsilon_0 \mathbf{E} + \mathbf{P}$  [219], this can be rewritten as

$$U_{\text{tot}} = U_{\text{DFT}} + \frac{1}{2} \epsilon_0 |\mathbf{E}|^2 + \frac{1}{2} \mathbf{E} \cdot \mathbf{P}. \quad (3.33)$$

To obtain  $\mathbf{P}$ , one uses the formalism outlined above, with eq. 3.31 for the electronic contribution. However, this will depend on the structure (via the Kohn-Sham orbitals), which will in turn depend on the imposed electric field. In a ferroelectric distortion such as that observed in GeTe, the positively charged Ge ions and the negatively charged Te ions displace slightly in opposite directions. The structure was therefore parameterised as a function of the soft phonon mode corresponding to the ferroelectric distortion. This phonon mode is obtained by running a phonon calculation on  $\beta$ -GeTe – i.e., the  $Fm\bar{3}m$  rocksalt phase which GeTe transitions into above the ferroelectric transition temperature of 705 K [220]. This structure is (as one would hope) found to be mechanically unstable in DFT due to the presence of the negative-frequency mode corresponding to the ferroelectric distortion. This is also true for the  $P\bar{4}mm$  GeTe nanowire structure, which the phase diagram, fig. 3.2, predicts to be the ground state for nanotube radii beyond 8.2 Å. The  $P\bar{4}mm$  structure was therefore used for the ferroelectricity calculations in this section.

The structure was parameterised via

$$\mathbf{r}_i = \mathbf{r}_i^\beta + Q \epsilon_i^{\text{soft}}, \quad (3.34)$$

where  $\mathbf{r}_i$  is the position of the  $i$ -th atom,  $\mathbf{r}_i^\beta$  is its position in the  $\beta$  phase (i.e. without the ferroelectric distortion),  $\epsilon_i^{\text{soft}}$  is the phonon eigenvector for the soft mode corresponding to the ferroelectric distortion, and  $Q$  is a normal mode coordinate parameterising the displacement along said phonon mode.

A range of values of the normal mode coordinate  $Q$  were considered, corresponding to a varying level of displacement along the soft mode. In each case the corresponding unit cell was constructed using eq. 3.34, and the resulting polarisation  $\mathbf{P}$  was calculated using Quantum Espresso. These values were interpolated to give a parameterisation for  $\mathbf{P}$  as a function of  $Q$ , which is shown on fig. 3.18. Also shown on the figure is the energy as a function of  $Q$ , which shows the characteristic quartic shape one finds in the soft modes of ferroelectric systems.

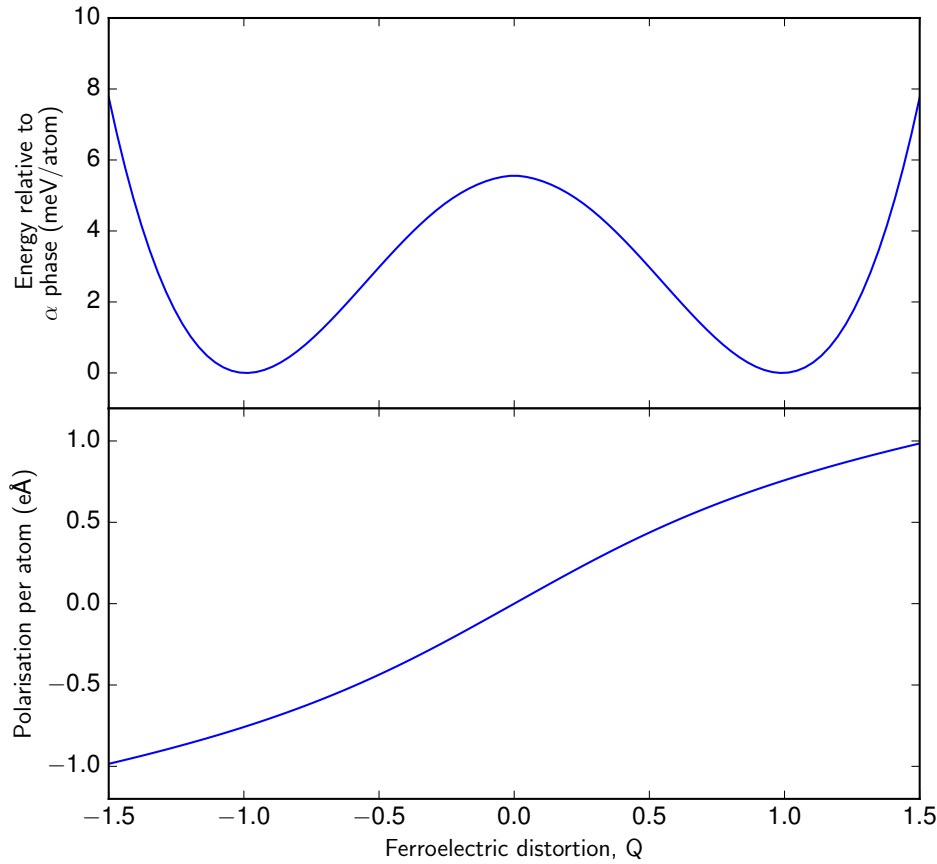


Figure 3.18 The total DFT energy per atom (top) and the induced dipole moment per atom (bottom) in the  $P\bar{4}mm$  GeTe nanowire structure, both parameterised as a function of the ferroelectric distortion,  $Q$ .

There is now sufficient information to calculate the ferroelectric hysteresis curve. To do this, the energy is first minimised with respect to  $Q$ , causing the system to fall into either of the minima in the quartic potential. Then a small electric field is applied, and the energy landscape for this new electric field is calculated as a function of  $Q$  using eq. 3.33. This causes the position of the minima to shift, as shown on fig. 3.19. One would expect the system to adjust the extent of its ferroelectric distortion in response to this change, and to allow it to do so the energy is once again minimised with respect to  $Q$ , with  $Q$  initialised at its previous value. This procedure is applied repeatedly, forming a two-part iterative scheme in which the imposed electric field is adjusted slightly, the energy landscape is recalculated for the new value of  $\mathbf{E}$ , and the system is re-relaxed by varying  $Q$  so as to minimise the energy.

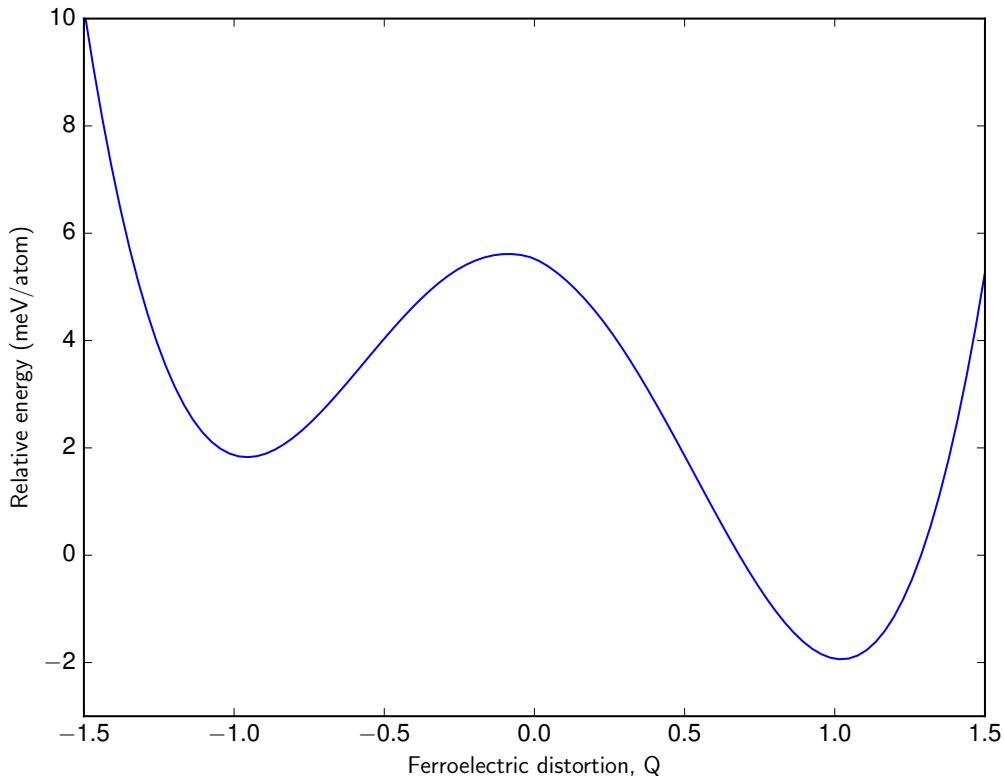


Figure 3.19 The total DFT energy per atom in a  $P\bar{4}mm$  GeTe nanowire as a function of the ferroelectric distortion,  $Q$ , with an applied electric field along the periodic direction of  $500 \text{ kV cm}^{-1}$ .

Using this scheme, the applied electric field was varied in small increments from  $E_{\text{max}} = 5000 \text{ kV cm}^{-1}$ , down to  $-E_{\text{max}}$ , and then back up to  $+E_{\text{max}}$  again. This brings the nanowire around the full hysteresis curve, and at each step both the electric field and the polarisation were recorded. Plotting the polarisation as a function of the electric field gives the hysteresis loop, which is shown on fig. 3.20.

Fig. 3.20 differs from experimental data in that the polarisation switches sign discontinuously when the applied electric field exceeds a certain threshold. This discontinuity occurs because of the shape of the energy landscape as seen on fig. 3.19. Once the electric field reaches a certain point, the minimum on the left becomes a point of inflection and the system is free to fall into the minimum on the right, and the direction of polarisation changes sign by jumping discontinuously with respect to  $E$ . By contrast, the polarisation is observed experimentally to vary smoothly because real systems

consist of domains of differing polarisation, and not all domains will reverse their polarisations simultaneously.

The remanent polarisation is defined as the polarisation remaining when the external electric field is removed. This means that the remanent polarisation is simply the point at which the hysteresis loop cuts the  $y$ -axis, which from fig. 3.20 is a polarisation of  $2.94 e$  per unit length.

The coercivity is defined as the electric field strength required to switch the direction of polarisation. The coercivity shown on fig. 3.20 of  $2350 \text{ kV cm}^{-1}$  is considerably larger than is generally found for ferroelectrics at ambient conditions – a table of literature values for five such systems given in ref. 221 contains no values higher than  $220 \text{ kV cm}^{-1}$ . The coercivity is generally found to depend strongly on temperature [222], due to the important role that thermal effects play in the switching process at higher temperatures. For this reason, the zero-temperature coercivity calculated in this method is unlikely to be a good estimate of the room temperature value. Additionally, phenomena such as ferroelectricity and ferromagnetism are fundamentally different in 1D: as is well-known, there is no global order in the thermodynamic limit. To improve on the simple approach taken in this section, a more sophisticated model of ferroelectricity in finite-length nanowires is considered in the next section.

### 3.4.2 Ising-like model

To more accurately model ferroelectricity in GeTe nanowires, we introduce an Ising-like Hamiltonian:

$$H = \sum_i U_{\text{DFT}}(q_i) + \sum_{\langle ij \rangle} J(q_i, q_j) + \frac{1}{2} \sum_i EP(q_i). \quad (3.35)$$

Here,  $i = 1 \dots N$  indexes the unit cells in the nanowire (each unit cell being of length  $6.15 \text{ \AA}$  for the  $P\bar{4}mm$  phase), and  $q_i$  represents the normal mode coordinate for the ferroelectric distortion in the  $i$ -th unit cell – i.e.,  $q_i$  is a ‘local’ version of the variable  $Q$  in eq. 3.34, and controls the displacement along the ferroelectric mode for the  $i$ -th unit cell only. The first term on the RHS gives the total DFT energy of each unit cell as a function of its displacement along the ferroelectric soft mode, and corresponds to the first term on the RHS of eq. 3.33 as plotted on fig. 3.18. However, if two adjacent cells adopt different normal mode coordinates,  $q_i \neq q_{i+1}$ , there effectively exists an interface between them. The second term on the RHS gives the energy cost for this interface as

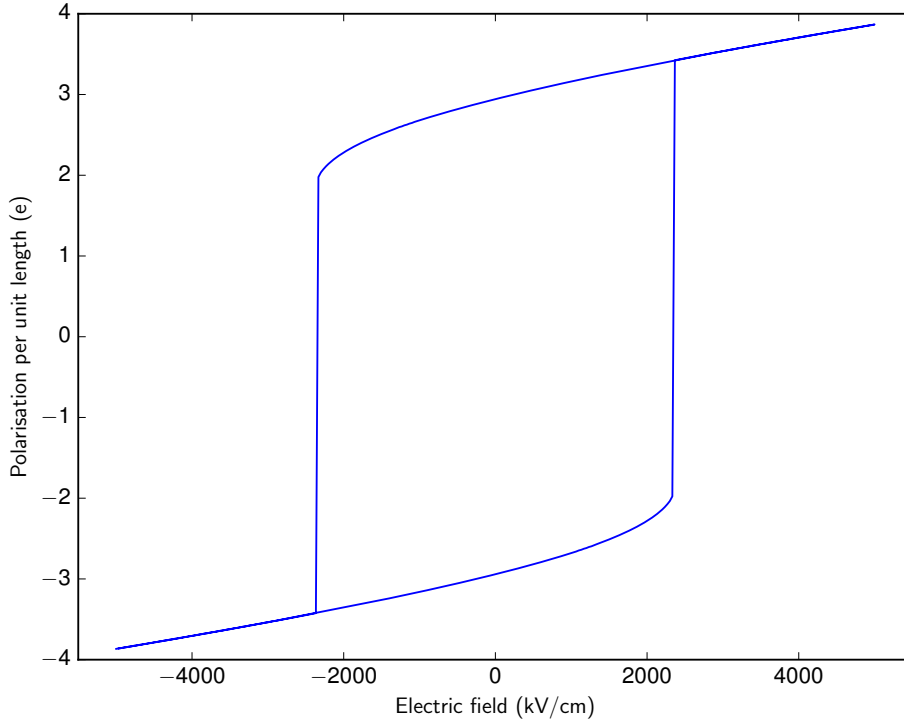


Figure 3.20 Hysteresis curve for the  $P\bar{4}mm$  GeTe nanowire structure, showing clearly the hysteresis loop.

a function of the normal mode coordinates of the neighbouring unit cells. Note that in principle one would have longer-range interactions corresponding to second-nearest neighbours, third-nearest neighbours, and so on; here this effect is neglected.

The final term on the RHS couples the unit cells to an external electric field  $\mathbf{E}$  via each cell's polarisation,  $P(q_i)$ . This term corresponds to the last term on eq. 3.33. Note that  $\mathbf{E}$  and  $\mathbf{P}$  are restricted here to the  $z$ -axis, and therefore may be treated as scalars. (The  $\epsilon_0|\mathbf{E}|^2/2$  term is dropped here since it does not couple to the unit cells' polarisations, and therefore will have no effect on the system's behaviour)

To perform a statistical-mechanical sampling of this model, rapid evaluation of the Hamiltonian  $H$  is necessary. To facilitate this, the functions  $U_{\text{DFT}}(q_i)$ ,  $J(q_i, q_j)$  and  $P(q_i)$  were represented as lookup tables rather than evaluated on the fly via DFT. Such lookup tables were already generated for  $U_{\text{DFT}}(q_i)$  and  $P(q_i)$  as part of calculating fig. 3.18. To calculate the lookup table for  $J$ , a number of DFT calculations were performed on interfaces between two unit cells with different  $q$ . For each of these cells,

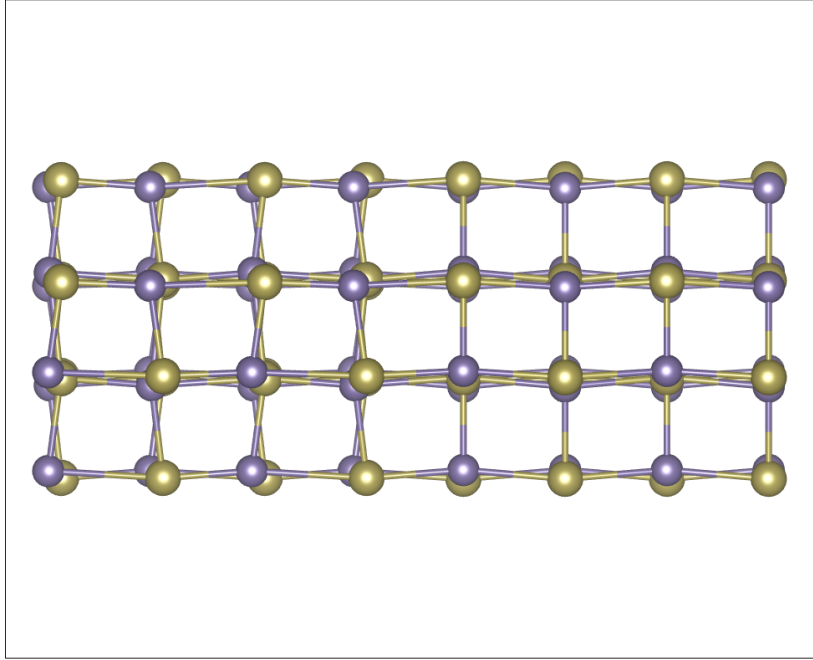


Figure 3.21 An interface within a GeTe nanowire between a polarised section with soft mode coordinates  $q = 1.6$  (left half of the cell) and an unpolarised section with  $q = 0$  (right half). The boundary of the unit cell is also shown. The periodic axis runs left to right.

the  $J$  term was calculated as

$$J(q_i, q_j) = \frac{1}{2} (U_{\text{DFT}}(q_i, q_j) - U_{\text{DFT}}(q_i) - U_{\text{DFT}}(q_j)), \quad (3.36)$$

which gives the difference between energy of the cell containing the interface and the energies of the two constituent subcells on their own. Note that the factor of  $1/2$  arises because the unit cell really contains two interfaces due to periodic boundary conditions. An example of the interface structures used to obtain  $U_{\text{DFT}}(q_i, q_j)$  in the above equation, and thereby construct the lookup table for  $J$ , is shown on fig. 3.21.

The calculations used to construct the lookup table for  $J$  were performed on an irregularly spaced 2D grid of values  $q_1$  and  $q_2$  for the two cells between which the interface is formed. The values for each  $q$  ran from  $-2.44$  and  $2.44$  (where  $q = \pm 1$  corresponds to the minimum DFT energy as shown on fig. 3.18), with a sparser concentration of grid points for points with large  $|q|$ . This is because less time is likely to be spent in the states where the polarisations are significantly larger in magnitude than is energetically favourable.

The grid contained  $17 \times 17 = 289$  points  $(q_1, q_2)$  in total. However, by symmetry,  $J$  is invariant under reflection about the diagonal, so  $J(q_1, q_2) = J(q_2, q_1)$ ; additionally,  $J$  is invariant under inversion about the origin:  $J(q_1, q_2) = J(-q_1, -q_2)$ . By imposing these symmetries the number of necessary calculations reduces to 92.

The DFT calculations were performed using a 500 eV plane-wave cutoff and the same on-the-fly pseudopotentials that were used for polishing, but with a  $k$ -point sampling of  $0.04 \times 2\pi \text{ \AA}^{-1}$ . Single-point energy calculations were used; strictly speaking a geometry optimisation in which the polarisations of the two subcells are constrained would be preferable, but the number of calculations involved makes this intractable.

The  $J$ -function was then interpolated onto a finer grid based on the DFT calculations, and is plotted on fig. 3.22. The function looks much as one would expect from an Ising-like model: misalignment of ‘spins’ is energetically disfavoured relative to alignment. This finer interpolation, onto a  $180 \times 180$  regular grid of points, was used as the lookup table for  $J$ . With lookup tables thus obtained, eq. 3.35 becomes extremely quick to evaluate; for each site, values for  $J$ ,  $P$  and  $U_{\text{DFT}}$  are simply interpolated linearly from each of the three lookup tables.  $P$  and  $U_{\text{DFT}}$  were also interpolated onto finer grids, of 1000 and 2000 points respectively.

Having constructed the model Hamiltonian, its statistical-mechanical behaviour was then investigated. Within the canonical ensemble, quantities of interest are given by thermal averages in which each state is weighted by its Boltzmann factor:

$$\langle X \rangle = \frac{\sum_i X_i e^{-\beta E_i}}{\mathcal{Z}}, \quad (3.37)$$

where  $X$  is the observable of interest,  $\beta = 1/k_B T$  is the inverse temperature,  $E_i$  and  $X_i$  are the energy and the value of  $X$  for the  $i$ -th state, the angled brackets indicate statistical expectation values, and  $\mathcal{Z}$  is the partition function. In this context  $X$  might be for example the total polarisation,  $P_{\text{tot}} = \sum_i P(q_i)$ .

Since an explicit enumeration of states is out of the question for anything more than a few sites, a better approach to statistically sampling this system would be the Metropolis algorithm. This is a well-established scheme in which the system is treated as a Markov chain. If the system is currently in state A, then another state is randomly selected and the probability that the system transitions from state A to state B is

$$P(A \rightarrow B) = \min(1, e^{-\beta(E_B - E_A)}), \quad (3.38)$$

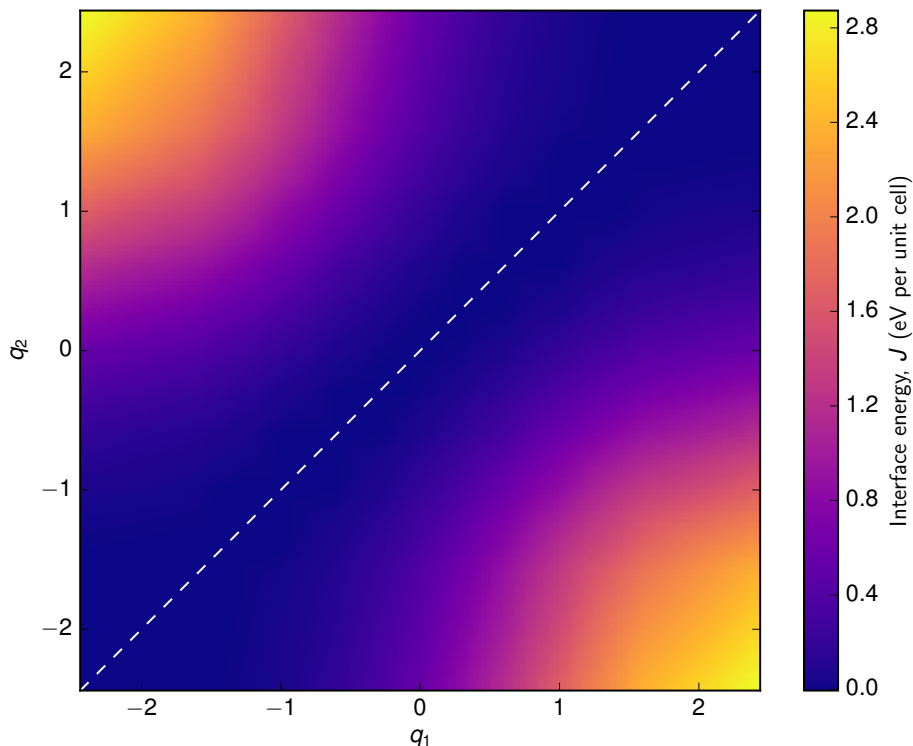


Figure 3.22 The interpolated  $J$ -function giving the interaction energy between two neighbouring ferroelectric 24-atom unit cells of the  $P4mm$  GeTe phase. The dotted white line is the diagonal  $q_1 = q_2$ .

where  $E_A$  and  $E_B$  are the energies of states A and B. This process is performed repeatedly, and in the limit that the number of repetitions tends to infinity, each state is visited in proportion to its Boltzmann weight. Thermodynamic quantities of interest may then be determined by calculating them for each visited state, and then calculating their expectation value via a simple average. (Note that if a proposed transition from A to B is rejected upon application of eq. 3.38, the value of the thermodynamic quantity gets counted again. That this is necessary can be easily seen by considering the application of the algorithm to a two-state system.)

The Metropolis algorithm is a powerful approach to the problem of sampling statistical ensembles. It has its limitations, however – most notably, it can perform poorly on systems with multiple minima due to the large number of iterations needed to clear any barrier in the energy landscape whose height is much greater than  $k_B T$ . Additionally, if one is interested in the variation in a system’s behaviour with respect to temperature – which is very often the case – then multiple runs at different temperatures are generally

necessary (though histogram reweighting techniques can ameliorate this issue to a limited extent [223]).

The Wang-Landau algorithm [224] was therefore used in this section, rather than the Metropolis algorithm. In this scheme, the rule used to determine acceptance or rejection of a state is, instead of eq. 3.38,

$$P(A \rightarrow B) = \min(1, e^{-\beta(S(E_B)-S(E_A))}), \quad (3.39)$$

where  $S(E)$  is the microcanonical entropy at energy  $E$ , which is proportional to the logarithm of the density of states,  $g(E)$ . Whereas the Metropolis rule leads asymptotically to a sampling of each state in proportion to its Boltzmann factor, this rule leads to a sampling that is flat in energy space, since the probability of selecting one of the states whose energy is  $E$  is proportional to the density of states at  $E$ , but the probability of accepting it is inversely proportional to its density of states if eq. 3.39 is used.

This scheme is complicated by the fact that unless the system is so simple that the function  $S(E)$  can be either calculated either analytically or via an explicit enumeration of states,  $S(E)$  is not actually known. Instead, the scheme builds up an estimate for  $S(E)$  that is improved dynamically over the course of the simulation, and it is this estimate that is actually used in eq. 3.39.

To build up a running estimate of  $S(E)$ , a set of equally spaced bins in energy space is defined. For each bin,  $S(E_i)$  is initialised to zero ( $E_i$  being the energy of the  $i$ -th bin). A histogram  $H(E_i)$  is also defined and initialised to zero, and keeps track of the number of visits in each bin. The algorithm then proposes states at random and accepts them with a probability given by eq. 3.39. At each iteration, a new state is proposed and then possibly accepted according to eq. 3.39; the associated histogram bin  $H(E_i)$  for the current energy of the system is identified, and is incremented by one; and  $S(E_i)$  is incremented by  $f$ . The quantity  $f$  is known as the modification factor, and is generally initialised to 1 (the precise value is not crucial).

The effect of this scheme, asymptotically, is to visit states such that the histogram  $H$  becomes flat; if through a statistical fluke the system spends an unusually large amount of time at some energy  $E_i$ , then  $S(E_i)$  will become progressively larger so that proposals to transition to some other energy will be more and more likely to be accepted, and thus the statistical fluke is self-correcting.

To gain a better estimate of  $S$ , the modification factor is reduced every so often. Because of this, adjustments to  $S$  become finer and less drastic as the estimate gets more precise, which improves its convergence to the true entropy function. The criterion for when to reduce  $f$  is that the histogram must be approximately flat. This is usually implemented as a rule requiring the maximum value in the histogram  $H$  not to exceed the minimum value by some fraction, conventionally around 5% [224]. The algorithm is generally terminated once  $f$  drops below some threshold value at which  $S$  is considered to be sufficiently converged.

It should be emphasised that at no point does the temperature enter this process. This is in contrast to the Metropolis algorithm, in which the probabilities for transitioning between states depend on temperature, as can be seen from eq. 3.38. Within the Wang-Landau scheme, the choice of temperature is a post-processing step<sup>2</sup>. In particular, once the algorithm has been finished, one can then obtain the density of states as  $g(E) = \exp(S)$ , and hence the partition function at some inverse temperature  $\beta$  via

$$\mathcal{Z} = \int \langle X(E) \rangle g(E) e^{-\beta E} dE, \quad (3.40)$$

which in practice becomes as a sum over the histogram energies  $E_i$ . Derived thermodynamic quantities such as the free energy  $F$  may then be obtained as usual from  $\mathcal{Z}$ .

In principle one could also obtain statistical expectation values in much the same way:

$$\langle X \rangle = \frac{\int \langle X(E) \rangle g(E) e^{-\beta E} dE}{\mathcal{Z}}, \quad (3.41)$$

where  $\langle X(E) \rangle$  represents the average of  $X$  over the states at an energy  $E$ , requiring the use of an array into which values of  $X$  are accumulated as the simulation progresses, and indexed analogously with the histogram so that the  $i$ -th entry in the array will correspond to an average over those states lying in the  $i$ -th bin of the histogram with energy  $E_i$ . However, one can obtain a more rapidly converging estimate of  $X$  by instead applying the Wang-Landau method not just with respect to energy, but also to

---

<sup>2</sup>This is not always precisely true: often the chosen energy range of the histogram will not encompass the entire density of states of the system, so that some states will not be included in the histogram. In this case the choice of where to put the borders of the histogram may be decided by identifying the temperature range of interest and choosing the histogram so that any energies for which the canonical weighting  $g(E)\exp(-\beta E)$  becomes large will lie inside the histogram.

$X$  [224]. This amounts to applying the algorithm to a 2D density of states  $g(E, X)$ , with corresponding histograms and entropy estimates  $H(E, X)$  and  $S(E, X)$ . This extension of the method comes at a cost: with the histogram subdivided by both  $E$  and  $X$  rather than just by  $E$ , the number of histogram bins increases, and therefore the number of iterations needed to visit each bin frequently enough for the histogram to be approximately flat increases as well. However, it means that one can obtain the full, temperature-dependent probability distribution for  $X$ , rather than just its expectation  $\langle X \rangle$ :

$$P(X) = \frac{\int g(E, X) e^{-\beta E} dE}{\int \int g(E, X') e^{-\beta E} dE dX'} \quad (3.42)$$

It should be noted that the Wang-Landau method does not provide the absolute density of states; the estimate is correct up to a multiplicative constant. (Equivalently, the estimate of  $S$  is correct up to an additive constant.) In some cases the constant may be fixed if e.g. the ground-state degeneracy is known, as in the Ising model. In this work, the absolute DOS is not required, since, as can be seen from eq. 3.42, multiplicative errors in  $g(E)$  will cancel when calculating probability distributions  $P(X)$ . The constant is therefore ignored.

The Wang-Landau method was implemented for the system described by eq. 3.35, using the variant described above in which histogram flatness is sought with respect not just to the energy but also to another parameter – in this case, the polarisation,  $P_{\text{tot}} = \sum_i P(q_i)$ . The implementation was written in C++ to allow for the very large number of iterations required for the Wang-Landau method to converge acceptably for all but the smallest systems. At each iteration, a Monte Carlo move is proposed in which a single cell's soft mode normal vector  $q_i$  is randomly adjusted by a value drawn from a normal distribution with a standard deviation of 0.9. The  $q_i$  were constrained to the region  $-2 < q_i < 2$ ; outside this region the energy cost would be extremely high (at  $q_i = \pm 2$ ,  $U_{\text{DFT}}(q_i) = 0.98 \text{ eV}$ ) such that these states are not likely to be occupied at physically accessible temperatures.

The criterion for considering the histogram flat – and therefore resetting it and reducing the modification factor – was chosen, as in ref. 225, to be a condition on the root-mean-square error of the histogram:

$$\sum_{ij} \frac{(H_{ij} - \bar{H})^2}{\bar{H}^2} < 20\%, \quad (3.43)$$

where  $\bar{H}$  is the average value of the histogram.

A modification to the algorithm was also used in which, at long times, the modification factor  $f$  is set to

$$f = 1/n_{\text{step}}, \quad (3.44)$$

where  $n_{\text{step}}$  is the number of Monte Carlo steps that have elapsed so far. The condition to switch to this mode is that  $f \leq 1/n_{\text{step}}$ . This scheme was proposed by Belardinelli *et al.* [226] based on an error analysis of the algorithm's convergence, and has been shown [227] to outperform the original algorithm.

Because of the nearest-neighbour coupling in the Hamiltonian, eq. 3.35, the cost of updating the energy following an accepted Monte Carlo move is independent of system size: the change in energy due to a change in one of the sites from  $q_i$  to  $q'_i$  is just

$$\begin{aligned} \Delta E = & U_{\text{DFT}}(q'_i) - U_{\text{DFT}}(q_i) + \frac{1}{2}E(P(q'_i) - P(q_i)) \\ & + J(q'_i, q_{i+1}) + J(q'_i, q_{i-1}) - J(q_i, q_{i+1}) - J(q_i, q_{i-1}). \end{aligned} \quad (3.45)$$

These evaluations are performed by linearly interpolating the lookup tables for  $U_{\text{DFT}}$ ,  $J$  and  $P$ . The cost in calculating eq. 3.45 in this way is sufficiently small that it is not much larger than the time spent generating random numbers (which is done via the Mersenne Twister [228]) in proposing a new spin, so evaluation is extremely fast. Of course, the fact that evaluating  $\Delta E$  is  $O(1)$  in system size does not imply that the algorithm as a whole is also  $O(1)$ : larger systems have larger phase spaces and therefore more iterations in total are required to achieve a given level of convergence of  $S(E, P)$ .

As is well-known, the Ising model contains no phase transition in 1D – the net magnetisation (or in this case, polarisation) is zero. However, this is in the thermodynamic limit. Finite systems can contain long-range order, and since the primary interest behind this work is in potential nanotechnological applications, it is reasonable to consider relatively small systems. Periodic boundary conditions were not used, leaving the two unit cells at the ends of the nanowire with only a single neighbour each to couple to.

First, the implementation was tested by running it for the trivial case of a single unit cell, with no applied electric field. Having obtained  $S(E, P)$ , the probability

distribution for the polarisation,  $p(P)$ , was calculated via eq. 3.42. A corresponding free energy was then obtained via

$$F(P) = -k_B T \log p(P). \quad (3.46)$$

The results are shown (at  $T = 300$  K) on fig. 3.23. The case of a single cell represents a special case in which a given value of the polarisation is sufficient to completely characterise the microstate. In this context the microstate is simply the set of variables  $q_1, q_2, \dots, q_N$ ; in the single-cell case there is only a single variable,  $q_1$ . Since it determines the microstate, it follows that the polarisation also determines the energy – that is, the exact energy, not just its thermal average. (In the  $N > 1$  case, a given value of the total polarisation corresponds to a number of possible microstates, so this is no longer true). As a result, the density of states  $g(E, P)$  shown on fig. 3.23 trivially becomes equivalent to the original energy function  $U_{\text{DFT}}(q)$  shown on fig. 3.18, via the one-to-one mapping between  $q$  and  $P$  that exists in the one-cell case. Consequently, the density of states is zero everywhere except where  $E = U_{\text{DFT}}(q(P))$ . To verify the ability of the method to recover the correct free energy, the polarisation-dependent free energy was computed from  $g(E, P)$  using eq. 3.46. The figure compares this Wang-Landau result with the true free energy, which is given (up to an additive constant) by

$$F(P) = U_{\text{DFT}}(q(P)) - k_B T \log \frac{dP}{dq}. \quad (3.47)$$

The second term on the RHS arises from the nonlinear relationship between  $P$  and  $q$ , as shown on the bottom of fig. 3.18. This relationship means that the number of microstates contained in an interval  $dP$  is dependent on  $P$ . Taking this into account increases the statistical weight for states at low  $|P|$ .

Although the main purpose of fig. 3.23 is to test the accuracy of the implementation of the Wang-Landau method, it is interesting to note the presence of van Hove singularities in  $g(E)$ , whose origin is exactly analogous to that of the singularities that arise in electronic densities of states.

Having tested the implementation on 1 site, it was then run on a number of sites with  $N > 1$ . Systems with larger  $N$  have higher-dimensional configuration spaces and therefore require more sampling to obtain accurate results. The number of Wang-Landau iterations was chosen to vary as  $N^3$ , from  $8 \times 10^7$  samples for  $N = 1$  to

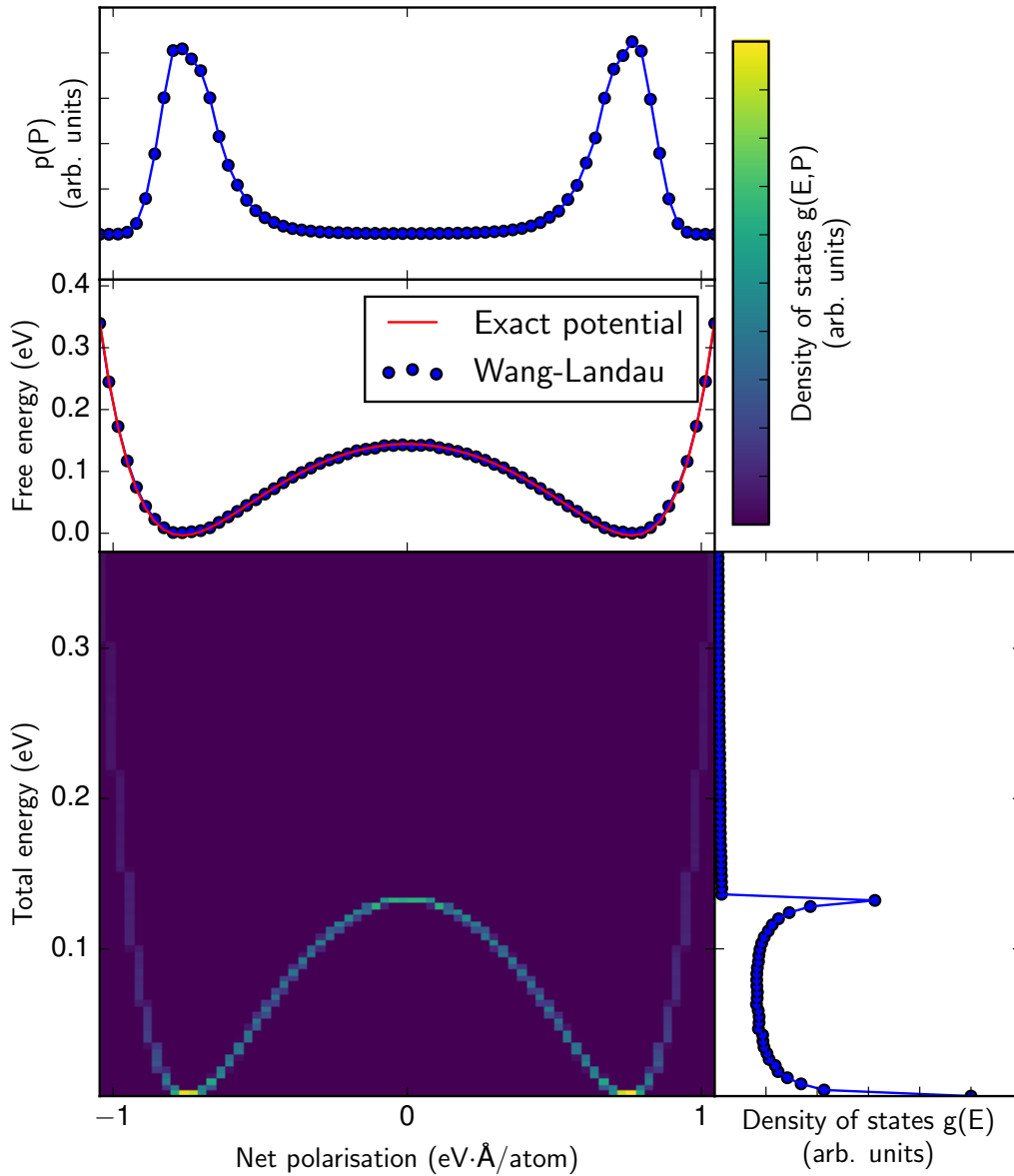


Figure 3.23 Results for Wang-Landau sampling at  $T=300$  K on the special case of a single site. The density of states in polarisation and energy,  $g(E, P)$  is shown at the bottom-left, with the colour bar on the top-right. Integrating  $g(E, P)$  along the polarisation axis gives  $g(E)$  (bottom-right). The resulting probability distribution for the polarisation is shown at the top, and the free energy implied by this probability distribution is shown in the middle. Also shown in the middle figure is the free energy calculated directly from the potential  $U_{\text{DFT}}(q)$ . The exact and Wang-Landau results have been offset to align them with each other.

$8 \times 10^{12}$  samples for  $N = 100$ . After running for the chosen number of iterations, each simulation's final modification factor,  $f$ , was found to be no larger than  $3 \times 10^{-5}$  after repeated halving from its initial value of 1. For all of these calculations, the applied electric field was set to zero.

Results for the  $N = 20$  case are shown on fig. 3.24. The DOS  $g(E, P)$  looks much as one would expect given the similarity of this model to the Ising model: two degenerate ground states in which all atoms are aligned, with the polarisation per atom corresponding to the minima of  $E_{\text{DFT}}(q)$  as shown on fig. 3.18. At low but nonzero energies, there are low-lying excitations in which atoms are no longer perfectly aligned (in contrast to the Ising model in which the sites are quantised, here this can be achieved by moving one of the  $q_i$  only slightly away from one of the minima of  $E_{\text{DFT}}$  rather than hopping to a different one). At higher energies, there exist a large number of states at almost zero  $|P|$ , with little long-range order in the system. This suggests the presence of an order-disorder transition in this system: at high temperatures, statistical averages are dominated by contributions from the high-energy, low- $|P|$ , disordered states. (Of course, this is not truly a phase transition in the strict sense because the system is finite and so the free energy and its derivatives will always be smoothly varying)

It should be noted that, since the temperatures plotted on fig. 3.24 extend beyond the melting point of GeTe, the upper end of the temperature range shown is certainly above the range of validity of the underlying model; it is shown regardless in order to illustrate the variation of the model's thermodynamics with respect to temperature. As can be seen, the free energy minima corresponding to the polarised states become shallower at higher  $T$ , and the polarisation at the minima shifts rightwards as the higher entropy of the low-lying excited states renders them more favourable than the perfectly aligned state. Since the positions of the minima correspond to the remanent polarisation, one can extract from this the variation of the remanent polarisation as a function of temperature. The bottom-right plot showing the canonical weighting function  $W(E) = g(E) \exp(-\beta E)$  also shows how the selection of an energy window within which to calculate the density of states limits the choices of temperature for which thermodynamic quantities can be accurately calculated: once 1300 K is reached, the weighting function begins to contain a significant amount of probability mass above the upper limit of the energy window at 2.4 eV. By cutting off these high-energy contributions, the accuracy of any thermodynamic quantities, such as  $p(P)$  or  $F(P)$ , is compromised.

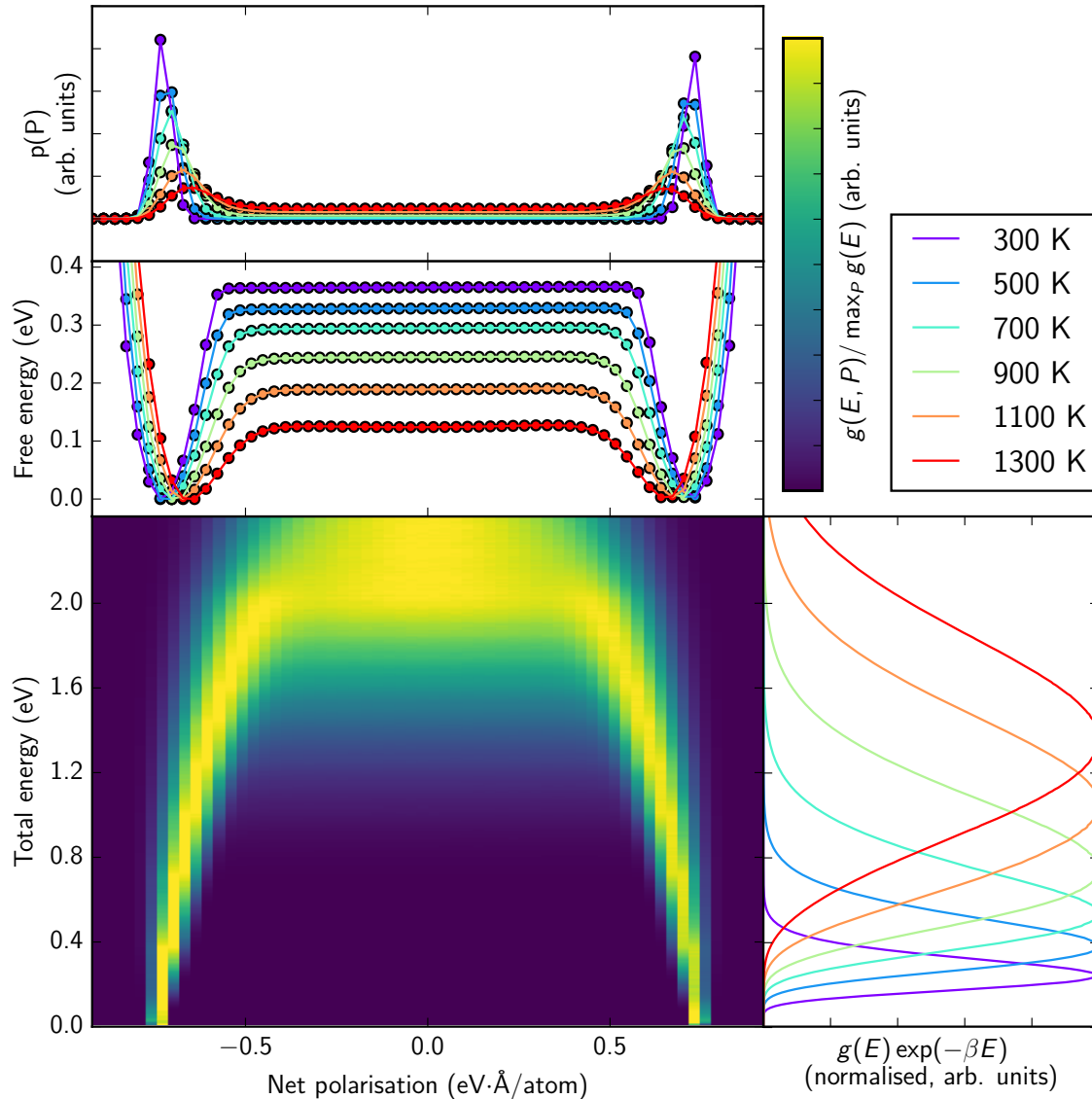


Figure 3.24 Results for the  $N = 20$  case, for a range of temperatures. Note that in contrast to fig. 3.23,  $g(E, P)$  is normalised here by  $\max_P g(E)$ , due to the fact that  $g(E, P)$  increases extremely rapidly at higher energies, which would make it almost invisible at lower energies. Additionally, the bottom-right plot shows not  $g(E)$ , but the weighting factor  $g(E) \exp(-\beta E)$ . This illustrates the tradeoff between entropy, which favours high-energy states, and the Boltzmann factor, which suppresses high-energy states.

It is instructive to look at some of the states directly, to see how the different points in  $(E, P)$  space – i.e., macrostates – correspond to microstates. Some randomly chosen states at different  $(E, P)$  are displayed on fig. 3.25. One can see how low-energy, low- $|P|$  states consist of otherwise ordered nanowires with a single phase boundary. While this is true in the Ising model, it is not a given when the sites are no longer constrained to  $\pm 1$ ; one potential low- $E$ , low- $|P|$  state could have consisted of a gradual transition from  $q = -1$  at one end of the wire to  $q = 1$  at the other. Whether one or the other is obtained depends on the nature of the functions  $J(q_1, q_2)$  and  $E_{\text{DFT}}(q)$ . The nature of these microstates also explains why  $g(E, P)$  is relatively flat with respect to polarisation for the low- $E$ , low- $|P|$  states: one can simply translate the phase boundary to produce another microstate with the same  $E$  but different  $P$ . Also immediately apparent from visual inspection is the difference in entropy between the high-energy and low-energy macrostates shown.

The calculations were repeated at a number of different nanowire lengths and temperatures, in each case calculating the free energy  $F(P)$  as a function of both. Some free energies as a function of  $T$  are shown on fig. 3.26. From the figure, one can see that larger  $N$  is associated with steeper minima, in keeping with the general principle that larger systems experience smaller fluctuations relative to system size. Another trend is that the free energy gap  $\Delta F$  between the polarised states at the minima of  $F$  and the unpolarised state at  $P = 0$  decreases as  $N$  increases, which suggests the existence of a transition from polarised states to unpolarised states as the system size grows.

This free energy gap is plotted on fig. 3.27 against  $N$  on a logarithmic scale, for various temperatures. The figure shows how  $\Delta F$  falls with respect to both  $T$  and  $N$ . A second-order polynomial function of  $\log N$  was fitted to these data for each  $T$ , and extrapolated to large  $N$ . This allows one to estimate the value of  $N$  at which  $\Delta F$  becomes zero, i.e. at which unpolarisation replaces polarisation as the thermodynamic ground state. This quantity – which we define as  $N_{\text{crit}}$  – is plotted against  $N$  on fig. 3.28. It is notable that at every point except 300 K there is a general trend towards  $N_{\text{crit}}$  decreasing with respect to temperature. Based on fig. 3.27, it is likely that the anomaly at 300 K is just the result of inaccuracies in the fit; since  $N_{\text{crit}}$  is very large at low  $T$ , the extrapolation is less trustworthy than it is at higher  $T$ . In general, though, one can infer from fig. 3.28 that at ambient conditions, the polarised state remains the ground state even at very long nanowire lengths. Again, it should be emphasised that at the upper end of the temperature range the model considered here is unlikely to be

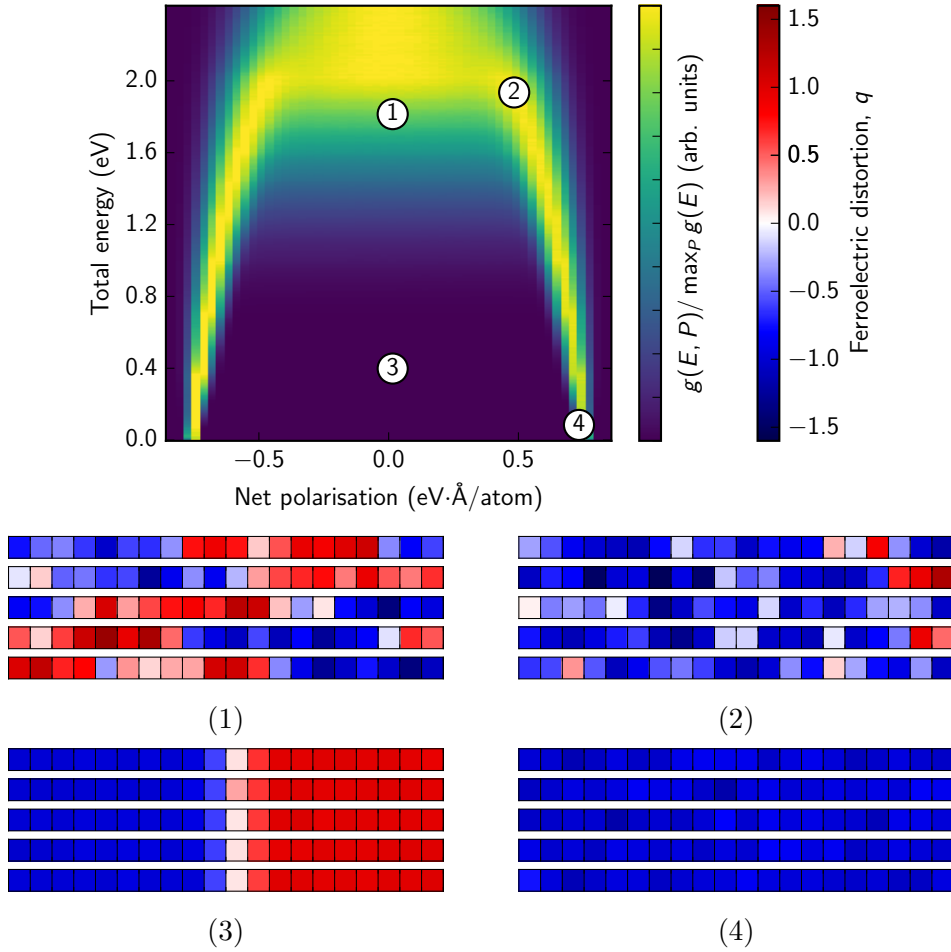


Figure 3.25 Some randomly selected microstates for four different macrostates  $(E, P)$  with  $N = 20$  sites. In each case five microstates are shown, with each site represented by a single box coloured according to its ferroelectric distortion as per the top-right colour bar.

physically relevant given the previous section's findings regarding the melting points of GeTe ENWs, and is included only to illustrate the behaviour of the model at high  $T$ .

Note that in the following we use  $h$  rather than  $|\mathbf{E}|$  to refer to the magnitude of the applied electric field to avoid confusion with the energy. As yet, only the case of zero electric field has been considered. However, one may take its effect into account without performing any new Wang-Landau simulations. This is because the coupling term,  $hP/2$ , depends only on the total polarisation,  $P$  – i.e., it depends only on the macrostate, not the microstate. It follows that if  $g(E, P)$  is known in the absence of an applied field, one can obtain the corresponding density of states in an applied field

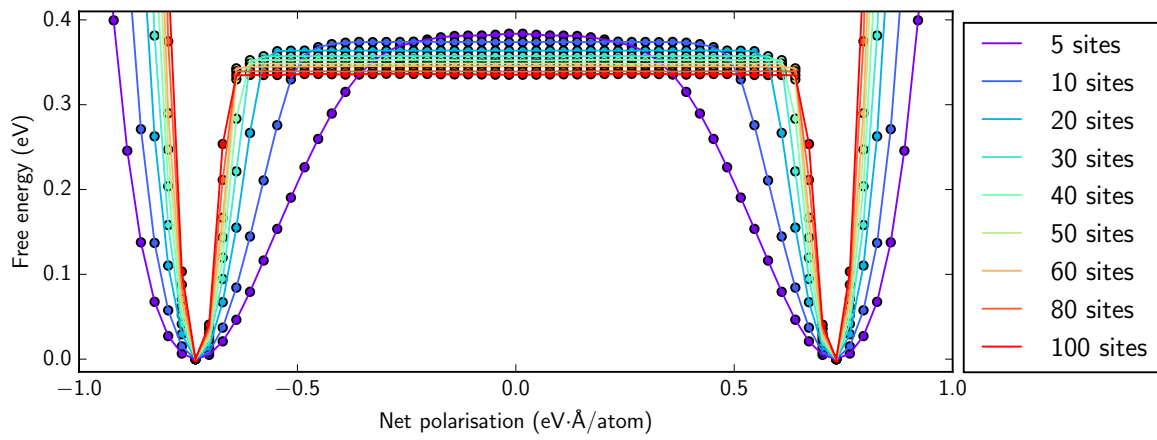


Figure 3.26 Polarisation-dependent free energies as a function of the number of cells,  $N$ , calculated at  $T = 300$  K.

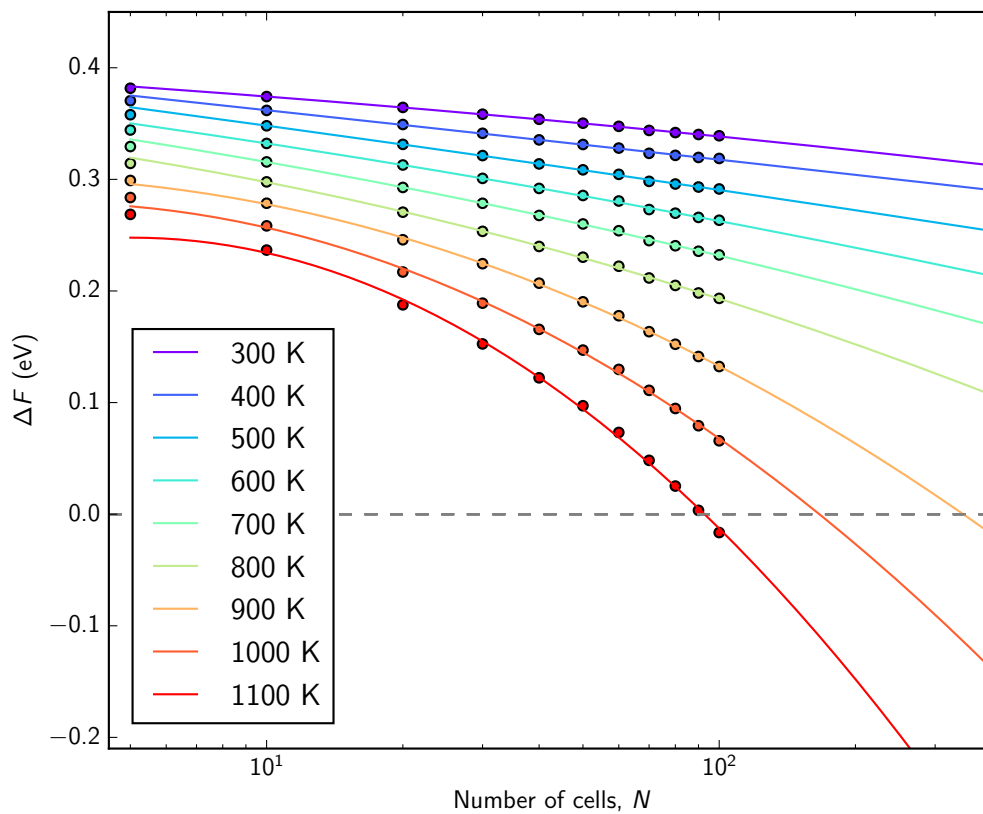


Figure 3.27 The free energy gap  $\Delta F$  between the polarised and unpolarised state as a function of  $N$  for varying  $T$ .

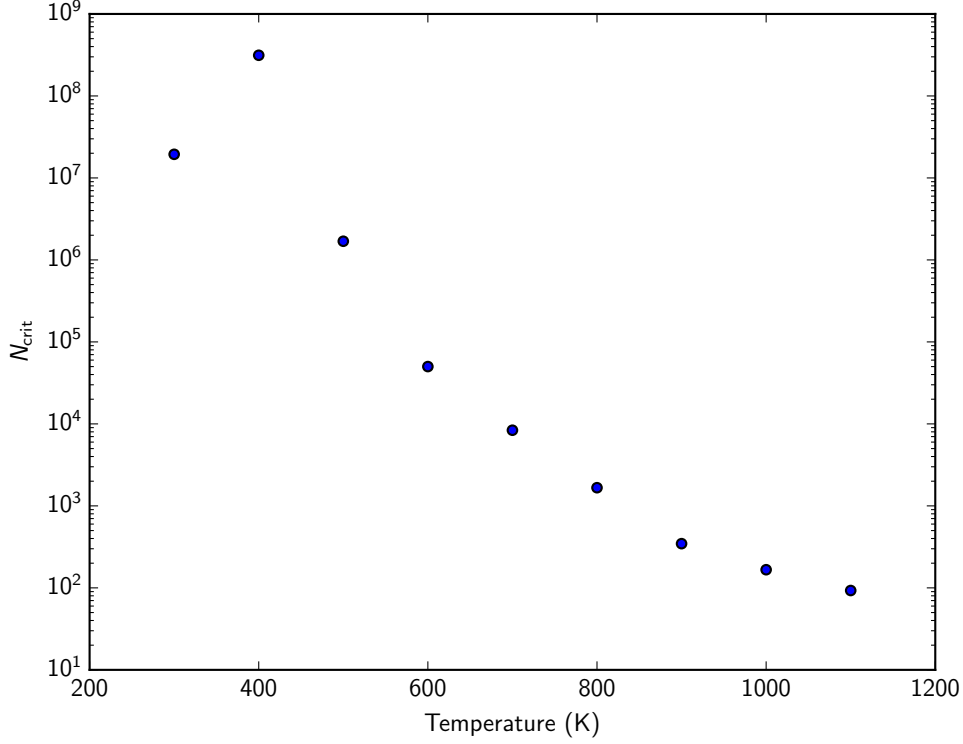


Figure 3.28 Maximum nanowire length  $N_{\text{crit}}$  (measured in the number of sites) beyond which the unpolarised state becomes lower in free energy than the polarised state, based on extrapolation from fig. 3.27.

$h$  via

$$g(E, P, h) = g\left(E - \frac{1}{2}hP, P, 0\right) \quad (3.48)$$

where  $g(E, P, 0)$  is the density of states with no applied field (i.e.  $h = 0$ ). This shows that the action of an applied field  $h$  on the function  $g(E, P)$  is that of a skew transformation about the line  $P = 0$ . As a result, the Boltzmann factors contributing to the probability distribution  $p(P)$  are suppressed by a factor  $\exp(-\beta hP/2)$ ; since  $F(P) = -k_B T \log p(P)$ , the corresponding effect on the free energy is then simply

$$F(P, h) = F(P, 0) - \frac{1}{2}hP \quad (3.49)$$

where  $F(P, 0)$  represents the free energy at zero applied field. This shows that the application of an electric field merely shifts the free energy by a linear gradient with respect to  $P$ .

Using this electric field-dependent free energy, one can compute the hysteresis properties of the system. This is done by initialising the system in one of the two polarisation states, and then gradually varying the applied electric field from large negative values, up to large positive values, and back again. After each small adjustment in the electric field, the system's polarisation  $P$  is re-optimised into the nearest local minimum of  $F(P)$ . This is the same scheme that was employed previously to obtain fig. 3.20, except using the full free energy rather than simply the total energy for a single site at 0 K. Because the free energy was calculated on a relatively coarse grid (as can be seen from the plot of  $g(E, P)$  on fig. 3.24), the minimisations of  $F$  with respect to  $P$  were performed using a cubic spline interpolation of  $F$ , allowing better estimates of the optimal values of  $P$  and of the free energy at those optimal  $P$ .

Performing these calculations at 300 K for a range of different nanowire lengths results in fig. 3.29. The general trend is that – at least within the range of  $N$  considered on the figure – the coercivity drops quite rapidly with  $N$ , but the remanent polarisation drops only slowly. One of the obstacles to scaling FRAM to small sizes is that in very small memory cells, the current produced by the ferroelectric upon reading can be too weak to easily detect [229], so the remanent polarisation per site is an important quantity. The fact that it remains large even for small  $N$  is encouraging, though of course the total charge will still fall roughly linearly as  $N$  is decreased. The lower coercivity for larger  $N$  may be beneficial in that the electric field required to switch states will be lower, and as a result so will the energy cost per write operation (since the area enclosed by a hysteresis loop corresponds to the work done over the cycle). However, it likely results in part from the decreased free energy barrier between the polarised and unpolarised states, which may imply shorter retention times for the memory, as thermal fluctuations could more easily drive the system over the barrier.

Recalculating the hysteresis loops at varying  $T$  but fixed  $N = 100$  leads to fig. 3.30. This diagram indicates that higher temperatures are associated with lower coercivity and lower remanent polarisation as one would expect, but there does not appear to be much variation in the hysteresis properties over temperature ranges that would be technologically relevant for FRAM (i.e. temperatures around 300 K). By recalculating this diagram at higher temperatures, it was found that the model undergoes a ferroelectric to paraelectric transition (at around 1250 K for  $N = 100$ ). This indicates that the model is sophisticated enough to predict such transitions where they occur, but is not shown on the figure since it is far above temperatures for which the model is

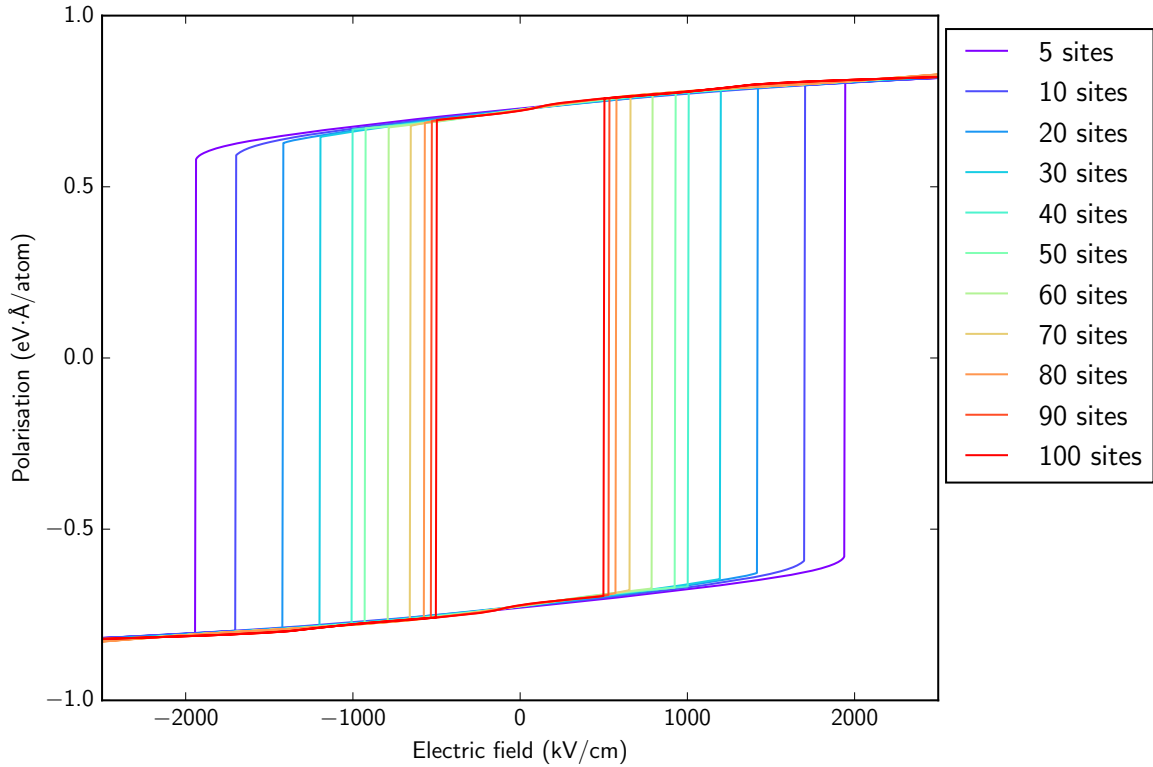


Figure 3.29 Hysteresis curves as a function of the length of the nanowire at  $T = 300$  K.

valid. Indeed, the molecular dynamics simulations from the previous section indicate that the upper end of the temperature range considered in fig. 3.30 is near the melting point, which may suggest that the model is already becoming inaccurate there (likely because the neglect of thermal motion along normal modes other than the ferroelectric distortion becomes increasingly unjustified at higher temperatures). This provides another example of a property that is potentially tunable for technological purposes: long nanowires have larger total polarisations, but also lower  $\Delta F$  between the polarised and unpolarised state due to entropic considerations.

Further work could involve an investigation of the effect of encapsulation on the ferroelectric properties. One potential problem would be that the encapsulating nanotube could in principle act like a kind of Faraday cage, shielding the nanowire's polarisation and making it more difficult to both read and write from the memory. This suggests that an insulating nanotube would be the better choice in such a device. One could investigate the effect of the nanotube by repeating the DFT polarisation calculations performed here for a full ENW rather than the bare nanowire, reparameterising the

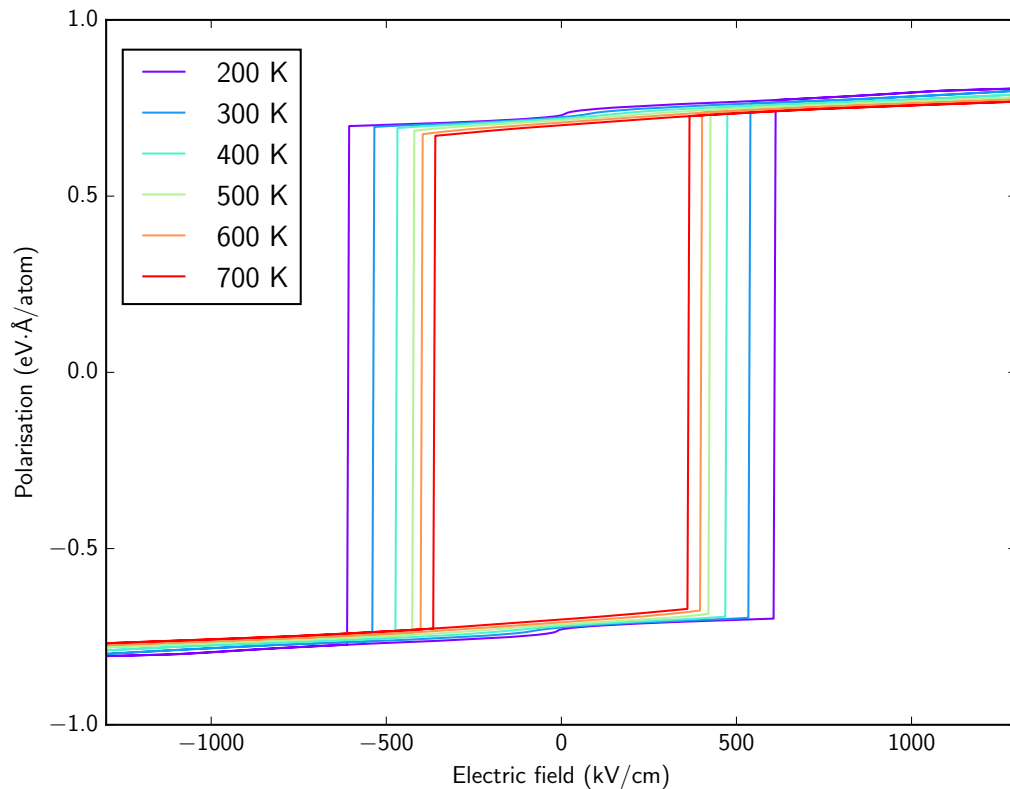


Figure 3.30 Ferroelectric hysteresis curves as a function of temperature at a nanowire length of  $N = 100$  sites.

Ising-like model, and repeating the statistical-mechanical calculations to investigate the resulting change in the ferroelectric behaviour.

### 3.5 Conclusion

In this chapter, the formation of 1D crystals by GeTe encapsulated within carbon nanotubes has been investigated using *ab initio* random structure searching (AIRSS). By computing their formation energy as a function of the radius of the encapsulating nanotubes, a phase diagram has been constructed for encapsulated GeTe nanowires that quantitatively maps out a sequence of structures as progressively wider nanotubes are considered. The results predict a range of novel phases which are often strikingly different from the bulk, and thereby shed light on the change in behaviour of GeTe when confined to atomically thin spaces. The predictions run across a large range of

nanotube radii, and where experimental imagery is available, the predictions are in agreement.

The finite-temperature behaviour of GeTe ENWs has been found to contain a number of crystalline-crystalline temperature-induced phase transitions. The presence of such phase transitions illustrates a key feature in the behaviour of encapsulated nanowire systems: because the formation energies of different phases are strongly dependent on the radius of the encapsulating nanotube, the choice of nanotubes in which to encapsulate the wire acts as a means of ‘tuning’ the relative energies of different phases, with corresponding effects on ground state structures and phase transition temperatures. In this sense, the nanotube radius plays a roughly analogous role to that of pressure in a traditional phase diagram, by adjusting the extent to which more compact structures are energetically incentivised.

The phase-change properties of GeTe encapsulated nanowires were investigated. It was found that the crystalline-amorphous switchability which has made GeTe the object of so much research interest is retained even in very narrow GeTe ENWs. Moreover, lower nanowire radius was found to be associated with a lower melting point. This is consistent with a trend that has been experimentally identified in larger nanowires, and suggests that encapsulated GeTe ENWs could have applications as low-power memory components (albeit at the cost of potentially slower switching times). Their glass transition temperature, an important quantity for characterising the transition from amorphous GeTe to supercooled liquid, was found to be unaffected by the choice of nanowire radius.

The ferroelectric properties of GeTe ENWs – and in particular those of the  $P\bar{4}mm$  phase – were then considered. Using DFT calculations within the formalism of the modern theory of polarisation, the energy and ferroelectric polarisation were parameterised as a function of the ferroelectric distortion. A naive energy-minimisation approach was found to generate an unrealistic hysteresis curve in which the remanent polarisation was excessively high compared to experimental values; therefore, an improved statistical-mechanical approach was used in which each unit cell in a nanowire of finite length is allowed to polarise separately. The model contains nearest-neighbour interactions between cells, also parameterised via DFT total energy calculations. The model was investigated by using Wang-Landau sampling to compute its density of states with respect to energy and polarisation. From these calculations, it was found that the

---

model remains ordered even up to relatively long lengths of nanowire, suggesting that GeTe nanowires could be technologically useful in ferroelectric memory.



# Chapter 4

## Encapsulated AgCl nanowires and Raman spectroscopy

The silver halides are noted for their photosensitivity, which is attributed to their unusually abundant concentrations of Frenkel defects [230]; as a result, they play a vital role in photographic technology [231], and have also been used in photochromic materials [232]. This chapter focuses on nanowires of the silver halide AgCl, with a particular focus on their response to vibrational spectroscopy. Such nanowires have drawn significant experimental attention [164, 233, 234], in part due to their technological potential as photocatalysts [235, 236]. The effects of the encapsulation of wide AgCl nanowires within double-walled carbon nanotubes (DWNTs) have been studied [237], but AgCl nanowires of atomically small widths as will be considered in this chapter have not yet been described in the literature.

The valence electronic configurations of Ag and Cl are  $4d^{10}5s^1$  and  $3s^23p^5$ . In the bulk, the result of this is an ionically bonded rocksalt crystal structure with a filled Cl  $p$  shell [238].

### 4.1 Structure search

Searches were carried out for encapsulated nanowires made of AgCl, using the same methods as described in section 3.1. As before, searches were performed in a confining potential, and the lowest-energy structures were identified for higher accuracy polishing

calculations. Initial searches were performed with a plane-wave basis set cut-off of 330 eV, and a BZ sampling density along the periodic direction of  $0.05 \times 2\pi \text{ \AA}^{-1}$  as before. Ultrasoft pseudopotentials were used which treated as valence the Ag 4*d* and 5*s* orbitals and the Cl 3*s* and 3*p* orbitals. By performing some calculations on representative nanowire systems, formation energies were found to be converged with respect to the chosen basis set cut-off to within 10 meV per atom, and with respect to the BZ sampling to within 3 meV per atom.

For the higher accuracy calculations performed on the lowest-energy structures identified in the search, different pseudopotentials generated on-the-fly by CASTEP were used. These pseudopotentials were harder than those used for the structure search, although they pseudised the same orbitals. The carbon pseudopotential treated the 2*s* and 2*p* orbitals as valence. A basis set cut-off of 500 eV was used for these calculations, along with a *k*-point sampling density of better than  $0.0325 \times 2\pi \text{ \AA}^{-1}$ . By again performing convergence tests on representative systems (this time including the nanotube), the errors in formation energies resulting from the basis set cut-off and the finite *k*-point sampling were found to be 1 meV and 5 meV per filling atom, respectively.

After the structure search the most promising candidate structures were then identified for polishing, and are shown on table 4.1. It was found that some of these structures' lengths depend strongly on the nanotube radius, with smaller radii extruding the filling material so that the periodicity of the nanowire expands dramatically, sometimes by as much as 20%. A 20% strain would introduce a large error in the energy (some test calculations on strained nanowires indicate that a strain of less than 5% is usually required in order to keep strain errors below about 0.01 eV per atom). Therefore, a more sophisticated technique is required when choosing the tube into which to insert the wire that takes into account the dependence of the wire's length on the radius of the tube.

For each filling structure, optimisations were performed in confining potentials of varying radii. This gives the dependence of the structure's periodic length,  $c$ , as a function of the nanotube radius,  $R$ . Then, the nanotubes into which to encapsulate the nanowire were selected by interpolating to find a curve for  $c(R)$  and identifying a range of tubes whose lengths and radii are commensurate to within 4% strain with the equilibrium nanowire length  $c(R)$  at each tube's radius,  $R$ .

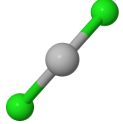
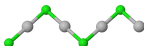
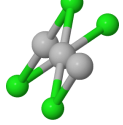
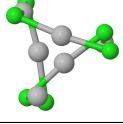
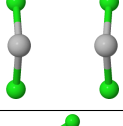
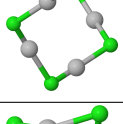
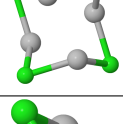
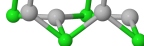
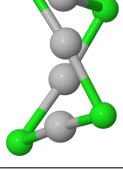
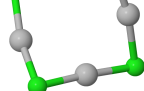
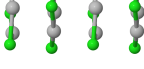
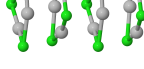
Structure	End-on view	Side-on view	3D view
$P_{\infty}/m$ (Linear chain)			
$Pmm2$ (Zig-zag)			
$P\bar{1}$ (Distorted zig-zag)			
$P3_1-I$ (Single helix)			
$P3_1-II$ (Angular double helix)			
$Pmm1$ (Double zig-zag)			
$P4_1$ (Double helix)			
$P\bar{4}$ (Distorted rocksalt)			
$P1$ (8-atom rings)			
$P3m1$ (Layered triangles)			

Table 4.1 All AgCl filling structures shown on fig. 4.2, ordered by their width. Grey atoms are silver, and green atoms are chlorine.

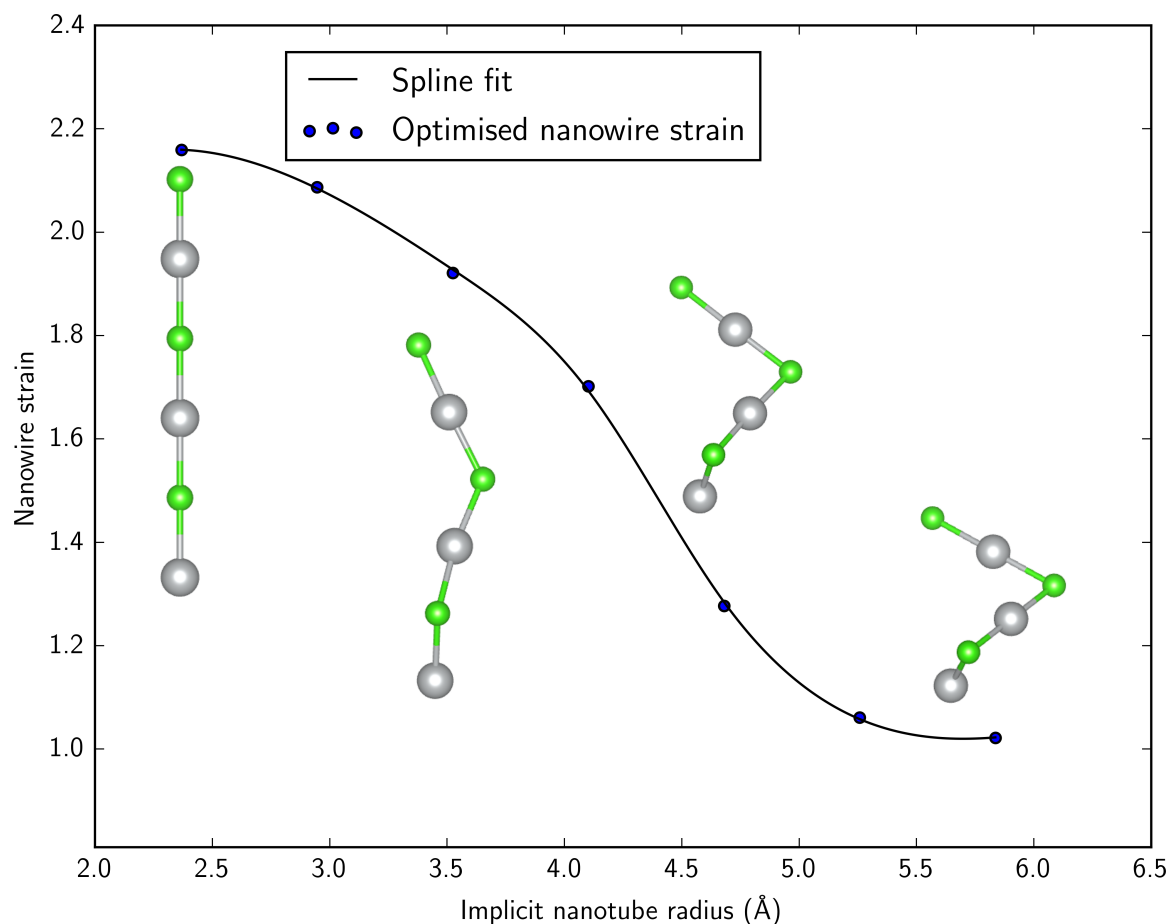


Figure 4.1 The variation of equilibrium nanotube length with implicit nanotube radius  $R$  for the  $P3_1$ -I structure. Every second data point is annotated with the structure at that radius. Strains are computed relative to the length of the structure at  $R = \infty$ , as calculated by relaxing the structure in a vacuum.

An example of the calculations of  $c(R)$  is plotted on fig. 4.1, for the helical  $P3_1$ -I phase. The figure shows that the nanowire's periodicity depends strongly on the nanotube's radius, as confinement causes it to elongate and ultimately collapse into a linear chain. One can see a distinctive 'S'-shape to the curve due to the fact that at very large radii the nanowire is only weakly interacting with the nanotube, and at small radii the nanowire becomes as narrow as it possibly can.

The phase diagram for AgCl encapsulated nanowires was calculated using the formation energies as a function of nanotube radius, and is shown on fig. 4.2. Once again, a series of phase transitions can be observed as the tube radius increases. As with GeTe, the first structure at small radii is a linear chain. This is physically inevitable, since as the nanotube radius decreases and overlap between the tube and wire increases, the

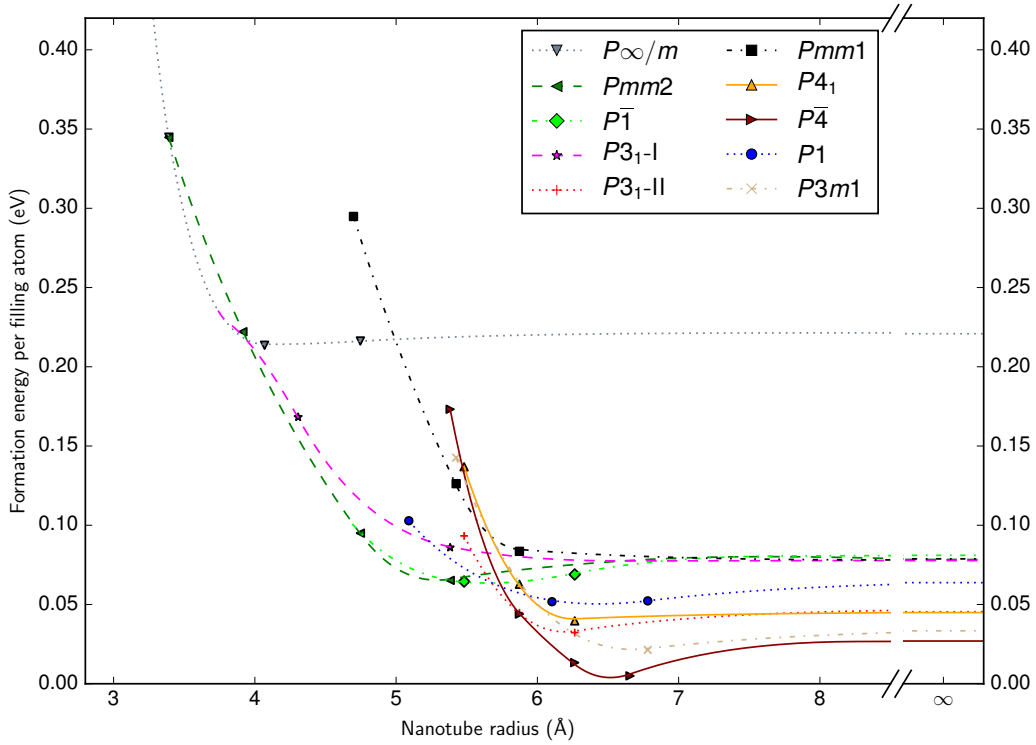


Figure 4.2 Phase diagram for encapsulated AgCl nanowires.

energetic cost of the wire having nonzero width increases without bound. As the tube radius increases, the energetic tradeoff associated with buckling the wire – between the cost of greater Pauli repulsion between the wire and the tube and the energy saved by having more favourable bonding environments – eventually favours buckling, and the first phase transition occurs at around 3.9 Å. After this transition the zigzag phase becomes thermodynamically stable. Then, at 4.69 Å, the  $P\bar{1}$  distorted zigzag phase becomes marginally more stable. The energy difference between the two is extremely small, but the distorted phase appears only to become the thermodynamic ground state beyond about 5.34 Å, well after it becomes mechanically stable. The energetic closeness of these structures means that these predictions are not certain, however, and it is likely that both could form at this radius.

At around 5.7 Å, multiple structures are energetically competitive, with the  $P3_1$ -II,  $P\bar{1}$  and  $P1$  phases becoming almost degenerate. After this point, however, the  $P\bar{4}$  structure becomes the ground state. This structure appears to correspond to a distorted version of a structure that has been observed empirically in HgTe ENWs [16].

It is notable that the structure search did not identify any structures that correspond to cut-throughs of the rocksalt-like bulk, in contrast to the findings of the GeTe structure search. However, the AgCl structure search did not run up to radii as high as in GeTe (Implicit radii were chosen to be at most 6.26 Å in AgCl compared to 7.83 Å in GeTe; though note that, as will be shown later in this section, implicit nanotube radii correspond to larger explicit nanotube radii). It is likely that such derivatives of the bulk would have been found if larger nanotube radii had been considered. Additionally, the  $P\bar{4}$  structure somewhat resembles a distorted version of  $2 \times 2$  rocksalt. It may therefore be regarded as a bulk cut-through which has been distorted by surface effects.

All structures appearing on the phase diagram are insulators, in contrast to the GeTe structure search in which some structures were conducting and some were insulating.

Instances were observed where, for certain nanotube radii, filling structures became mechanically unstable and relaxed into different structures. On fig. 4.2, these take the form of bifurcations in which, below a certain critical radius, two curves merge into one. Three bifurcations appear on the phase diagram: at 3.39 Å, the linear diatomic chain can buckle into a zigzag chain, with the zigzag phase eventually overtaking the linear chain energetically in tubes wide enough to accommodate it. At 3.73 Å, the linear diatomic chain branches once again into a buckled chain structure – this time into a diatomic helix with  $P3_1$  symmetry. The helix in turn branches at 4.69 Å, with a distorted zigzag with  $P\bar{1}$  symmetry becoming stable.

The bifurcations on the phase diagram were dealt with as follows: where a geometry optimisation was performed and a structure was observed to have relaxed into a different phase, the corresponding data point on the phase diagram was removed and the formation energy curve for the transforming structure is constrained to match the curve for the structure into which it has transformed at the particular radius where it did so. This means that the precise critical radius at which the bifurcation occurs could in principle be somewhat higher than is indicated; because only a discrete set of nanotube radii are available, the exact point cannot be identified precisely. For example, consider the bifurcation at 3.73 Å in which the diatomic helix becomes stable. This bifurcation is identified from the fact that in a tube at 3.73 Å, the helix collapses into a chain, whereas at 4.31 Å it remains mechanically stable. This limits the critical radius at which the transition occurs to somewhere between 3.73 and 4.31 Å.

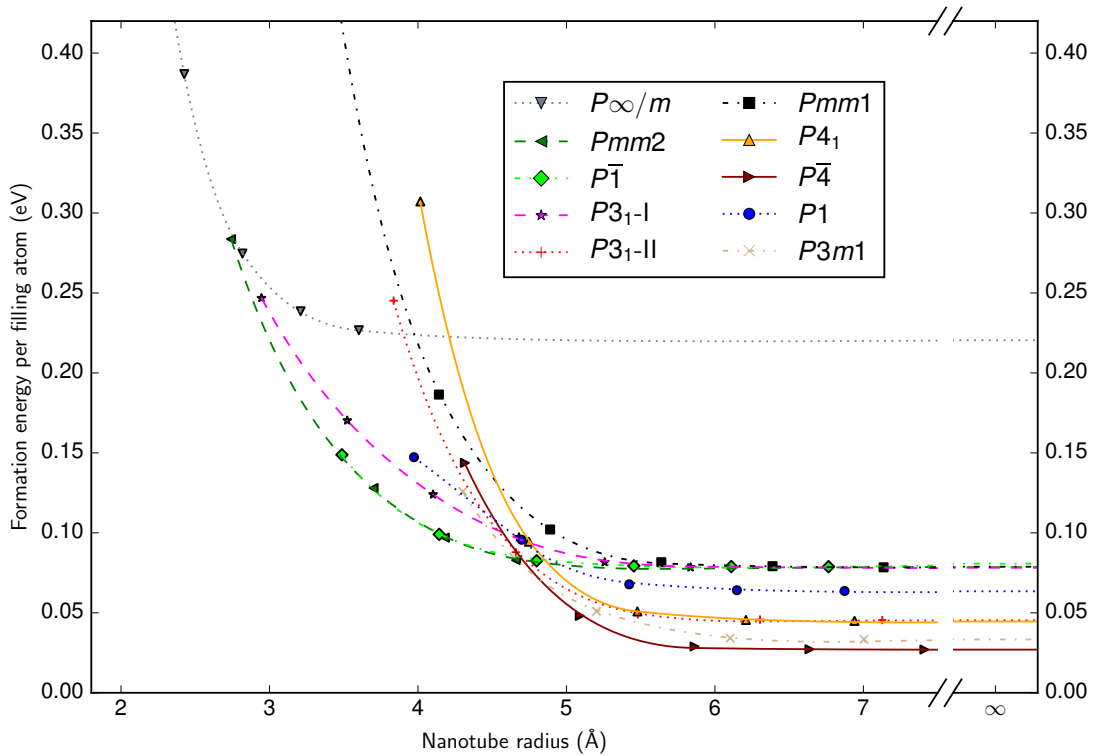


Figure 4.3 The phase diagram for encapsulated AgCl nanowires, recalculated within the implicit nanotube approximation.

The calculations that were used to obtain the dependence of the nanowires' equilibrium lengths on the radius of the nanotube present a useful opportunity to check the validity of the implicit nanotube approximation. Since they consist of geometry optimisations of each structure for multiple nanotube radii, one can extract the energy of each structure as a function of nanotube radius (whereas previously they were just used to extract the periodicity as a function of radius). This enables the construction of a phase diagram for the implicit nanotube, which is shown on fig. 4.3.

The most obvious difference between figs. 4.3 and 4.2 can be seen on the  $x$ -axis: the implicit nanotube phase diagram is essentially shifted to the left relative to the explicit phase diagram by about  $1 \text{ \AA}$ . For the purposes of structure searching, however, this is not a problem: a structure that would be identified as low-energy in the structure search at (say)  $5 \text{ \AA}$  if the radius of the implicit nanotube corresponded exactly to that of the explicit nanotube would instead be identified at  $4 \text{ \AA}$ . Thus the low-energy structures will still be found, and the final explicit nanotube phase diagram will look the same. (Note that this offset between the implicit and explicit nanotube radii

was taken into account when these calculations were used to choose the radii of the encapsulating nanotubes.)

Other than the shift in nanotube radius, the clearest discrepancy between the two phase diagrams is the lack of bonding minima in the implicit nanotube diagram, which is a result of the purely repulsive nature of the confining potential. The cause of the bonding minimum when the nanotube is taken into account explicitly is likely a mix of charge transfer between the nanowire and nanotube, and also a weak covalent bond between them. Overall, however, the agreement between the two phase diagrams is very good: the formation energy curves are very similar for every structure, and the sequence of phase transitions in the implicit phase diagram is largely a recapitulation of that seen in the explicit diagram, except at the point around  $5.7 \text{ \AA}$  at which many structures are energetically competitive. The similarity between these diagrams indicates that the implicit nanotube approximation is sufficiently accurate for the initial AIRSS search.

## 4.2 Raman spectroscopy

The Raman scattering behaviour of carbon nanotubes is quite well-understood, to the extent that the chiral vector of a nanotube can be quantitatively identified from its Raman spectrum [239]. However, the insertion of a nanowire into the tube will affect its Raman scattering behaviour, firstly by altering the frequencies of the modes associated with the tube, and secondly (assuming the nanowire structure has Raman-active modes) by introducing modes associated with the wire itself into the spectrum. Since the encapsulated nanowire will be of reduced symmetry compared to the tube on its own and the wire on its own, degeneracies in the phonon spectrum are likely to be lifted.

Studying the vibrational spectroscopy of encapsulated nanowires is useful not only because it provides a ‘fingerprint’ by which the structure can be confirmed experimentally, but also because it provides a probe of the coupling between the tube and the wire. For example, the extent to which inserting the wire generates an upshift in the RBM of the tube contains information about the level of physical interaction between the atoms in the tube and the atoms in the wire. SWNTs with different carbon isotope ratios – and, as a result, different G-band peak positions – have been used to perform

multicolour imaging of cancer cells by functionalising different kinds of SWNT with different ligand molecules and performing Raman spectroscopy [240]. Therefore, if the insertion of AgCl into nanotubes affects their Raman spectra, there are potential applications in biological imaging.

However, the extreme computational cost of *ab initio* Raman spectroscopy makes these calculations intractable in many cases, partly because of the large number of atoms involved and partly because of the symmetry-lowering effect of inserting a nanowire which means that fewer modes' Raman intensities can be known to be exactly zero by symmetry, without needing to calculate them explicitly. This means that Raman intensities must be calculated for many more modes than if calculations were performed for the tube and wire separately. It is likely because of this exceptional cost that no such calculations appear ever to have been performed previously for encapsulated nanowires; ref. [16] presents *ab initio* Raman calculations for HgTe ENWs, but neglects the nanotube entirely, and as a result is unable to predict the impact of the nanowire on the nanotube's spectrum or vice versa. It should also be noted that Raman spectroscopy is usually performed resonantly, i.e. with the laser energy tuned to correspond to the energy for an electronic transition. Under the standard DFT approach to theoretical Raman spectroscopy, such effects are generally neglected. While this produces some level of error in predicted peak intensities, those errors are generally small enough that one can still correctly identify using DFT which peaks will be the most prominent in a resonant Raman experiment.

### 4.2.1 Linear chains

Because of the computational expense involved, Raman calculations on encapsulated nanowires are limited to those materials which are commensurate with very short nanotubes. A search was performed for linear 1D chain nanowires made from various binary metal halides. In each case, the wire was optimised and its equilibrium length was checked against a pre-compiled database of possible nanotube lengths for a range of chiral vectors. Based on this search, AgCl was identified as a strong candidate because its diatomic 1D chain is commensurate (to within 4% strain) in its primitive cell with certain armchair CNTs. This means that a supercell need not be used, making Raman calculations potentially feasible.

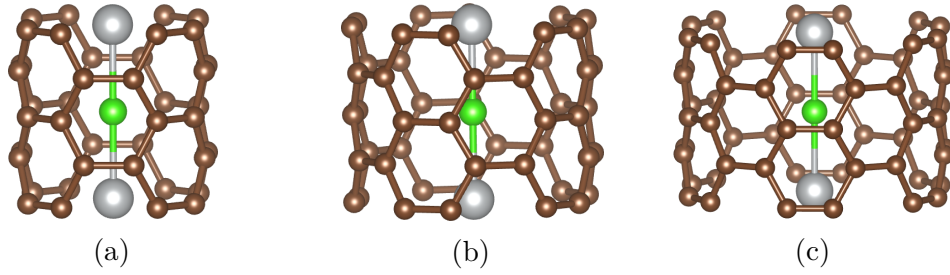


Figure 4.4 The three AgCl encapsulated nanowire systems on which Raman calculations were performed. From left to right, the nanotubes' chiral vectors are  $(4, 4)$ ,  $(5, 5)$  and  $(6, 6)$ .

A 1D linear chain of AgCl was inserted into three nanotubes with chiral vectors  $(4, 4)$ ,  $(5, 5)$  and  $(6, 6)$ . The resulting ENW structures are shown on fig. 4.4. Phonon calculations on these systems were performed using norm-conserving pseudopotentials at a plane-wave basis set cutoff of 900 eV and a  $1 \times 1 \times 8$  MP grid, corresponding (given the cell's length, for all three chiral vectors, of 4.93 Å in the periodic direction) to a spacing of  $0.025 \times 2\pi \text{Å}^{-1}$ . By repeating the phonon calculation once at a higher basis set cutoff and once at finer BZ sampling, the calculated phonon frequencies were all determined to be converged to within better than  $20 \text{cm}^{-1}$ . We are however interested primarily in differences in frequencies with and without an encapsulated nanowire inside, for which cancellation of errors will occur. The length of 4.93 Å was obtained by geometry optimising the nanotube on its own with the cell length allowed to vary so that the stress in the  $z$ -direction was at a minimum. The cell containing the encapsulated nanotube was then constrained to this length. This was done to get a better cancellation of the errors arising from wire-tube mismatch when relative differences in mode frequencies between the encapsulated and non-encapsulated case are considered.

After geometry optimising the structures on fig. 4.4 so that the forces on all the atoms were under  $1 \text{meV Å}^{-1}$ , phonon calculations were performed using the density functional perturbation theory (DFPT) scheme introduced by Gonze and Lee [102] as implemented for the generalised gradient approximation (GGA) by Refson *et al.* [99] as part of CASTEP. Using the calculated normal mode eigenvectors, Raman intensity calculations were also performed in CASTEP. For each of the three chiral vectors chosen, these calculations were repeated for the nanotube on its own as well. (For symmetry reasons, 1D diatomic chains are not Raman active and so the wire on its own has no Raman spectrum.) The result of these calculations is, for each of the

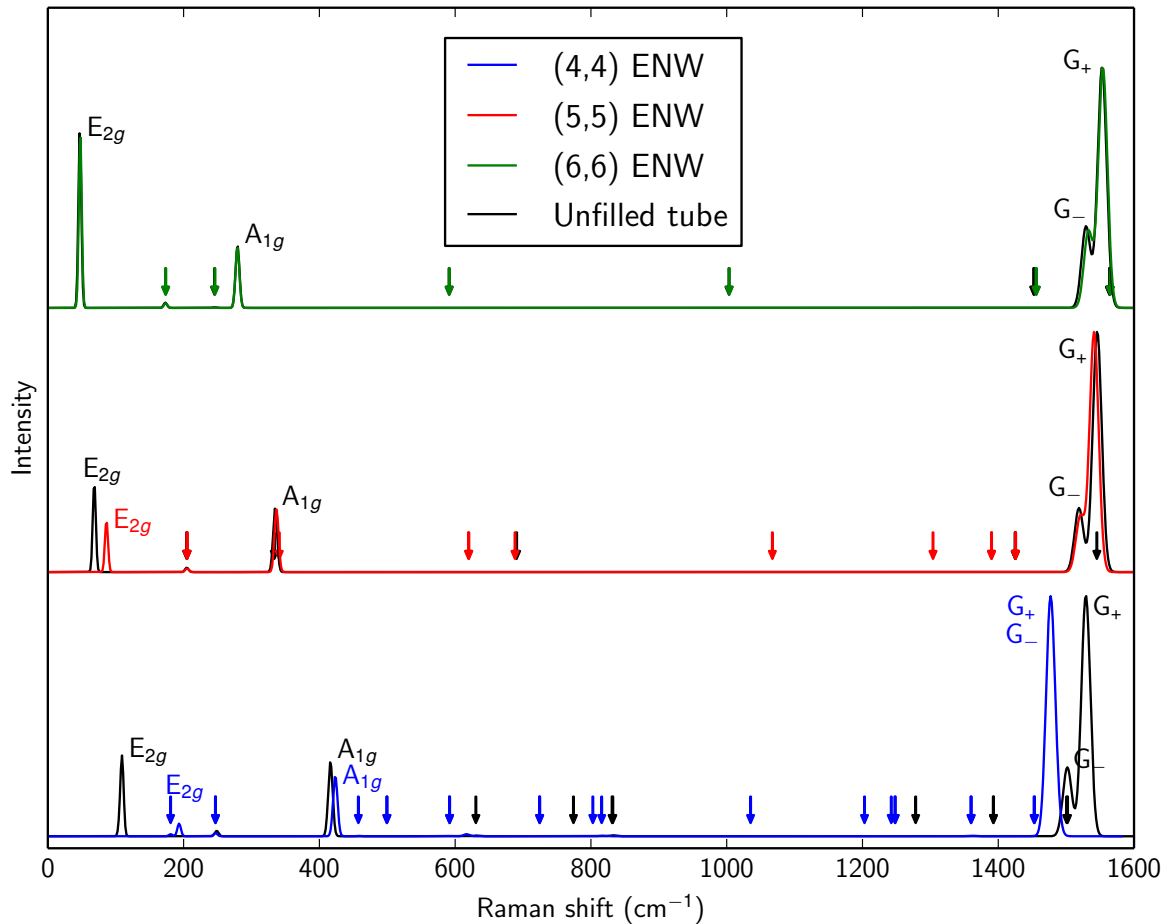


Figure 4.5 Raman spectra for linear 1D AgCl chains encapsulated within the three different sizes of nanotubes shown on fig. 4.4. The four most intense modes are labelled, with the colouring indicating whether the peak is in the spectrum of the filled or unfilled tube. Where a mode's frequency is almost unchanged between the filled and unfilled spectra, its symmetry label is annotated only once. Modes which are weakly Raman-active are identified with downward-pointing arrows.

three chiral vectors in which the calculations were performed, the Raman spectrum for both the filled and unfilled tube. Fig. 4.5 shows these spectra for each of the three chiralities.

At the lower end of the Raman spectra are the radial breathing modes, consisting of low-frequency, long-wavelength collective oscillations. In this case, the two most intense modes – the totally symmetric  $A_{1g}$  mode and the lower frequency  $E_{2g}$  mode – are annotated on fig. 4.5, and the eigenvectors are shown explicitly on fig. 4.6.

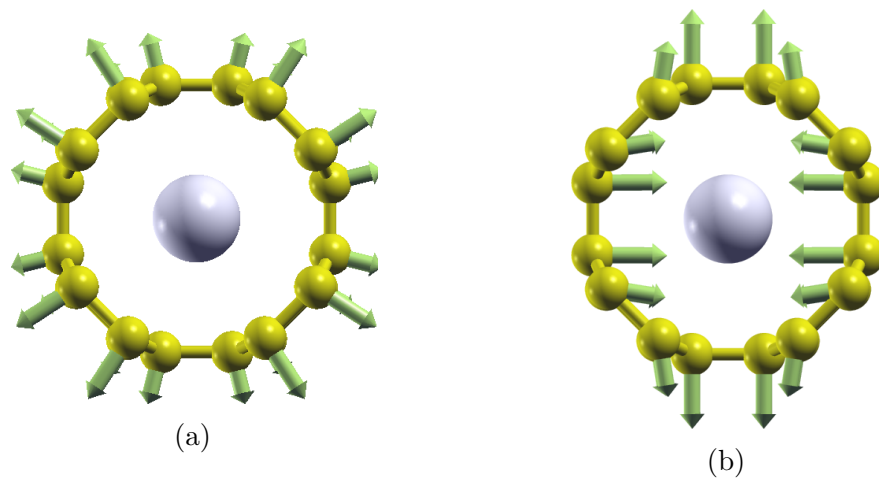


Figure 4.6 The two most Raman-intense low-frequency modes: the  $A_{1g}$  radial breathing mode (a) and the  $E_{2g}$  squash mode (b). The nanotube pictured is a (4,4) armchair tube.

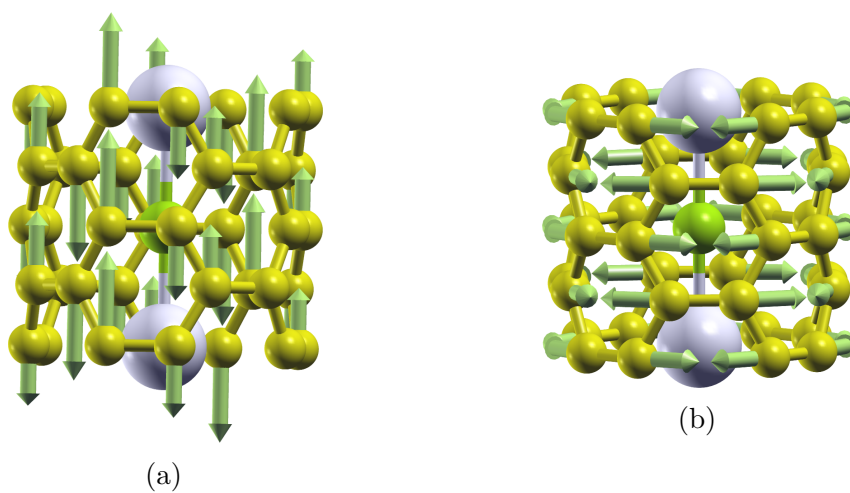


Figure 4.7 The two most Raman-intense modes in the G-band,  $G_-$  (a) and  $G_+$  (b), pictured for the (4,4) armchair tube.

At much higher frequencies is the G-band, arising from the oscillation of carbon-carbon bonds. Again, two modes stand out from the rest in intensity: these are known as the  $G_-$  and  $G_+$  modes [241], and both are shown on fig. 4.7.

A clear progression is apparent on fig. 4.5, from the spectrum of the relatively wide (6, 6) tube which is barely affected at all by the wire, to the (4, 4) case where there are large differences between the filled and unfilled case.

One can identify two primary mechanisms by which the nanotube affects the vibrational modes: the first is that inserting the nanowire affects the equilibrium structure, most notably by pushing the nanotube outwards, expanding its radius. The second is that it affects the energetic cost of perturbing the positions of the C atoms.

An example of the first kind of effect can be seen in the decrease in the G band frequencies. The two modes both decrease significantly in frequency, which might seem surprising given the G band consists of high-frequency C-C bond oscillations involving displacements along the tube wall rather than in the radial direction; it may seem that the presence of the tube should have no relevance to these modes. However, when the tube expands due to repulsion with the wire, the C-C bonds increase correspondingly in length, which reduces their natural frequency of oscillation. This also explains why the higher-frequency mode decreases more than the lower-frequency mode (leaving them, by coincidence, almost degenerate): the higher-frequency eigenvector's atomic displacements are strictly around the tube, whereas the atomic displacements of the lower-frequency mode have some nonzero components in the  $z$ -direction. Since the wire-induced expansion of the tube is almost exclusively a radial expansion (rather than a stretch along  $z$ ), bonds which are perpendicular to  $c$  expand the most. The higher frequency mode, since it consists of atomic displacements purely in the  $xy$  plane, therefore decreases the most in frequency. Another cause of the downshifting of the G-band frequencies is likely that of charge transfer from the nanotube to the nanowire. The resulting deficit of charge in the nanotube has the effect of softening the carbon-carbon bonds, and thereby suppresses the vibrational frequencies. This phenomenon of charge transfer causing a shift in the G-band frequencies has been observed experimentally [242, 243].

On the other hand, the RBM frequency shifts show the second kind of effect: because of the presence of the nanowire, the outward force induced by shrinking the tube inwards is higher than in the unfilled case. As a result, the radial breathing mode increases in

frequency for the filled tubes. (There is likely a competing effect from the lengthening of the bonds, working to *decrease* the RBM frequency, but this seems not to be the dominant factor since there is an increase overall.)

An exceptionally large frequency shift is visible for the lowest frequency Raman-active mode, the  $E_{2g}$  squash mode, which consists of an elliptical distortion of the tube. This mode almost doubles in frequency upon encapsulation in the (4, 4) tube. The mode is much lower in frequency because the ‘surface area’ of the tube is unchanged, so that – in contrast to the RBM – the bonds do not increase in length. The restoring force for the mode is therefore the restoring force due to the rotation of bond angles, which is much less than the resistance to changes in bond length. As a result, a significant contribution to the ‘spring constant’ for this mode comes from overlap with the tube, whereas the spring constant for the RBM is dominated by the cost of bond lengthening. The prospects for experimentally observing this mode in unfilled nanotubes are generally poor because it tends to be overwhelmed by the large Rayleigh scattering peak centred about the origin [239]. However, it may become observable in the filled case due to the large upward frequency shift which pushes it into areas where the signal-to-noise (i.e. Raman to Rayleigh scattering) ratio is better. The upshifts described here are sufficiently large as to be measurable with the  $\sim 1 \text{ cm}^{-1}$  resolutions achievable in modern Raman spectroscopy, so the results presented here provide a useful means of experimental verification that a linear 1D chain structure has been formed.

Noticeably more modes become weakly Raman-active as the tube radius decreases, as shown by the arrows on fig. 4.5, despite the fact that a decrease in radius means a decrease in the total number of normal modes since there are  $3N$  normal modes in an  $N$ -atom system. This is probably a consequence of the fact that the symmetry of the tube becomes increasingly broken as it interacts more with the wire; there is a small effect where the tube becomes slightly ‘moulded’ to the shape of the wire (or rather to its electron density), and this lifts symmetries that previously (i.e. in the unfilled case) caused matrix elements for some modes to be zero.

It should be noted that in practice Raman experiments are generally resonant, meaning that the wavelength of the laser corresponds to the energy for an electronic transition in the sample, which produces an enhancement of multiple orders of magnitude in the scattering intensity [244]. The theoretical approach used here is in principle valid only under the assumption that the scattering is non-resonant. However, the range of

variation in the predicted intensities of the Raman-active modes is extremely large, with the largest peaks several orders of magnitude larger than the smallest peaks. Because of this, the question of which of the peaks are the most intense remains largely unchanged in the resonant case. For this reason, fig. 4.5 is enough to qualitatively identify the most significant peaks observed in experimental spectra despite the fact that the underlying theory is, strictly speaking, valid only in the non-resonant case. There exist more sophisticated theoretical approaches using techniques from many-body theory to accurately compute the excitonic contributions to the Raman spectra associated with resonance [245], but due to their extreme computational cost they are not at all viable for the system sizes involved in these calculations.

### 4.2.2 Larger systems

In addition to the 1D linear chain, there is another AgCl structure with a primitive cell whose length is commensurate with the periodicity of a nanotube. Specifically, the  $P\bar{4}$  distorted rocksalt structure matches the nanotube's length to within 3% strain. This system is physically important because the  $P\bar{4}$  nanowire phase is predicted to be stable over a wide range of nanotube radii; additionally, the wire itself is Raman active whereas the 1D chains described previously are not. However, even though the nanowire's primitive cell is commensurate with the tube, the system size (64 atoms) is still too large for a Raman calculation to be viable on the full encapsulated nanowire system. A Raman calculation is viable for the tube on its own, and for the wire on its own, but not for the encapsulated nanowire. The primary reason for this (in addition to the smaller number of atoms in the component systems) is that there are no symmetries common to both the tube and the wire, so that the ENW has symmetry group  $P1$ . Symmetry plays an important role in reducing the computational expense of Raman intensity calculations: where multiple modes are symmetrically equivalent, a calculation on only one of them is required, and where a mode's Raman activity is zero by symmetry, the calculation for that mode can be avoided entirely. As a result, the lack of symmetry of the ENW structure makes a Raman calculation for that structure unreasonably expensive in terms of computational time.

In summary, the set of calculations that are computationally viable for this system is phonon calculations on the ENW, empty tube, and bare wire; and Raman calculations on the empty tube and the bare wire. This set of calculations gives the phonon mode

frequencies of the tube, wire and ENW, as well as the Raman spectra of the wire and tube. In this section a method is developed to use this information, together with Raman intensity calculations on a select few ENW phonon modes, to gain a close approximation to the Raman spectrum of the ENW. This is desirable because it provides a direct link with experiment without incurring the extreme computational cost that would follow from running a Raman calculation on the ENW directly.

The main assumption is that, in the ENW system, the tube and wire are sufficiently weakly coupled that each ENW mode corresponds to a particular mode either in the wire on its own or the tube on its own. Clearly this assumption is most justified in the limit where the tube is much larger than the wire and hardly interacts with it at all; and it will become unjustified in the limit where the tube is narrow and interacts very strongly with the wire.

Given this assumption, we must identify the correspondence between the modes in the ENW and those in the bare wire and empty tube. To do this, let  $D_{\text{ENW}}$  be the dynamical matrix (as defined in eq. 2.22) of the ENW. Further, let  $D_{\text{tube}}$  and  $D_{\text{wire}}$  be defined as the dynamical matrix of the tube on its own and the wire on its own. Now suppose we take the ENW and ‘switch off’ all interaction between the tube and the wire (and allow their geometries to relax accordingly). Having done this, the tube and wire are completely uncoupled and therefore the dynamical matrix of the ENW will be block-diagonal:

$$D_0 = \left( \begin{array}{c|c} D_{\text{wire}} & 0 \\ \hline 0 & D_{\text{tube}} \end{array} \right) \quad (4.1)$$

Because of its block-diagonal nature, the eigenvectors and eigenvalues of this matrix will simply be those of  $D_{\text{wire}}$  and  $D_{\text{tube}}$ , as one would expect of a dynamical matrix describing two non-interacting systems.

We now draw an analogy with quantum-mechanical perturbation theory, in which one writes  $H = H_0 + \lambda V$  to describe a system whose Hamiltonian was originally  $H_0$  being perturbed by some interaction  $V$ . Correspondingly, we now write

$$D = D_0 + \lambda(D_{\text{ENW}} - D_0). \quad (4.2)$$

Just as in the quantum-perturbative case,  $\lambda$  allows us to smoothly and continuously switch on and off the coupling between the tube and the wire. Setting  $\lambda = 0$  gives the block-diagonal, non-interacting case where  $D = D_0$ . Gradually increasing  $\lambda$  is

equivalent to switching on the interaction between the tube and the wire; off-diagonal elements coupling the wire to the tube appear and increase until  $\lambda = 1$  is reached, at which point  $D = D_{\text{ENW}}$  and the fully interacting case is recovered. The benefit of this perturbative treatment is that it allows us to rigorously identify a one-to-one mapping between the set of modes of the ENW and those of the separate tube and wire. (Note that for this process to work, the rows of  $D_{\text{ENW}}$  must be chosen so that both the  $i$ -th row or column of  $D_{\text{ENW}}$  and the  $i$ -th row or column of  $D_0$  correspond to the same Cartesian component of the same atom; in other words, the basis must match between the unperturbed and interacting dynamical matrices.)

To test this scheme, the previously discussed case of a 1D diatomic chain was used. This is a useful test system because it is small enough that the exact results are available (as shown in fig. 4.5).  $D_{\text{wire}}$ ,  $D_{\text{tube}}$  and  $D_{\text{ENW}}$  were extracted from the  $\Gamma$ -point phonon calculations previously performed on this system in the case of a (4,4) nanotube. Then  $D_0$  in eq. 4.2 was constructed, and  $\lambda$  was gradually varied from 0 to 1. At each value of  $\lambda$ ,  $D$  was calculated and diagonalised to find the phonon eigenvalues, and thereby the phonon modes were continuously tracked from the noninteracting  $\lambda = 0$  case to the fully interacting  $\lambda = 1$  case. This establishes a mapping between those modes of the tube alone and the wire alone ( $\lambda = 0$ ), and those of the encapsulated nanowire ( $\lambda = 1$ ). Using this mapping, we then approximate the Raman intensity of each mode in the encapsulated nanowire as being equal to that of its corresponding mode in the bare wire or unfilled tube. This generates an approximate set of Raman intensities for each mode of the encapsulated nanowire. This approximation is compared with the exact results which were shown in the previous section on fig. 4.8.

The comparison shown on fig. 4.8 is encouraging: without performing full Raman calculations on the encapsulated nanowire, the method is able to identify the mapping between the non-interacting modes and the interacting modes, and hence predict the locations and approximate intensities of the most significant peaks in the Raman spectrum. The small discrepancies in the peak intensities between the exact calculation and our approximation scheme are not a significant problem, since even without using the approximation scheme, the theoretical modelling of Raman intensities within ordinary DFT can only be expected to qualitatively identify the main peaks in the spectrum, especially in the resonant case. Note that the chosen (4,4) encapsulated nanowire can be expected to provide an especially stringent test of our scheme, since its narrow radius causes a very strong interaction between the tube and the wire,

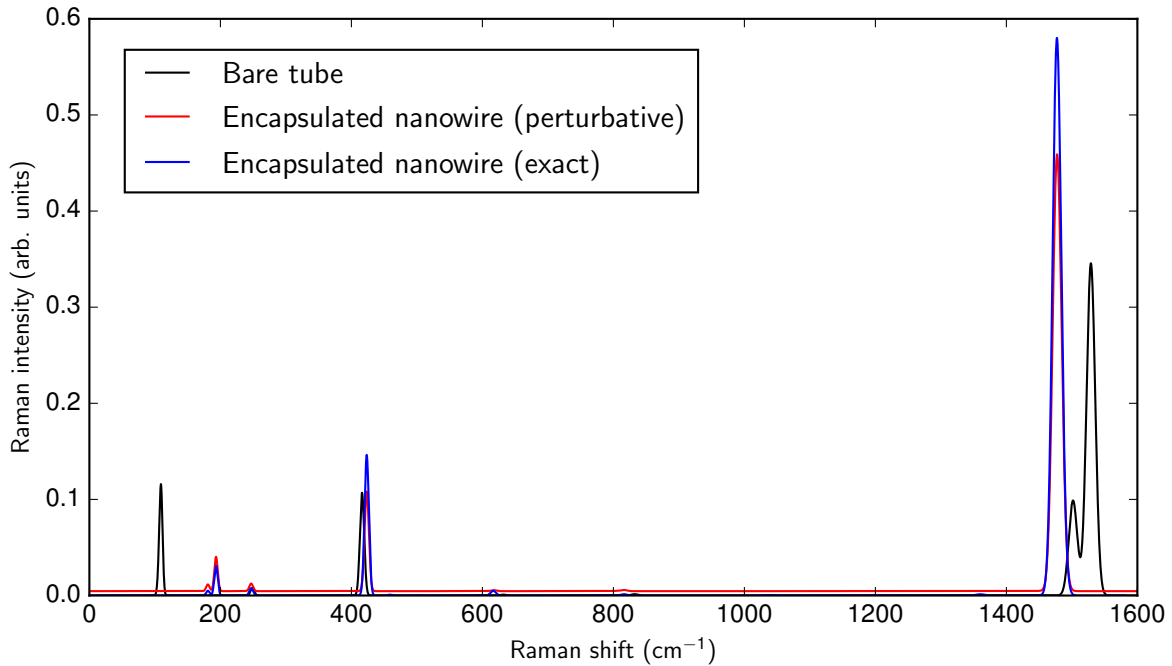


Figure 4.8 A comparison between the prediction of the interpolative scheme for the calculation of Raman spectra introduced here (red) and the exact DFT calculation within CASTEP (blue), using the  $P\bar{4}$  nanowire encapsulated inside the (4, 4) carbon nanotube whose spectrum is shown on fig. 4.5. The predicted spectrum is shifted vertically upwards slightly for clarity. There are no Raman-active modes in the bare nanowire, so the only ‘unperturbed’ spectrum that can be shown is that of the tube (black).

leading to a greater change in the modes’ Raman intensities and more pronounced mixing of the normal mode eigenvectors in the ENW with respect to the noninteracting basis.

Having validated the scheme, we return to the case of the  $P\bar{4}$  nanowire under consideration.  $D_{\text{wire}}$ ,  $D_{\text{tube}}$  and  $D_{\text{ENW}}$  were calculated in  $\Gamma$ -point phonon calculations on the three respective systems. By applying the methodology just described, the phonon modes were tracked from the noninteracting case to the interacting case; the variation of the mode frequencies with  $\lambda$  is shown on fig. 4.9.

Thus far, each ENW normal mode’s Raman intensity has been approximated as that of the corresponding mode in the bare wire or unfilled tube. However, it may sometimes be feasible to calculate (non-resonantly) the intensity of just the few strongest peaks in the spectrum. This is particularly relevant in low-symmetry cases where very few of those modes’ intensities can be identified as being zero by symmetry without needing

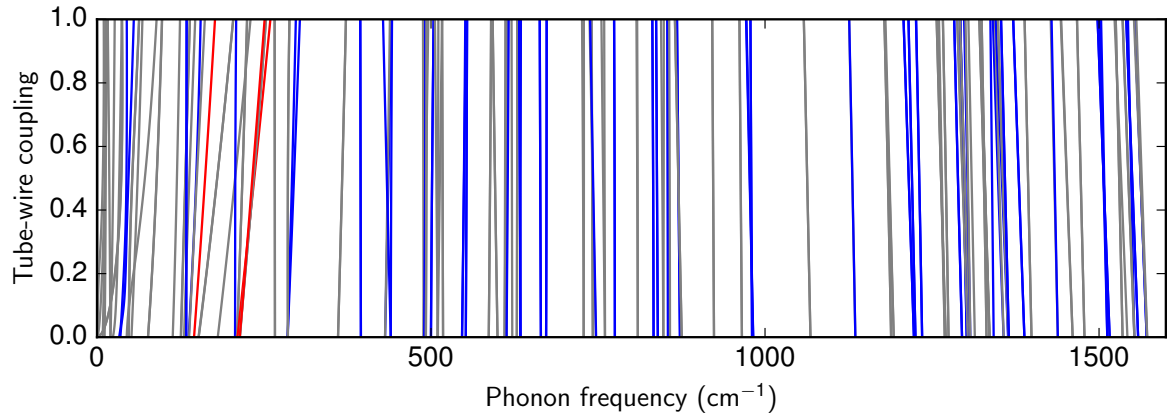


Figure 4.9 The variation in the phonon mode frequencies of the encapsulated  $P\bar{4}$  nanowire as the tube-wire coupling  $\lambda$  runs from 0 (the non-interacting case) to 1 (the fully interacting case). Modes which are Raman-active in the bare wire and the unfilled tube are shown in red and blue, respectively; non-Raman active modes are shown in grey.

to explicitly calculate them, leading to a large number of very weakly Raman-active modes and a few strongly Raman-active ones. Based on the Raman calculations on the bare wire and the unfilled tube, eight modes were identified in the  $P\bar{4}$  structure (four in the wire and four in the tube) which are much more Raman-intense than all others, and therefore are likely to be the dominant features in the ENW Raman spectrum. The previously described dynamical matrix interpolation method was used to find the modes in the ENW which correspond to these (the mapping is shown on fig. 4.9), and perform Raman intensity calculations on these modes only. For those ENW modes whose Raman intensity was nonzero but small, the Raman intensity was approximated as that of the corresponding modes in the noninteracting case (i.e. the empty nanotube or bare nanowire) without recalculating them, since these modes do not contribute significantly to the Raman spectrum. This scheme means that the most salient features of the ENW Raman spectrum can be accurately described with feasible amounts of computational expense. The resulting Raman spectrum is shown on fig. 4.10, and as in the linear chain case indicates significant shifts in the radial breathing modes and G-band; this suggests a commonality in the way in which different nanowire phases affect the Raman spectrum of the encapsulating nanotube. Note that unlike the linear chain, the  $P\bar{4}$  nanowire phase is itself Raman-active.

There are in principle simpler methods for identifying the mapping of the vibrational modes between the non-interacting and interacting case, but these were tested and

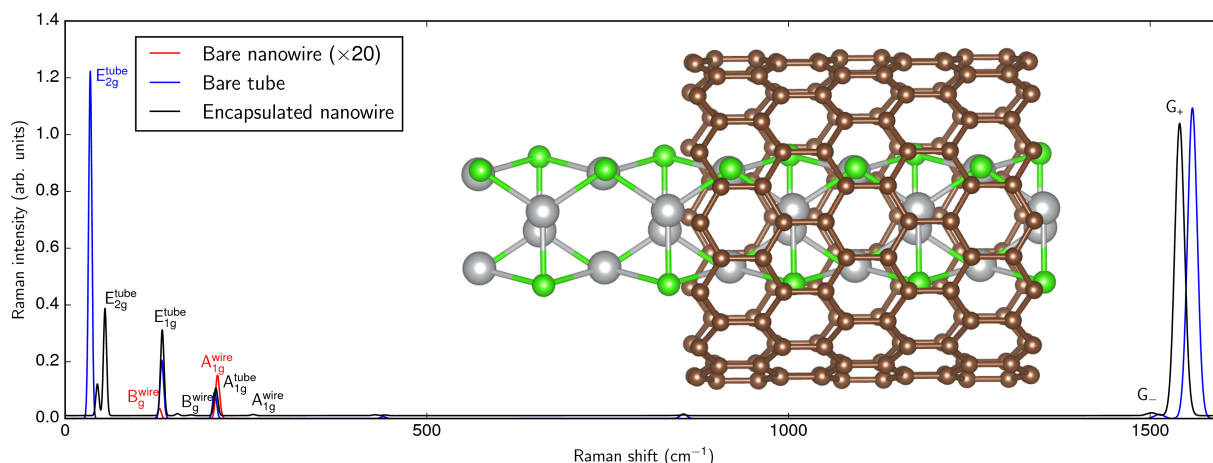


Figure 4.10 The Raman spectrum of the  $P\bar{4}$  encapsulated nanowire structure, predicted using the perturbative scheme described in this chapter. Plotted along with it are the spectra of the empty tube and bare nanowire. The encapsulated structure is also displayed, with a cut-through showing the wire only.

found them to be inadequate. The simplest scheme would be to simply compare the vibrational frequencies in the interacting and noninteracting case and pair them up in increasing order of frequency. However, this scheme fails if there are any cases of ‘band crossings’ in which the frequency ordering of modes changes as one switches on the interaction. Inspection of fig. 4.9 reveals that this is a fairly common occurrence. As a result, this method is insufficient. A better scheme would be to compare the cosine similarity of eigenvectors in the noninteracting and interacting cases and match them accordingly; however, this method was tested on the  $P\bar{4}$  ENW considered in this section and was found to perform poorly, with 40.6% of the 192 vibrational modes matched incorrectly. Such a method would therefore likely be adequate only for the very weakest of perturbations. Given this, to reliably match up the modes between the interacting and noninteracting cases (and, therefore, to calculate approximate Raman spectra for large systems) one needs a physically reasonable way to smoothly interpolate between them, which the scheme outlined here provides.

The size of the efficiency savings provided by the interpolation method used in this section to obtain the  $P\bar{4}$  ENW’s Raman spectrum were estimated using the time taken for each of the calculations. Due to the lowering of symmetry upon encapsulation, all of the ENW’s  $3N = 192$  vibrational modes other than its three acoustic modes are Raman-active to some extent. However, using the interpolation scheme, just 8 modes with significant Raman intensities were identified. The method therefore represents a

saving in computational cost of around 96% in calculating the ENW's Raman spectrum, relative to doing so by brute force (around 645 core-hours using the interpolative scheme compared to 15,498 core-hours that would have been necessary for the brute force calculation), with only a small decrease in accuracy. If the Raman spectra of the empty nanotube and bare nanowire are not already calculated, the total saving is around 82%. This latter figure is the saving in calculating explicitly the Raman spectra of the empty nanotube and bare nanowire and then using the scheme described here to calculate the spectrum of the ENW, as compared to calculating all three spectra explicitly.

### 4.2.3 Double-walled nanotubes

There exist experimental data on the Raman spectrum of AgCl encapsulated inside a double-walled nanotube (DWNT) [233]. Here we consider this in the particular case of a linear chain AgCl nanowire inside a DWNT of (5, 5) and (10, 10) chirality (for the inner and outer nanotubes respectively), as shown on fig. 4.11. This presents another case in which the system under consideration is too large to perform a Raman calculation on. However, the scheme once again allows us to approximate its Raman spectrum nevertheless. This was done by decomposing the system into three weakly interacting subsystems: the outer wall of the DWNT, the inner wall of the DWNT, and the nanowire itself. Then the same procedure as outlined in the previous section was followed, with the sole difference being that the non-interacting dynamical matrix  $D_0$ , which was previously  $2 \times 2$  block-diagonal as in eq. 4.1, now becomes  $3 \times 3$ :

$$D_0 = \left( \begin{array}{c|cc} D_{\text{wire}} & 0 & 0 \\ \hline 0 & D_{\text{tube}}^{\text{inner}} & 0 \\ \hline 0 & 0 & D_{\text{tube}}^{\text{outer}} \end{array} \right) \quad (4.3)$$

where  $D_{\text{tube}}^{\text{inner}}$  and  $D_{\text{tube}}^{\text{outer}}$  represent the inner and outer nanotubes' dynamical matrices respectively. Phonon and Raman calculations were carried out on the bare wire, the inner nanotube on its own, and the outer nanotube on its own, and from these,  $D_0$  was constructed; then, as before, the interacting dynamical matrix  $D_{\text{ENW}}$  was extracted from a phonon calculation on the full system, and by interpolating between  $D_0$  and  $D_{\text{ENW}}$  the modes in the noninteracting case were mapped onto those of the interacting system. In section 4.2.2 the most strongly Raman-active modes were then identified and Raman intensities were recalculated; however, due to the large size of this system's cell

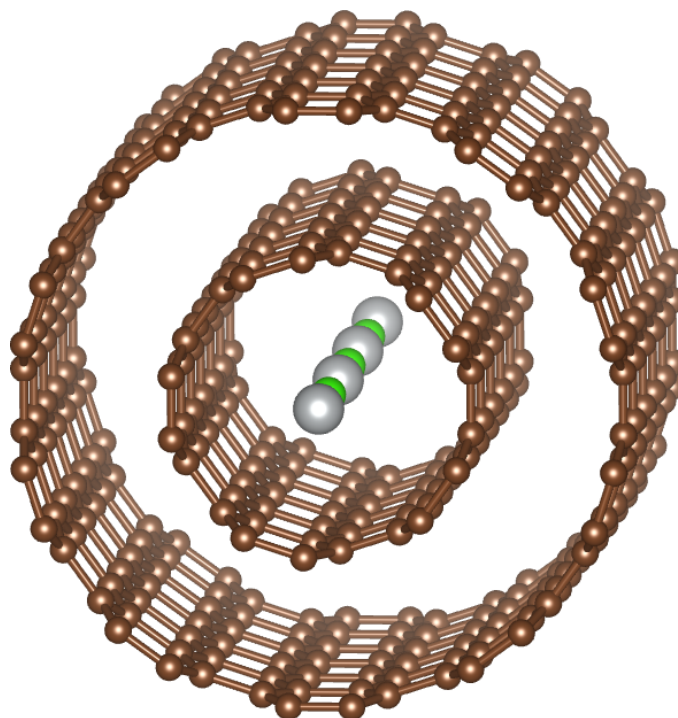


Figure 4.11 End-on view of an AgCl linear chain inside a DWNT of inner and outer chirality (5, 5) and (10, 10) respectively. Note that this is a supercell showing three repeats along the periodic direction.

(122 atoms), this would be extremely expensive. Instead, the ENW modes' intensities were approximated as the same as those of the corresponding modes in the bare wire or empty tube, as was nearly the case on fig. 4.10. (Note that the height of a mode's peak on the spectrum may vary between the non-interacting and interacting cases even if its intensity is the same, since the Raman scattering cross section contains terms dependent explicitly on a mode's frequency as well as on its Raman intensity.)

In order to study the effects of filling the nanotube, a phonon calculation was performed on the empty DWNT and the interpolative scheme was applied once again, using the dynamical matrices of the inner and outer tubes on their own as starting points for the interpolation. The resulting Raman spectra are shown on fig. 4.12. This allows one to examine how the vibrational spectrum of the DWNT compares to those of its component nanotubes on their own; additionally, it shows how filling the DWNT affects its vibrational properties. In general, vibrational modes associated with the outer tube are seen to fall in frequency, while those associated with the inner tube increase.

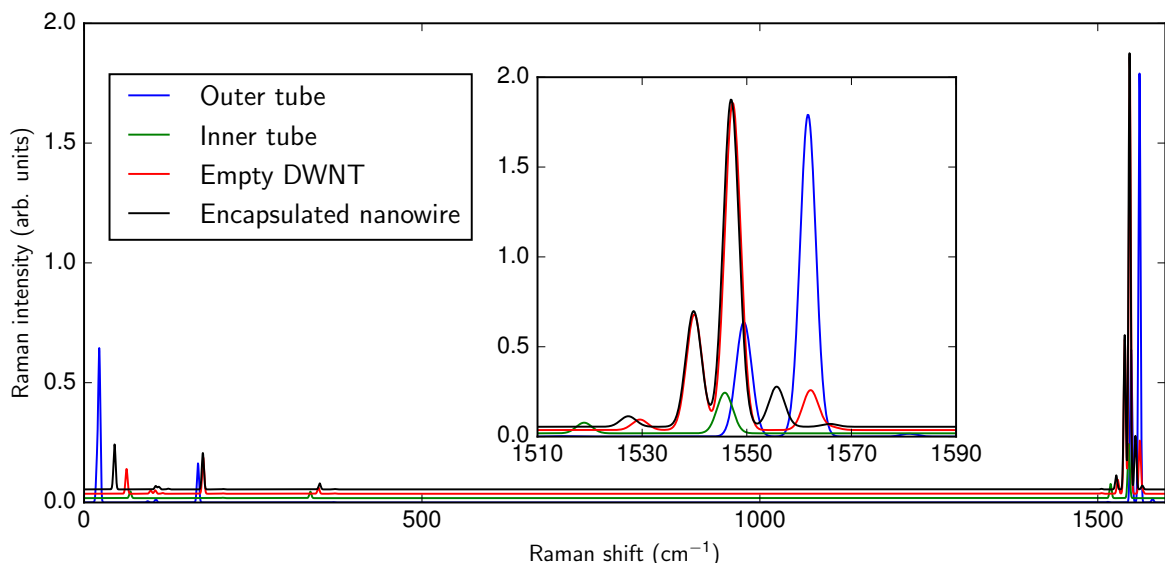


Figure 4.12 Raman spectra for a linear chain encapsulated inside a (5,5) and (10,10) DWNT. The inset shows the G-band.

Changes in the G-band modes observed on fig. 4.12 can be explained by considering the nanotubes' radii, which are shown for the three cases considered here in table 4.2. The outer (10,10) nanotube is found to be significantly wider when forming the outer wall of the DWNT than as a SWNT on its own, and widens slightly more when the nanotube is inserted; On the other hand, the inner (5,5) nanotube shrinks when going from SWNT to DWNT, but then expands when the nanotube is inserted. In each case, when one of the nanotubes shrinks its G-band modes are seen on fig. 4.12 to increase in frequency, and vice versa. This is because the vibrational modes in the G-band consist of carbon-carbon bond vibrations, with no components in the radial direction; their frequencies are therefore primarily determined by the radius of the nanotube, since that is proportional to the C-C bond lengths. Since different nanowire structures affect the nanotube's radius in different ways, this suggests that the G-band could function as a useful experimental diagnostic for identifying which nanowire structure is forming inside a nanotube (whether single- or double-walled). The variation in the lower-frequency vibrational modes is less simple, since they consist of soft, collective motions with significant radial components, and therefore are affected more sensitively by the presence of the other nanotube and the nanowire.

It is difficult to meaningfully compare these results with the experimental data of Chen *et al.* [233], firstly because in this work four significant peaks were identified in the

	Bare nanotube	Unfilled DWNT	Filled DWNT
(5,5)	3.439	3.426	3.431
(10,10)	6.823	6.850	6.851

Table 4.2 Relaxed nanotube radii in Å for three cases: as single-walled nanotubes, as a double-walled nanotube, and as a double-walled nanotube filled with an AgCl chain. In each case the radii of both the inner and outer nanotubes of the DWNT are shown.

G-band whereas they fit the sum of three Gaussians to their spectra, secondly because their nanowires and nanotubes are significantly wider than those considered here, and thirdly the linewidths in their spectra are quite large, making it difficult to pick out contributions from individual modes.

### 4.3 Conclusion

In this chapter the AIRSS method for ENWs has been used to identify the low-energy structures of AgCl encapsulated nanowires, resulting in the identification of a number of novel structures.

For two of these new structures, their Raman spectra have been predicted, and the way in which the interaction between the nanotube and nanowire affects their Raman spectrum has been calculated. Observed shifts in the normal mode frequencies have been rationalised in terms of the bonding and geometry of the system. Firstly, DFT Raman calculations have shown how the insertion of a linear AgCl chain affects the vibrational properties of a single-walled nanotube, and how their interaction varies as a function of the radius of the encapsulating nanotube. Secondly, the encapsulation of the  $P\bar{4}$  structure in both single- and double-walled nanotubes has also been considered. To assist with this case, a novel scheme for the approximate prediction of Raman spectra in systems for which an explicit calculation would be computationally intractable has been developed and applied.

Applying the approximation scheme to calculate the Raman spectra of encapsulated AgCl nanowires inside carbon nanotubes has provided a sensitive, experimentally testable probe of their structures; moreover, the generality of the method means that it is applicable to other encapsulated nanowire systems as well, and more generally to

other systems which can be decomposed into multiple weakly interacting subsystems, such as layered structures.



# Chapter 5

## Encapsulated MoSe<sub>2</sub> nanowires and elasticity

Transition metal dichalcogenides (TMDCs) are interesting materials due in part to their propensity to form layered structures. In such structures, the stoichiometry is  $\text{MX}_2$  where M is the transition metal and X is the chalcogen, with the chalcogen atoms sitting at the top and bottom of the layer and providing interlayer bonding [246]. The structure of the TMDC MoSe<sub>2</sub> is shown on fig. 5.1.

Due to the weakness of the interlayer bonding within TMDCs, they can be readily exfoliated to produce monolayers [247], with important applications in nanotechnology: single-layer MoS<sub>2</sub> transistors have been produced, for example [248]. Other applications include photodetectors and electroluminescent devices (which emit light in response to electrical current) [249], as well as photoluminescent devices [250].

In this chapter, nanowires formed by the TMDC molybdenum diselenide (MoSe<sub>2</sub>) are considered. Nanowires of the 1:1 stoichiometry MoSe (in which the system becomes metallic) have previously been studied theoretically [251, 252], but here the 2:1 stoichiometry which is found in the bulk is studied. Such MoSe<sub>2</sub> nanowires have been synthesised experimentally, although at larger radii (4 nm to 5 nm) than considered here [253].

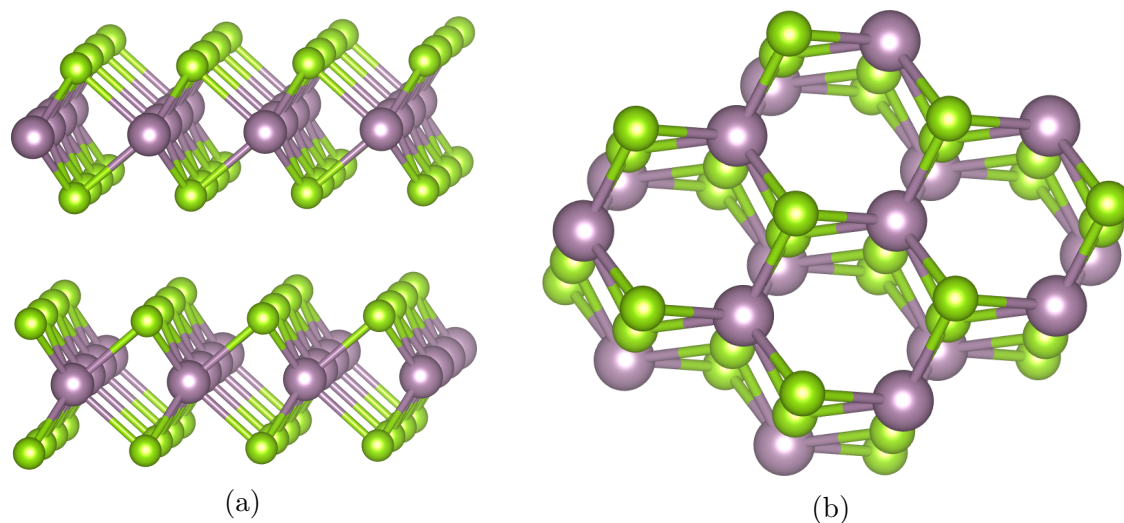


Figure 5.1 The layered structure formed by MoSe<sub>2</sub>. (a) shows a side view showing two layers from the side, and (b) shows a view from the top, revealing the hexagonal nature of each layer's structure.

## 5.1 Structure search

Once again, a structure search was performed using the method described previously in section 2.9, with implicit nanotube radii up to at most 7.4 Å. A plane wave cut-off energy of 300 eV was used, together with a  $k$ -point sampling density of no worse than  $0.04 \times 2\pi \text{ \AA}^{-1}$ . The Mo pseudopotential treated the 4s, 4p, 4d and 5s electrons as valence and all others as core. The Se pseudopotential treated the 3d, 4s and 4p as valence. Convergence tests were performed with respect to both  $k$ -point sampling density and plane wave cut-off energy, and suggested that the per-atom error in formation energies associated with the truncation of the plane wave basis set is around 10 meV, and that the corresponding error associated with the  $k$ -point sampling is around 2 meV.

The structure search generated 2113 geometry-optimised nanowire structures in total. As before, the most promising of these at each nanotube radius were selected for further study. Each of them was re-optimised in a range of explicit nanotubes of different radii, with energetic strain corrections applied as in chapter 3. Different Mo and Se pseudopotentials were used in the re-optimisations which were harder than those used for the AIRSS search (but which pseudised the same orbitals). A higher basis set cut-off of 500 eV was used, along with a finer Brillouin zone sampling of better than  $0.0325 \times 2\pi \text{ \AA}^{-1}$ .

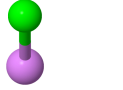
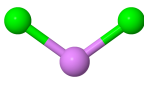
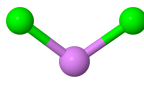
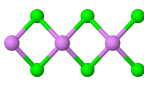
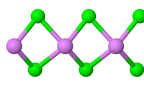
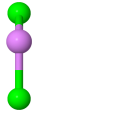
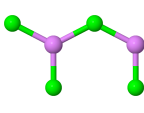
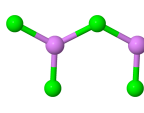
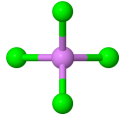
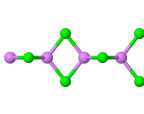
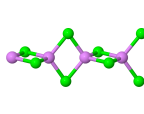
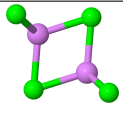
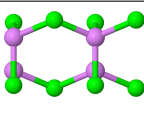
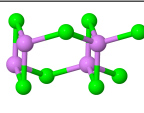
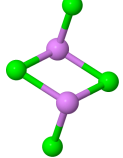
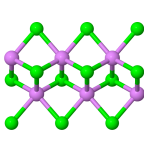
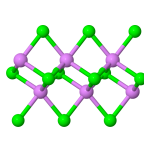
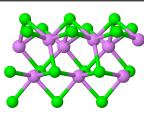
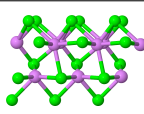
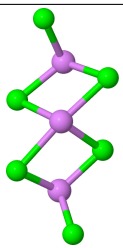
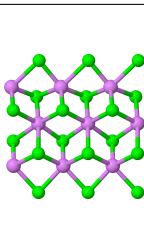
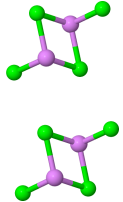
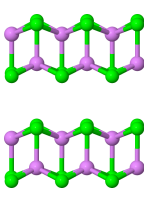
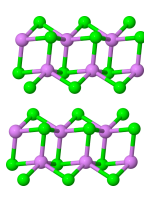
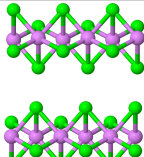
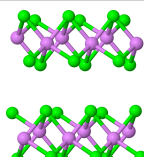
Structure	End-on view	Side-on view	3D view
$P11m$ (Molecule-like)			
$Pm2m$ -I (Zigzag)			
$Pm2m$ -II (Half-ladder)			
$P\bar{4}mm$ (Alternating zigzag)			
$P112/m$ (Chain)			
$Pm$ -I (Narrow layer)			
$P3_2$ (Triangular)			
$P1$ (Wide layer)			
$Pm$ -II (Bonded double layer)			
$P\bar{1}$ (Double layer)			

Table 5.1 All  $\text{MoSe}_2$  filling structures shown on fig. 5.2, ordered by their width. Pairs of structures with the same symmetry are distinguished by appending a number in Roman numerals (e.g.  $Pm2m$ -I and  $Pm2m$ -II).

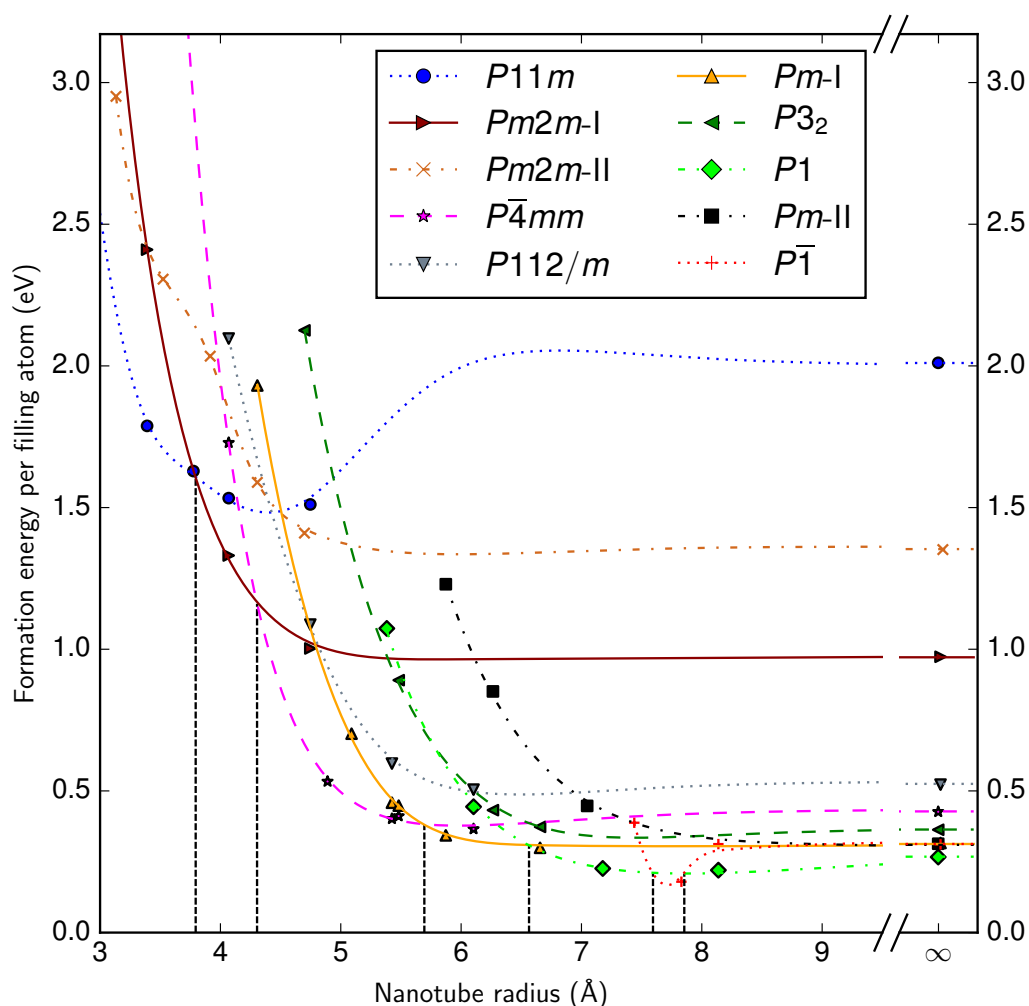


Figure 5.2 The variation in the formation energy of the lowest-energy MoSe<sub>2</sub> nanowire structures identified by the AIRSS search as a function of the nanotube radius.

The phase diagram resulting from the polishing calculations is shown on fig. 5.2, and the filling structures featured on the phase diagram are shown on table 5.1. Perhaps the most obvious feature of the phase diagram is the unusually deep bonding minima, most notably in the case of the  $P11m$  phase. At around 0.5 eV per filling atom (expressed as the difference between the minimum and the point at  $R = \infty$ ), this is an exceptionally strong bond between the nanowire and the nanotube. By contrast, the deepest tube-wire bonding minima in the previously considered cases of GeTe and AgCl nanowires were around an order of magnitude shallower in both cases.

To investigate the cause of this exceptionally strong attraction between the nanowire and the nanotube, the band structure of a  $P11m$  ENW was calculated. A (6,6)

nanotube was chosen to encapsulate the nanowire, since its radius of 4.07 Å is near to the bonding minimum, where whatever effects drive the apparent attraction between the nanowire and the nanotube are likely to be at their strongest. The band structure was calculated by solving the Kohn-Sham equations self-consistently on a  $1 \times 1 \times 5$  Monkhorst-Pack grid, and then – using the resulting electron density – solving them non-self-consistently on a  $1 \times 1 \times 101$  grid. This gives an extremely fine sampling of the band structure.

After calculating the band structure, the density of states was computed using the OptaDOS code [254, 255], which generates densities of states (and other spectral properties) from the output of CASTEP calculations. When converting from the discrete set of energy eigenvalues generated by the DFT calculation to a continuous density of states, one generally applies a Gaussian broadening scheme in which a Gaussian of some arbitrary width is placed at the location (in energy space) of each eigenvalue. However, this can be problematic when dealing with sharply peaked features such as van Hove singularities, which in 1D systems arise whenever a band flattens out. OptaDOS’ adaptive broadening [256] functionality was therefore used, in which the width of the Gaussian is proportional to the gradient of the associated band. This leads to a DOS which retains most of the sharpness of van Hove singularities, without becoming excessively jagged elsewhere.

In addition to the total density of states, projected densities of states were also calculated. In this case the overlap integrals between each Kohn-Sham state and a basis of atomic orbitals (or rather linear combinations thereof) are calculated, enabling the density of states to be resolved into different angular momentum channels.

The resulting band structures and densities of states are shown for the (6,6) nanotube on fig. 5.3 and for the ENW on fig. 5.4. Strikingly, comparison of the two band structures reveals that the encapsulation of the nanowire opens up a band gap in the nanotube which was previously conducting. In monolayer MoSe<sub>2</sub>, the states in the vicinity of the Fermi level,  $\mu$ , are of predominantly Mo *d*-like character, mixed with some Se *p* character (with analogous results applying to related TMDCs such as MoS<sub>2</sub> and WSe<sub>2</sub>) [257]. However, in this case the band structure indicates that in states close to  $\mu$  there exists a significant amount of mixing between Mo *d* and C *p* orbitals.

This supposition is confirmed by inspecting the Kohn-Sham wavefunctions in the vicinity of the Fermi level, which are shown at  $\Gamma$  on fig. 5.5. The wavefunctions were

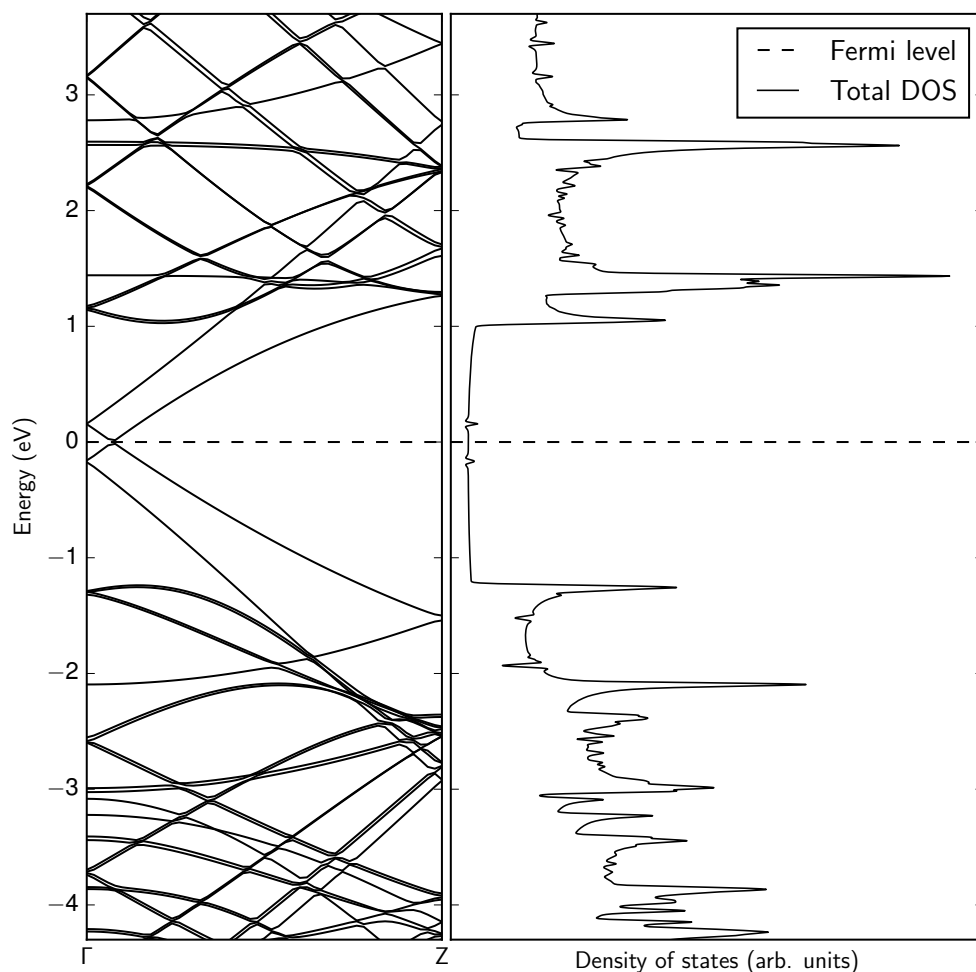


Figure 5.3 The band structure and electronic density of states of a (6,6) carbon nanotube.

extracted from a CASTEP checkpoint file using the program C2x [258]. One can see clearly the hybridisation between the Mo 4*d* orbitals and the  $\pi$  bonds formed between nearby carbon atoms in the tube wall. By inspection of fig. 5.5, the Molybdenum wavefunctions shown may be identified as  $d_{z^2}$  (a),  $d_{xz}$  (b),  $d_{yz}$  (c), and  $d_{z^2-x^2}$  (d). (Note that here the standard convention has been used in which the  $z$ -axis is aligned with the lobes of the  $m = 0$  orbital, in contrast to the convention used elsewhere in this thesis in which the  $z$  axis runs along the periodic direction. Here the periodic direction is chosen to correspond to the  $y$ -axis instead.)

One possible alternative explanation for the emergence of a band gap upon encapsulation is that the structure of the tube inevitably warps somewhat in response to the filling. As such, it could be that the band gap is the result of a ‘mechanical’ interaction with

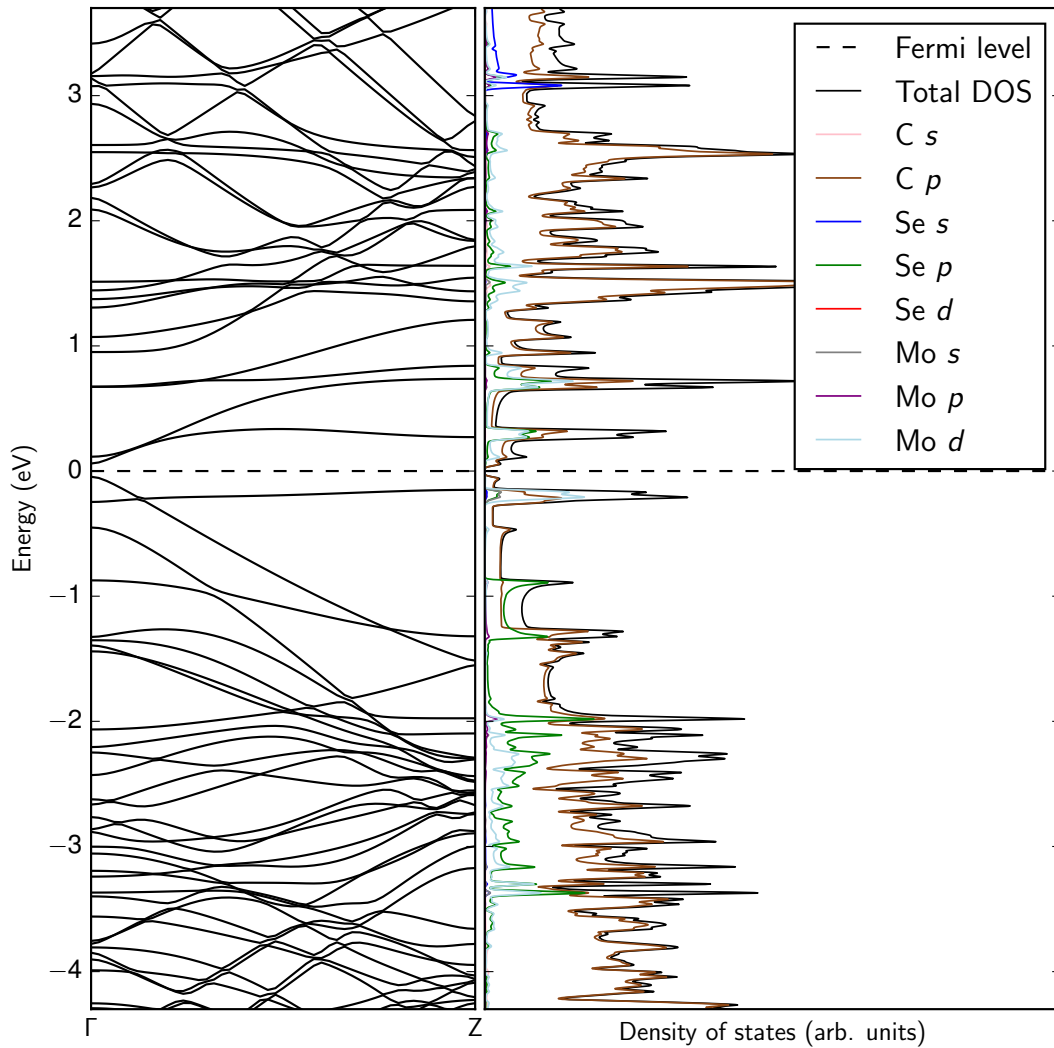


Figure 5.4 The band structure and electronic density of states of an encapsulated  $P11m$   $\text{MoSe}_2$  nanowire structure.

the filling rather than a ‘chemical’ one, with the band structure shifting due to the change in the atomic structure of the nanotube. To test this hypothesis, the density of states calculations were repeated with the nanowire atoms removed, but with the nanotube atoms frozen in the positions they adopt in response to the insertion of the nanowire, rather than allowed to relax back to their equilibrium state. Although such a structure is not mechanically stable, it does provide a test of the origin of the ENW’s band gap. The calculations indicated that no gap was present, which confirms that the band gap is a direct result of the bonding between the nanowire and the nanotube

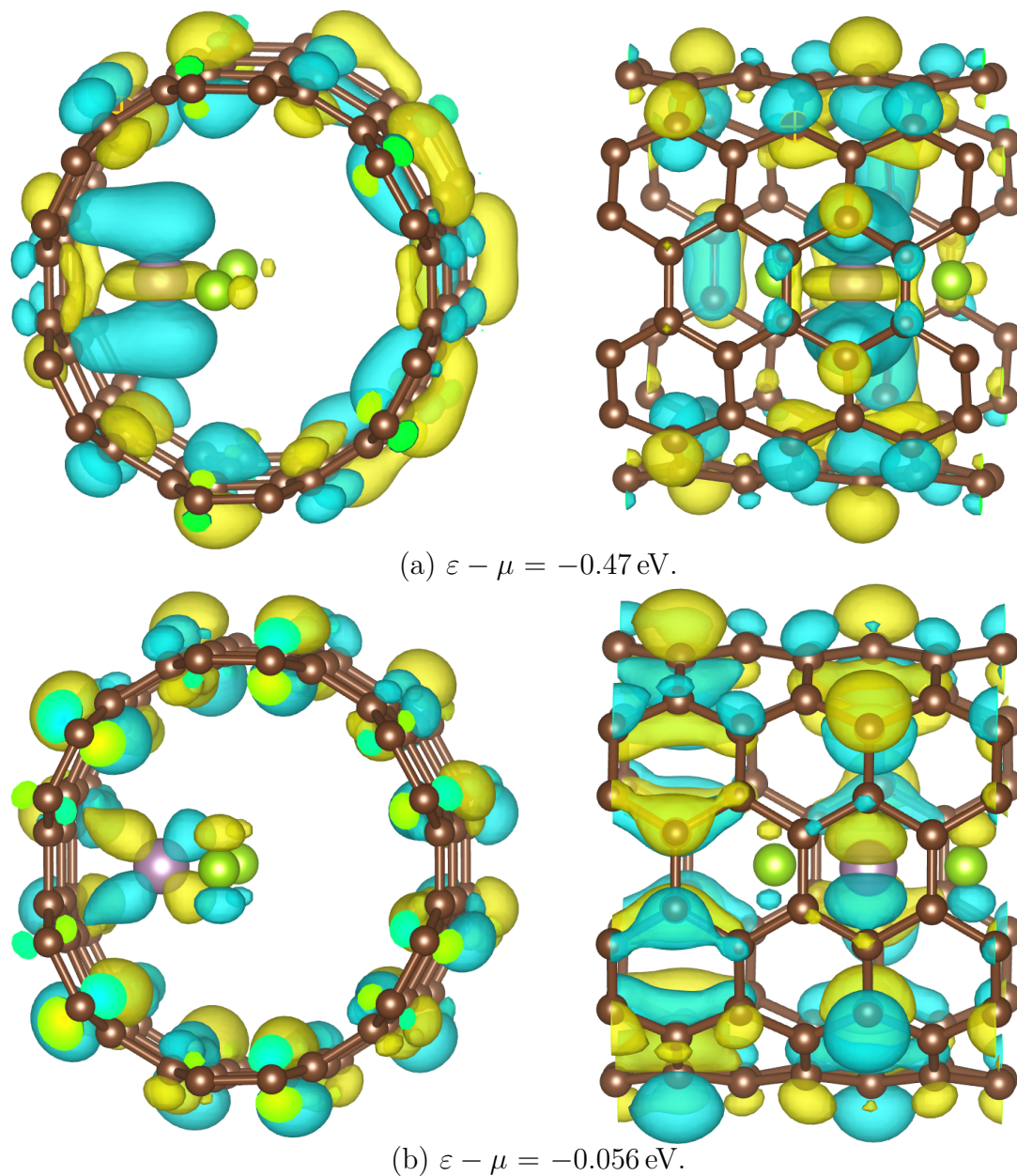
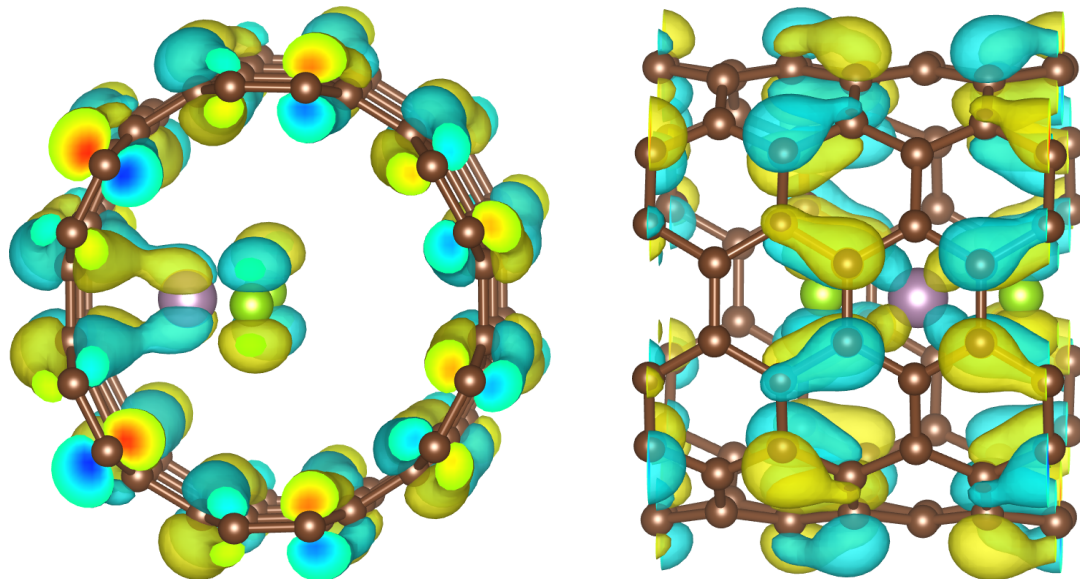
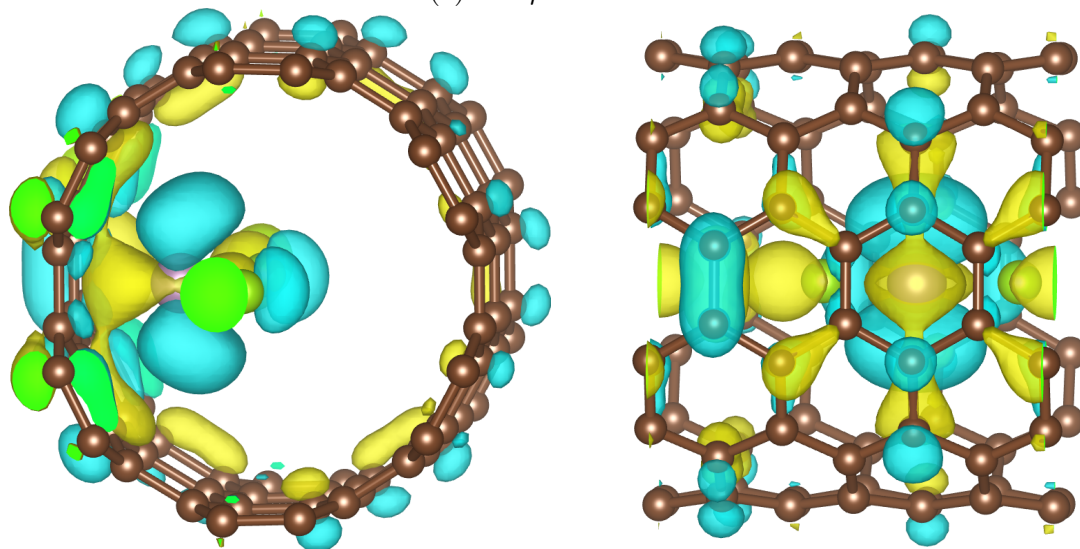


Figure 5.5 Kohn-Sham orbitals near the Fermi level for the encapsulated  $P11m$  nanowire phase, with positive and negative isosurfaces of the wavefunction shown in blue and yellow. In each case, a view looking down the nanotube is shown on the left and the view from the side is shown on the right, and the energy of the orbital relative to the Fermi level is given.



(c)  $\varepsilon - \mu = 0.049$  eV.



(d)  $\varepsilon - \mu = 0.096$  eV.

Figure 5.5 (cont.)

rather than the indirect result of the structural distortion of the tube in response to the wire.

In the (6, 6) nanotube in which the above calculations were performed, the  $P11m$  phase is not actually the ground state; the radius is 4.06 Å, so the ground state phase is  $Pm2m-I$ . (The (6, 6) nanotube was chosen because its radius coincides with the  $P11m$  phase's deep bonding minimum.) However, by repeating the same calculations, the same phenomenon was identified in a narrower (5, 5) nanotube in which  $P11m$  is the ground state: once again, the initially conducting nanotube acquires a small band gap upon encapsulation of the  $P11m$  phase, in this case equal to  $E_g = 0.13$  eV.

The possibility of creating a band gap within a carbon nanotube simply by filling it with MoSe<sub>2</sub> is potentially a technologically interesting one. Since both the radius of carbon nanotubes and the existence and size of their band gaps are a function of the chiral vector, one cannot choose independently the radius and the conductivity of an unfilled nanotube, which for technological purposes is an unfortunate limitation. The ability to convert a conducting nanotube into a semiconducting one simply by filling it lifts this limitation partially, affording a greater level of control over the properties of nanotubes.

The practice of deliberately manipulating a material's band gap in this way is known as band gap engineering [259], and can be achieved through a variety of means in other materials such as using the impact of finite-size effects on the band structure [260], controlling the stoichiometry of an alloy [261], or through the application of strain [262]. Band gap engineering in carbon nanotubes has previously been predicted to be possible through the addition of covalently bonded functional groups [263], the creation of grain boundaries within the nanotube [264], and the introduction of point defects into the nanotube [265]. The potential use of MoSe<sub>2</sub> differs from these schemes in that it leaves the external structure of the nanotube intact – which may be desirable if the nanotube's mechanical properties are to be preserved as much as possible – and may also be easier to achieve on a practical level, since it does not require the precise manipulation of the nanotube's atomic structure.

The fact that one can identify unusually deep bonding minima from the phase diagram provides a useful test of the assumption that the interaction between the nanowire and nanotube is (to a reasonable approximation) of a repulsive nature, rather than a

chemical bond: in so far as that assumption is true, then the bonding minima should be shallow. In this case, the assumption appears not to hold for the  $P11m$  phase.

The unusual behaviour of  $\text{MoSe}_2$  at low nanotube radius can be traced back to its stoichiometry. Because  $\text{GeTe}$  and  $\text{AgCl}$  both form in a 1:1 stoichiometry, they tend (at narrow nanotube radii) to form linear chain-like structures which alternate between the two elements. However, in non-1:1 systems it is not possible, when the tube is very narrow, to create structures that alternate between the two elements in a manner compatible with the bonding requirements. The formation of the molecule-like  $P11m$  structure can be identified as a consequence of this fact: due to their low coordination, the Mo atoms are unable to bond sufficiently with the nearby Se and as a result form bonds with nearby carbon atoms instead.

Returning to the phase diagram, beyond radii of  $3.79 \text{ \AA}$  there is sufficient width in the nanotube that it becomes energetically viable to fit two atoms at the same  $z$ -position as each other. As a result, this is the critical radius above which it becomes possible for the nanowire to form extended structures inside the nanotube. The first such structure that appears is the  $Pm2m$ -I zigzag phase, which is structurally analogous to the  $\text{GeTe}$   $Pmm2$  phase (but with 2:1 stoichiometry). This is followed at  $4.30 \text{ \AA}$  by the slightly wider  $P\bar{4}mm$  structure which differs from  $Pm2m$ -I in that the pairs of Se atoms rotate by  $90^\circ$  each time, such that the Mo atoms form a tetrahedral bonding pattern with them. This motif is known as a bitetrahedral structure, and has been identified in a number of other materials such as silicon diselenide, whose bulk phase is formed by stacking bitetrahedral  $\text{SiSe}_2$  ‘nanowires’ together in parallel [238].

At larger radii, the structures that appear begin to bear a much closer resemblance to the bulk phase. At  $5.69 \text{ \AA}$  the  $Pm$ -I phase forms, which resembles a very narrow cut-through of a  $\text{MoSe}_2$  monolayer, repeated down the nanotube. This is replaced at  $6.56 \text{ \AA}$  by the  $P1$  phase, which effectively amounts to a wider version of  $Pm$ -I. Finally, at  $7.59 \text{ \AA}$ , a double-layered phase forms. However, it only briefly overtakes  $P1$  apparently due to the bonding minimum with the nanotube, and as a result,  $P1$  then becomes the ground state once again at  $7.85 \text{ \AA}$ . A pattern of transitions on a phase diagram of the form  $A \rightarrow B \rightarrow A$  is a relatively unusual and interesting one. It is also of note that the two-layered phase is overtaken by the one-layer phase at all, given that the bulk consists of many layers stacked on top of each other. In this case, the energetic trade-off between one broad layer and two narrow layers seems to favour

the single layer, but as the nanotube radius increases further, one would expect that ultimately the ground state should favour many layers.

Having considered the structure of encapsulated MoSe<sub>2</sub> ENWs, in the next section their response to applied stress is studied.

## 5.2 Elastic response

### 5.2.1 Method

Thus far we have not yet considered the influence of external forces on systems of encapsulated nanowires. However, while carbon nanotubes exhibit exceptional tensile strength, the ‘within-layer’ nature of the bonding within them means that they offer rather less resistance along the radial direction: typical values for the radial elasticity of carbon nanotubes (with the strain defined as the fractional change in radius) are of the order of a few tens of GPa [266], as opposed to Young’s moduli along the periodic direction of the order of a few TPa [267]. It is plausible that the presence of a nanowire inside the nanotube may bolster it against such forces. It is also plausible – especially in cases such as MoSe<sub>2</sub>, where some phases are associated with significant elastic deformation of the nanotube – that the application of external forces to an ENW may differentially affect different structures’ formation energies to a sufficient extent as to induce a phase transition. In this section we therefore consider both of these cases.

To incorporate the role of external forces acting on the system, we modify eq. 2.15 from section 2.4 as follows:

$$E(\{\mathbf{u}_i\}) = E_0 + \frac{1}{2} \sum_{i\alpha j\beta} u_{i\alpha} u_{j\beta} \left. \frac{\partial^2 E}{\partial u_{i\alpha} \partial u_{j\beta}} \right|_{\{\mathbf{u}_i\}=0} + \sum_i \mathbf{F}_i \cdot \mathbf{u}_i, \quad (5.1)$$

where  $\mathbf{F}_i$  is the externally imposed force acting on the  $i$ -th atom. The last term gives the total work done due to these external forces. Next, we perform a change of variables in which the atomic displacements  $u_{i\alpha}$  are recast in terms of normal mode coordinates  $q_m$ :

$$u_{i\alpha} = \sum_m \epsilon_{i\alpha}^m q_m, \quad (5.2)$$

where  $i$  indexes atoms,  $\alpha$  indexes the three Cartesian directions, and  $m$  indexes the  $3N$  normal modes (with  $N$  the number of atoms). Note that here the eigenvectors are chosen (without loss of generality) to be normalised so that for each eigenvector  $\epsilon^m$ ,

$$\|\epsilon^m\| = \sqrt{\sum_{i\alpha} |\epsilon_{i\alpha}^m|^2} = 1. \quad (5.3)$$

Substituting eq. 5.2 into eq. 5.1 and setting  $dE/du_{i\alpha} = 0$  then gives

$$q_m = \frac{\sum_i \mathbf{F}_{\text{ext}}^i \cdot \epsilon_m^i}{\omega_m^2}. \quad (5.4)$$

This is an intuitive result: the displacement along a normal mode is simply the dot product of the mode's eigenvector with the external forces.

To apply the above equation in practice, one must convert the imposed stress tensor into the resultant set of forces acting on the atoms. As per Cauchy's rule [268], the force per area  $\mathbf{T}$  acting on a surface due to an externally applied stress  $\sigma$  is given by

$$\mathbf{T} = \hat{\mathbf{n}} \cdot \sigma. \quad (5.5)$$

In the above,  $\hat{\mathbf{n}}$  is the surface's unit normal vector and  $\sigma$  is the applied stress tensor, with the dot representing matrix multiplication, so that  $\mathbf{T}$  is a vector.

To obtain stress forces for each atom in the carbon nanotube a polygonal representation of the nanotube's surface is constructed so that eq. 5.5 may be used. The structure is decomposed into sixfold rings of C atoms, and for each of those rings the centroid of their positions is taken. Fig. 5.6 highlights one such sixfold ring, along with its centroid. Then, travelling around the ring, triangles are constructed whose three vertices are 1) a carbon atom, 2) one of that carbon atom's two immediate neighbours within the sixfold ring, and 3) the ring's centroid, P. This generates 6 triangles per ring. The result of this processes is a polygonal decomposition of the surface structure of the nanotube.

Having triangulated the surface, one can obtain the forces on each atom. For each triangle, the normal vector,  $\mathbf{n}$ , is computed as half of the cross product of two of the triangle's edge vectors, and then the Cauchy stress force is calculated using eq. 5.5. This force is then shared between the two atoms lying on the boundary of the triangle, with each atom receiving half of the force. By repeating this procedure for every

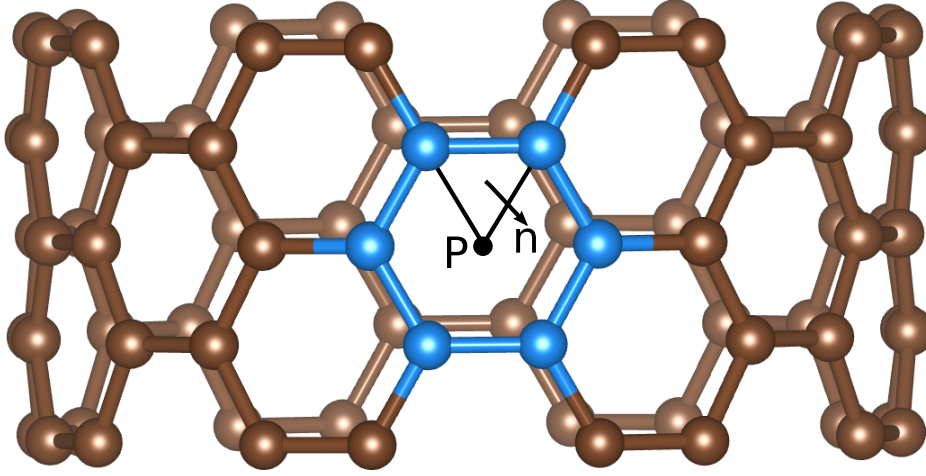


Figure 5.6 The scheme used in this work to build up a polygonal representation of the surface of a carbon nanotube. One of the loops of carbon atoms is shown in blue, and its centroid is labelled P. One of the six triangles derived from this loop is also shown, as well as its surface normal vector,  $\mathbf{n}$ .

triangle on the surface, the net force on every atom due to the externally imposed stress is calculated.

The atom-by-atom net forces are then inserted into eq. 5.4 to give the displacement along each phonon mode as a function of the external forces, and thus of the applied external stress. Having determined the displacement along each normal mode, one can evaluate the total energy using eq. 5.1. Since the energy is diagonal with respect to the basis of normal mode coordinates, this leads to a sum over contributions from each mode:

$$\Delta E = -\frac{1}{2} \sum_m \omega_m^2 q_m^2, \quad (5.6)$$

where  $\Delta E$  is the change in energy relative to the undistorted case, and the normal mode coordinates  $q_m$  are calculated as given by eq. 5.4.

Since the vibrational modes of a system provide a complete basis set for any arbitrary set of atomic displacements, the scheme presented here, which describes the system's behaviour in terms of the set of normal mode coordinates  $q_m$ , is ultimately equivalent to one working in terms of the set of atomic displacements  $\mathbf{u}_i$ . However, resolving the system's elastic response by vibrational modes has a number of benefits: firstly, it lends itself well to using the output of a phonon calculation, which is implemented in almost every DFT code. It also becomes straightforward to apply the acoustic sum rule in this case: one simply skips over the acoustic modes in eq. 5.4, since uniform translations of

the entire system do not contribute to its elastic properties. Additionally, it makes clear the linkage between the system's vibrational modes and its elastic response: if for example one were to soften a particular mode, the displacement along that mode would increase due to the presence of the frequency  $\omega_m$  in the denominator of eq. 5.4. The same applies to the relationship between the symmetry of a given normal mode eigenvector and the symmetry of the applied forces – for example, if the forces on a nanotube point isotropically inwards then the displacement along the asymmetric  $E_{2g}$  mode (pictured on fig. 4.6) will be zero by symmetry, with contributions to the sum in eq. 5.4 from outwards-facing atomic displacements cancelling with those from inwards-facing atomic displacements. As a result of these symmetry considerations and of the fact that the energetic contribution to eq. 5.6 for a given mode  $m$  is suppressed by a factor  $\omega_m^2$  (since there is a factor of  $1/\omega_m^4$  implicit in the  $q_m^2$  term of eq. 5.6 as per eq. 5.4), the elastic response for a given pattern of external forces is generally dominated by contributions from a few of the system's softest modes.

It should be noted that, for a given system, this process requires only a single phonon calculation as input; determining the first-order response of the system to any arbitrary set of external forces is then simply a postprocessing step, with no requirement to run a further DFT calculation.

Although the energetic contribution from work done by the stress forces on the system is captured by eq. 5.6, even if the nanotube were infinitely strong and therefore did not move at all – in which case eq. 5.6 would equal zero – there would still need to be a static contribution to the energy (or more properly, the enthalpy). In the case of isotropic pressure, this contribution would be  $pV$ , with  $p$  the pressure and  $V$  the total volume of the nanotube. However, this must be generalised for the case of arbitrary, anisotropic stresses. To do this, we calculate the energy required to construct the system against the applied stress forces, by analogy to the usual definition of the enthalpy as the energy required to construct the system against the applied pressure. In particular, let the polygonal representation of the surface, as obtained by the method just described, be described by a series of normal vectors  $\mathbf{n}_i^0$  (each of surface area  $|\mathbf{n}_i^0|$ ), whose centres are located at position vectors  $\mathbf{r}_i^0$ , with  $i$  running from 1 up to the number of polygons making up the surface. We then write for each of the surfaces:

$$\begin{aligned}\mathbf{n}_i &= \lambda^2 \mathbf{n}_i^0 \\ \mathbf{r}_i &= \lambda \mathbf{r}_i^0\end{aligned}\tag{5.7}$$

with  $\lambda$  functioning as a parameter that uniformly scales the size of the system, from  $\lambda = 0$  – in which case the system is infinitely small – to  $\lambda = 1$ , in which case the system is at its actual size. Note the  $\lambda^2$  in the above equation due to the fact that under a uniform scaling of a system by a factor of  $\lambda$ , surface areas scale as  $\lambda^2$ .

The anisotropic equivalent of the  $pV$  term is then given by the total integrated work done against an applied stress tensor  $\sigma$  as a result of scaling  $\lambda$  from 0 to 1. The differential work done due to a change in  $\lambda$  is

$$dW = \sum_i \mathbf{F}_i \cdot d\mathbf{r}_i = \sum_i \mathbf{F}_i \cdot \frac{d\mathbf{r}_i}{d\lambda} d\lambda, \quad (5.8)$$

with  $\mathbf{F}_i$  the total force on the  $i$ -th surface polygon. Since the force per area on a particular polygon is given by eq. 5.5, one can substitute in for the  $\mathbf{F}_i$  terms to obtain:

$$dW = \sum_i (\mathbf{n}_i \cdot \sigma) \cdot \frac{d\mathbf{r}_i}{d\lambda} d\lambda, \quad (5.9)$$

or, using eq. 5.7,

$$dW = \sum_i (\mathbf{n}_i^0 \cdot \sigma) \cdot \mathbf{r}_i^0 \lambda^2 d\lambda. \quad (5.10)$$

Integrating from  $\lambda = 0$  to  $\lambda = 1$  is now trivial (all other dependence on  $\lambda$  having dropped out) and gives

$$W = \frac{1}{3} \sum_i (\mathbf{n}_i^0 \cdot \sigma) \cdot \mathbf{r}_i^0. \quad (5.11)$$

This is the anisotropic generalisation of the  $pV$  term. One can show that it reduces as expected to  $pV$  in the isotropic case for systems with a closed surface. In this case the stress tensor is simply  $\sigma_{ij} = \delta_{ij}p$ , with  $\delta_{ij}$  the Kronecker delta and  $p$  the pressure. Inserting this into eq. 5.11 and converting the sum into an integral over the surface,  $S$ , gives

$$W = \frac{1}{3} p \int_S d\mathbf{S} \cdot \mathbf{r}. \quad (5.12)$$

Applying the divergence theorem then gives

$$W = pV, \quad (5.13)$$

which is the correct result for isotropic stress. In the general case, the total energy due to the applied stress in this scheme is then the sum of the static contribution given by eq. 5.11 and the contribution from the response of the system given by eq. 5.6.

To predict the possible occurrence of a stress-induced phase transition between two known phases, one can apply this scheme to both of the phases and calculate the difference between their energies as a function of the applied stress tensor,  $\sigma$ :

$$\Delta E = E_{\text{form,a}} - E_{\text{form,b}} + E_{\text{str,a}}(\sigma) - E_{\text{str,b}}(\sigma), \quad (5.14)$$

with  $E_{\text{form,a}}$  and  $E_{\text{form,b}}$  being the formation energies for phases A and B prior to the application of strain, and  $E_{\text{str,a}}$  and  $E_{\text{str,b}}$  being the strain energies as computed via the scheme outlined above. However, an important consideration is that the line densities of the two phases may differ. As a result, in the case where the number of atoms is fixed, a phase transition would leave some length of the nanotube unfilled. This is shown on fig. 5.7. Because the response to stress of an empty nanotube to strain will in general differ from that of a filled nanotube, there will be a corresponding impact on the energetics. In particular, on fig. 5.7, the total formation energy of the upper structure will be

$$E = E_{\text{form,a}}^{\text{pa}} N_{\text{fill}} + E_{\text{str,a}}^{\text{pca}} \lambda_C L_a, \quad (5.15)$$

where  $E_{\text{form,a}}^{\text{pa}}$  is the formation energy of phase A per filling atom,  $E_{\text{str,a}}^{\text{pca}}$  is the strain energy of phase A per *carbon* atom,  $\lambda_C$  is the line density of carbon atoms (i.e. the number of carbon atoms per unit length in the periodic direction),  $L_a$  is the length of the unit cell, and  $N_{\text{fill}}$  is the number of filling atoms.

Meanwhile the total formation energy of the lower structure on fig. 5.7 will be

$$E = E_{\text{form,b}}^{\text{pa}} N_{\text{fill}} + E_{\text{str,b}}^{\text{pca}} \lambda_C L_b + E_{\text{str,0}}^{\text{pca}} \lambda_C (L_a - L_b), \quad (5.16)$$

where the first two terms on the RHS are defined analogously to those of eq. 5.15, and  $E_{\text{str,0}}^{\text{pca}}$  is the strain energy per carbon atom of an unfilled nanotube, so that the last term gives the strain energy of the unfilled region of the nanotube, which is of length  $L_a - L_b$ . (This is also the reason for writing the strain energies of phases A and B as per-carbon-atom rather than per-filling-atom quantities: they are then directly comparable to the strain energy of an empty nanotube.)

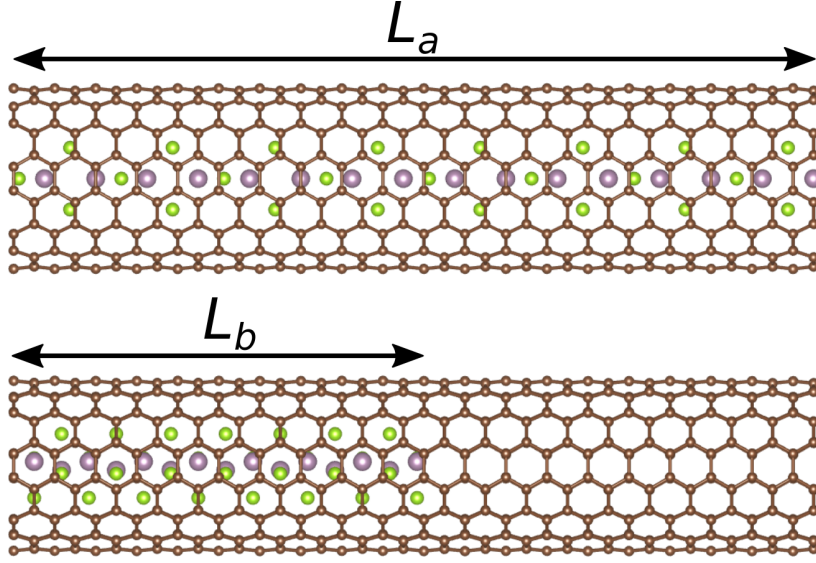


Figure 5.7 Two encapsulated nanowire phases of different line densities, so that if the total number of atoms is fixed then one of the nanotubes contains an unfilled section.

Next, we introduce the atomic line densities  $\lambda_a$  and  $\lambda_b$  of the two nanowire filling phases, and rewrite  $L_a$  as  $\lambda_a N_{\text{fill}}$  and  $L_b$  likewise in equations 5.15 and 5.16. Subtracting them from each other to get the strain-corrected formation energy difference between the two phases gives:

$$\frac{\Delta E}{N_{\text{fill}}} = E_{\text{form,b}}^{\text{pa}} - E_{\text{form,a}}^{\text{pa}} + \frac{\lambda_C}{\lambda_b} [E_{\text{str,b}}^{\text{pca}} - E_{\text{str,0}}^{\text{pca}}] - \frac{\lambda_C}{\lambda_a} [E_{\text{str,a}}^{\text{pca}} - E_{\text{str,0}}^{\text{pca}}] \quad (5.17)$$

This equation determines which of the two phases is the ground state, and may therefore be used to construct a strain-dependent phase diagram by varying the applied strain and recalculating  $\Delta E$ . The equation expresses the relative favourability of the two phases not simply by the difference of the ENWs' strain energies, but by the difference of their strain energies *relative to the unfilled nanotube*. The exception to this is if  $\lambda_b = \lambda_c$ , in which case the amount of nanotube left unfilled is the same in both cases and as a result the dependence on  $E_{\text{str,0}}^{\text{pca}}$  drops out and eq. 5.14 is recovered.

### 5.2.2 Application to MoSe<sub>2</sub> nanowires

The formalism developed over the previous section is now applied to the case of MoSe<sub>2</sub> ENWs. Because we are particularly interested in the possibility of a pressure-induced phase transition, we choose a point on the phase diagram in which the ground state

nanowire phase is nearly degenerate with some other phase, and consider whether external stresses could induce a phase transition. In particular, we consider the point on the phase diagram in the vicinity of the phase transition at  $5.69 \text{ \AA}$ , where the  $P\bar{4}mm$  phase is overtaken by the  $Pm\text{-I}$  phase.

Ideally, one would compute the stresses precisely at the phase boundary. However, in practice only a discrete set of nanotube radii are possible. Additionally, the unit cells used for the phonon calculations from which the dynamical matrices are to be extracted should be of the same length for both of the two phases considered. This is firstly because of the extreme sensitivity of phonon calculations to  $k$ -point sampling and the resulting cancellation of errors of the two cells are the same shape, and secondly because a normal mode at  $\Gamma$  in a longer cell may not appear at  $\Gamma$  in a shorter cell, making it difficult to compare the resulting stress responses on equal footing. The closest radius to  $5.69 \text{ \AA}$  with which both the  $P\bar{4}mm$  and  $Pm\text{-I}$  phases are commensurate (without requiring computationally unviable supercell lengths) is an  $(8, 8)$  armchair nanotube of radius  $5.43 \text{ \AA}$ .

Phonon calculations were performed for the empty  $(8, 8)$  nanotube, and for the  $P\bar{4}mm$  and  $Pm\text{-I}$  structures encapsulated inside that nanotube. In each case the cell length was  $9.86 \text{ \AA}$ , the equilibrium length of the nanotube itself. Again, the fixing the cell lengths in this way provides better cancellation of  $k$ -point sampling errors. The finite difference method was used, giving the phonons at  $\Gamma$ . This could introduce errors in the elasticity calculations if the external forces are incommensurate with the unit cell, but no such incommensurate forces are considered in this section, so there is no need to obtain the normal modes away from  $\Gamma$ . The same ultrasoft pseudopotentials were used as in the polishing calculations, with a plane-wave cutoff of  $500 \text{ eV}$  and a Brillouin zone sampling density of  $0.026 \times 2\pi \text{ \AA}^{-1}$ .

The dynamical matrices for the unfilled tube and for the two ENW phases were extracted from the output of the phonon calculations. These dynamical matrices were used to calculate the elastic response of the three systems using the formalism outlined in the previous section. Stress-dependent formation energy differences between the two phases were computed using eq. 5.17.

Note that to obtain the atomic line number densities  $\lambda_a$  and  $\lambda_b$ , the equilibrium lengths of the nanowires on their own were used, since constraining them to match the periodicity of a nanotube introduces a small error in their lengths; in reality, the

nanowire would be able to expand independently of the periodicity of the nanotube to reach its own equilibrium periodicity.

To calculate eq. 5.17 nearer to the transition point, strain energies based on the calculation at 5.43 Å were used in combination with formation energies obtained from the phase diagram at a range of nanotube radii. Implicit in this is the approximation that the response to strain at 5.43 Å is a good estimate of the response to strain at other radii, which will remain valid as long as the particular radius under consideration is not too far from 5.43 Å.

Using this scheme, phase diagrams as a function of stress and nanotube radius were created for the  $P\bar{4}mm$  and  $Pm\text{-}I$  phases. Fig. 5.8 shows the diagrams for two cases: the fully anisotropic case where the applied stress is chosen to be  $\sigma = \text{diag}(\sigma_{xx}, 0)$  or the fully isotropic case where  $\sigma = \delta_{ij}p$ . The total strain energy for the  $P\bar{4}mm$  phase on its own is given on fig. 5.9. The diagram indicates that the strain energy is far larger in magnitude for more anisotropic stresses.

The nature of the nanotubes' response to stress can be rationalised in terms of their vibrational spectra. In particular, the response is for the most part dominated by contributions from the asymmetric squash mode, which is the lowest-frequency mode, and from the radial breathing mode (RBM) which is higher in frequency. The vibrational frequencies of these two modes are shown in table 5.2. The fact that the response is so much smaller in the case of isotropic stress ultimately derives from the fact that the dot product between the stress forces and the normal mode eigenvector in eq. 5.4 is zero by symmetry if the stress tensor is symmetric. As a result, the largest contribution to the elastic response comes from the RBM, whose frequency is significantly higher, which suppresses the response (both in terms of the strain energy and in terms of the amount of atomic displacement) due to the  $1/\omega_m^2$  factor in the denominator of eq. 5.4.

As previously discussed, the energetics of the system under stress may be decomposed into the static contribution from eq. 5.11 and the elastic contribution from eq. 5.6. The static contribution, which depends only on the geometry of the system (not on its phonon spectrum), is first-order in the applied stress, whereas the elastic contribution is second-order. As a result, for small stresses the static contribution dominates. However, for the cases considered here, the static contribution is extremely small, as is evident from the isotropic phase diagram on fig. 5.8.

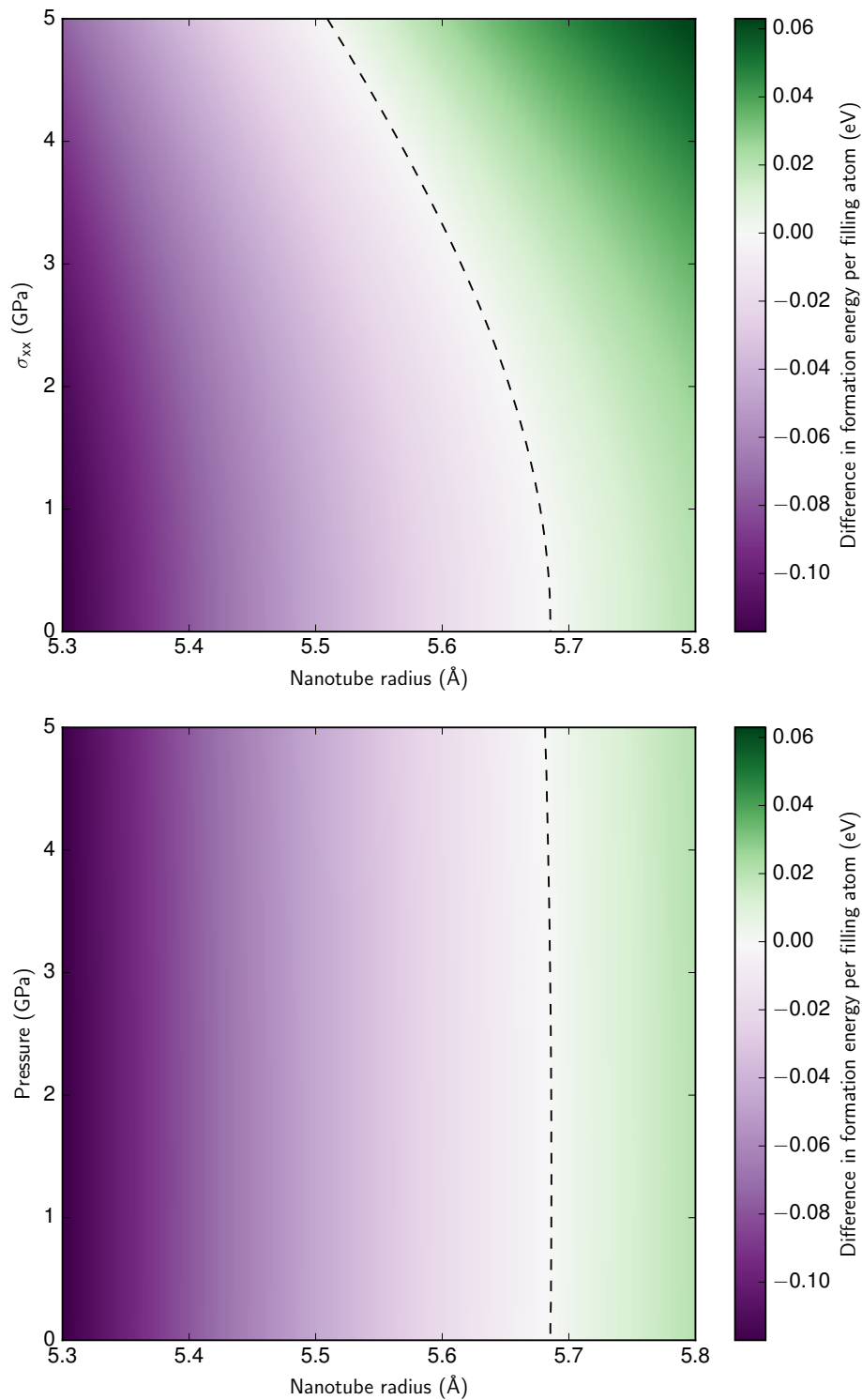


Figure 5.8 Anisotropic (top) and isotropic (bottom) stress-radius phase diagrams for MoSe<sub>2</sub> ENWs in the vicinity of the phase transition between the  $P4mm$  phase ( $\Delta E < 0$ ) and the  $Pm-I$  phase ( $\Delta E > 0$ ). One can see that the response is far stronger for anisotropic stress, due to the squash mode being lower in frequency than the RBM.

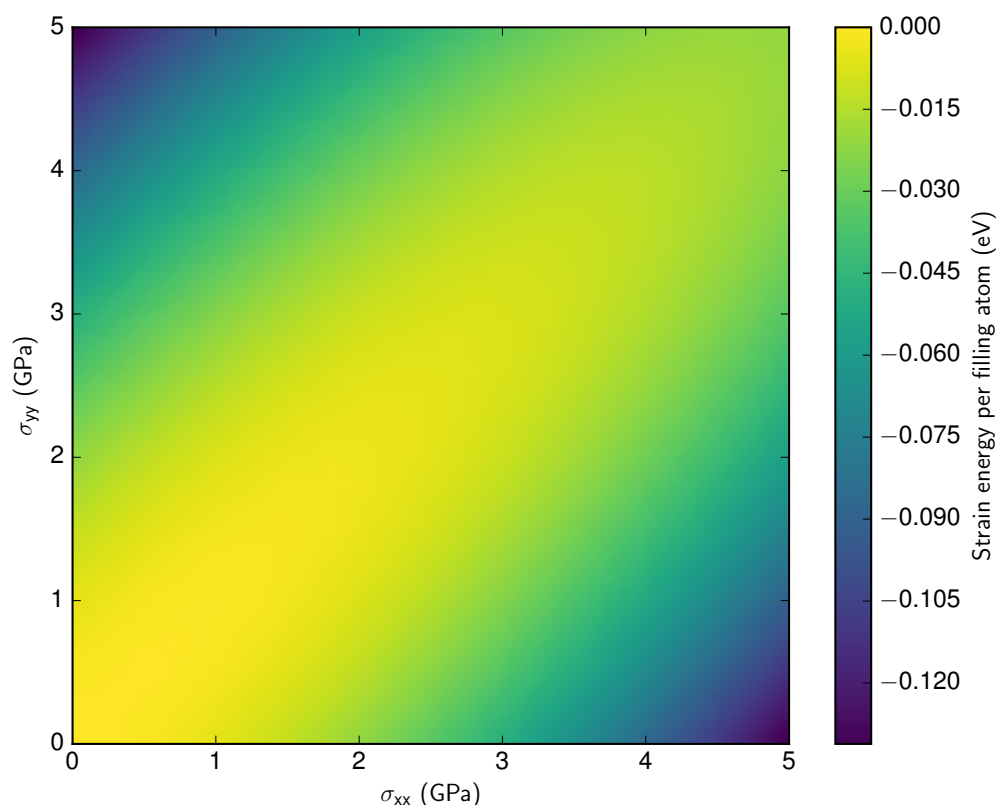


Figure 5.9 The strain energy of the  $P\bar{4}mm$  phase in an  $(8,8)$  nanotube, as calculated using eq. 5.6.

Whilst the pressures required to significantly shift the radius at which the phase transition occurs are large (of the order of gigapascals), it should be emphasised that the nanoscale nature of the system means that the corresponding energies required to apply such a pressure are considerably smaller. As a result, although realising such high pressures in a nanoscale device would be challenging, the energetics of such a device would not be unreasonably costly (of the order of 0.1 eV per filling atom in a system where the total number of filling atoms may potentially be quite small due to the nanoscale nature of the ENW).

Given the large upshifts in the nanotube's squash mode that occur upon encapsulation of the nanowires, as shown on table 5.2, another potential use of ENWs is for their additional mechanical strength relative to the nanotubes on their own, since those upshifts indicate a large increase in mechanical resistance to anisotropic stresses. This could be useful in applications for which it is desirable for the nanotubes to

	Empty nanotube	$P\bar{4}mm$	$Pm-I$
Squash mode	25.6	41.1	65.7, 72.9
Radial breathing mode	209.6	212.7	219.0

Table 5.2 Frequencies (in  $\text{cm}^{-1}$ ) of the softest modes in the three different cases considered in  $\text{MoSe}_2$ . The  $Pm-I$  RBM undergoes a splitting into two modes upon insertion into the nanotube; both of the resulting frequencies are reported.

be mechanically strong not just in the periodic direction but also in the transverse direction.

Finally, it should also be noted that another benefit of analysing ENWs' elastic properties in terms of their normal modes is that their vibrational spectra are measurable via Raman spectroscopy, and as a result one can empirically obtain information about the elastic properties of the nanotube without needing to measure them directly by applying stress and measuring the response, which could be rather more difficult.

Although chirality has largely been found not to be important when controlling for nanotube radius (hence the validity of the implicit nanotube approximation), it is worth considering here in the specific context of elastic properties. As shown in this section, the most important contributions to the elastic response of an ENW come from the squash mode and the RBM. It is well-established experimentally [269] that the RBM's frequency  $\omega_{\text{RBM}}$  depends almost solely on the radius  $R$  of the nanotube according to the relation

$$\omega_{\text{RBM}} = \frac{\alpha}{R} + \beta, \quad (5.18)$$

where  $\alpha$  and  $\beta$  are constants. As previously discussed, the squash mode is more difficult to measure due to its low frequency, so the experimental evidence on the dependence of the squash mode's frequency on the chirality is somewhat sparser. However, theoretical calculations have indicated that, as with the RBM, the squash mode's frequency is also determined almost exclusively by the radius of the encapsulating nanotube [270]. More recently, experimental evidence has suggested that this is indeed true [271]. It is therefore reasonable to conclude that the elastic properties of ENWs will also be primarily dependent on nanotube radius rather than on chirality *per se*.

### 5.3 Conclusion

In this chapter, the structures of MoSe<sub>2</sub> ENWs have been predicted and analysed. AIRSS has been used to identify a number of novel nanowire structures, including (at larger nanotube radii) a number of layered phases which derive structurally from the MoSe<sub>2</sub> bulk. At small nanotube radii, the impossibility of satisfying bonding requirements in a sufficiently narrow nanotube has been found to lead to an unusually strong bond between the nanowire and the nanotube. By calculating the electronic structure of this bonding, it has been shown that the bond opens up a band gap in previously conducting nanotubes, a finding which may have technological applications.

The response of encapsulated MoSe<sub>2</sub> ENWs to applied stress has also been studied. A formalism has been presented to convert applied stress tensors into forces on each atom based on a polygonal representation of the surface of the nanotube. The second-order representation of the energy landscape in the vicinity of the equilibrium state is then extracted from a DFT phonon calculation and the elastic response of the system is decomposed into components along each normal mode. This formalism is fully general and therefore may readily be applied to other low-dimensional systems. Under sufficiently high pressures, differences in elastic properties between the  $Pm-I$  and  $P\bar{4}mm$  phases have been found to lead to the possibility of a stress-induced phase transition. In addition, both phases have been shown to bolster the nanotube's strength against transverse forces, which follows from the increase in frequency of the two most important modes for the nanotube's elastic response: the squash mode and the RBM.

Further work could consist of applying the formalism presented here to other ENW systems. A lower pressure than identified here may be sufficient for phase change between two nearly degenerate structures to occur where the two nanowires differ dramatically either in their softness in the transverse direction, or in their equilibrium volumes. In the former case, there would be a large difference in the contributions from eq. 5.6; in the latter case, there would be a large difference in the contributions from eq. 5.11.

In addition, here the effects of transverse stress inducing an elongation in the nanotube have not been taken into account, due to the difficulties of calculating normal modes in the case where the lattice parameter may vary. The ratio of transverse to longitudinal strain is known as the Poisson ratio,  $\nu$ , and typical values for SWNTs are around

---

0.3 [272]. Sheets of carbon nanotubes have been shown to exhibit the unusual property of a sign change in  $\nu$  in the case of sheets of nanotubes (also known as ‘buckypaper’) [273]. One could extend this method by also calculating the elastic properties associated with longitudinal strain and thereby including the periodicity of the nanotube as a degree of freedom in the model.



# Chapter 6

## Diffraction in ENWs

Diffraction is a powerful tool for structure determination within 1D systems; most famously, an X-ray diffraction image played a critical role in the determination of the double-helix structure of DNA [274]. Here we consider the application of diffraction to encapsulated nanowire structures.

We consider a coordinate system in which incoming photons have an incoming wavevector  $\mathbf{k}_I = |\mathbf{k}_I| \hat{\mathbf{z}}$ , and then scatter off the sample so that their final wavevector is (using spherical polar coordinates with azimuthal angle  $\theta$  and polar angle  $\phi$ )

$$\mathbf{k}_F = |\mathbf{k}_F| \begin{bmatrix} \sin(\theta) \cos(\phi) \\ \sin(\theta) \sin(\phi) \\ \cos(\theta) \end{bmatrix} \quad (6.1)$$

Note that here we consider elastic scattering, i.e. the energy remains unchanged by the scattering event and therefore  $|\mathbf{k}_F| = |\mathbf{k}_I|$ .

If the detector screen is aligned along the  $xy$  plane, then the position on the screen is given by

$$\begin{bmatrix} u \\ v \end{bmatrix} = \begin{bmatrix} r \sin(\theta) \cos(\phi) \\ r \sin(\theta) \sin(\phi) \end{bmatrix} \quad (6.2)$$

where  $r$  is the separation between the sample and the screen.

The above equations provide a map between the momentum transfer,  $\mathbf{q} = \mathbf{k}_F - \mathbf{k}_I$ , and the position on the detector screen. This is useful because the scattering amplitude at momentum transfer  $\mathbf{q}$  is proportional to the Fourier transform of the sample's charge

density [275]:

$$A(\mathbf{q}) \propto \int \rho(\mathbf{r}) e^{-i\mathbf{q}\cdot\mathbf{r}} d^3\mathbf{r}, \quad (6.3)$$

where  $A(\mathbf{q})$  is the scattering amplitude,  $\rho(\mathbf{r})$  is the charge density, and the integral is over all space.

This gives a scheme for calculating the diffraction pattern for a given sample: one first calculates (on a sufficiently fine grid of  $\mathbf{q}$ -values) the function  $A(\mathbf{q})$ , parameterised as a function of  $\theta$  and  $\phi$ , via equations 6.1 and 6.3. Then the position  $(u, v)$  on the detector screen for each  $\mathbf{q}$  on the grid is also calculated, via eq. 6.2, which enables one to give the scattering amplitude as a function of position on the detector screen rather than of  $\mathbf{q}$ . Finally, since  $A(\mathbf{q})$  is a complex amplitude, the final intensity is obtained by taking the square modulus of  $A$ .

To calculate the function  $A(\mathbf{q})$  using eq. 6.3 in the case of periodic (i.e. crystalline) samples, it is useful to express  $\rho(\mathbf{r})$  as a convolution:

$$\rho(\mathbf{r}) = \rho_{\text{cell}}(\mathbf{r}) \otimes \rho_{\text{latt}}(\mathbf{r}), \quad (6.4)$$

where  $\rho_{\text{cell}}$  gives the charge density of a single unit cell, and the lattice contribution is given by

$$\rho_{\text{latt}}(\mathbf{r}) = \left( \sum_{j=-\infty}^{\infty} \delta(\mathbf{r} - j\mathbf{a}) \right) \otimes \left( \sum_{k=-\infty}^{\infty} \delta(\mathbf{r} - k\mathbf{b}) \right) \otimes \left( \sum_{l=-\infty}^{\infty} \delta(\mathbf{r} - l\mathbf{c}) \right), \quad (6.5)$$

with lattice vectors  $\mathbf{a}$ ,  $\mathbf{b}$  and  $\mathbf{c}$ .

As per the convolution theorem, the Fourier transform of  $\rho$  is then the product of the individual Fourier transforms of the two terms of the convolution:

$$\tilde{\rho}(\mathbf{q}) = \tilde{\rho}_{\text{cell}}(\mathbf{q}) \tilde{\rho}_{\text{latt}}(\mathbf{q}). \quad (6.6)$$

Using the standard result for the Fourier transform of a Dirac comb, the reciprocal-space contribution from the lattice term is

$$\tilde{\rho}_{\text{latt}}(\mathbf{q}) = \left( \sum_{j=-\infty}^{\infty} \delta(\mathbf{q} \cdot \mathbf{a} - 2\pi j) \right) \left( \sum_{k=-\infty}^{\infty} \delta(\mathbf{q} \cdot \mathbf{b} - 2\pi k) \right) \left( \sum_{l=-\infty}^{\infty} \delta(\mathbf{q} \cdot \mathbf{c} - 2\pi l) \right). \quad (6.7)$$

In the case of low-dimensional systems, one or two of the delta-function terms disappear from eq. 6.5 and thus from eq. 6.7. As a result there is no ‘selectivity’ due to the lattice periodicity along non-periodic directions, which is the origin of the distinctive streaks observed in the diffraction patterns of low-dimensional systems. In the 1D case, for example, the condition

$$\sum_{l=-\infty}^{\infty} \delta(\mathbf{q} \cdot \mathbf{c} - 2\pi l) \neq 0 \quad (6.8)$$

defines a series of planes in reciprocal space, which manifest as streaks on the diffraction pattern perpendicular to the periodic axis.

A code was written to implement this scheme and thereby obtain the corresponding image on the diffraction screen for a given sample. The real-space charge density,  $\rho$ , is read in from a given CASTEP checkpoint file (using the program C2x [258]), and a fast Fourier transform (FFT) is applied to obtain its reciprocal-space counterpart,  $\tilde{\rho}$ . This allows a more accurate calculation of the diffraction pattern than many other diffraction codes which work only from the atomic positions as input data and therefore do not incorporate bonding-induced changes to  $\rho(\mathbf{r})$ . One complication is that when ultrasoft pseudopotentials are used, CASTEP’s charge density does not contain the charge of the core electrons and is as a result inaccurate in the vicinity of atomic nuclei. To work around this,  $\rho(\mathbf{r})$  is augmented with a narrow Gaussian centred on each atom’s nucleus which integrates to the charge of its core electrons. This will introduce a small inaccuracy since it will differ from the exact charge distribution, but in general the wavelengths of X-ray diffraction used for crystallography are too long to probe the fine details of the charge distribution very near the nucleus anyway (a typical wavelength being of order 1 Å [276]). An example of the total charge density, whose Fourier transform is used in calculating the diffraction pattern, is shown on fig. 6.1.

Having obtained  $\tilde{\rho}$ , the delta-function terms in eq. 6.7 are then applied. This is done in practice by smearing the delta functions into narrow Gaussian functions (whose width is an adjustable parameter of the code). This is because in real diffraction patterns, the spots are never perfectly sharp due to a number of effects including the finite sample size, instrumental errors, and the thermal motion of the nuclei. After calculating the diffraction intensity, some postprocessing is performed to show more clearly the features of the diffraction pattern by adjusting the image’s brightness and saturation.

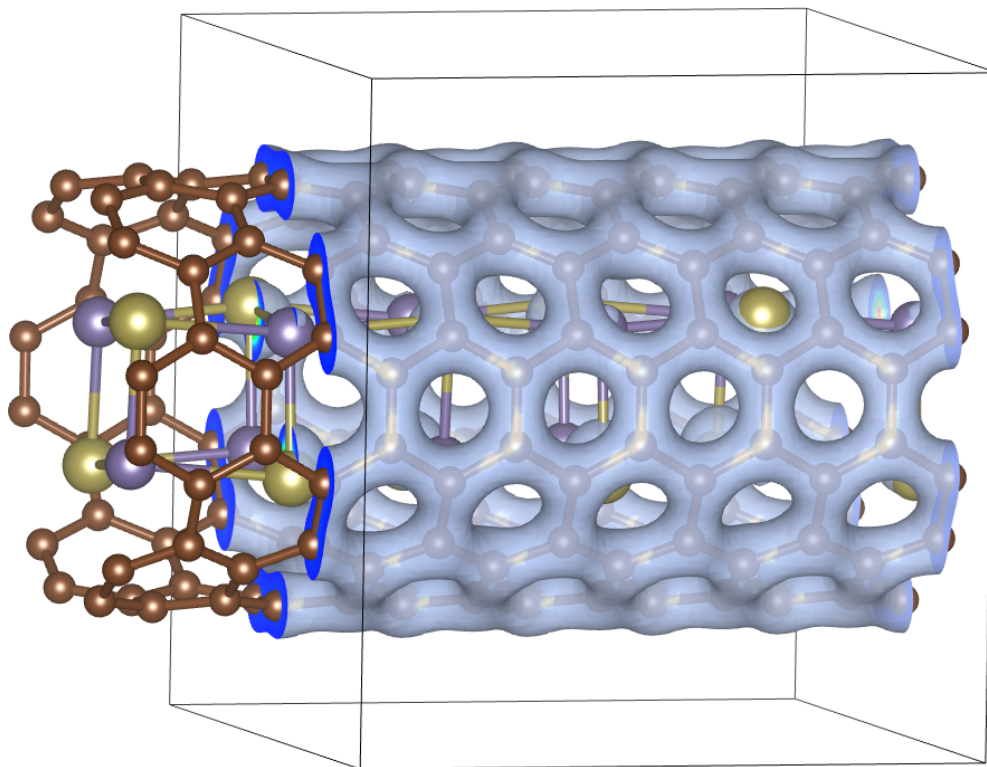


Figure 6.1 Total DFT charge density for a GeTe ENW. Shown in blue is a charge isosurface for a single unit cell. The structure itself is on fig. 6.2.

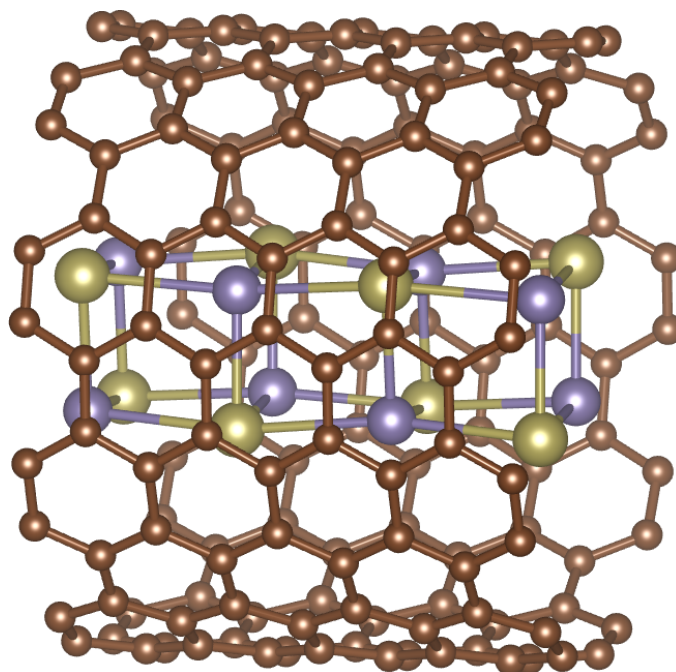


Figure 6.2 The structure of a (9,9) SWNT containing a GeTe nanotube of the  $P\bar{4}m2$  phase, from which the diffraction patterns on figs. 6.3 and 6.4 are derived.

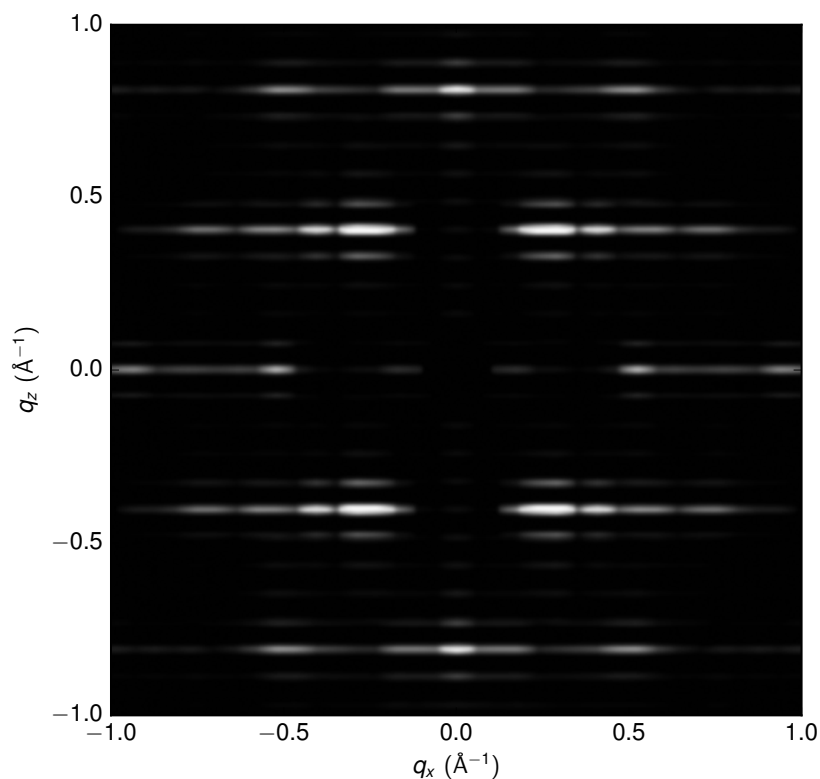


Figure 6.3 Diffraction pattern of a (9,9) SWNT.

The result of applying the diffraction code to a single (9,9) SNWT is shown on fig. 6.3, which matches well published experimental images of diffraction from individual nanotubes in the literature [277]. The structure of the SWNT is shown on fig. 6.2 (but the figure shows an encapsulated GeTe ENW which was not included in this first calculation). As is typical in the case of diffraction on low-dimensional systems, the streaks generally have a roughly sinc-like character, with oscillations of regular periodicity and an amplitude that becomes smaller as  $|q_x|$  increases. One can identify the positions of the maxima on the image with the nearest-neighbour distances between the carbon atoms in the SWNT, with distinct streaks at  $q_z = 0.40 \text{ \AA}^{-1}$  corresponding to a real-space distance of  $2.5 \text{ \AA}$ , which is the periodicity of the nanotube (i.e. the length of the primitive unit cell). The incident electron wavenumber used in all diffraction patterns calculated in this chapter was  $q_I = 10.0 \text{ \AA}^{-1}$ , corresponding to a wavelength of  $0.1 \text{ nm}$ , which falls roughly in the middle of the  $0.01 \text{ nm}$  to  $10 \text{ nm}$  X-ray wavelength range.

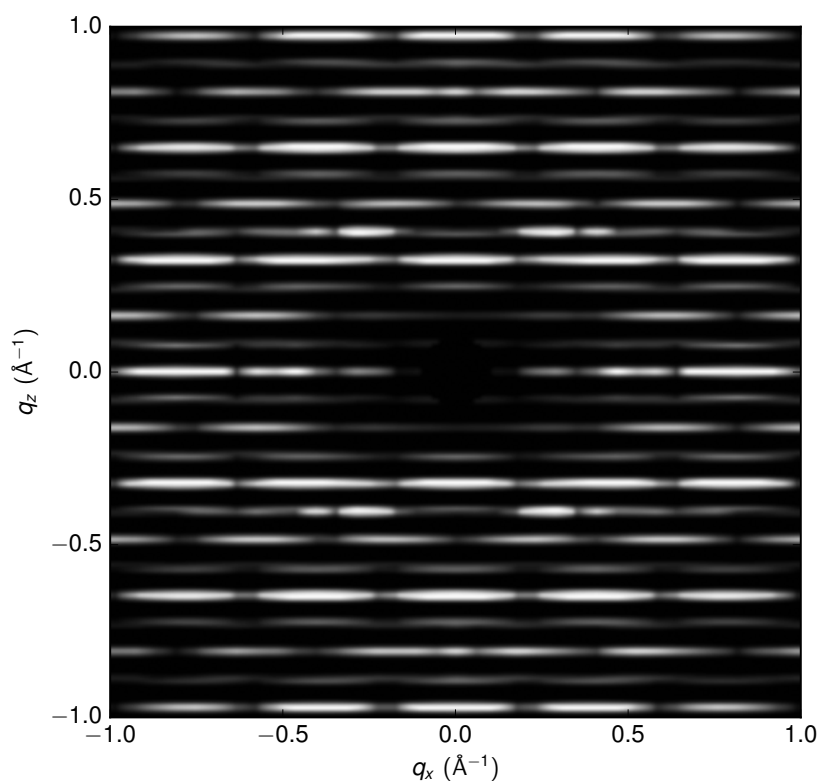


Figure 6.4 Diffraction pattern of the ENW shown on fig. 6.2.

When the full ENW shown on fig. 6.2 is considered, rather than just the empty nanotube, the resulting diffraction pattern – shown on fig. 6.4 – is considerably more complex. More streaks appear whose  $q_z$  implies association with the nanowire itself, rather than with the nanotube. In particular, the distance along the periodic axis between the successive layers of 4 Ge and Te atoms is  $3.08 \text{ \AA}$ , the reciprocal of which is  $0.32 \text{ \AA}^{-1}$ . One can therefore attribute to the nanowire the streaks visible at  $0.32$ ,  $0.64$  and  $0.96 \text{ \AA}^{-1}$ . Together figs. 6.4 and 6.3 present a compelling argument for the utility of diffraction in imaging ENWs: the incommensurability of the nanotube and nanowire, while making theoretical calculations difficult, here becomes a considerable asset because it leads to diffraction spectra in which features arising from the nanotube lie at different  $q_z$  than those arising from the nanowire, making it easy to resolve the two subsystems' respective contributions.

The streaks arising from the nanowire are also distinguished from those associated with the nanotube by the fact that they drop off more slowly in intensity as one moves away

from  $q_x = 0$  than do the streaks associated with the nanotube. This is a consequence of the fact that narrower real-space functions correspond to broader reciprocal space functions, and provides additional assistance in attributing features of the ENW's diffraction pattern to the two subsystems.

It should be emphasised that the meaningfulness of assigning individual features of the diffraction spectrum to the nanowire or the nanotube hinges on the assumption that the charge distribution of the ENW is almost equal to the sum of the individual charge distributions of the bare nanowire and empty nanotube. This is because – if that assumption is true – the linearity of the Fourier transform means that if  $\rho_{\text{ENW}}(\mathbf{r}) \approx \rho_{\text{tube}}(\mathbf{r}) + \rho_{\text{wire}}(\mathbf{r})$  then  $\tilde{\rho}_{\text{ENW}}(\mathbf{q}) \approx \tilde{\rho}_{\text{tube}}(\mathbf{q}) + \tilde{\rho}_{\text{wire}}(\mathbf{q})$ , i.e. the diffraction pattern of the whole system becomes a simple sum of the patterns of the two subsystems. Based on this observation, one can quantitatively decompose the diffraction image into contributions from the nanowire and contributions from the nanotube. This was done by calculating (using the same method as before) the diffraction intensities  $I_{\text{tube}}$ ,  $I_{\text{wire}}$  and  $I_{\text{ENW}}$  for the empty nanotube, bare nanowire, and the full ENW respectively. The lightness of each point was chosen to be proportional to  $I_{\text{ENW}}$ , and the hue was set by calculating

$$f_{\text{hue}} = \frac{I_{\text{tube}} - I_{\text{wire}}}{I_{\text{tube}} + I_{\text{wire}}}, \quad (6.9)$$

which runs between -1 (where  $I_{\text{wire}} \gg I_{\text{tube}}$ ) and 1 ( $I_{\text{tube}} \gg I_{\text{wire}}$ ), with the resulting hue being a continuous function of  $f_{\text{hue}}$ , as shown on the colour bar. The figure resulting from this scheme is shown on fig. 6.5, in which the colouring provides a quantitative decomposition of the intensity into the two subsystems' contributions that matches with the qualitative attributions given previously.

## 6.1 Bundles of ENWs

The above method is sufficient to obtain good results for diffraction where the sample is a single ENW. Experimentally, however, a common situation is that a large sample of nanotubes is filled with some material to create a bundle of ENWs. This is problematic, since it requires knowledge of the bundle's structure. Moreover, the relative weakness of the dispersion interactions that bind nanotubes together suggests that thermal perturbations could have a significant effect on said structure. Due to the numbers of atoms involved, a first-principles simulation of the dynamics of such a large system is

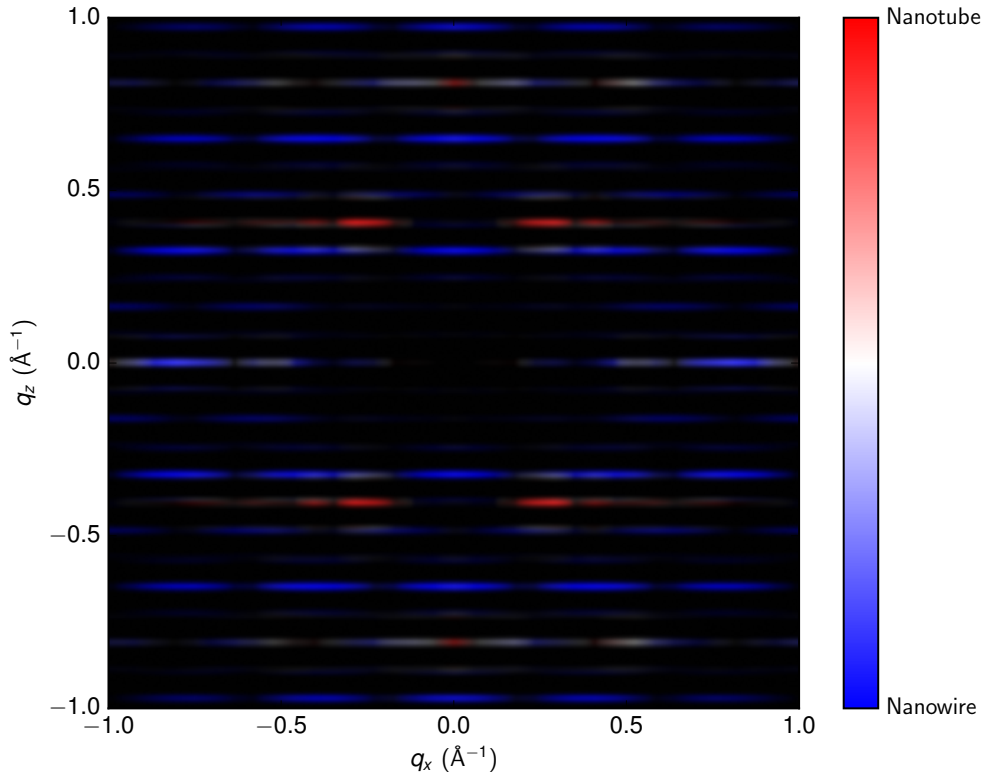


Figure 6.5 Diffraction pattern shown on fig. 6.4, with features automatically coloured according to the subsystem from which they arise as described in the main text.

not computationally tractable. Instead, we use a simple coarse-grained model in which a nanotube is modelled as a single, rigid object, with a two-body interaction between nanotubes of the form

$$V = \sum_{\substack{ij \\ i \neq j}} \frac{1}{2} E_{\text{DFT}}(|\mathbf{r}_i - \mathbf{r}_j|), \quad (6.10)$$

where  $i$  and  $j$  index all nanotubes in the simulation box, and  $\mathbf{r}_i$  is the position of the *centre* of the  $i$ -th nanotube. (In practice there is likely to be some dependence on the relative orientations and positions along the  $z$ -axis of the nanotubes, but these dependencies are unlikely to be comparable in magnitude to the dependency on  $R$ , and we therefore neglect them.) The function  $E_{\text{DFT}}$  was parameterised by performing DFT calculations on two adjacent nanotubes at various distances, fitting a cubic spline function, and tabulating the results. To improve computational efficiency, the potential was cut off beyond a distance of  $R_{\text{max}} = 13.5 \text{ \AA}$ , and a constant was added to

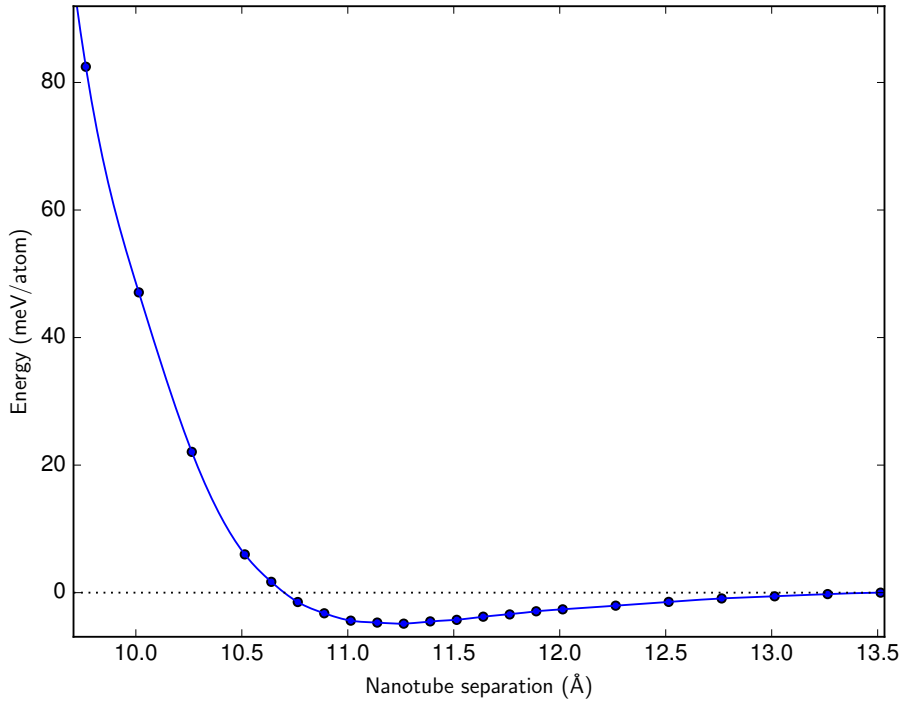


Figure 6.6 The interaction energy between two (9,9) nanotubes parameterised as a function of the distance between their centres. The points represent the DFT single point energy calculations, and the line is a spline interpolant.

remove the resulting discontinuity at  $R_{\max}$ . Because of the importance of dispersion effects in the interaction between nanotubes, the correction scheme of Tkatchenko and Scheffler[169] was used in the DFT calculations. This scheme was applied to the case of two interacting (9,9) nanotubes, and the result is shown on fig. 6.6. The fitted spline shown on the figure was then converted into a LAMMPS potential in the form of a lookup table.

Using LAMMPS [186], a 2D simulation was run on a simulation cell containing 558 nanotubes of (9,9) chirality interacting via the tabulated potential (with linear interpolation used on the table to obtain the value of the potential for a given nanotube-nanotube distance). The lengths of the cell along the  $x$  and  $y$  directions were allowed to vary according to a Nosé-Hoover [278] barostat, while the length along  $z$  was fixed and motion along it was forbidden. After an equilibration period (which was not included in the subsequent calculation of the contribution to the diffraction pattern), a 10 ns molecular dynamics trajectory at standard temperature and pressure was simulated. A

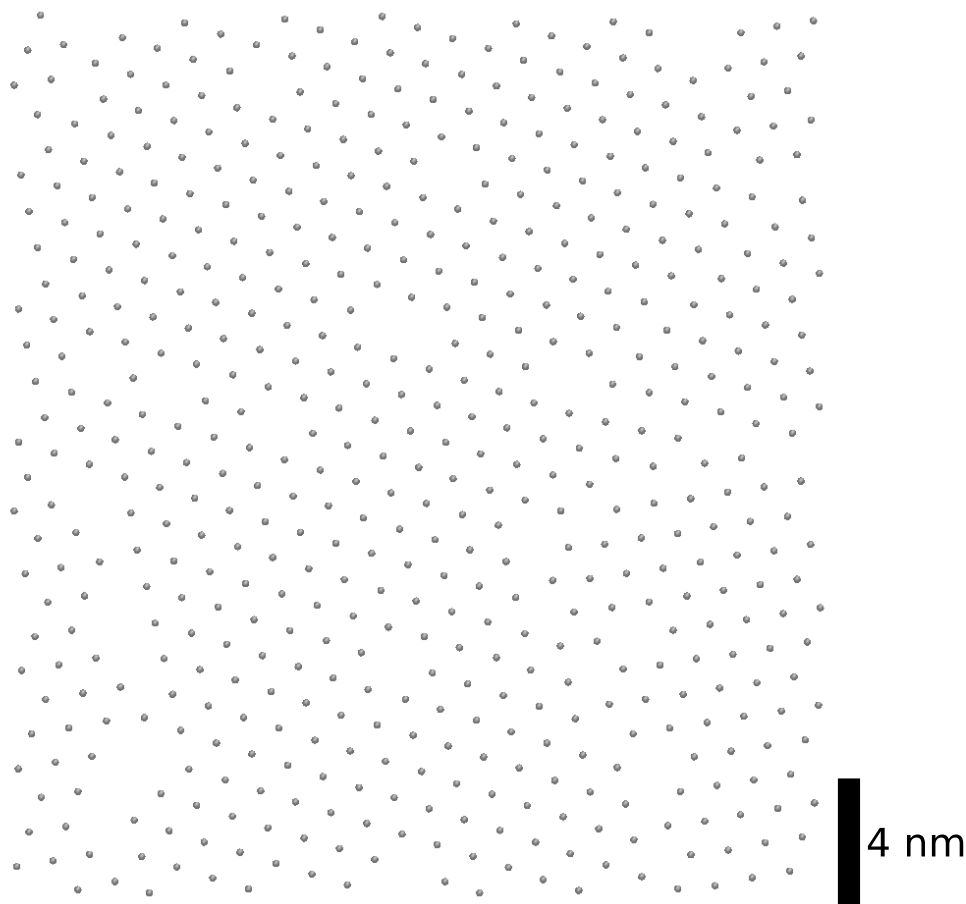


Figure 6.7 Real-space snapshot of the MD simulation of a bundle. Each ‘atom’ represents one nanotube interacting with the others via the effective potential described in the text.

snapshot of the simulation is shown on fig. 6.7. (The existence of a phase in which the nanotubes condense into a hexagonally close-packed structure is unsurprising given the angular independence of the potential and its Lennard-Jones-like behaviour with respect to distance.)

In the case of a bundle of ENWs, an extra term appears in equation 6.4 corresponding to a convolution with the real-space distribution of ENWs in the bundle:

$$\rho_{\text{bundle}}(\mathbf{r}) = \sum_i \delta(\mathbf{r} - \mathbf{r}_i), \quad (6.11)$$

where  $\mathbf{r}_i$  is the position of the  $i$ -th ENW in the bundle. This represents an approximation whereby the ENWs are assumed to be aligned with each other and to be of the same

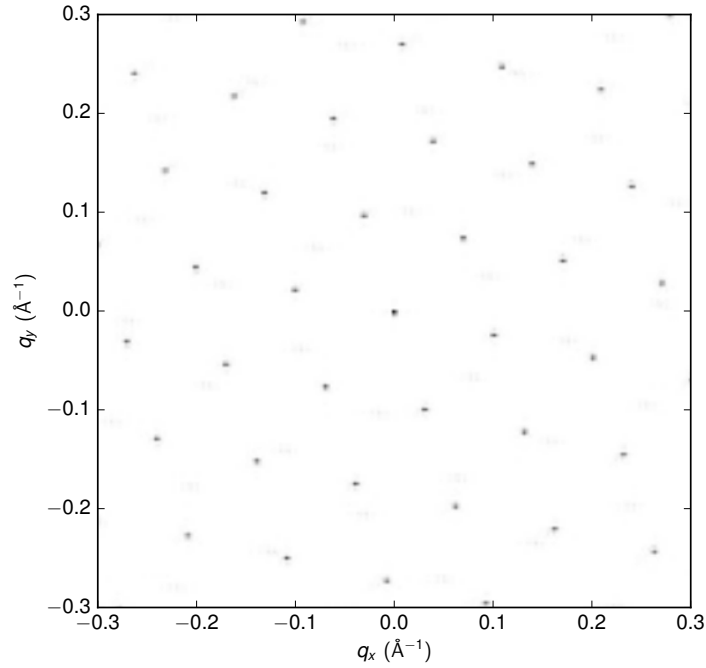


Figure 6.8 The multiplicative contribution (in arbitrary units) to the diffraction pattern arising from the bundle shown in real space on fig. 6.7.

chiral vector (experimentally one generally has a distribution of chiral vectors). The resulting multiplicative contribution to the diffraction intensity is given by the Fourier transform,

$$\langle |\tilde{\rho}_{\text{bundle}}|^2 \rangle = \left\langle \sum_i \sum_j e^{-i\mathbf{k} \cdot (\mathbf{r}_j - \mathbf{r}_i)} \right\rangle. \quad (6.12)$$

The above is sometimes referred to as the structure factor. The angular brackets have been introduced to indicate thermal averaging. This function was calculated from the MD trajectory and the result is shown on fig. 6.8, which shows the result one would expect for the structure factor of a hexagonally close-packed system.

The diffraction pattern was then integrated over all possible orientations of the sample. This integral was performed numerically by parameterising the sample orientation in terms of a rotation about its periodic axis through an angle  $\gamma$ , followed by rotations through  $\theta$  and then  $\phi$ , where  $\theta$  and  $\phi$  are defined respectively as the azimuthal and polar angles of a spherical polar coordinate frame whose  $z$ -axis is aligned with the periodic axis. A grid in  $(\gamma, \theta, \phi)$ -space was then constructed, and in each case the diffraction pattern was calculated and accumulated into an averaged pattern. This

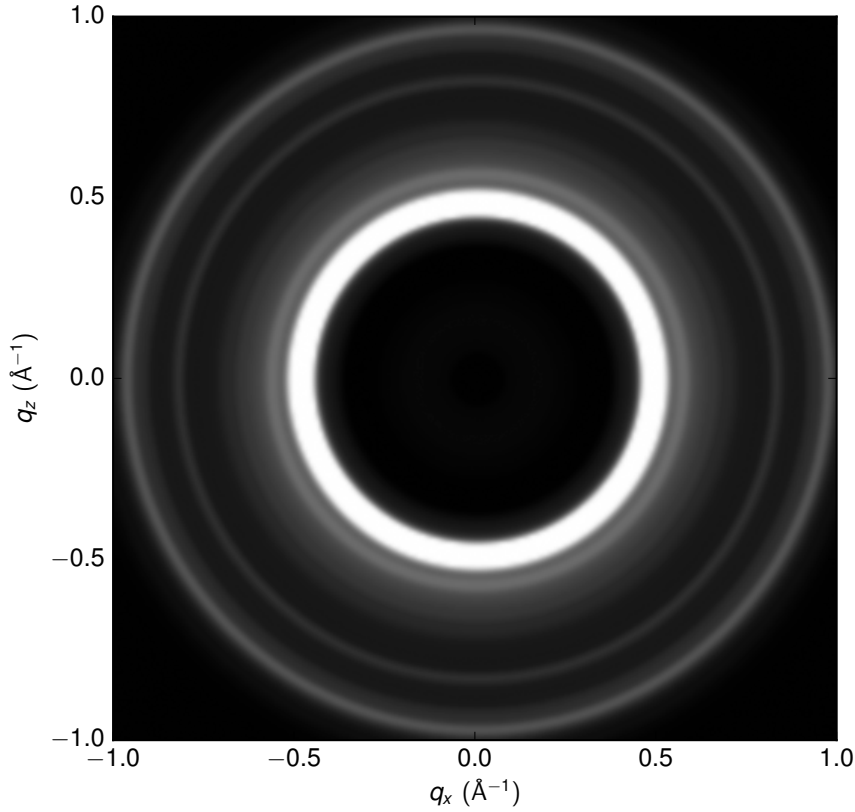


Figure 6.9 The diffraction pattern for a bundle of empty (9,9) SWNTs.

amounts to calculating the diffraction intensity via the following integral:

$$I \propto \int_0^{2\pi} \int_0^\pi \int_0^{2\pi} \langle |\tilde{\rho}_{\text{bundle}}|^2 \rangle |\tilde{\rho}_{\text{cell}}|^2 |\tilde{\rho}_{\text{latt}}|^2 \sin^2(\theta) d\gamma d\theta d\phi \quad (6.13)$$

Using this procedure, diffraction patterns were calculated for a bundle of the (9,9) nanotubes without any filling, and then filled as shown on fig. 6.2. The patterns are shown on figs. 6.9 and 6.10. As in the single-tube diffraction case, there are distinct differences between the filled and unfilled cases. The most prominent feature in both patterns is a bright ring at around  $0.5 \text{ \AA}$  corresponding to rotational averaging over the red spots visible on fig. 6.5. However, the diffraction pattern of the ENW bundle once again contains a number of features not present in that of the bundle of empty nanotubes, such as the rings visible at around  $0.25 \text{ \AA}$ . These results are, once again, promising with regard to the utility of using diffraction to analyse encapsulated nanowire systems: the diffraction pattern in the filled case is highly distinct from

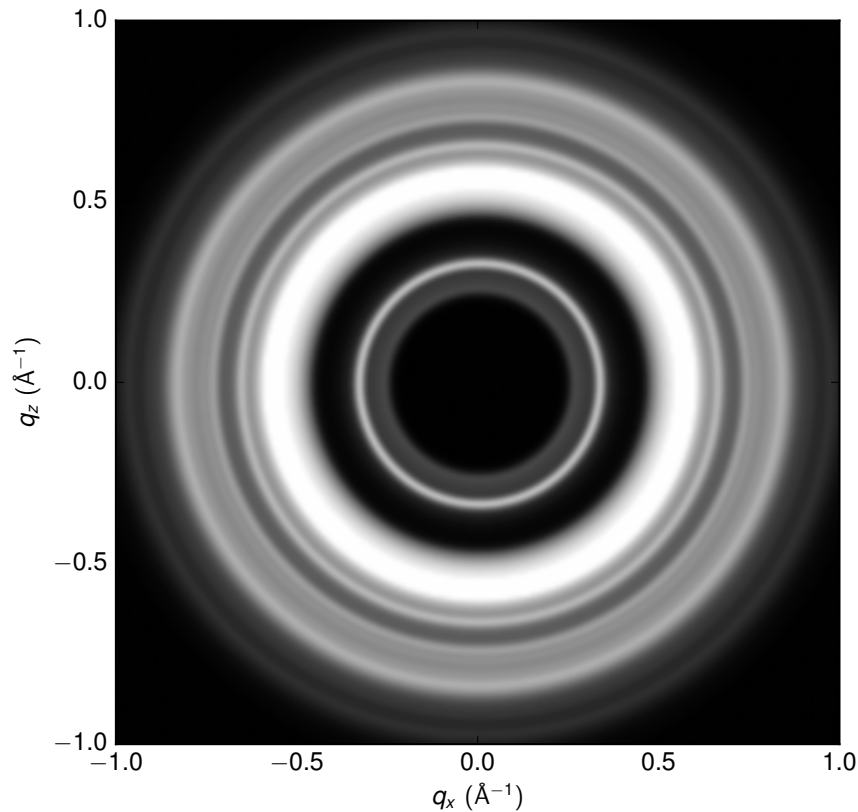


Figure 6.10 The diffraction pattern for a bundle of (9,9) carbon nanotubes filled with  $P4m2$  GeTe nanowires.

the unfilled case, in a way that will be sensitive to the particular structure of the nanowire.

## 6.2 Conclusion

In this chapter the behaviour of ENWs in diffraction experiments has been considered. A code has been written to calculate diffraction patterns for low-dimensional systems. In addition to the results described in this chapter, the code has also been used by collaborators to investigate diffraction in SnTe ENWs.

While there is relatively little experimental data on the diffraction patterns of extreme nanowires, the results presented in this chapter strongly suggest that diffraction experiments are a useful tool for investigating such systems, with clearly visible features arising from the nanowire. The resulting diffraction patterns have also been elucidated

by quantitatively decomposing them into the contributions from the nanotube and from the nanowire.

By parameterising a potential describing the dispersion interactions between SWNTs, and performing coarse-grained simulations of the dynamics of nanotube bundles using this potential, diffraction patterns have also been predicted in the case of bundles of ENWs. Once again, the results indicate that despite the presence of the nanotube, the diffraction pattern remains sensitive to the encapsulated nanowire.

The application of diffraction theory to bundles of ENWs could be extended in a number of ways beyond the methods presented in this chapter. For example, one could investigate the impact on the bundling (and, consequently, on the diffraction pattern) of having an ensemble of different chiralities within the bundle, or of the thermal motion of individual nanotubes and nanowires themselves. The method could also be applied to the case of a nanowire filled with amorphous GeTe, to assist with experimental observations of phase change in GeTe ENWs. Finally, the generality of the diffraction code written as part of this chapter means that any other ENW system of interest could also be investigated.

# Chapter 7

## Conclusion

In this thesis, the structures and properties of nanowires encapsulated inside carbon nanotubes have been considered. The AIRSS algorithm has been adapted to predict their structures with a computationally reasonable cost, using a hybrid approach to the symmetry of initial structures, a confining potential-based scheme to relax them, and then more accurate calculations inside an explicit nanotube with energetic corrections for strain. The PyAIRSS structure prediction code has been extended with an implementation of this functionality, and has been used to map out for the first time the ground-state phases of some ENW systems as a function of nanotube radius. The emphasis throughout has been on extreme nanowires: systems of almost atomically thin width, for which finite-size effects are at their most pronounced.

In chapter 3, the scheme was applied to GeTe. The low-energy phases were predicted, and those predictions were found to agree with experimental TEM imagery. Temperature-induced transitions between crystalline states were then identified via phonon calculations. The phase-change properties of GeTe ENWs were then studied using molecular dynamics calculations. It was found that GeTe retains its technologically useful phase-switching behaviour even in narrow ( $\sim 14$  Å) nanotubes, and with a lower melting point also, which makes GeTe ENWs potential components for low-power memory devices. The ferroelectricity of GeTe ENWs was then considered, using the Berry phase method of polarisation to compute lookup tables parameterising an Ising-like model. By applying Wang-Landau sampling to this model it was found that at the relevant operating temperatures for ferroelectric memory, encapsulated GeTe nanowires retain their polarisation even up to relatively long nanowire lengths.

One extension would be to repeat the phase-switching calculations with a more accurate interatomic potential, perhaps constructed using a more modern, machine learning-based scheme. This could be used to verify the predictions made regarding crystallisation and the glass transition in GeTe ENWs. The calculations on GeTe's ferroelectric properties could also be made more accurate by allowing each atom to polarise separately, which introduces more degrees of freedom than simply considering each unit cell in the nanowire to polarise as a whole according to a single variable. Additionally, one could introduce additional terms in the model Hamiltonian coupling each ferroelectric unit cell to the strain field, as was done in e.g. [279] for ferroelectric perovskites. Another possible avenue for further work would be to apply the scheme to GST (germanium tin telluride) as well, since GST is an intensively studied phase change material. An expensive but potentially fruitful option would be to consider the influence of the stoichiometry of GST on nanowire structure, though the full radius-dependent ternary diagram of GST ENWs may be computationally out of reach for a while yet.

A potential extension which applies to all ENW materials generically would be to investigate the role of defects. It is often seen in TEM images of encapsulated nanowires that the concentration of structural defects is quite high, both in the tube (often in the form of kinks) and in the wire [19, 16, 237, 16, 25, 280]. Following a structure search for 1D crystalline phases, AIRSS could be used to identify low-lying defects in those phases. This is particularly relevant to the case of GeTe, which in the bulk contains substantial concentrations of Ge vacancies, which function as acceptors by creating states at the top of the valence band and thereby lead to *p*-type conduction [281, 146]. Given the large variation in electronic structure that was identified in GeTe ENWs, it may be that this effect could differ in ENWs relative to the bulk, especially if the defect formation energies differ significantly as well.

Chapter 4 focused on AgCl ENWs, and on their vibrational properties. AIRSS was used to predict their ground state structures, including a more precise strain correction scheme that takes into account the dependence of the ground state nanowire periodicity on the radius of the nanotube. Again, this resulted in a number of new nanowire structures. A novel scheme was then developed to predict, at much less computational expense, the Raman spectra of systems which consist of weakly interacting subsystems. This scheme was used to predict the Raman spectroscopy of AgCl ENWs, in both the linear chain and  $P\bar{4}$  structures. In the former case, the calculation was also used

---

to identify the difference in the spectrum upon encapsulation inside a double-walled nanotube rather than a single-walled nanotube. While the scheme has only been applied to AgCl ENWs in this work, its generality means that it can be re-applied without modification to other encapsulated nanowire systems.

In chapter 5, MoSe<sub>2</sub> nanowires were considered. The structure search for this system resulted in a number of interesting structures, including some unusual behaviour in very narrow nanotubes at which the 2:1 stoichiometry makes it impossible for the material to bond properly, as a result of which an unusually large interaction with the nanotube is predicted. Bulk MoSe<sub>2</sub> is a layered material, and at larger nanotube radii, a number of structures derived from this bulk structure were observed, including a double-layered nanowire which distorts the nanotube significantly.

The effects of stress on MoSe<sub>2</sub> ENWs were then considered. A method was developed in which the surface of the nanotube is decomposed into a polygonal mesh, allowing the Cauchy stress forces on the system to be computed. Together with the second-order energy landscape extracted from a DFT phonon calculation, the elastic response of the system may then be obtained as a summation over contributions from each normal mode. By generalising the usual formula for the formation energy to account for the possibility of nanowire length change after a phase transition, a stress-radius phase diagram was then calculated for a point on the MoSe<sub>2</sub> phase diagram in the vicinity of a phase transition. It was found that anisotropic stresses of more than around a gigapascal can cause a significant shift in the critical nanotube radius for the phase transition, and also that encapsulation of MoSe<sub>2</sub> inside carbon nanotubes increases their resistance to applied stress in the transverse direction.

Finally, the diffraction properties of ENWs were studied. A diffraction code for systems of arbitrary periodicity was written, and the code was applied to GeTe ENWs to predict their diffraction spectra. It was found that due to the incommensurability of the nanotube and nanowire, the diffraction patterns of ENWs contain highly distinct contributions from the nanowire and the nanotube. To highlight these distinctions, diffraction patterns were decomposed into contributions from various subsystems – in this context, the nanotube and nanowire. Next, diffraction of bundles of ENWs rather than single ENWs were considered. Calculations within the Tkatchenko-Scheffler dispersion correction scheme were used to parameterise an effective inter-nanotube interaction potential. Under the approximation that the nanotubes remain aligned along their periodic axes, molecular dynamics calculations were performed on a bundle

of nanotubes, and from this the associated contribution to the diffraction pattern was obtained. Future work on this project could consist of relaxing the assumption regarding the collinearity of the nanotubes, and thereby obtaining a more accurate diffraction pattern. Additionally, one could consider the case of a bundle of nanotubes of differing chiralities, which is the most common situation experimentally.

More generally, AIRSS could be extended for other low-dimensional systems: for example, one could predict the structures of thin films using analogous methods to those employed here, with layer groups taking the place of rod groups.

There is still much more work to be done in the field of extreme nanowires. Though this project has uncovered examples of interesting new phenomena that result from encapsulation, it has only scratched the surface in terms of the full space of structures and behaviour that can arise. ENWs represent an exciting new frontier in nanoscience, and will no doubt yield many discoveries in the years to come.

# Bibliography

- [1] M. S. Dresselhaus *et al.*, “New directions for low-dimensional thermoelectric materials,” *Adv. Mater.*, vol. 19, no. 8, pp. 1043–1053, 2007.
- [2] A. D. Yoffe, “Semiconductor quantum dots and related systems: Electronic, optical, luminescence and related properties of low dimensional systems,” *Adv. Phys.*, vol. 50, no. 1, pp. 1–208, 2001.
- [3] A. I. Hochbaum *et al.*, “Enhanced thermoelectric performance of rough silicon nanowires,” *Nature*, vol. 451, no. 7175, pp. 163–167, 2008.
- [4] X. Duan, Y. Huang, Y. Cui, J. Wang, and C. M. Lieber, “Indium phosphide nanowires as building blocks for nanoscale electronic and optoelectronic devices,” *Nature*, vol. 409, no. 6816, pp. 66–69, 2001.
- [5] P. Krogstrup *et al.*, “Single-nanowire solar cells beyond the Shockley-Queisser limit,” *Nat. Photonics*, vol. 7, no. 4, pp. 306–310, 2013.
- [6] J. Xiang *et al.*, “Ge/Si nanowire heterostructures as high-performance field-effect transistors,” *Nature*, vol. 441, no. 7092, pp. 489–493, 2006.
- [7] A. C. Ferrari *et al.*, “Raman Spectrum of Graphene and Graphene Layers,” *Phys. Rev. Lett.*, vol. 97, no. 18, p. 187401, 2006.
- [8] P. Zhang, Y. Tan, Y. W. Stormer, H. L. Kim, “Experimental observation of the quantum Hall effect and Berry’s phase in graphene,” *Nature*, vol. 438, no. 7065, pp. 201–204, 2005.
- [9] M. Monthieux and V. L. Kuznetsov, “Who should be given the credit for the discovery of carbon nanotubes?” *Carbon*, vol. 44, no. 9, pp. 1621–1623, 2006.

- 
- [10] S. Iijima, “Helical microtubules of graphitic carbon,” *Nature*, vol. 354, no. 6348, pp. 56–58, 1991.
- [11] C. J. Pickard and R. J. Needs, “Ab initio random structure searching,” *J. Phys. Condens. Matter*, vol. 23, no. 5, p. 53201, 2011.
- [12] X. Sun, E. Thelander, J. W. Gerlach, U. Decker, and B. Rauschenbach, “Crystallization kinetics of GeTe phase-change thin films grown by pulsed laser deposition,” *J. Phys. D. Appl. Phys.*, vol. 48, no. 29, p. 295304, 2015.
- [13] B. Chen, D. De Wal, G. H. Ten Brink, G. Palasantzas, and B. J. Kooi, “Resolving Crystallization Kinetics of GeTe Phase-Change Nanoparticles by Ultrafast Calorimetry,” *Cryst. Growth Des.*, vol. 18, no. 2, pp. 1041–1046, 2018.
- [14] G. S. Pawley, W. Cochran, R. A. Cowley, and G. Dolling, “Diatomic ferroelectrics,” *Phys. Rev. Lett.*, vol. 17, no. 14, pp. 753–755, 1966.
- [15] R. D. King-Smith and D. Vanderbilt, “Theory of polarization of crystalline solids,” *Phys. Rev. B*, vol. 47, no. 3, pp. 1651–1654, 1993.
- [16] J. H. Spencer *et al.*, “Raman spectroscopy of optical transitions and vibrational energies of  $\sim 1$  nm HgTe extreme nanowires within single walled carbon nanotubes,” *ACS Nano*, vol. 8, no. 9, pp. 9044–9052, 2014.
- [17] M. Dresselhaus, G. Dresselhaus, R. Saito, and A. Jorio, “Raman spectroscopy of carbon nanotubes,” *Phys. Rep.*, vol. 409, no. 2, pp. 47–99, 2005.
- [18] A. Govindaraj, B. C. Satishkumar, M. Nath, and C. N. R. Rao, “Metal Nanowires and Intercalated Metal Layers in Single-Walled Carbon Nanotube Bundles,” *Chem. Mater.*, vol. 12, no. 1, pp. 202–205, 2000.
- [19] C. E. Giusca *et al.*, “Confined Crystals of the Smallest Phase-Change Material,” *Nano Lett.*, vol. 13, no. 9, pp. 4020–4027, 2013.
- [20] M. R. Pederson and J. Q. Broughton, “Nanocapillarity in fullerene tubules,” *Phys. Rev. Lett.*, vol. 69, no. 18, pp. 2689–2692, 1992.
- [21] P. M. Ajayan and S. Iijima, “Capillarity-induced filling of carbon nanotubes,” *Nature*, vol. 361, no. 6410, pp. 333–334, 1993.

- [22] R. D. Gately and M. in het Panhuis, "Filling of carbon nanotubes and nanofibres," *Beilstein J. Nanotechnol.*, vol. 6, no. 1, pp. 508–516, 2015.
- [23] G. Tobias, L. Shao, C. G. Salzmann, Y. Huh, and M. L. H. Green, "Purification and opening of carbon nanotubes using steam," *J. Phys. Chem. B*, vol. 110, no. 45, pp. 22 318–22 322, 2006.
- [24] S. Sandoval, E. Pach, B. Ballesteros, and G. Tobias, "Encapsulation of two-dimensional materials inside carbon nanotubes: Towards an enhanced synthesis of single-layered metal halides," *Carbon*, vol. 123, pp. 129–134, 2017.
- [25] P. V. Medeiros *et al.*, "Single-Atom Scale Structural Selectivity in Te Nanowires Encapsulated Inside Ultranarrow, Single-Walled Carbon Nanotubes," *ACS Nano*, vol. 11, no. 6, pp. 6178–6185, 2017.
- [26] T. Zhang, S. Mubeen, N. V. Myung, and M. A. Deshusses, "Recent progress in carbon nanotube-based gas sensors." *Nanotechnology*, vol. 19, no. 33, p. 332001, 2008.
- [27] C. Li *et al.*, "Complementary detection of prostate-specific antigen using  $\text{In}_2\text{O}_3$  nanowires and carbon nanotubes," *J. Am. Chem. Soc.*, vol. 127, no. 36, pp. 12 484–12 485, 2005.
- [28] T. Kawano *et al.*, "An electrothermal carbon nanotube gas sensor," *Nano Lett.*, vol. 7, no. 12, pp. 3686–3690, 2007.
- [29] G. Chimowa *et al.*, "Improving methane gas sensing properties of multi-walled carbon nanotubes by vanadium oxide filling," *Sens Actuators B Chem.*, vol. 247, pp. 11–18, 2017.
- [30] A. L. Elias *et al.*, "Production and characterization of single-crystal FeCo nanowires inside carbon nanotubes," *Nano Lett.*, vol. 5, no. 3, pp. 467–472, 2005.
- [31] G. Larrieu and X. L. Han, "Vertical nanowire array-based field effect transistors for ultimate scaling," *Nanoscale*, vol. 5, no. 6, pp. 2437–2441, 2013.
- [32] A. Fujiwara *et al.*, "Single electron tunneling transistor with tunable barriers using silicon nanowire metal-oxide-semiconductor field-effect transistor," *Appl. Phys. Lett.*, vol. 88, no. 5, pp. 1–3, 2006.

- 
- [33] R. S. Friedman, M. C. McAlpine, D. S. Ricketts, D. Ham, and C. M. Lieber, “Nanotechnology: High-speed integrated nanowire circuits,” *Nature*, vol. 434, no. 7037, p. 1085, 2005.
- [34] F. M. Brunbauer, E. Bertagnolli, J. Majer, and A. Lugstein, “Electrical transport properties of single-crystal Al nanowires,” *Nanotechnology*, vol. 27, no. 38, p. 385704, 2016.
- [35] V. Rodrigues and D. Ugarte, “Metal nanowires: atomic arrangement and electrical transport properties,” *Nanotechnology*, vol. 13, no. 3, pp. 404–408, 2002.
- [36] X. Q. Zhang, H. Li, and K. M. Liew, “The structures and electrical transport properties of germanium nanowires encapsulated in carbon nanotubes,” *J. Appl. Phys.*, vol. 102, no. 7, p. 073709, 2007.
- [37] N. Tombros *et al.*, “Charge transport in a single superconducting tin nanowire encapsulated in a multiwalled carbon nanotube,” *Nano Lett.*, vol. 8, no. 9, pp. 3060–3064, 2008.
- [38] T. W. Ebbesen *et al.*, “Electrical conductivity of individual carbon nanotubes,” *Nature*, vol. 382, no. 6586, pp. 54–56, 1996.
- [39] A. Lekawa-Raus, J. Patmore, L. Kurzepa, J. Bulmer, and K. Koziol, “Electrical properties of carbon nanotube based fibers and their future use in electrical wiring,” *Adv. Funct. Mater.*, vol. 24, no. 24, pp. 3661–3682, 2014.
- [40] C. Qiu *et al.*, “Scaling carbon nanotube complementary transistors to 5-nm gate lengths,” *Science*, vol. 355, no. 6322, pp. 271–276, 2017.
- [41] A. Vasylenko *et al.*, “Encapsulated nanowires: Boosting electronic transport in carbon nanotubes,” *Phys. Rev. B*, vol. 95, no. 12, p. 121408, 2017.
- [42] D. M. Sun *et al.*, “Flexible high-performance carbon nanotube integrated circuits,” *Nat. Nanotechnol.*, vol. 6, no. 3, pp. 156–161, 2011.
- [43] Y. Gao and Y. Bando, “Carbon nanothermometer containing gallium,” *Nature*, vol. 415, no. 6872, pp. 599–599, 2002.
- [44] H. Jiang, B. Liu, Y. Huang, and K. C. Hwang, “Thermal Expansion of Single Wall Carbon Nanotubes,” *J. Eng. Mater. Technol.*, vol. 126, no. 3, p. 265, 2004.

- [45] K. Svensson, H. Olin, and E. Olsson, "Nanopipettes for metal transport," *Phys. Rev. Lett.*, vol. 93, no. 14, p. 145901, 2004.
- [46] N. de Jonge and J.-M. Bonard, "Carbon nanotube electron sources and applications," *Philos. Trans. R. Soc. A Math. Phys. Eng. Sci.*, vol. 362, no. 1823, pp. 2239–2266, 2004.
- [47] W. Zhu, C. Bower, O. Zhou, G. Kochanski, and S. Jin, "Large current density from carbon nanotube field emitters," *Appl. Phys. Lett.*, vol. 75, no. 6, pp. 873–875, 1999.
- [48] R. Lv *et al.*, "Enhanced field emission of open-ended, thin-walled carbon nanotubes filled with ferromagnetic nanowires," *Carbon*, vol. 47, no. 11, pp. 2709–2715, 2009.
- [49] N. Du *et al.*, "Porous Co<sub>3</sub>O<sub>4</sub> Nanotubes Derived From Co<sub>4</sub>(CO)<sub>12</sub> Clusters on Carbon Nanotube Templates: A Highly Efficient Material For Li-Battery Applications," *Adv. Mater.*, vol. 19, no. 24, pp. 4505–4509, 2007.
- [50] X. H. Sun *et al.*, "Formation of silicon carbide Nanotubes and nanowires via reaction of silicon (from disproportionation of silicon monoxide) with carbon nanotubes," *J. Am. Chem. Soc.*, vol. 124, no. 48, pp. 14 464–14 471, 2002.
- [51] X. Zhao, Y. Ando, Y. Liu, M. Jinno, and T. Suzuki, "Carbon Nanowire Made of a Long Linear Carbon Chain Inserted Inside a Multiwalled Carbon Nanotube," *Phys. Rev. Lett.*, vol. 90, no. 18, p. 4, 2003.
- [52] A. Chuvilin *et al.*, "Self-assembly of a sulphur-terminated graphene nanoribbon within a single-walled carbon nanotube," *Nat. Mater.*, vol. 10, no. 9, pp. 687–692, 2011.
- [53] C. Li *et al.*, "In<sub>2</sub>O<sub>3</sub> nanowires as chemical sensors," *Appl. Phys. Lett.*, vol. 82, no. 10, pp. 1613–1615, 2003.
- [54] A. Kolmakov and M. Moskovits, "Chemical sensing and catalysis by one-dimensional metal-oxide nanostructures," *Annu. Rev. Mater. Res.*, vol. 34, no. 1, pp. 151–180, 2004.
- [55] G. Shen, P.-C. Chen, K. Ryu, and C. Zhou, "Devices and chemical sensing applications of metal oxide nanowires," *J. Mater. Chem.*, vol. 19, no. 7, pp. 828–839, 2009.

- [56] Z. Fan and J. G. Lu, "Chemical sensing with ZnO nanowire field-effect transistor," *IEEE Trans. Nanotechnol.*, vol. 5, no. 4, pp. 393–396, 2006.
- [57] H. Lu and C. Gang, "Analysis of optical absorption in silicon nanowire arrays for photovoltaic applications," *Nano Lett.*, vol. 7, no. 11, pp. 3249–3252, 2007.
- [58] K. Peng *et al.*, "Aligned single-crystalline Si nanowire arrays for photovoltaic applications," *Small*, vol. 1, no. 11, pp. 1062–1067, 2005.
- [59] B. Z. Tian *et al.*, "Coaxial silicon NWs as solar cells and nanoelectronic power sources," *Nature*, vol. 449, pp. 885–888, 2007.
- [60] Z. Fan *et al.*, "Three-dimensional nanopillar-array photovoltaics on low-cost and flexible substrates," *Nat. Mater.*, vol. 8, no. 8, pp. 648–653, 2009.
- [61] G. Brambilla, "Optical fibre nanowires and microwires: A review," *J. Opt.*, vol. 12, no. 4, p. 043001, 2010.
- [62] C. Frondel and U. B. Marvin, "Lonsdaleite, a hexagonal polymorph of diamond," *Nature*, vol. 214, no. 5088, pp. 587–589, 1967.
- [63] J. Robertson, "Amorphous carbon," *Adv. Phys.*, vol. 35, no. 4, pp. 317–374, 1986.
- [64] K. S. Novoselov *et al.*, "Electric field in atomically thin carbon films," *Science*, vol. 306, no. 5696, pp. 666–669, 2004.
- [65] D. R. Cooper *et al.*, "Experimental review of graphene," *ISRN Condens. Matter Phys.*, vol. 2012, pp. 1–56, 2011.
- [66] S. Reich, J. Maultzsch, C. Thomsen, and P. Ordejón, "Tight-binding description of graphene," *Phys. Rev. B*, vol. 66, no. 3, pp. 354 121–354 125, 2002.
- [67] K. S. Novoselov *et al.*, "Two-dimensional gas of massless Dirac fermions in graphene," *Nature*, vol. 438, no. 7065, pp. 197–200, 2005.
- [68] M. S. Dresselhaus, G. Dresselhaus, and R. Saito, "Physics of carbon nanotubes," *Carbon*, vol. 33, no. 7, pp. 883–891, 1995.
- [69] R. Saito, M. Fujita, G. Dresselhaus, and M. S. Dresselhaus, "Electronic structure of chiral graphene tubules," *Appl. Phys. Lett.*, vol. 60, no. 18, pp. 2204–2206, 1992.

- [70] L. Van Hove, “The occurrence of singularities in the elastic frequency distribution of a crystal,” *Phys. Rev.*, vol. 89, no. 6, pp. 1189–1193, 1953.
- [71] H. Kataura *et al.*, “Optical properties of single-wall carbon nanotubes,” *Synth. Met.*, vol. 103, no. 1-3, pp. 2555–2558, 1999.
- [72] F. Li, H. M. Cheng, S. Bai, G. Su, and M. S. Dresselhaus, “Tensile strength of single-walled carbon nanotubes directly measured from their macroscopic ropes,” *Appl. Phys. Lett.*, vol. 77, no. 20, pp. 3161–3163, 2000.
- [73] E. W. Wong, P. E. Sheehan, and C. M. Lieber, “Nanobeam mechanics: Elasticity, strength, and toughness of nanorods and nanotubes,” *Science*, vol. 277, no. 5334, pp. 1971–1975, 1997.
- [74] L. M. Ericson *et al.*, “Macroscopic, neat, single-walled carbon nanotube fibers,” *Science*, vol. 305, no. 5689, pp. 1447–1450, 2004.
- [75] N. M. Pugno, “Space elevator: out of order?” *Nano Today*, vol. 2, no. 6, pp. 44–47, 2007.
- [76] A. Bianco, K. Kostarelos, and M. Prato, “Applications of carbon nanotubes in drug delivery,” *Curr. Opin. Chem. Biol.*, vol. 9, no. 6, pp. 674–679, 2005.
- [77] Z. Liu, S. Tabakman, K. Welsher, and H. Dai, “Carbon nanotubes in biology and medicine: In vitro and in vivo detection, imaging and drug delivery,” *Nano Res.*, vol. 2, no. 2, pp. 85–120, 2009.
- [78] J. Dong and Q. Ma, “Advances in mechanisms and signaling pathways of carbon nanotube toxicity,” *Nanotoxicology*, vol. 9, no. 5, pp. 658–676, 2015.
- [79] J. Cumings and A. Zettl, “Low-friction nanoscale linear bearing realized from multiwall carbon nanotubes,” *Science*, vol. 289, no. 5479, pp. 602–604, 2000.
- [80] M. Born and R. Oppenheimer, “Zur Quantentheorie der Molekeln,” *Ann. Phys.*, vol. 389, no. 20, pp. 457–484, 1927.
- [81] R. M. Martin, *Electronic Structure: Basic Theory and Practical Methods*. Cambridge: Cambridge University Press, 2004.
- [82] P. A. M. Dirac, “On the theory of quantum mechanics,” in *R. Soc. London A Math. Phys. Eng. Sci.*, vol. 112, no. 762. Royal Society, 1926, pp. 661–677.

- [83] A. J. Cohen, P. Mori-Sánchez, and W. Yang, “Insights into current limitations of density functional theory,” *Science*, vol. 321, no. 5890, pp. 792–794, 2008.
- [84] J. C. Slater, “A simplification of the Hartree-Fock method,” *Phys. Rev.*, vol. 81, no. 3, pp. 385–390, 1951.
- [85] P. Hohenberg and W. Kohn, “Inhomogeneous Electron Gas,” *Phys. Rev.*, vol. 136, no. 3B, pp. B864–B871, 1964.
- [86] W. Kohn and L. J. Sham, “Self-Consistent Equations Including Exchange and Correlation Effects,” *Phys. Rev.*, vol. 140, no. 4A, pp. A1133–A1138, 1965.
- [87] J. P. Perdew and A. Zunger, “Self-interaction correction to density-functional approximations for many-electron systems,” *Phys. Rev. B*, vol. 23, no. 10, pp. 5048–5079, 1981.
- [88] J. P. Perdew, K. Burke, and M. Ernzerhof, “Generalized Gradient Approximation Made Simple,” *Phys. Rev. Lett.*, vol. 77, no. 18, pp. 3865–3868, 1996.
- [89] S. J. Clark *et al.*, “First principles methods using CASTEP,” *Zeitschrift für Krist.*, vol. 220, no. 5-6, pp. 567–570, 2005.
- [90] J. M. Soler *et al.*, “The SIESTA method for ab initio order-N materials simulation,” *J. Phys. Condens. Matter*, vol. 14, no. 11, pp. 2745–2779, 2002.
- [91] C. K. Skylaris, P. D. Haynes, A. A. Mostofi, and M. C. Payne, “Introducing ONETEP: Linear-scaling density functional simulations on parallel computers,” *J. Chem. Phys.*, vol. 122, no. 8, p. 084119, 2005.
- [92] F. Bloch, “Über die Quantenmechanik der Elektronen in Kristallgittern,” *Zeitschrift für Phys.*, vol. 52, no. 7-8, pp. 555–600, 1929.
- [93] H. Monkhorst and J. Pack, “Special points for Brillouin zone integrations,” *Phys. Rev. B*, vol. 13, no. 12, pp. 5188–5192, 1976.
- [94] D. Vanderbilt, “Optimally smooth norm-conserving pseudopotentials,” *Phys. Rev. B*, vol. 32, no. 12, pp. 8412–8415, 1985.
- [95] N. Ramer and A. Rappe, “Designed nonlocal pseudopotentials for enhanced transferability,” *Phys. Rev. B*, vol. 59, no. 19, pp. 12 471–12 478, 1999.

- [96] N. Troullier and J. Martins, “A straightforward method for generating soft transferable pseudopotentials,” *Solid State Commun.*, vol. 74, no. 7, pp. 613–616, 1990.
- [97] D. Hamann, M. Schlüter, and C. Chiang, “Norm-Conserving Pseudopotentials,” *Phys. Rev. Lett.*, vol. 43, no. 20, pp. 1494–1497, 1979.
- [98] D. Vanderbilt, “Soft self-consistent pseudopotentials in a generalized eigenvalue formalism,” *Phys. Rev. B*, vol. 41, no. 11, pp. 7892–7895, 1990.
- [99] K. Refson, P. R. Tulip, and S. J. Clark, “Variational density-functional perturbation theory for dielectrics and lattice dynamics,” *Phys. Rev. B*, vol. 73, no. 15, 2006.
- [100] R. P. Feynman, “Forces in molecules,” *Phys. Rev.*, vol. 56, no. 4, pp. 340–343, 1939.
- [101] D. C. Liu and J. Nocedal, “On the limited memory BFGS method for large scale optimization,” *Math. Program.*, vol. 45, no. 1-3, pp. 503–528, 1989.
- [102] X. Gonze and C. Lee, “Dynamical matrices, Born effective charges, dielectric permittivity tensors, and interatomic force constants from density-functional perturbation theory,” *Phys. Rev. B*, vol. 55, no. 16, pp. 10 355–10 367, 1997.
- [103] C. Kittel and H. Y. Fan, “Introduction to Solid State Physics,” *Am. J. Phys.*, vol. 25, no. 5, pp. 330–330, 1957.
- [104] A. Debernardi, S. Baroni, and E. Molinari, “Anharmonic phonon lifetimes in semiconductors from density-functional perturbation theory,” *Phys. Rev. Lett.*, vol. 75, no. 9, pp. 1819–1822, 1995.
- [105] O. K. Al-Mushadani and R. J. Needs, “Free-energy calculations of intrinsic point defects in silicon,” *Phys. Rev. B*, vol. 68, no. 23, p. 235205, 2003.
- [106] E. Smith and G. Dent, *Modern Raman Spectroscopy - A Practical Approach*. John Wiley & Sons, Ltd, 2005.
- [107] J. R. Ferraro, K. Nakamoto, and C. W. Brown, *Introductory Raman spectroscopy*. Academic Press, 2003.

- [108] S. Brown *et al.*, “Anti-Stokes Raman spectra of single-walled carbon nanotubes,” *Phys. Rev. B*, vol. 61, no. 8, pp. R5137–R5140, 2000.
- [109] M. P. Allen, “Introduction to Molecular Dynamics Simulation,” in *Computational Soft Matter From Synthetic Polymers to Proteins, Lecture Notes*, vol. 23. John von Neumann Institute for Computing, 2004, pp. 1–28.
- [110] J. Behler and M. Parrinello, “Generalized neural-network representation of high-dimensional potential-energy surfaces,” *Phys. Rev. Lett.*, vol. 98, no. 14, p. 146401, 2007.
- [111] J. Behler, “Atom-centered symmetry functions for constructing high-dimensional neural network potentials,” *J. Chem. Phys.*, vol. 134, no. 7, p. 074106, 2011.
- [112] A. P. Bartók, M. C. Payne, R. Kondor, and G. Csányi, “Gaussian approximation potentials: The accuracy of quantum mechanics, without the electrons,” *Phys. Rev. Lett.*, vol. 104, no. 13, p. 136403, 2010.
- [113] A. P. Bartók, R. Kondor, and G. Csányi, “On representing chemical environments,” *Phys. Rev. B*, vol. 87, no. 18, p. 184115, 2013.
- [114] N. L. Abraham and M. I. Probert, “A periodic genetic algorithm with real-space representation for crystal structure and polymorph prediction,” *Phys. Rev. B*, vol. 73, no. 22, 2006.
- [115] Y. Wang, J. Lv, L. Zhu, and Y. Ma, “CALYPSO: A method for crystal structure prediction,” *Comput. Phys. Commun.*, vol. 183, no. 10, pp. 2063–2070, 2012.
- [116] D. J. Wales and J. P. Doye, “Global optimization by basin-hopping and the lowest energy structures of Lennard-Jones clusters containing up to 110 atoms,” *J. Phys. Chem. A*, vol. 101, no. 28, pp. 5111–5116, 1997.
- [117] G. G. Rondina and J. L. Da Silva, “Revised basin-hopping monte carlo algorithm for structure optimization of clusters and nanoparticles,” *J. Chem. Inf. Model.*, vol. 53, no. 9, pp. 2282–2298, 2013.
- [118] M. C. Prentiss, D. J. Wales, and P. G. Wolynes, “Protein structure prediction using basin-hopping,” *J. Chem. Phys.*, vol. 128, no. 22, p. 225106, 2008.

- [119] S. Goedecker, “Minima hopping: An efficient search method for the global minimum of the potential energy surface of complex molecular systems,” *J. Chem. Phys.*, vol. 120, no. 21, pp. 9911–9917, 2004.
- [120] M. Amsler and S. Goedecker, “Crystal structure prediction using the minima hopping method,” *J. Chem. Phys.*, vol. 133, no. 22, p. 224104, 2010.
- [121] K. Bao, S. Goedecker, K. Koga, F. Lançon, and A. Neelov, “Structure of large gold clusters obtained by global optimization using the minima hopping method,” *Phys. Rev. B*, vol. 79, no. 4, p. 041405, 2009.
- [122] C. J. Pickard and R. J. Needs, “Structure of phase III of solid hydrogen,” *Nat. Phys.*, vol. 3, no. 7, pp. 473–476, 2007.
- [123] C. J. Pickard and R. J. Needs, “Aluminium at terapascal pressures,” *Nat Mater.*, vol. 9, no. 8, pp. 624–627, 2010.
- [124] C. J. Pickard and R. J. Needs, “Highly compressed ammonia forms an ionic crystal,” *Nat Mater.*, vol. 7, no. 10, pp. 775–779, 2008.
- [125] C. J. Pickard and R. J. Needs, “High-Pressure Phases of Silane,” *Phys. Rev. Lett.*, vol. 97, no. 4, p. 045504, 2006.
- [126] M. Mayo, K. J. Griffith, C. J. Pickard, and A. J. Morris, “Ab Initio Study of Phosphorus Anodes for Lithium- and Sodium-Ion Batteries,” *Chem. Mater.*, vol. 28, no. 7, pp. 2011–2021, 2016.
- [127] K. A. See *et al.*, “Ab Initio Structure Search and in Situ  $^7\text{Li}$  NMR Studies of Discharge Products in the Li–S Battery System,” *J. Am. Chem. Soc.*, vol. 136, no. 46, pp. 16 368–16 377, 2014.
- [128] H. Jung *et al.*, “Elucidation of the Local and Long-Range Structural Changes that Occur in Germanium Anodes in Lithium-Ion Batteries,” *Chem. Mater.*, vol. 27, no. 3, pp. 1031–1041, 2015.
- [129] A. J. Morris, C. P. Grey, and C. J. Pickard, “Thermodynamically stable lithium silicides and germanides from density functional theory calculations,” *Phys. Rev. B*, vol. 90, no. 5, p. 054111, 2014.

- [130] A. J. Morris, C. J. Pickard, and R. J. Needs, “Hydrogen/nitrogen/oxygen defect complexes in silicon from computational searches,” *Phys. Rev. B*, vol. 80, no. 14, p. 144112, 2009.
- [131] A. J. Morris, R. J. Needs, E. Salager, C. P. Grey, and C. J. Pickard, “Lithiation of silicon via lithium Zintl-defect complexes from first principles,” *Phys. Rev. B*, vol. 87, no. 17, p. 174108, 2013.
- [132] J. Mulroue, A. J. Morris, and D. M. Duffy, “Ab initio study of intrinsic defects in zirconolite,” *Phys. Rev. B*, vol. 84, no. 9, p. 094118, 2011.
- [133] R. W. G. Wyckoff, *The Analytical Expression of the Results of the Theory of Space Groups*. Carnegie Institution of Washington, 1922.
- [134] J. W. Wright, “The change-making problem,” *J. Assoc. Comput. Mach.*, vol. 22, no. 1, pp. 125–128, 1975.
- [135] A. Togo, “Spglib,” accessed 2016-06-20. URL: <http://atztogo.github.io/spglib/>
- [136] A. L. Spek, “Single-crystal structure validation with the program PLATON,” *J. Appl. Crystallogr.*, vol. 36, no. 1, pp. 7–13, 2003.
- [137] V. Kopský and D. B. Litvin, Eds., *International Tables for Crystallography, Vol. E*. International Union of Crystallography, 2010.
- [138] M. I. Aroyo *et al.*, “Bilbao Crystallographic Server: I. Databases and crystallographic computing programs,” *Zeitschrift für Krist.*, vol. 221, no. 1, pp. 15–27, 2006.
- [139] M. I. Aroyo *et al.*, “Crystallography online: Bilbao crystallographic server,” *Bulg. Chem. Commun.*, vol. 43, no. 2, pp. 183–197, 2011.
- [140] M. I. Aroyo, A. Kirov, C. Capillas, J. M. Perez-Mato, and H. Wondratschek, “Bilbao Crystallographic Server. II. Representations of crystallographic point groups and space groups,” *Acta Crystallogr. A*, vol. 62, no. 2, pp. 115–128, 2006.
- [141] G. Bruns *et al.*, “Nanosecond switching in GeTe phase change memory cells,” *Appl. Phys. Lett.*, vol. 95, no. 4, p. 43108, 2009.

- [142] P. Nukala, C.-C. Lin, R. Composto, and R. Agarwal, “Ultralow-power switching via defect engineering in germanium telluride phase-change memory devices.” *Nat. Commun.*, vol. 7, p. 10482, 2016.
- [143] W. W. Koelmans *et al.*, “Projected phase-change memory devices.” *Nat. Commun.*, vol. 6, p. 8181, 2015.
- [144] J. Y. Raty *et al.*, “Aging mechanisms in amorphous phase-change materials.” *Nat. Commun.*, vol. 6, p. 7467, 2015.
- [145] K. Shportko *et al.*, “Resonant bonding in crystalline phase-change materials,” *Nat. Mater.*, vol. 7, no. 8, pp. 653–658, 2008.
- [146] A. H. Edwards *et al.*, “Electronic structure of intrinsic defects in crystalline germanium telluride,” *Phys. Rev. B*, vol. 73, no. 4, p. 45210, 2006.
- [147] G. C. Sosso, G. Miceli, S. Caravati, J. Behler, and M. Bernasconi, “Neural network interatomic potential for the phase change material GeTe,” *Phys. Rev. B*, vol. 85, no. 17, p. 174103, 2012.
- [148] J. Akola and R. O. Jones, “Structural phase transitions on the nanoscale: The crucial pattern in the phase-change materials  $\text{Ge}_2\text{Sb}_2\text{Te}_5$  and GeTe,” *Phys. Rev. B*, vol. 76, no. 23, p. 235201, 2007.
- [149] S. Gabardi *et al.*, “Atomistic Simulations of the Crystallization and Aging of GeTe Nanowires,” *J. Phys. Chem. C*, vol. 121, no. 42, pp. 23 827–23 838, 2017.
- [150] J. Akola *et al.*, “Experimentally constrained density-functional calculations of the amorphous structure of the prototypical phase-change material  $\text{Ge}_2\text{Sb}_2\text{Te}_5$ ,” *Phys. Rev. B*, vol. 80, no. 2, p. 020201, 2009.
- [151] K. S. Andrikopoulos, S. N. Yannopoulos, A. V. Kolobov, P. Fons, and J. Tominaga, “Raman scattering study of GeTe and  $\text{Ge}_2\text{Sb}_2\text{Te}_5$  phase-change materials,” *J. Phys. Chem. Solids*, vol. 68, no. 5-6, pp. 1074–1078, 2007.
- [152] J. M. Skelton, A. R. Pallipurath, T. H. Lee, and S. R. Elliott, “Atomistic origin of the enhanced crystallization speed and n-type conductivity in Bi-doped Ge-Sb-Te phase-change materials,” *Adv. Funct. Mater.*, vol. 24, no. 46, pp. 7291–7300, 2014.

- [153] S. Raoux *et al.*, “Phase-change random access memory: A scalable technology,” *IBM J. Res. Dev.*, vol. 52, no. 4.5, pp. 465–479, 2008.
- [154] A. Lacaita *et al.*, “Electrothermal and phase-change dynamics in chalcogenide-based memories,” in *IEDM Technical Digest. IEEE International Electron Devices Meeting*, 2004, pp. 3–6.
- [155] D. S. Chao *et al.*, “Low programming current phase change memory cell with double GST thermally confined structure,” in *International Symposium on VLSI Technology, Systems, and Applications, Proceedings*, 2007.
- [156] M. Wuttig and N. Yamada, “Phase-change materials for rewriteable data storage,” *Nat. Mater.*, vol. 6, no. 11, pp. 824–832, 2007.
- [157] M. A. Caldwell, S. Raoux, R. Y. Wang, H.-S. Philip Wong, and D. J. Milliron, “Synthesis and size-dependent crystallization of colloidal germanium telluride nanoparticles,” *J. Mater. Chem.*, vol. 20, no. 7, p. 1285, 2010.
- [158] P. Nukala *et al.*, “Direct observation of metal-insulator transition in single-crystalline germanium telluride nanowire memory devices prior to amorphization,” *Nano Lett.*, vol. 14, no. 4, pp. 2201–2209, 2014.
- [159] A. T. Jennings, Y. Jung, J. Engel, and R. Agarwal, “Diameter-controlled synthesis of phase-change germanium telluride nanowires via the vapor-liquid-solid mechanism,” *J. Phys. Chem. C*, vol. 113, no. 17, pp. 6898–6901, 2009.
- [160] D. Yu, J. Wu, Q. Gu, and H. Park, “Germanium Telluride Nanowires and Nanohelices with Memory-Switching Behavior,” *J. Am. Chem. Soc.*, vol. 128, no. 25, pp. 8148–8149, 2006.
- [161] M.-K. Lee, T. G. Kim, B.-K. Ju, and Y.-M. Sung, “Bismuth Seed-Assisted Liquid-Phase Synthesis of Germanium Telluride Nanowires,” *Cryst. Growth Des.*, vol. 9, no. 2, pp. 938–941, 2009.
- [162] J. W. L. Yim, B. Xiang, and J. Wu, “Sublimation of GeTe Nanowires and Evidence of Its Size Effect Studied by in Situ TEM,” *J. Am. Chem. Soc.*, vol. 131, no. 40, pp. 14 526–14 530, 2009.
- [163] D. Yu, J. Wu, Q. Gu, and H. Park, “Germanium Telluride Nanowires and Nanohelices with Memory-Switching Behavior,” *J. Am. Chem. Soc.*, vol. 128, no. 25, pp. 8148–8149, 2006.

- [164] C. Sun, P. Chen, and S. Zhou, “AgCl nanoparticle nanowires fabricated by template method,” *Mater. Lett.*, vol. 61, no. 8, pp. 1645–1648, 2007.
- [165] S. H. Lee, D. K. Ko, Y. Jung, and R. Agarwal, “Size-dependent phase transition memory switching behavior and low writing currents in GeTe nanowires,” *Appl. Phys. Lett.*, vol. 89, no. 22, p. 223116, 2006.
- [166] E. F. Steigmeier and G. Harbeke, “Soft phonon mode and ferroelectricity in GeTe,” *Solid State Commun.*, vol. 8, no. 16, pp. 1275–1279, 1970.
- [167] T. Hayashi *et al.*, “Smallest freestanding single-walled carbon nanotube,” *Nano Lett.*, vol. 3, no. 7, pp. 887–889, 2003.
- [168] A. Gómez-Rodríguez, L. M. Beltrán-del Río, and R. Herrera-Becerra, “SimulaTEM: Multislice simulations for general objects,” *Ultramicroscopy*, vol. 110, no. 2, pp. 95–104, 2010.
- [169] A. Tkatchenko and M. Scheffler, “Accurate molecular van der Waals interactions from ground-state electron density and free-atom reference data,” *Phys. Rev. Lett.*, vol. 102, no. 7, p. 073005, 2009.
- [170] X. Wang, S. Scandolo, and R. Car, “Carbon phase diagram from ab initio molecular dynamics,” *Phys. Rev. Lett.*, vol. 95, no. 18, p. 185701, 2005.
- [171] L. K. Béland, P. Brommer, F. El-Mellouhi, J. F. Joly, and N. Mousseau, “Kinetic activation-relaxation technique,” *Phys. Rev. E*, vol. 84, no. 4, p. 046704, 2011.
- [172] A. V. Kolobov *et al.*, “Understanding the phase change mechanism of rewritable optical media,” *Nat. Mater.*, vol. 3, pp. 703–708, 2004.
- [173] M. Chen, K. A. Rubin, and R. W. Barton, “Compound materials for reversible, phase-change optical data storage,” *Appl. Phys. Lett.*, vol. 49, no. 9, pp. 502–504, 1986.
- [174] T. Siegrist *et al.*, “Disorder-induced localization in crystalline phase-change materials,” *Nat. Mater.*, vol. 10, no. 3, pp. 202–208, 2011.
- [175] X. Sun, B. Yu, G. Ng, and M. Meyyappan, “One-dimensional phase-change nanostructure: Germanium telluride nanowire,” *J. Phys. Chem. C*, vol. 111, no. 6, pp. 2421–2425, 2007.

- [176] S. H. Lee, Y. Jung, and R. Agarwal, “Highly scalable non-volatile and ultra-low-power phase-change nanowire memory,” *Nat. Nanotechnol.*, vol. 2, no. 10, pp. 626–630, 2007.
- [177] A. L. Lacaíta, “Phase change memories: State-of-the-art, challenges and perspectives,” *Solid. State. Electron.*, vol. 50, no. 1, pp. 24–31, 2006.
- [178] R. Mantovan *et al.*, “Atomic-scale study of the amorphous-to-crystalline phase transition mechanism in GeTe thin films,” *Sci. Rep.*, vol. 7, no. 1, p. 8234, 2017.
- [179] F. Zipoli and A. Curioni, “Reactive potential for the study of phase-change materials: GeTe,” *New J. Phys.*, vol. 15, 2013.
- [180] F. Zipoli, D. Krebs, and A. Curioni, “Structural origin of resistance drift in amorphous GeTe,” *Phys. Rev. B*, vol. 93, no. 11, p. 115201, 2016.
- [181] J. Tersoff, “New empirical approach for the structure and energy of covalent systems,” *Phys. Rev. B*, vol. 37, no. 12, pp. 6991–7000, 1988.
- [182] S. R. Billeter, A. Curioni, D. Fischer, and W. Andreoni, “Ab initio derived augmented Tersoff potential for silicon oxynitride compounds and their interfaces with silicon,” *Phys. Rev. B*, vol. 73, no. 15, 2006.
- [183] R. F. Brebrick, “Partial pressures in equilibrium with group IV tellurides. III. Germanium telluride,” *J. Chem. Phys.*, vol. 41, no. 4, pp. 1140–1146, 1964.
- [184] H. Wiedemeier and P. A. Siemers, “The Thermal Expansion of GeS and GeTe,” *Z. Allorg. Alg. Chem.*, vol. 431, no. 1, pp. 299–304, 1977.
- [185] T. Nonaka, G. Ohbayashi, Y. Toriumi, Y. Mori, and H. Hashimoto, “Crystal structure of GeTe and Ge<sub>2</sub>Sb<sub>2</sub>Te<sub>5</sub> meta-stable phase,” *Thin Solid Films*, vol. 370, no. 1, pp. 258–261, 2000.
- [186] S. Plimpton, “Fast parallel algorithms for short-range molecular dynamics,” *J. Comput. Phys.*, vol. 117, no. 1, pp. 1–19, 1995.
- [187] S. Raoux, H. Y. Cheng, M. A. Caldwell, and H.-S. S. Wong, “Crystallization times of Ge-Te phase change materials as a function of composition,” *Appl. Phys. Lett.*, vol. 95, no. 7, p. 071910, 2009.

- [188] G. C. Sosso, J. Behler, and M. Bernasconi, “Breakdown of Stokes-Einstein relation in the supercooled liquid state of phase change materials,” *Phys. status solidi*, vol. 249, no. 10, pp. 1880–1885, 2012.
- [189] M. D. Ediger, P. Harrowell, and L. Yu, “Crystal growth kinetics exhibit a fragility-dependent decoupling from viscosity,” *J. Chem. Phys.*, vol. 128, no. 3, p. 034709, 2008.
- [190] S. Nosé, “A unified formulation of the constant temperature molecular dynamics methods,” *J. Chem. Phys.*, vol. 81, no. 1, pp. 511–519, 1984.
- [191] W. G. Hoover, “Canonical dynamics: Equilibrium phase-space distributions,” *Phys. Rev. A*, vol. 31, no. 3, pp. 1695–1697, 1985.
- [192] P. J. Steinhardt, D. R. Nelson, and M. Ronchetti, “Icosahedral Bond Orientational Order in Supercooled Liquids,” *Phys. Rev. Lett.*, vol. 47, no. 18, pp. 1297–1300, 1981.
- [193] G. A. Tribello, M. Bonomi, D. Branduardi, C. Camilloni, and G. Bussi, “PLUMED 2: New feathers for an old bird,” *Comput. Phys. Commun.*, vol. 185, no. 2, pp. 604–613, 2014.
- [194] W. S. Cleveland, “LOWESS : A Program for Smoothing Locally Weighted Regression,” *Am. Stat.*, vol. 35, no. 1, 1981.
- [195] G. C. Sosso, M. Salvalaglio, J. Behler, M. Bernasconi, and M. Parrinello, “Heterogeneous crystallization of the phase change material GeTe via atomistic simulations,” *J. Phys. Chem. C*, vol. 119, no. 11, pp. 6428–6434, 2015.
- [196] C. V. Thompson and F. Spaepen, “On the approximation of the free energy change on crystallization,” *Acta Metall.*, vol. 27, no. 12, pp. 1855–1859, 1979.
- [197] M. Goldstein, “Viscous liquids and the glass transition. V. Sources of the excess specific heat of the liquid,” *J. Chem. Phys.*, vol. 64, no. 11, pp. 4767–4774, 1976.
- [198] N. O. Birge and S. R. Nagel, “Specific-heat spectroscopy of the glass transition,” *Phys. Rev. Lett.*, vol. 54, no. 25, pp. 2674–2677, 1985.
- [199] M. D. Ediger, C. A. Angell, and S. R. Nagel, “Supercooled liquids and glasses,” *J. Phys. Chem.*, vol. 100, no. 31, pp. 13 200–13 212, 1996.

- [200] M. J. Richardson and N. G. Savill, "Derivation of accurate glass transition temperatures by differential scanning calorimetry," *Polymer*, vol. 16, no. 10, pp. 753–757, 1975.
- [201] Y. P. Handa and D. D. Klug, "Heat capacity and glass transition behavior of amorphous ice," *J. Phys. Chem.*, vol. 92, no. 12, pp. 3323–3325, 1988.
- [202] A. R. C. Baljon, M. H. M. Van Weert, R. B. Degraaff, and R. Khare, "Glass transition behavior of polymer films of nanoscopic dimensions," *Macromolecules*, vol. 38, no. 6, pp. 2391–2399, 2005.
- [203] W. E. Wallace, J. H. Van Zanten, and W. L. Wu, "Influence of an impenetrable interface on a polymer glass-transition temperature," *Phys. Rev. E*, vol. 52, no. 4, pp. R3329–R3332, 1995.
- [204] G. Beaucage, R. Composto, and R. S. Stein, "Ellipsometric study of the glass transition and thermal expansion coefficients of thin polymer films," *J. Polym. Sci. B*, vol. 31, no. 3, pp. 319–326, 1993.
- [205] R. Busch, E. Bakke, and W. L. Johnson, "Viscosity of the supercooled liquid and relaxation at the glass transition of the  $Zr_{46.75}Ti_{8.25}Cu_{7.5}Ni_{10}Be_{27.5}$  bulk metallic glass forming alloy," *Acta Mater.*, vol. 46, no. 13, pp. 4725–4732, 1998.
- [206] C. T. Moynihan, "Correlation between the Width of the Glass Transition Region and the Temperature Dependence of the Viscosity of High-Tg Glasses," *J. Am. Ceram. Soc.*, vol. 76, no. 5, pp. 1081–1087, 1993.
- [207] I. Hughes and T. P. A. Hase, *Measurements and their uncertainties: a practical guide to modern error analysis*. Oxford University Press, 2010.
- [208] A. Fantini *et al.*, "Comparative assessment of GST and GeTe materials for application to embedded phase-change memory devices," in *2009 IEEE International Memory Workshop*. IEEE, 2009, pp. 1–2.
- [209] W. L. Johnson *et al.*, "Beating crystallization in glass-forming metals by millisecond heating and processing," *Science*, vol. 332, no. 6031, pp. 828–833, 2011.
- [210] L. Perniola *et al.*, "Electrical behavior of phase-change memory cells based on GeTe," *IEEE Electron Device Lett.*, vol. 31, no. 5, pp. 488–490, 2010.

- [211] P. G. Debenedetti and F. H. Stillinger, “Supercooled liquids and the glass transition,” *Nature*, vol. 410, no. 6825, pp. 259–267, 2001.
- [212] “JEDEC Standard No. 79F: Double Data Rate (DDR) SDRAM Specification,” 2008, accessed 2018-04-05. URL: <http://www.jedec.org/sites/default/files/docs/JESD79F.pdf>
- [213] P. Thanigai and W. Goh, “Maximizing Write Speed on the MSP430™ FRAM,” 2011, accessed 2018-06-26. URL: <http://www.ti.com/lit/an/slaa498b/slaa498b.pdf>
- [214] G. Niu, G. Saint-Girons, and B. Vilquin, “Epitaxial systems combining oxides and semiconductors,” in *Mol. Beam Ep.* Elsevier, 2013, pp. 451–475.
- [215] R. Guo *et al.*, “Non-volatile memory based on the ferroelectric photovoltaic effect,” *Nat. Commun.*, vol. 4, no. 1, p. 1990, 2013.
- [216] E. I. Blount, “Formalisms of Band Theory,” *Solid State Phys. - Adv. Res. Appl.*, vol. 13, pp. 305–373, 1962.
- [217] P. Giannozzi *et al.*, “QUANTUM ESPRESSO: A modular and open-source software project for quantum simulations of materials,” *J. Phys. Condens. Matter*, vol. 21, no. 39, p. 395502, 2009.
- [218] P. Giannozzi *et al.*, “Advanced capabilities for materials modelling with Quantum ESPRESSO,” *J. Phys. Condens. Matter*, vol. 29, no. 46, p. 465901, 2017.
- [219] D. J. Griffiths and C. Inglefield, *Introduction to Electrodynamics*. Prentice Hall, 2005.
- [220] T. Chattopadhyay, J. X. Boucherle, and H. G. von Schnering, “Neutron diffraction study on the structural phase transition in GeTe,” *J. Phys. C Solid State Phys.*, vol. 20, no. 10, pp. 1431–1440, 1987.
- [221] M. Lilienblum and E. Soergel, “Determination of the effective coercive field of ferroelectrics by piezoresponse force microscopy,” in *J. Appl. Phys.*, vol. 110, no. 5. American Institute of Physics, 2011, p. 052012.
- [222] W. J. Hu *et al.*, “Universal ferroelectric switching dynamics of vinylidene fluoride-trifluoroethylene copolymer films,” *Sci. Rep.*, vol. 4, no. 1, p. 4772, 2014.

- [223] A. M. Ferrenberg and R. H. Swendsen, “New Monte Carlo technique for studying phase transitions,” *Phys. Rev. Lett.*, vol. 61, no. 23, pp. 2635–2638, 1988.
- [224] F. Wang and D. P. Landau, “Determining the density of states for classical statistical models: A random walk algorithm to produce a flat histogram,” *Phys. Rev. E*, vol. 64, no. 5, p. 16, 2001.
- [225] C. H. Chan, G. Brown, and P. A. Rikvold, “Macroscopically constrained Wang-Landau method for systems with multiple order parameters and its application to drawing complex phase diagrams,” *Phys. Rev. E*, vol. 95, no. 5, p. 053302, 2017.
- [226] R. E. Belardinelli and V. D. Pereyra, “Wang-Landau algorithm: A theoretical analysis of the saturation of the error,” *J. Chem. Phys.*, vol. 127, no. 18, p. 184105, 2007.
- [227] R. E. Belardinelli, S. Manzi, and V. D. Pereyra, “Analysis of the convergence of the  $1/t$  and Wang-Landau algorithms in the calculation of multidimensional integrals,” *Phys. Rev. E*, vol. 78, no. 6, p. 067701, 2008.
- [228] M. Matsumoto and T. Nishimura, “Mersenne twister: a 623-dimensionally equidistributed uniform pseudo-random number generator,” *ACM Trans. Model. Comput. Simul.*, vol. 8, no. 1, pp. 3–30, 1998.
- [229] E. Y. Tsybal and A. Gruverman, “Ferroelectric tunnel junctions: Beyond the barrier,” *Nat. Mater.*, vol. 12, no. 7, pp. 602–604, 2013.
- [230] D. J. Wilson, A. A. Sokol, S. A. French, and C. R. Catlow, “Defect structures in the silver halides,” *Phys. Rev. B*, vol. 77, no. 6, p. 064115, 2008.
- [231] R. D. Fouchaux and R. O. Simmons, “Measurements of thermal expansion and thermal equilibrium defects in silver chloride,” *Phys. Rev.*, vol. 136, no. 6A, pp. A1664–A1674, 1964.
- [232] H. Tomonaga and T. Morimoto, “Photochromic coatings including silver halide microcrystals via sol-gel process,” *Thin Solid Films*, vol. 392, no. 2, pp. 355–360, 2001.
- [233] G. Chen, J. Qiu, and H. Qiu, “Filling double-walled carbon nanotubes with AgCl nanowires,” *Scr. Mater.*, vol. 58, no. 6, pp. 457–460, 2008.

- [234] Y. Zhu, H. Liu, L. Yang, and J. Liu, "Study on the synthesis of Ag/AgCl nanoparticles and their photocatalytic properties," *Mater. Res. Bull.*, vol. 47, no. 11, pp. 3452–3458, 2012.
- [235] Y. Sun, "Conversion of Ag nanowires to AgCl nanowires decorated with Au nanoparticles and their photocatalytic activity," *J. Phys. Chem. C*, vol. 114, no. 5, pp. 2127–2133, 2010.
- [236] Y. Bi and J. Ye, "In situ oxidation synthesis of Ag/AgCl core-shell nanowires and their photocatalytic properties," *Chem. Commun.*, no. 43, p. 6551, 2009.
- [237] G. Chen, J. Qiu, and H. Qiu, "Filling double-walled carbon nanotubes with AgCl nanowires," *Scr. Mater.*, vol. 58, no. 6, pp. 457–460, 2008.
- [238] J. Peters and B. Krebs, "Silicon disulphide and silicon diselenide: a reinvestigation," *Acta Crystallogr. B*, vol. 38, no. 4, pp. 1270–1272, 1982.
- [239] A. M. Rao, "Diameter-Selective Raman Scattering from Vibrational Modes in Carbon Nanotubes," *Science*, vol. 275, no. 5297, pp. 187–191, 1997.
- [240] Z. Liu *et al.*, "Multiplexed multicolor raman imaging of live cells with isotopically modified single walled carbon nanotubes," *J. Am. Chem. Soc.*, vol. 130, no. 41, pp. 13 540–13 541, 2008.
- [241] A. Jorio *et al.*, "G-band resonant Raman study of 62 isolated single-wall carbon nanotubes," *Phys. Rev. B*, vol. 65, no. 15, p. 155412, 2002.
- [242] B. Das, R. Voggu, C. S. Rout, and C. N. R. Rao, "Changes in the electronic structure and properties of graphene induced by molecular charge-transfer," *Chem. Commun.*, vol. 2, no. 41, p. 5155, 2008.
- [243] C. N. Rao and R. Voggu, "Charge-transfer with graphene and nanotubes," *Mater. Today*, vol. 13, no. 9, pp. 34–40, 2010.
- [244] C. M. Lieber *et al.*, "Electronic transition energy  $E_{ii}$  for an isolated  $(n, m)$  single-wall carbon nanotube obtained by anti-Stokes/Stokes resonant Raman intensity ratio," *Phys. Rev. B*, vol. 63, no. 24, p. 241404, 2001.
- [245] Y. Gillet, M. Giantomassi, and X. Gonze, "First-principles study of excitonic effects in Raman intensities," *Phys. Rev. B*, vol. 88, no. 9, 2013.

- [246] R. M. A. Lieth and J. C. J. M. Terhell, “Transition Metal Dichalcogenides,” in *Preparation and Crystal Growth of Materials with Layered Structures*. Springer Netherlands, 1977, pp. 141–223.
- [247] K. S. Novoselov *et al.*, “Two-dimensional atomic crystals,” *Proc. Natl. Acad. Sci.*, vol. 102, no. 30, pp. 10 451–10 453, 2005.
- [248] B. Radisavljevic, A. Radenovic, J. Brivio, V. Giacometti, and A. Kis, “Single-layer MoS<sub>2</sub> transistors,” *Nat. Nanotechnol.*, vol. 6, no. 3, pp. 147–150, 2011.
- [249] Q. H. Wang, K. Kalantar-Zadeh, A. Kis, J. N. Coleman, and M. S. Strano, “Electronics and optoelectronics of two-dimensional transition metal dichalcogenides,” *Nat. Nanotechnol.*, vol. 7, no. 11, pp. 699–712, 2012.
- [250] A. Splendiani *et al.*, “Emerging photoluminescence in monolayer MoS<sub>2</sub>,” *Nano Lett.*, vol. 10, no. 4, pp. 1271–1275, 2010.
- [251] J. Lin *et al.*, “Flexible metallic nanowires with self-adaptive contacts to semiconducting transition-metal dichalcogenide monolayers,” *Nat. Nanotechnol.*, vol. 9, no. 6, pp. 436–442, 2014.
- [252] F. J. Ribeiro, D. J. Roundy, and M. L. Cohen, “Electronic properties and ideal tensile strength of MoSe nanowires,” *Phys. Rev. B*, vol. 65, no. 15, pp. 1–4, 2002.
- [253] Y. Shi *et al.*, “Highly Ordered Mesoporous Crystalline MoSe<sub>2</sub> Material with Efficient Visible-Light-Driven Photocatalytic Activity and Enhanced Lithium Storage Performance,” *Adv. Funct. Mater.*, vol. 23, no. 14, pp. 1832–1838, 2013.
- [254] A. J. Morris, R. J. Nicholls, C. J. Pickard, and J. R. Yates, “OptaDOS: A tool for obtaining density of states, core-level and optical spectra from electronic structure codes,” *Comput. Phys. Commun.*, vol. 185, no. 5, pp. 1477–1485, 2014.
- [255] R. J. Nicholls, A. J. Morris, C. J. Pickard, and J. R. Yates, “OptaDOS - A new tool for EELS calculations,” in *J. Phys. Conf. Ser.*, vol. 371, 2012.
- [256] J. R. Yates, X. Wang, D. Vanderbilt, and I. Souza, “Spectral and Fermi surface properties from Wannier interpolation,” *Phys. Rev. B*, vol. 75, no. 19, p. 195121, 2007.

- [257] C. H. Chang, X. Fan, S. H. Lin, and J. L. Kuo, “Orbital analysis of electronic structure and phonon dispersion in MoS<sub>2</sub>, MoSe<sub>2</sub>, WS<sub>2</sub>, and WSe<sub>2</sub> monolayers under strain,” *Phys. Rev. B*, vol. 88, no. 19, p. 195420, 2013.
- [258] M. J. Rutter, “C2x: A tool for visualisation and input preparation for CASTEP and other electronic structure codes,” *Comput. Phys. Commun.*, vol. 225, pp. 174–179, 2018.
- [259] M. Y. Han, B. Özyilmaz, Y. Zhang, and P. Kim, “Energy band-gap engineering of graphene nanoribbons,” *Phys. Rev. Lett.*, vol. 98, no. 20, 2007.
- [260] A. M. Smith and S. Nie, “Semiconductor nanocrystals: Structure, properties, and band gap engineering,” *Acc. Chem. Res.*, vol. 43, no. 2, pp. 190–200, 2010.
- [261] T. Makino *et al.*, “Band gap engineering based on Mg<sub>x</sub>Zn<sub>1-x</sub>O and Cd<sub>y</sub>Zn<sub>1-y</sub>O ternary alloy films,” *Appl. Phys. Lett.*, vol. 78, no. 9, pp. 1237–1239, 2001.
- [262] R.-W. Shao *et al.*, “Bandgap engineering and manipulating electronic and optical properties of ZnO nanowires by uniaxial strain.” *Nanoscale*, vol. 6, no. 9, pp. 4936–41, 2014.
- [263] E. Y. Li, “Band gap engineering of carbon nanotubes via regular addition patterns of covalent functional groups,” *Carbon*, vol. 100, pp. 187–195, 2016.
- [264] Z. Wang, Y. Zhou, Y. Zhang, and F. Gao, “Band-Gap Engineering of Carbon Nanotubes with Grain Boundaries,” *J. Phys. Chem. C*, vol. 116, no. 3, pp. 2271–2277, 2012.
- [265] V. Crespi, M. L. Cohen, and A. Rubio, “In Situ Band Gap Engineering of Carbon Nanotubes,” *Phys. Rev. Lett.*, vol. 79, no. 11, p. 2093, 1997.
- [266] Y. H. Yang and W. Z. Li, “Radial elasticity of single-walled carbon nanotube measured by atomic force microscopy,” *Appl. Phys. Lett.*, vol. 98, no. 4, p. 041901, 2011.
- [267] D. Sánchez-Portal, E. Artacho, J. M. Soler, A. Rubio, and P. Ordejon, “Ab-initio structural, elastic, and vibrational properties of carbon nanotubes,” *Phys. Rev. B*, vol. 59, no. 19, pp. 12 678–12 688, 1998.
- [268] G. Thomas Mase and G. E. Mase, *Continuum Mechanics for Engineers, Second Edition*. CRC Press, 1999.

- [269] P. T. Araujo *et al.*, “Resonance Raman spectroscopy of the radial breathing modes in carbon nanotubes,” *Phys. E Low-Dimensional Syst. Nanostructures*, vol. 42, no. 5, pp. 1251–1261, 2010.
- [270] R. Saito, T. Takeya, T. Kimura, G. Dresselhaus, and M. Dresselhaus, “Raman intensity of single-wall carbon nanotubes,” *Phys. Rev. B*, vol. 57, no. 7, pp. 4145–4153, 1998.
- [271] Y. Shen, N. Quirke, and D. Zerulla, “Polarisation dependence of the squash mode in the extreme low frequency vibrational region of single walled carbon nanotubes,” *Appl. Phys. Lett.*, vol. 106, no. 20, p. 201902, 2015.
- [272] J. P. Lu, “Elastic properties of carbon nanotubes and nanoropes,” *Phys. Rev. Lett.*, vol. 79, no. 7, pp. 1297–1300, 1997.
- [273] L. J. Hall *et al.*, “Sign change of poisson’s ratio for carbon nanotube sheets,” *Science*, vol. 320, no. 5875, pp. 504–507, 2008.
- [274] J. Watson and F. Crick, “Molecular structure of nucleic acids,” *Nature.*, vol. 171, no. 4356, pp. 737–8, 1953.
- [275] J. Goodman, *Introduction to Fourier Optics, 2nd Edition*. Roberts and Co., 2005.
- [276] C. Suryanarayana and M. G. Norton, *X-Ray diffraction: a practical approach*. Springer Science + Business Media, 1998.
- [277] J. M. Zuo, T. Kim, A. Celik-Aktas, and J. Tao, “Quantitative structural analysis of individual nanotubes by electron diffraction,” *Zeitschrift für Krist.*, vol. 222, no. 11, pp. 625–633, 2007.
- [278] H. A. Posch, W. G. Hoover, and F. J. Vesely, “Canonical dynamics of the Nosé oscillator: Stability, order, and chaos,” *Phys. Rev. A*, vol. 33, no. 6, pp. 4253–4265, 1986.
- [279] R. D. King-Smith and D. Vanderbilt, “First-principles investigation of ferroelectricity in perovskite compounds,” *Phys. Rev. B*, vol. 49, no. 9, pp. 5828–5844, 1994.

- 
- [280] A. Vasylenko *et al.*, “Electronic Structure Control of Sub-Nanometer 1D SnTe via Nanostructuring within Single-Walled Carbon Nanotubes,” *ACS Nano*, vol. 12, no. 6, pp. 6023–6031, 2018.
- [281] A. H. Edwards *et al.*, “Theory of persistent, p-type, metallic conduction in c-GeTe,” *J. Phys. Condens. Matter*, vol. 17, no. 32, pp. L329–L335, 2005.

